Multi-scale models for the prediction of bone remodelling due to musculoskeletal interventions

Saira Mary Farage-O'Reilly

A thesis submitted in fulfilment of the requirements of the degree of Doctor of Philosophy

Supervisors

Prof Enrico Dall'Ara

Prof Visakan Kadirkamanathan

Dr Vee San Cheong

Prof Ilaria Bellantuono

Prof Peter Pivonka (Queensland University of Technology, Australia)

The University of Sheffield

School of Medicine and Population Health

Division of Clinical Medicine

August 2024

A product of countless minds and hearts, this work is dedicated to the unwavering support of my family, friends and beloved.

I: Acknowledgements

As I reflect on my PhD journey, I'm surprised by how much can happen in a few short years. When I think that this began during a pandemic – something that now feels so far away – I wouldn't have believed then that this journey would come to an end. I've met so many wonderful people, and I'm grateful for the opportunities for growth that I've gained through this experience.

I'm especially thankful to my primary supervisor, Professor Enrico Dall'Ara, for his guidance and support over the years. I'm grateful for the many hours he has spent sharing his knowledge – particularly through his drawings, which were always quite special. Thank you to Dr Vee San Cheong for her consistent support, despite the varying miles between us. Her encouragement and mentorship have been invaluable. I would also like to thank my supervisors Professor Peter Pivonka, Professor Ilaria Bellantuono and Professor Visakan Kadirkamanathan for their ideas and contributions.

Besides my supervisors I'd also like to thank Ms Holly Evans, Dr Rebecca Andrews and Dr Michelle Lawson for their support and expertise, which they generously shared with me as they welcomed me into the world of myeloma research. I also thank the HELSI ECR community, the lovely Dr Gemma Stephens who created so many fun experiences (in and out of the university), and all those on the C+ floor who shared many kitchen chats with me. Finally, I thank the University of Sheffield for the scholarship without which none of this would have been possible.

On a personal note, I'm deeply grateful to my beautiful family and friends for their support and belief in me. They have had such patience listening to oh so many rehearsals for conference presentations and have been instrumental in building my confidence.

Lastly, thank you to my beloved Eloise. Half of this should really belong to her. Her love and support really were the foundation of this journey.

II: Abstract

Bone is a dynamic tissue that constantly adapts to biomechanical and biochemical stimuli. Imbalances in the bone remodelling processes underlie skeletal diseases such as osteoporosis and myeloma bone disease, leading to increased fracture risk. This thesis aimed to develop and utilise *in silico* biomechanical models to enhance the understanding of how these diseases affect the bone properties.

A literature review highlighted the limitations in existing *in silico* biomechanical models of osteoporotic bone. The current research demonstrated that the micro-finite element (micro-FE) models used to calculate the strain distribution and, hence, predict the bone properties usually only investigate one loading condition. It is assumed that any load applied is axial to the bone, and hence, they ignore any uncertainties in the loading direction and magnitude from experimental measurements. To address this, a sensitivity analysis of the loading direction on the mechanical properties and strain distributions within the mouse tibia was conducted. This analysis is crucial for optimising the protocols for *in vivo* loading experiments and provides insights into how the loading direction influences bone remodelling.

Furthermore, the literature review revealed a lack of accurate predictions of bone resorption in biomechanical models coupled with mechanoregulation algorithms. To address this, an exploratory multi-scale model was developed, integrating validated micro-FE models with a bone cell population model. This model enabled an investigation of the sensitivity of biochemical stimuli on bone remodelling over time, providing insights into the model's complexity and potential for simplification.

Finally, a scarcity of micro-FE models based on high-resolution images depicting osteocyte lacunae was identified. To address this, the tools developed in the previous chapters were adapted to create a micro-FE model of bone tissue that included osteocyte lacunae. This enabled the investigation of the effect of osteocyte lacunae on local bone properties in both healthy and myeloma-affected mice.

III: Declaration

I, Saira Mary Farage-O'Reilly, confirm that the Thesis is my own work. I am aware of the University's Guidance on the Use of Unfair Means (www.sheffield.ac.uk/ssid/unfair-means). This work has not previously been presented for an award at this, or any other, university.

This thesis incorporates one peer-reviewed and published research article, which has been adapted to include a further study. This publication is title: The loading direction dramatically affects the mechanical properties of the mouse tibia. The author list is as follows: Farage-O'Reilly S.M., Cheong V.S., Pickering E., Pivonka P., Bellantuono I., Kadirkamanathan V., Dall'Ara E. Author contributions: SF: conceptualisation, planning and conducting computational modelling, analysing the data, drafting the original manuscript, review and editing, and funding acquisition. VC: conceptualisation, developed the micro-CT to FE pipeline, analysing data, review, and editing. EP: conceptualisation, analysing data, review, and editing. PP: conceptualisation, analysing data, review, and editing. IB: review and editing. VK: review and editing. ED: conceptualisation, analysing the data, funding acquisition, project administration, supervision, review, and editing. All authors contributed to the article and approved the submitted version.

This thesis also incorporates three manuscripts in preparation. The first is titled: Quantifying the local strain energy density distribution in the mouse tibia: the critical role of the loading direction. The author list is as follows: Farage-O'Reilly S.M., Cheong V.S., Pivonka P., Kadirkamanathan V., Dall'Ara E. Author contributions: SF: conceptualisation, planning and conducting computational modelling, analysing the data, drafting the original manuscript, review and editing, and funding acquisition. VC: conceptualisation, developed the micro-CT to FE pipeline, analysing data, review, and editing. PP: conceptualisation, analysing data, review, and editing. VK: analysing the data, review and editing. ED: conceptualisation, analysing the data, funding acquisition, project administration, supervision, review, and editing.

The second manuscript in preparation (a short communication) is titled: Assessing the heterogeneity of biomechanical and biochemical influence in a multiscale biomechano-chemo model of bone adaptation within a cortical section of the mouse tibia. The author list is as follows: Farage-O'Reilly S.M., Miller C., Cheong V.S., Pivonka P., Dall'Ara E. Author contributions: SF: conceptualisation, planning and conducting computational modelling, analysing the data, drafting the original manuscript, review and editing, and funding acquisition. CM: developed the bone cell population model (originally developed by QUT Centre for Biomechanics research group). VC: developed the micro-CT to FE pipeline, analysing data, review, and editing. PP: conceptualisation, analysing data, review, and editing. ED:

conceptualisation, analysing the data, funding acquisition, project administration, supervision, review, and editing.

The third manuscript in preparation is titled: Myeloma bone disease affects the local mechanical properties of the mouse femur. The author list is as follows: Farage-O'Reilly S.M., Evans H., Andrews R., Trend J., Lovric G., Cheong V.S., Lawson M., Dall'Ara E. Author contributions: SF: conceptualisation, planning and conducting computational modelling, analysing the data, drafting the original manuscript, review and editing, and funding acquisition. HE: data collection, conducting computational analysis (region of interest extraction, porosity calculation), analysing the data, review and editing. RA: data collection, analysing the data, review and editing. JT: data collection, review and editing. GL: data collection, experimental methodology, review and editing. ML: data collection, analysing the data, review and editing, and funding acquisition. VC: developed the micro-CT to FE pipeline, analysing data, review, and editing. ED: conceptualisation, analysing the data, funding acquisition, project administration, supervision, review, and editing.

Saira Mary Farage-O'Reilly

August 2024

IV: Scientific output

Awards and recognition

European Society of Biomechanics Travel Award 2024

Division of Clinical Medicine Travel and Conference Bursary 2024

Associate Fellow of Higher Education Academy recognition 2023

Healthy Lifespan Institute Travel Bursary 2023

Runner up for the 'Best PhD Talk' at BioMedEng 2022

University of Sheffield EPSRC Doctoral Training Partnership (DTP) Scholarship (X/0139912-12)

Publications

Farage-O'Reilly S.M., Cheong V.S., Pickering E., Pivonka P., Bellantuono I., Kadirkamanathan V., Dall'Ara E., 2024. The loading direction dramatically affects the mechanical properties of the mouse tibia. *Frontiers in Bioengineering and Biotechnology, Volume 12.* doi: 10.3389/fbioe.2024.1335955

Abstracts accepted for oral presentations

Farage-O'Reilly S.M., Evans H., Andrews R., Trend J., Lovric G., Cheong V.S., Lawson M., Dall'Ara E. Multiple myeloma increases local bone mechanical anisotropy in a murine model. Bone Research Society Annual Meeting, 10th-12th July 2024.

Farage-O'Reilly S.M., Evans H., Andrews R., Trend J., Lovric G., Cheong V.S., Lawson M., Dall'Ara E. Multiple myeloma decreases the local stiffness of the anterior and posterior distal femur of a murine model. European Society of Biomechanics, 31st June - 3rd August 2024.

Farage-O'Reilly S.M. Exploring the use of finite element (FE) modelling in preclinical research. Healthy Lifespan Computer Science and Statistics Symposium, 10th June 2024.

Farage-O'Reilly S.M., Evans H., Andrews R., Trend J., Lovric G., Cheong V.S., Lawson M., Dall'Ara E. Multiple myeloma increases local bone mechanical anisotropy in a murine model. Mellanby Research Day, 15th March 2024.

Farage-O'Reilly S.M., Evans H., Andrews R., Trend J., Lovric G., Cheong V.S., Lawson M., Dall'Ara E. Multiple myeloma increases local bone mechanical anisotropy in a murine model. Mellanby Research Day, 15th March 2024.

Farage-O'Reilly S.M., Cheong V.S, Bellantuono I., Kadirkamanathan V., Dall'Ara E. Effect of the loading direction on the predicted local mechanical properties of the tibia in the ovariectomised mouse model. International Society of Biomechanics, 30th July - 3rd August 2023.

Farage-O'Reilly S.M., Cheong V.S, Bellantuono I., Kadirkamanathan V., Dall'Ara E. Effect of the loading direction on the predicted mechanical properties of the mouse tibia. European Society of Biomechanics, 9th-12th July 2023.

Farage-O'Reilly S.M., Cheong V.S, Dall'Ara E. Effect of the loading direction on the predicted local mechanical properties of the mouse tibia. BioMedEng, 8th-9th September 2022.

Abstracts accepted for poster presentations

Farage-O'Reilly S.M., Cheong V.S, Dall'Ara E. Relationship between the mouse cortical thickness and its failure load evaluated along different loading directions. British Orthopeadic Research Society, 9th-10th September 2024.

Farage-O'Reilly S.M., Cheong V.S, Dall'Ara E. Relationship between the mouse cortical thickness and its failure load evaluated along different loading directions. BioMedEng, 5th-6th September 2024.

Farage-O'Reilly S.M., Evans H., Andrews R., Trend J., Lovric G., Cheong V.S., Lawson M., Dall'Ara E. Multiple myeloma decreases the local stiffness of the anterior, posterior and lateral distal femur of a murine model. Insigneo Showcase, 14th June 2024.

Farage-O'Reilly S.M., Cheong V.S, Dall'Ara E. Effect of the loading direction on the predicted failure load of the mouse tibia. Healthy Lifespan Institute Annual Meeting, 2nd October 2023.

Farage-O'Reilly S.M., Cheong V.S, Dall'Ara E. Effect of the loading direction on the predicted failure load of the mouse tibia. Insigneo Showcase, 14th July 2023.

Farage-O'Reilly S.M., Cheong V.S, Dall'Ara E. Effect of the loading direction on the predicted local mechanical properties of the mouse tibia. Mellanby Research Day, 24th March 2023.

Farage-O'Reilly S.M., Cheong V.S, Dall'Ara E. Effect of the loading direction on the predicted local mechanical properties of the mouse tibia. Healthy Lifespan Institute Annual Meeting, 5th October 2022.

Farage-O'Reilly S.M., Cheong V.S, Dall'Ara E. Effect of the loading direction on the predicted local mechanical properties of the mouse tibia. Insigneo Showcase, 8th July 2022.

V: Contents

VI: List of tables

VII: List of figures

VIII: List of abbreviations

2D	Two-dimensional
3D	Three-dimensional
95P_SED	Median of the 95^{th}-100^{th} percentile of the strain energy density
A	Anterior
ABM	Agent-based model
absΔ95t_SED	Absolute difference in 95P_SED from the finite element model between time points
absΔFLt_FE	Absolute difference in failure load from the finite element model between time points
AP	Anterior-posterior
Bcl-2	B-cell lymphoma 2
BCPM	Bone cell population model
BMC	Bone mineral content
BMD	Bone mineral density
BMU	Bone multicellular unit
BT	Beam theory
BV	Bone volume
BV/TV	Bone volume fraction
Ct.Th	Cortical thickness
CV	Coefficient of variation
DA	Degree of anisotropy
DIC	Digital image correlation
DVC	Digital volume correlation
E	Young's modulus
F^{AP}	Force in the anterior-posterior direction
FE	Finite element
F^{IS}	Force in the inferior-superior direction
FL_FE	Failure load from the finite element model
F^{ML}	Force in the medio-lateral direction
IQR	Interquartile range
L	Lateral
LC	Bone lining cell

LCN	Lacuna-canaliculi network
LRP5/6	Low-density lipoprotein-related receptors 5 and 6
M	Medial
M^{AP}	Moment about the anterior-posterior axis
MBD	Myeloma bone disease
M-CSF	Macrophage colony-stimulating factor
Micro-CT	Micro-computed tomography
Micro-FE	Micro-finite element
M^{IS}	Moment about the inferior-superior axis
ML	Medio-lateral
MM	Multiple myeloma
M^{ML}	Moment about the medio-lateral axis
N95P_SED	Normalised median of the 95th-100th percentiles of the strain energy density
NFL_FE	Normalised failure load from the finite element model
NO	Nitric oxide
NSG	NOD.Cg-PrkdcscidIl2rgtm1Wjl/SzJ
OB_a	Osteoblast
OB_p	Osteoblast precursor
OC_a	Osteoclast
Ocy.L V	Osteocyte lacunae volume
Ocy.L/BV	Osteocyte lacunae density
ODE	Ordinary differential equation
OPG	Osteoprotegerin
OVX	Ovariectomy
OVX+ML	Ovariectomy and mechanical loading
P	Posterior
pCREB	Phosphorylation of CREB
PD	Pharmacodynamic
P^E	Endosteal array
PK	Pharmacokinetic
PK/PD	Pharmacokinetic/pharmacodynamic
PLR	Perilacunar remodelling
P^P	Periosteal array
PTH	Parathyroid hormone

RANK	Receptor activator of nuclear factor kappa-B
RANKL	Receptor activator of nuclear factor kappa-B ligand
RF	Reaction forces
ROI	Region of interest
RSE	Representative surface element
Runx2	Runt-related transcription factor 2
RVE	Representative volume element
S_FE	Apparent bone stiffness from the finite element model
Scl	Sclerostin
SD	Standard deviation
SED	Strain energy density
SF	Safety factor
SI	Superior-inferior
SR-micro-CT	Synchrotron radiation computed tomography
Tb.BV/TV	Trabecular bone volume fraction
Tb.N	Trabecular number
Tb.Sp	Trabecular spacing
TGF-β	Transforming growth factor type beta
TMD	Tissue mineral density
U266	U266-GFP-luc cells
UK	United Kingdom
W18	Week 18
W20	Week 20
WHO	World Health Organisation
Wnt	Wingless-related integration site
Δ95Pg_FE	Percentage point difference of the median 95^{th}-100^{th} percentiles from the SED between groups
Δ95Pt_FE	Percentage difference in the median 95^{th}-100^{th} percentiles from the SED between time points
ΔFLg_FE	Percentage point difference of the failure load from the finite element model between groups
ΔFLt_FE	Percentage difference in failure load from the finite element model between time points

ε	Strain
ν	Poisson’s ratio
σ	Stress

IX: Third-party copyright permissions

Copyright permissions were obtained for all third-party content used in this thesis and are listed in Table 1.

Table 1: *Third party copyright permissions showing the original source, figure location and permissions.*

Original source	Figure number	Permission granted (Y/N)
Yu, B., Pacureanu, A., Olivier, C., Cloetens, P., and Peyrin, F. (2021). Quantification of the bone lacunocanalicular network from 3D X-ray phase nanotomography images. *J. Microsc.* 282, 30–44. doi: 10.1111/JMI.12973	Figure 1.6	Y
Ferguson, S.J., Steffen, T. (2003). Biomechanics of the aging spine. *Eur Spine J* 12 (Suppl 2), S97–S103. doi: 10.1007/s00586-003-0621-0	Figure 1.10	Y
Hemmatian, H., Bakker, A. D., Klein-Nulend, J., and van Lenthe, G. H. (2021). Alterations in osteocyte lacunar morphology affect local bone tissue strains. *J. Mech. Behav. Biomed. Mater.* 123. doi: 10.1016/J.JMBBM.2021.104730	Figure 2.6	Y
Stadelmann, V. A., Hocke, J., Verhelle, J., Forster, V., Merlini, F., Terrier, A., et al. (2009). 3D strain map of axially loaded mouse tibia: a numerical analysis validated by experimental measurements. *Comput. Methods Biomech. Biomed. Engin.* 12, 95–96. doi: 10.1080/10255840903077287	Figure 2.7	Y
Schulte, F. A., Zwahlen, A., Lambers, F. M., Kuhn, G., Ruffoni, D., Betts, D., et al. (2013b). Strain-adaptive in silico modeling of bone adaptation--a computer simulation validated by in vivo micro-computed tomography data. *Bone* 52, 485–492. doi: 10.1016/J.BONE.2012.09.008	Figure 2.13	Y
Lerebours, C., Buenzli, P. R., Scheiner, S., and Pivonka, P. (2016). A multiscale mechanobiological model of bone remodelling predicts site-specific bone loss in the femur	Figure 2.14	Y

during osteoporosis and mechanical disuse. *Biomech. Model. Mechanobiol.* 15, 43–67. doi: 10.1007/S10237-015-0705-X		
Ashrafi, M., Gubaua, J. E., Pereira, J. T., Gahlichi, F., and Doblaré, M. (2020). A mechano-chemo-biological model for bone remodeling with a new mechano-chemo-transduction approach. *Biomech. Model. Mechanobiol.* 19, 2499–2523. doi: 10.1007/S10237-020-01353-0	Figure 2.15	Y

Chapter 1: Introduction and theoretical background

1.1 Introduction

1.1.1 Motivation

Bone diseases, such as osteoporosis and myeloma bone disease (MBD), pose significant challenges to both individuals and healthcare systems worldwide. These conditions not only diminish individuals' quality of life but also incur substantial costs for diagnosis, treatment, and fracture management.

Osteoporosis, characterised by reduced bone mass and architectural deterioration, leads to heightened bone fragility and increased fracture risk (European Foundation for Osteoporosis, 1993). A 2021 report conducted in the United Kingdom (UK) revealed that an estimated 3.8 million individuals are affected by osteoporosis (Kanis et al., 2021). This condition disproportionately impacts older adults, with roughly 21.9% of women and 6.7% of men, aged 50 years and older, estimated to have osteoporosis. The report further highlights the significant public health burden, estimating that one fragility fracture occurs per minute due to falls from standing height or less (Kanis et al., 2021). These fractures can lead to individuals being in pain, becoming disabled, and can also contribute to premature mortality. The cost of osteoporotic fractures in the UK accounted for approximately 2.4% of healthcare spending, equating to approximately £4.7 billion (Kanis et al., 2022). Furthermore, as the population in the UK aged 50 or more is predicted to increase by 13.2% between 2019 and 2034, the number of fragility fractures are likely to increase, increasing the burden on healthcare providers.

Although multiple myeloma, a type of bone marrow cancer affecting around 6,200 individuals in the UK annually (Northern Ireland Cancer Registry, 2021; Public Health Scotland, 2021; Welsh Cancer Intelligence and Surveillance Unit, 2022; NHS England, 2023), is itself not a bone disease, an alarming 80-90% of diagnosed patients will develop MBD (Coleman, 1997; Kyle et al., 2003). Similar to osteoporosis, MBD increases the risk of fracture, with affected individuals experiencing a 20% increase in mortality compared to those without fracture (Saad et al., 2007). Moreover, given that multiple myeloma is typically diagnosed around the age of 74, it is probable that individuals may already be living with osteoporosis prior to diagnosis (Turesson et al., 2010). This is particularly concerning considering that higher multiple myeloma mortality rates were found in post-menopausal women (Rosko et al., 2018).

Developing a deeper understanding of how these conditions affect bone is paramount for optimising treatment strategies and thus alleviating the burden on healthcare services. Regulators require new pharmacological interventions to be tested in animals preclinically before clinical trials, with mouse models being the most commonly used animal in drug development (Gould et al., 2015). *In silico* (computational) models offer a powerful tool for simulating disease and predicting treatment responses. Not only do *in silico* models help decrease the time taken for a drug to go from identification to marketing, but they also reduce the number of animals used in the drug development process (NC3Rs, 2021). Furthermore, *in silico* modelling opens avenues for exploring and understanding phenomena that may be difficult or impossible to investigate experimentally, allowing for rapid evaluation of various scenarios (Shaker et al., 2021).

The objective of this chapter is to provide an introductory overview on bone, spanning its anatomy and physiology, and the dynamic processes inherent to bone. Additionally, it aims to present the skeletal diseases examined within this thesis and their respective interventions, explore the biomechanical phenomena associated with bone, and discuss the utilisation of mouse models in preclinical research.

1.1.2 Research aims and objectives

The aim of this project is to develop biomechanical *in silico* models to enhance the understanding of how skeletal diseases, such as osteoporosis and MBD, affect the bone properties. This understanding is critical for improving the ability to predict bone remodelling during treatments for these conditions. To do this, four objectives have been set:

> ***Objective 1*** **-** To create a biomechanical micro-finite element (micro-FE) model of the mouse tibia, including both cortical and trabecular bone to investigate the effect of the loading direction on the bone's mechanical properties, and use these micro-FE models to investigate the relationship between the mouse tibia midshaft cortical thickness and the bone strength, across a range of loading directions.
>
> ***Objective 2*** **-** To use these micro-FE models to investigate the effect of the loading direction on the distribution of local mechanical properties such as the strain and strain energy density within the mouse tibia.
>
> ***Objective 3*** **-** To combine a section of the micro-FE model with a cellular and molecular level model to measure the sensitivity of biochemical stimuli on the bone remodelling.

Objective 4 - To create a biomechanical micro-FE model of the mouse femur bone tissue at high resolution, including the osteocyte lacunae, to investigate the effect of myeloma bone disease on the bone's local mechanical properties.

The following sections of this chapter provide an overview of bone, covering its anatomy and physiology across dimensional scales. This is followed by an outline of the relevant dynamical processes bone undergoes, a characterisation of the skeletal diseases investigated in this thesis and their corresponding treatments, the biomechanical processes of bone, and the use of mouse models in preclinical research.

After this, there are four research chapters, each chapter corresponds to an objective, i.e. Chapter 3 covers Objective 1, Chapter 4 covers Objective 2, Chapter 5 covers Objective 3, and Chapter 6 covers Objective 4. Each chapter is a stand-alone piece of work, in a publication-style format. Therefore, each chapter contains an Introduction, Methods, Results, and Discussion section. The last chapter of this thesis, Chapter 7, serves as a concluding chapter, covering the current limitations of the work presented in this thesis, the contributions to the field of biomechanics and ending with closing thoughts.

Following this, four research chapters are presented, each dedicated to a specific objective. Chapter 3 addresses Objective 1, Chapter 4 addresses Objective 2, Chapter 5 addresses Objective 3, and Chapter 6 addresses Objective 4. Each chapter constitutes a standalone piece of work, adopting a publication-style format, including an Introduction, Materials and Methods, Results, and Discussion section.

The final chapter of this thesis, Chapter 7, serves as a concluding chapter. This chapter addresses the current limitations of the work presented, highlights the contributions made to the field of biomechanics, and concludes with final thoughts.

1.2 Bone anatomy & physiology

1.2.1 Introduction to bone

Bone is a remarkable tissue. It not only serves as the structural framework of the body, offering support, protection, and mobility, but also plays a crucial role in metabolic regulation of the body. Bone provides biomechanical functions, such as facilitating movement and bearing loads (Betts et al., 2013). For instance, the femur, the longest bone in the human body, supports the body's weight and enables

activities such as walking, running, and jumping. Additionally, bone contributes to metabolic regulation by serving as a reservoir for minerals and fats, storing 99% of the body's calcium reserves (Bilezikian et al., 2008) and 85% of its phosphorus (Diem and Lentner, 1970), which are essential for biochemical processes, such as nerve impulse transmission, muscle contraction and hormone secretion (Blanco and Blanco, 2022).

Bone is a dynamic tissue, capable of responding to biomechanical and biochemical stimuli. It possesses the ability to adapt and repair itself, enabling it to withstand mechanical stresses and heal from injuries. This dynamic nature ensures the maintenance of bone over time. Additionally, bone is characterised by a highly hierarchical organisation, ranging across length scales. The subsequent sections of this introduction are structured to progressively explore the hierarchical scales of bone tissue, moving from the whole body and organ level – to the tissue level – to the cellular and molecular level.

1.2.2 Body and organ level

1.2.2.1 Types of bone

Bone is typically classified into four groups: long, short, flat, and irregular (Betts et al., 2013). Each bone is tailored to its specific function within the body. Long bones, such as those found in the arms and legs, support the weight of the body, and facilitate movement. Short bones, such as those found in within the wrist and ankle, provide strength, stability, and support with small movements. Flat bones, such as the skull or sternum, have broad surfaces to provide protection. Lastly, irregular bones, such as the vertebrae, defy categorisation due to their unique shapes. These bones have specialised functions, for example the vertebrae protect and support the spinal cord.

1.2.2.2 Anatomical terminology

To promote an understanding of the position of these bones and their different components within the body, it is worth explaining some of the standardised language that has been employed in order to organise this knowledge. To describe one point in relation to another, for example, the adjectives proximal and distal are used; the region of the tibia which is closest to the femur is the proximal portion of the tibia, while the region of the tibia which is closest to the ankle is the distal portion of the tibia. When describing a point in reference to the front or the back of an entity, the adjectives anterior and posterior are used; the anterior being towards the front of the body and posterior being towards the back (Figure 1.1). Finally, medial describes a point towards the midline while lateral describes a point away from the midline (Figure 1.1).

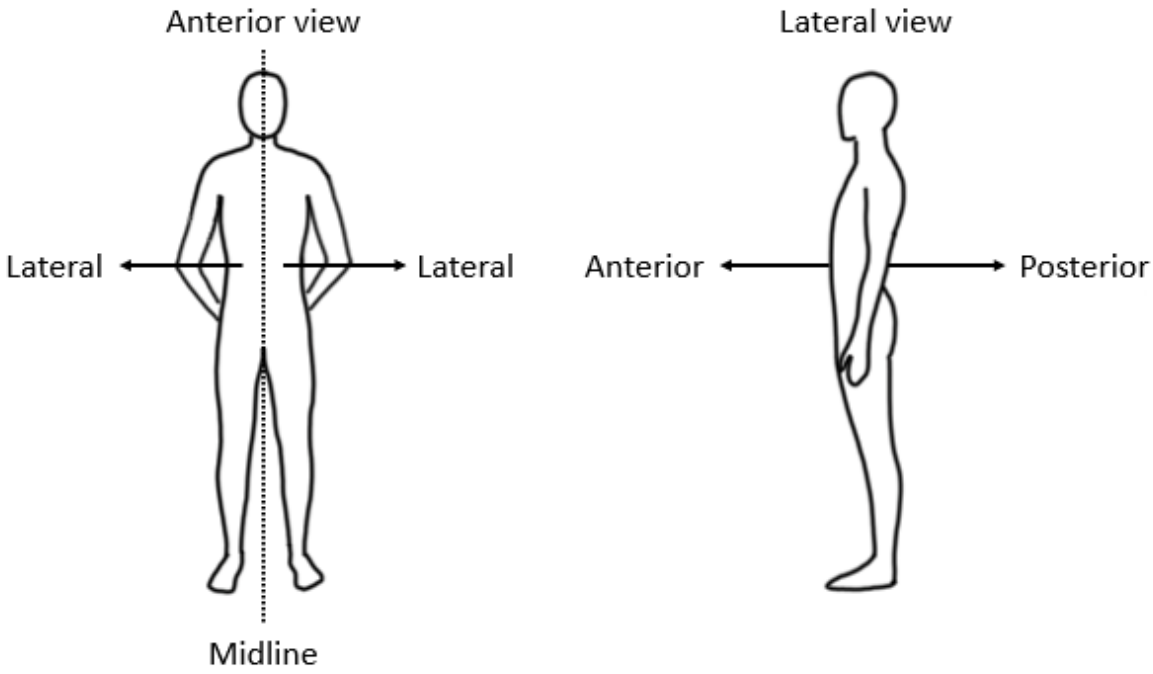

Figure 1.1: *Anatomical terms: anterior, posterior, lateral, and midline.*

1.2.2.3 Morphology of bone at the organ level

Bones exhibit various shapes and sizes, each serving different functions within the body. The four different groups of bone are categorised by their morphology. Long bones are longer than they are wide and consist of a long shaft, known as the diaphysis, as well as two heads situated at either end, called the epiphyses (Figure 1.2). In adult bones, the epiphyseal line lies between the diaphysis and the epiphysis (Figure 1.2) (Betts et al., 2013). The epiphyseal line is a remnant of the flat plate of hyaline cartilage that is found in growing bones, known as the epiphyseal plate, which allows for the elongation of a long bone (Betts et al., 2013).

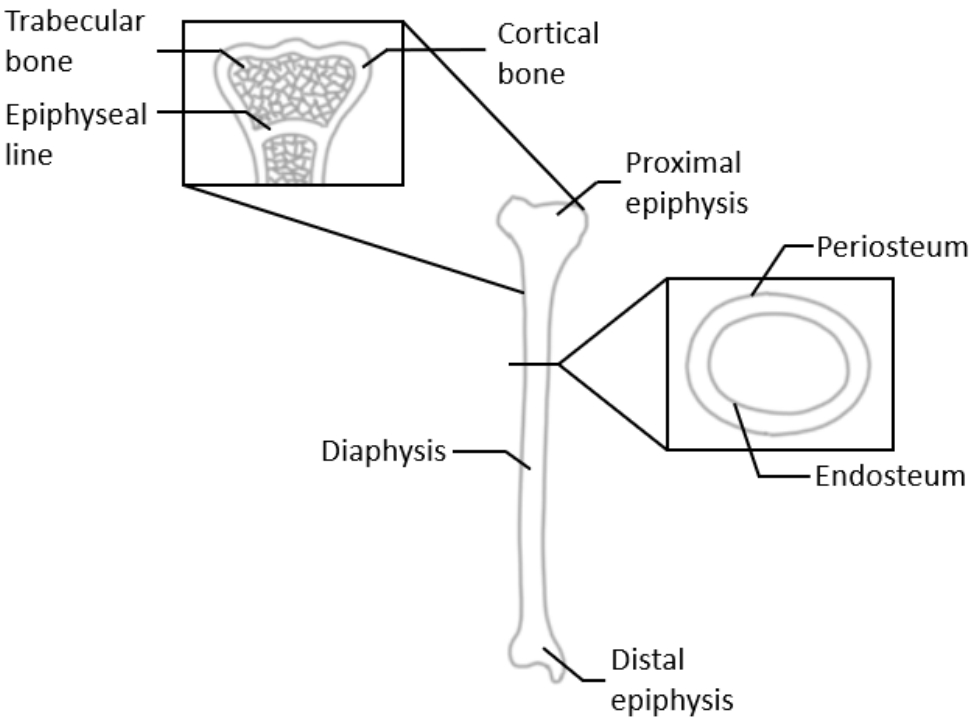

Figure 1.2: *Anatomy of a long bone, illustrating the diaphysis, the epiphyses, cortical and trabecular bone, epiphyseal line (growth plate), periosteum and endosteum.*

The diaphysis of a long bone has an inner medullary cavity composed of yellow bone marrow (Betts et al., 2013). The medullary cavity is lined by a thin vascular membrane of connective tissue, known as the endosteum, and the outer layer of the bone is surrounded by a thin layer of connective tissue, known as the periosteum (Figure 1.2) (Betts et al., 2013). The epiphyses are surrounded by articular cartilage, made from hyaline cartilage, which reduces the friction at joint surfaces (Betts et al., 2013).

1.2.3 Tissue level

There are two basic macrostructures of bone: cortical and trabecular bone. While long bones are composed of both cortical and trabecular bone, the diaphysis of a long bone is composed primarily of cortical bone (Clarke, 2008). The epiphyses, however, are composed of trabecular bone that is enclosed by a thin layer of cortical bone (Figure 1.2) (Clarke, 2008).

Cortical bone, also known as compact bone, is a dense connective tissue that makes up approximately 80% of bone mass (Eriksen, 1994). The porosity of the cortical bone is approximately 5-15%, depending on the location of the tissue (Cowin and Telega, 2003). In humans, the tissue is made up of closely packed osteons (which are also known as Haversian systems) embedded in interstitial bone (Betts et al., 2013). At the centre of this system is a Haversian canal that contains blood vessels, nerve fibres, and lymphatic vessels connected to the periosteal surface (Figures 1.3 & 1.4) (Betts et al., 2013). Around this, each osteon is organised into thin layers of tissue called lamellae. Located between the concentric lamellae of the osteon, are small gaps, called lacunae. These are occupied by osteocyte bone cells (Figures 1.3 & 1.4) (Betts et al., 2013). Between the lacunae, there are small channels known as canaliculi, that link together the lacunae with the Haversian canal, providing passage for nutrients and waste through the system's hard matrix (Betts et al., 2013). This network is known as the lacuna-canaliculi network (LCN). Volkmann canals interconnect the Haversian canals and the periosteum (Betts et al., 2013). Usually being oriented transversally to the length of the bone, they allow for blood vessels to enter bone through the periosteum.

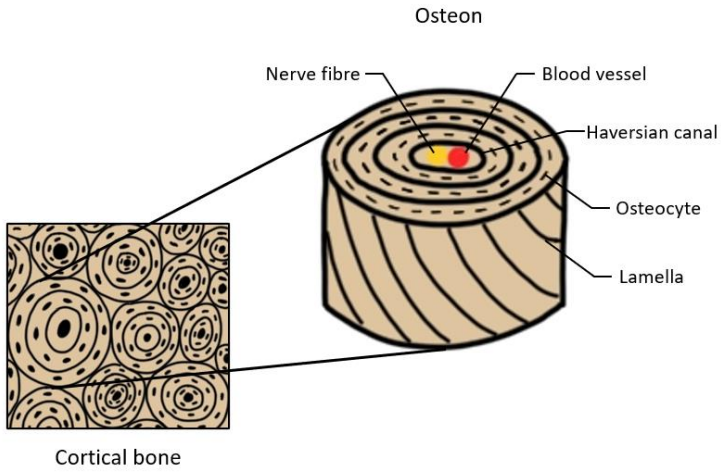

Figure 1.3: *Cortical bone structure, illustrating the osteon and its components (blood vessels (in red and blue), nerve fibre (in yellow), Haversian canal, lamellae, and osteocytes).*

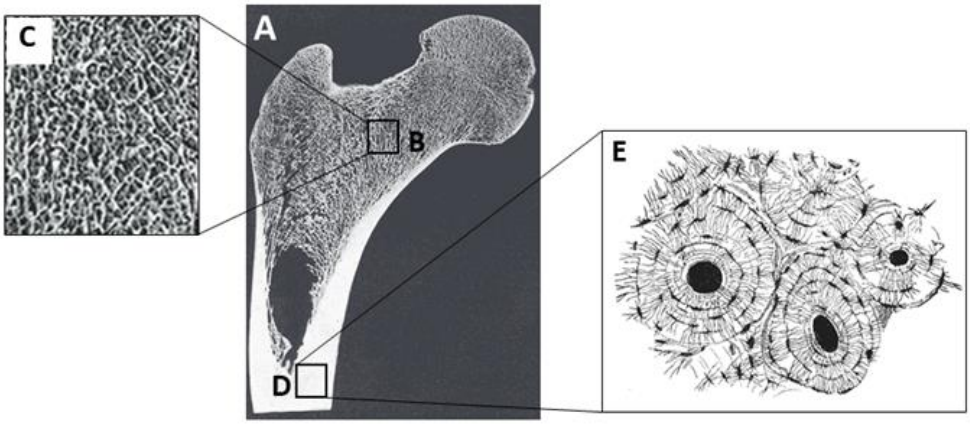

Figure 1.4: *(A) Frontal midsection of proximal femur. (B) Trabecular bone. (C) Magnified segment of trabecular bone. (D) Cortical bone. (E) Magnified segment of cortical bone. Adapted from Gray & Lewis (1918).*

Trabecular bone tissue, also known as cancellous or spongy bone, makes up approximately 20% of bone mass (Eriksen, 1994). Its porosity varies from around 55-95% depending on the exact location of the tissue (Cowin and Telega, 2003). The trabecular bone is composed of trabeculae, which are assembled into a three-dimensional (3D) structure (Figures 1.4 & 1.5), the spaces between them are filled with red or yellow marrow (Betts et al., 2013). Each trabecula is composed of circular lamellae (Figure 1.5) (Betts et al., 2013). Similar to cortical bone, the lacune within the trabecular bone are connected together via the LCN (Figure 1.6).

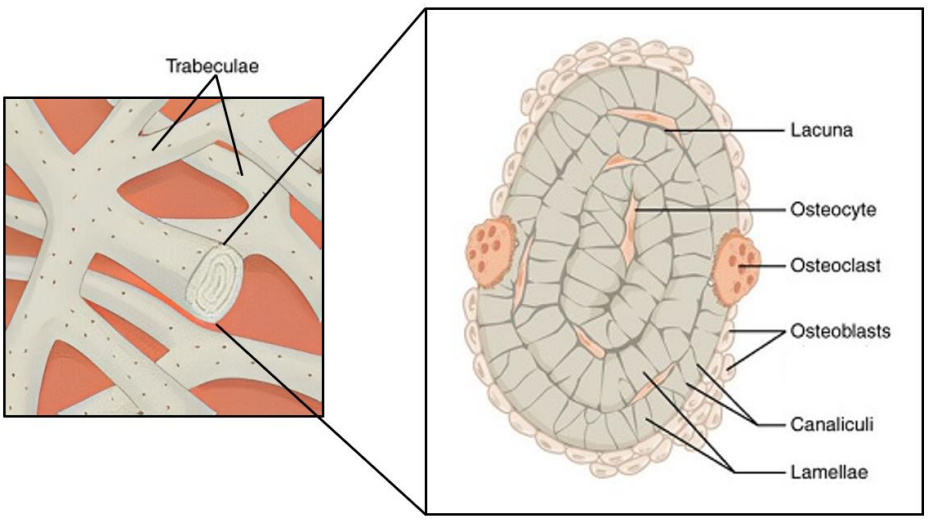

Figure 1.5: *Trabecular bone structure, illustrating the trabeculae and its components (the lacuna, osteocytes, lamellae, and canaliculi). Adapted from Betts et al. (2013).*

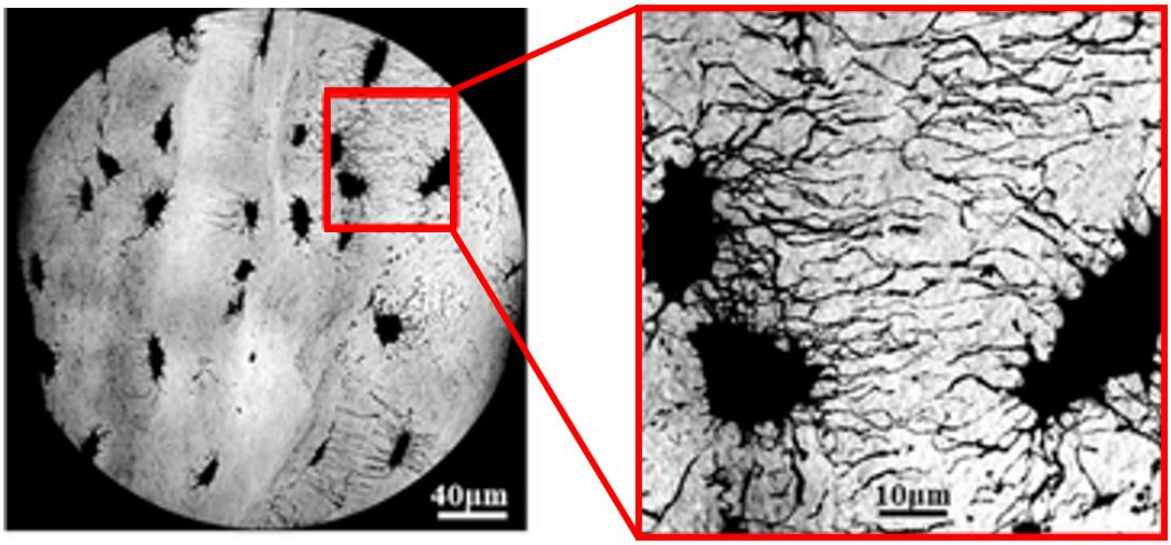

Figure 1.6: *3D X-ray phase nanotomography image showing the bone lacunar-canalicular network (LCN). Adapted from* Yu et al. *(2021).*

1.2.4 Cellular and molecular level

1.2.4.1 Bone Composition

While the adaptation of bone is undertaken at a cellular and molecular level, it is the composition of bone that determines the material properties of the extracellular matrix. Bone is composed of an organic matrix, carbonate-hydroxyapatite, and water (Currey, 2006). The matrix is widely regarded as the scaffolding of the bone and is known to provide it with its stiffness and strength. However, in order to understand these properties, it is worth looking at the microstructural level. Here it becomes possible to observe that 90% of the organic matrix proteins are accounted for through type I collagen (Currey, 2006), and that this is what allows the bone to undergo tensile stress (Viguet-Carrin et al., 2006). The organic matrix is mineralised with carbonate-hydroxyapatite, an insoluble form of calcium and phosphates, that gives the bone its resistance to compression (Le et al., 2018).

1.2.4.2 The bone cells

The bone cells include osteoblasts, osteoclasts, osteocytes, bone lining cells, and their pre-cursors (Figure 1.7). The function of osteoclasts is to resorb bone. They are derived from monocytes and macrophages, two types of white blood cells (Betts et al., 2013). Their activity is normally coupled with osteoblasts, which form new bone tissue. Osteoblasts derive from mesenchymal progenitor stem cells

and can differentiate into either osteocytes or become lining cells (Betts et al., 2013). The exact function of the bone lining cells is unknown. However, due to their position, it has been suggested that they act as the gatekeepers of hormonally controlled bone resorption (Streicher et al., 2017). Additionally, it has been suggested that quiescent bone lining cells along the cortical surface can convert into active osteoblasts, allowing for them to contribute to bone formation along the surface of the bone (Ominsky et al., 2015; Matic et al., 2016). After this formation, they can then covert back into bone lining cells. This continuous reactivation of bone lining cells allows for them to be a major source of active osteoblasts. Osteocytes function as key mechanosensors: they direct bone remodelling by sensing the mechanical strain on the bone and recruiting the relevant bone cells (Chen et al., 2015; Prideaux et al., 2016; Robling and Bonewald, 2020; Palumbo and Ferretti, 2021). This is done through the osteocyte dendrites, which extend outwards from the osteocyte cell body through the canaliculi, making up the LCN (Wang and Wein, 2022). Therefore, they have a significant role in the ongoing process of bone remodelling. It is also debated that an additional function of the osteocytes is to undertake perilacunar remodelling (PLR). This is local bone remodelling, modifying the osteocyte lacunae (Yee et al., 2019; Evans et al., 2024).

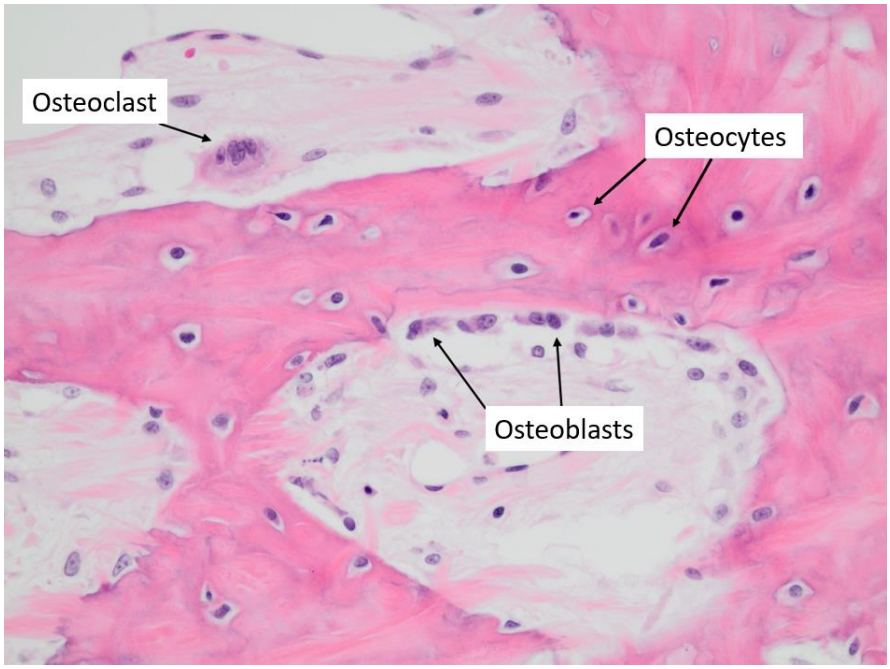

Figure 1.7: *Bone histology images showing the osteoclast, osteoblast, and osteocyte bone cells. Adapted from* Ryan and Premanandan *(2017).*

1.2.5 Bone (re)modelling

1.2.5.1 Bone modelling

Bone modelling facilitates bone growth and alterations in bone shape and size (Betts et al., 2013). Modelling allows for resorption (undertaken by the osteoclasts) and formation (by the osteoblasts) to occur uncoupled, on different surfaces, and at different rates. For example, during growth, the long bone increases in diameter. This is done through osteoblasts depositing bone matrix on the periosteal surface, expanding the bone diameter, while osteoclasts resorb bone on the endosteum surface, expanding the marrow cavity. Modelling also enables changes in bone architecture in response to alterations in mechanical loading. For example, the increased mechanical stress experienced by an athlete's bones during intense physical training stimulates bone modelling, allowing the bone to adapt to changes in mechanical demands.

1.2.5.2 Bone remodelling

The maintenance of bone is undertaken by bone multicellular units (BMU), which maintain equilibrium within the bone remodelling process (Raggatt and Partridge, 2010). Bone modelling can be distinguished from remodelling as the former defines skeletal development and growth, whilst the latter is the lifelong process by which bone is continuously maintained, allowing for the adaptation of bone to external biomechanical and biochemical stimuli (Raggatt and Partridge, 2010). It is the remodelling process of bone that allows it to act as a responsive living tissue, changing in accordance with biomechanical and biochemical stimuli (Hadjidakis and Androulakis, 2006). This process is currently classified into five stages: quiescence, activation, resorption, formation, and mineralisation (Figure 1.8) (Kini and Nandeesh, 2012; Owen and Reilly, 2018). Quiescent bone describes the state of inactivity when zero net remodelling occurs. The activation stage is triggered by an event, for example, a microfracture or an imbalance in molecular concentrations within the bone. During this stage, osteoclast precursors are activated, which allow osteoclasts to be recruited to the site of remodelling. Resorption begins once the osteoclasts bind to the bone surface and secrete acid. When the osteoclasts have finished resorbing the bone, they undergo apoptosis (programmed cell death). Formation occurs when the mature osteoblasts occupy the resorbed cavity and secrete osteoid, an unmineralised organic tissue, primarily composed of collagen fibres (Betts et al., 2013). This is then mineralised over time by the osteoblasts. Some of the osteoblasts differentiate into lining cells, some become trapped in the matrix and differentiate (undergo osteocytogenesis) into osteocytes, while the rest undergo apoptosis (Raggatt and Partridge, 2010; Kini and Nandeesh, 2012; Owen and Reilly, 2018). In healthy bone, the resorption and formation stages are paired, and this pairing is orchestrated by the

BMU (Andersen et al., 2009). The BMU consists of coupled osteoclasts and osteoblasts, which work in unison to maintain a healthy balance of resorption and formation respectively, thus restoring the healthy bone (Hadjidakis and Androulakis, 2006).

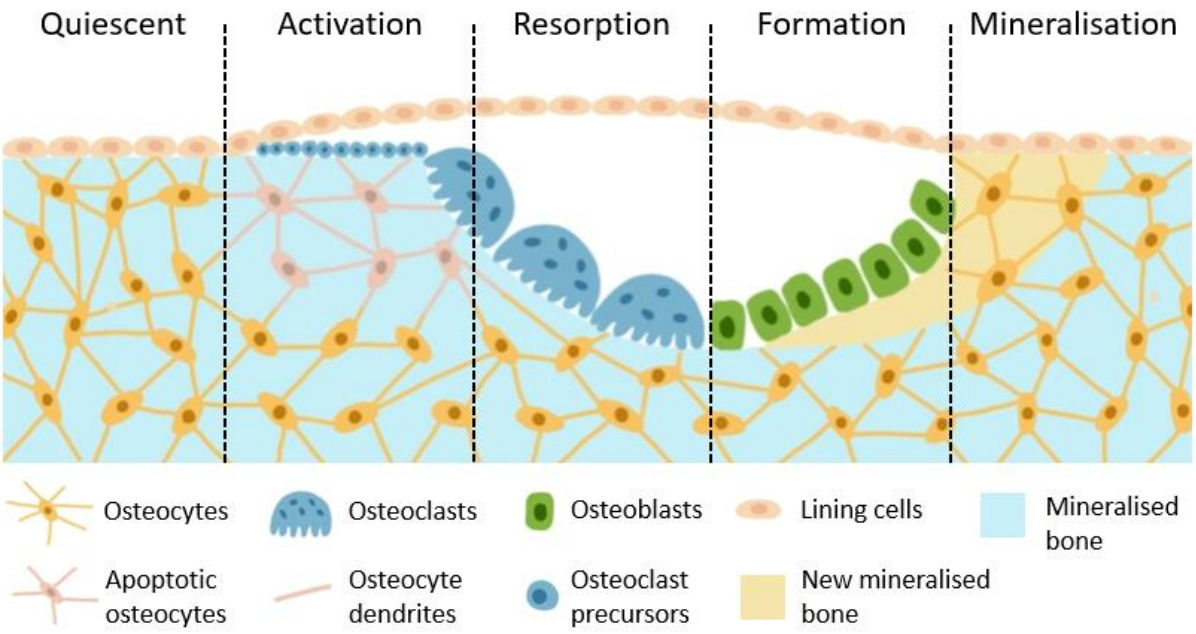

Figure 1.8: *The bone remodelling process, illustrating the five stages of remodelling: quiescent, activation, resorption, formation, mineralisation.*

1.2.5.3 Bone remodelling pathways

Numerous molecules exist that enable the bone cells to orchestrate bone adaptation (Raggatt and Partridge, 2010). Among these, the macrophage colony-stimulating factor (M-CSF) molecules and the receptor activator of nuclear factor kappa-B (RANK)/ the receptor activator of nuclear factor kappa-B ligand (RANKL) signalling pathway regulates osteoclast formation. RANKL, secreted by osteoblasts, binds to RANK receptors on osteoclast precursors (Figure 1.9), facilitating the formation of mature osteoclasts (Lacey et al., 1998). Additionally, osteoprotegerin (OPG), formed in the bone marrow, binds to RANKL, preventing its interaction with RANK, and hence regulating bone resorption (Hofbauer et al., 2000).

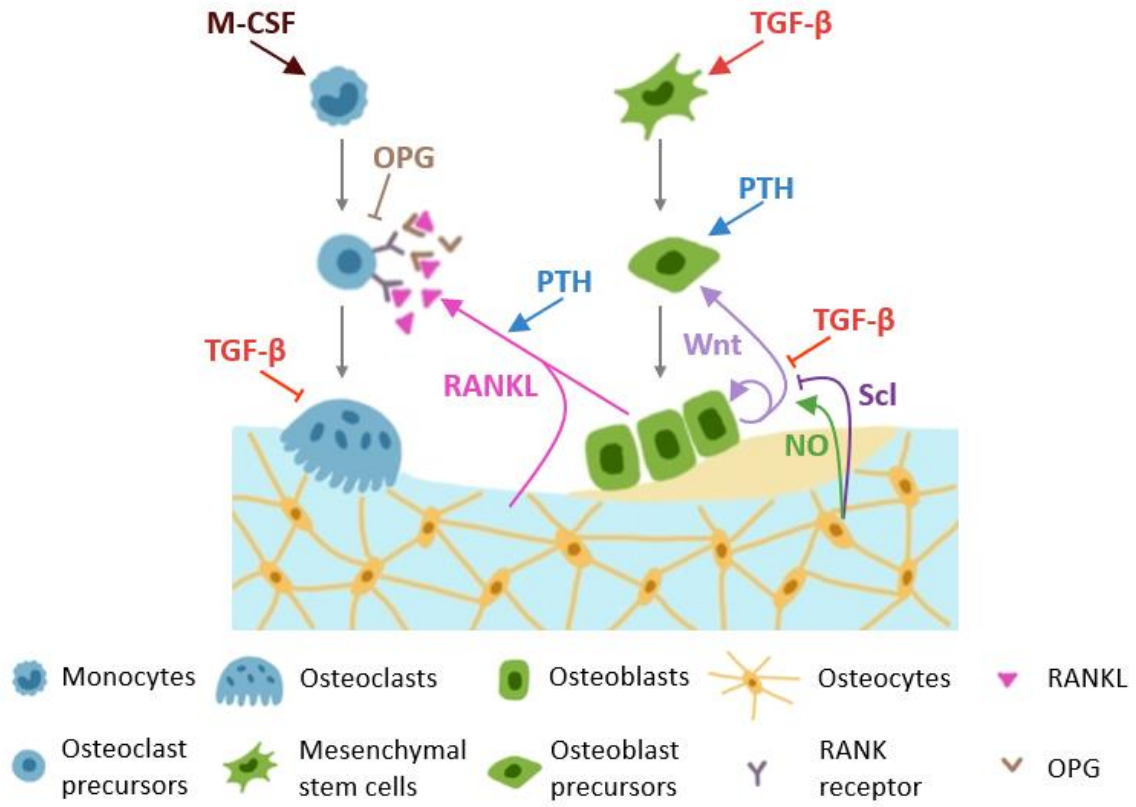

Figure 1.9: *Overview of the bone remodelling signalling pathways and molecules, illustrating the signalling pathways: RANK/RANKL/OPG and Wnt/β-catenin/Scl, and the molecules: PTH, M-CSF, TGF-β and NO.*

The wingless-related integration site (Wnt)/β-catenin signalling pathway (Figure 1.9) is another crucial regulator of bone adaptation. Activation of this pathway promotes osteogenic differentiation, proliferation, and activity of mesenchymal stem cells, leading to increased bone formation (Baron and Rawadi, 2007; Bonewald, 2011). However, this pathway can be inhibited by sclerostin (Scl), which is secreted by osteocytes. Scl binds to the cell surface of osteoblasts, inhibiting Wnt/β-catenin signalling and decreasing the activation of osteoblasts (Li et al., 2005; Baron and Rawadi, 2007). Nitric oxide (NO), released by osteocytes during mechanical loading (Vatsa et al., 2007; Bakker et al., 2009), can upregulate the Wnt/ β-catenin signalling (Du et al., 2013), leading to an increase in osteoblast differentiation (Jin et al., 2021).

Moreover, the transforming growth factor type beta (TGF-β) regulates osteoblasts and osteoclasts (Figure 1.9), by binding to its receptors on the cells (Wu et al., 2016). TGF-β upregulates the differentiation of osteoblast precursor cells from mesenchymal cells and upregulates the apoptosis of

osteoclasts (Wu et al., 2016). TGF-β also regulates Wnt activity, downregulating the differentiation of osteoblast precursors into mature osteoblasts (Wu et al., 2024).

Parathyroid hormone (PTH), produced by the parathyroid glands, regulates calcium metabolism (Fraser et al., 2004; Silva and Bilezikian, 2015; Martin, 2016). This is largely done through its effect on bone adaptation. PTH enhances osteoblast differentiation and activity (Figure 1.9), directly impacting bone formation (Zhao et al., 1999). Additionally, PTH augments the production and secretion of RANKL by osteoblasts, leading to increased osteoclast differentiation and activity, indirectly influencing bone resorption (Zhao et al., 1999).

Beyond this extensive network of molecules, there exist other molecules and proteins, such as vitamin D, oestrogen, and low-density lipoprotein-related receptors 5 and 6 (LRP5/6) that interact with the bone adaptation process (Crockett et al., 2011; Kenkre and Bassett, 2018; Robling and Bonewald, 2020; Ren et al., 2021).

1.3 Skeletal diseases and interventions

1.3.1 Osteoporosis

Osteoporosis is a skeletal disease that causes a reduction in bone mineral density (BMD) and mass, a consequent reduction of bone strength and an increased risk of fracture (Rachner et al., 2011). According to the World Health Organisation (WHO) criteria, a patient is considered osteoporotic if their BMD is at least 2.5 standard deviations below the average value of young healthy women (WHO, 1992). Postmenopausal osteoporosis is the most common form of the condition, making it pertinent to define osteoporosis based on criteria specific to women (Tournis and Makris, 2018).

In osteoporotic patients, an imbalance is produced in the remodelling process, resulting in the uncoupling of the osteoclasts and osteoblasts, leading to a decrease in trabecular bone and a decrease in BMD as bone resorption exceeds bone formation (Figure 1.10). Treatments for osteoporosis include antiresorptive and bone anabolic treatments. Antiresorptive treatments, such as bisphosphonates (e.g., Alendronate and Risedronate) and Denosumab, function by targeting the osteoclasts and suppressing their activity, but do not promote bone formation (Gasser, 2006; Grey, 2007). Denosumab binds to RANKL, preventing it from binding with RANK receptors on the osteoclast precursors, and thereby preventing the formation of mature osteoclasts, hence reducing bone resorption (Dore, 2011).

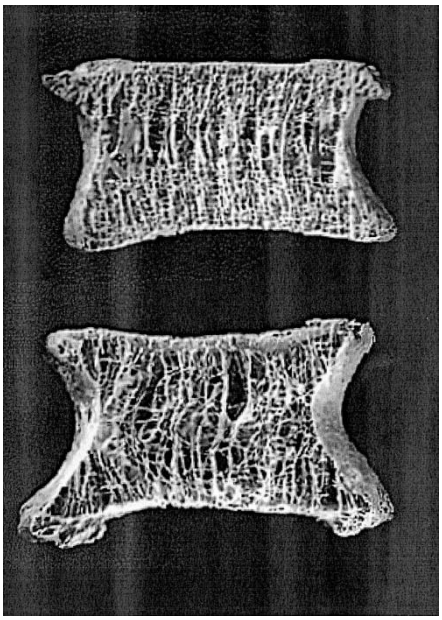

Figure 1.10: *Healthy (top) and osteoporotic (bottom) vertebral bodies. The decrease in trabecular bone can be seen in the osteoporotic case Ferguson and Steffen (2003).*

On the other hand, bone anabolic treatments, such as Teriparatide and Romosozumab, stimulate both osteoclasts and osteoblasts, with an imbalance towards the latter (Rubin and Bilezikian, 2005; Gasser, 2006; Grey, 2007; Rachner et al., 2011), elevating bone formation (Rubin and Bilezikian, 2005; Gasser, 2006; Grey, 2007). Teriparatide (also known as PTH(1-34), or more commonly PTH) is administered via injection (Tay et al., 2018). Its response depends on the treatment regime used. If it is administered continuously (via a pump), then the treatment can have catabolic effects (i.e., bone resorption occurs), however, it can have an anabolic effect (i.e., bone formation occurs) if intermittently administered (Frolik et al., 2003; Potter et al., 2005; Trichilo et al., 2019; Lavaill et al., 2020). This is due to the time that it takes for the PTH to enhance osteoblast differentiation and activity compared to the time it takes for the osteoblast to increase its production and secretion of RANKL, which increases osteoclast differentiation and activity (Young et al., 2005; Mekhemar et al., 2024). The latter requires more time, and hence intermittent administration of PTH may stimulate the osteoblast anabolic activity, while not triggering the osteoclast catabolic effects (Osagie-Clouard et al., 2017).

Long-term use of bisphosphonates has been associated with atypical stress fractures, reported as >100 in every 100,000 users (Shane et al., 2014). Romosozumab, a relatively new anti-sclerostin treatment, works by impeding an inhibitor of Wnt signalling and thus enhances the Wnt pathway allowing for an elevation in osteoblast activity, and increasing bone formation (Li et al., 2005; Baron and Rawadi, 2007;

Fabre et al., 2020). The long-term use of PTH also presents an issue as it has been associated with an increase in bone loss (Rubin and Bilezikian, 2005). In light of the drawbacks and limitations of the current osteoporosis treatments, there is a critical need for the development of new and improved treatments.

1.3.2 Multiple myeloma & myeloma bone disease

Multiple myeloma (MM) is a type of bone marrow cancer, which comes with life-altering complications such as MBD. MBD affects between 80-90% of patients during their cancer journey (Coleman, 1997; Kyle et al., 2003). This is caused by the uncoupling of osteoblasts and osteoclasts, resulting in a loss of trabecular bone, a decrease in BMD, and the formation of lytic lesions (Figure 1.11). All of which increase the patient's risk of fracture. Patients who experience fracture have an increased mortality rate of 20% compared to those without fracture (Saad et al., 2009). Current therapies for MBD, including bisphosphonates and denosumab, commonly used for osteoporosis, target osteoclasts, often leaving patients who reach remission from their cancer with chronic pain, decreased mobility, and reduced quality of life due to the bone loss, highlighting the need for new and improved treatments.

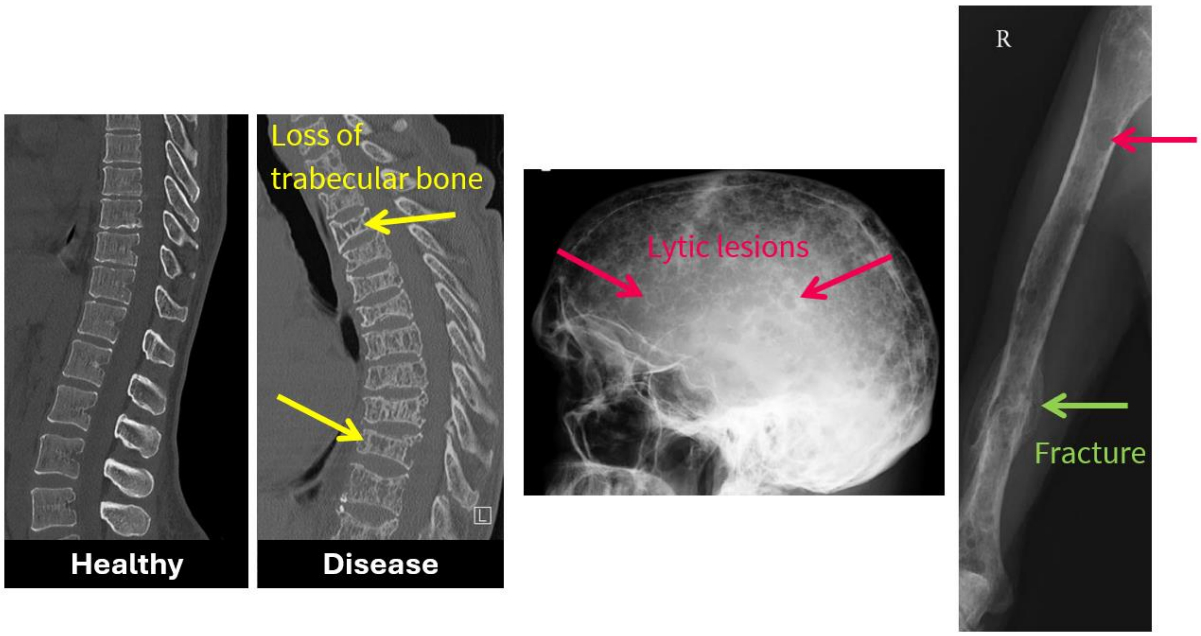

Figure 1.11: *Left: CT images of the spine showing a healthy and disease (multiple myeloma) case (Healthy – Gaillard (2016), Diseased – Yap et al. (2010)). Middle: Lateral radiograph of the skull, showing the lytic lesions as a result of multiple myeloma (Healy et al., 2011). Right: Anterior-posterior radiograph of the right humerus, showing lytic lesions and a fracture due to multiple myeloma (Healy et al., 2011). The yellow arrows highlight the loss of trabecular bone, the red arrows highlight the lytic lesions, and the green arrow highlights the fracture.*

1.4 Bone biomechanics

When tackling skeletal diseases, such as osteoporosis and myeloma bone disease, reducing the risk of fracture for patients is crucial. The propensity for fractures is proportionally related to the bone strength, emphasising the importance of studying this property. To do this, an understanding of the bone's material properties and the current bone adaptation theories are required.

1.4.1 Material properties

Bone is a very complex material to characterise at every dimensional level. It is heterogeneous – that is, its material properties are not uniform across the bone, but instead depend upon the location within the bone (Rho et al., 1998). It is anisotropic too, which means that the properties of the bone are contingent on loading direction (Rho et al., 1998). Bone is viscoelastic and exhibits different mechanical behaviour depending on the loading rate (Rho et al., 1998). It is also hierarchical, displaying a number of properties depending on the dimensional level (Rho et al., 1998). Moreover, bone is a dynamic tissue

and must instead be evaluated and understood as a developing material that changes over time. Its material properties are dependent not only on spatial qualities, but on temporally variable aspects too, on the age of the bone and whether there is any bone disease present (Morgan et al., 2018).

1.4.2 Bone remodelling theories

Bone (re)modelling enables the material properties and the shape of the bone to change; an adaptation that can result from biomechanical and/or biochemical stimuli (Section 1.2.5.3) (Hadjidakis and Androulakis, 2006). For example, the trabeculae form in the direction of stress and can realign if the direction of stress changes. The aspect of this phenomenon that relates to the strain within the bone is characterised by Wolff's law, which states that bone adaptation is triggered by mechanical stimuli (Wolff, 1892). A mechanical stimulus could be, for example, exercises such as walking, running, or jumping. One theory of remodelling suggests that the mechanical stimulus causes a deformation in the bone matrix, which activates the osteocytes to trigger the remodelling process (Scheiner et al., 2013). Similarly, another theory of remodelling suggests that when loading the bone, the pressure in the fluid within the canaliculi increases. This change in fluid pressure is felt by the osteocytes' dendrites (Figure 1.8), and the remodelling process is triggered (Scheiner et al., 2013). For both theories, there exists a link between the deformation of the matrix and the activation of the osteocytes to start the remodelling process.

1.4.3 Frost's mechanostat theory

The bone remodelling process can be expanded upon through Frost's 'mechanostat' theory for bone adaptation, which takes Wolff's law further by stating that mechanical stimulus causes bone adaptation (Frost, 2003). What is vital about mechanostat theory, for our purposes, is that it suggests that below a certain strain threshold, bone is resorbed and above another threshold, bone is formed (Figure 1.12). It becomes possible to assert that, when an exercise is conducted which exposes bone to a greater typical peak mechanical strain, the osteocytes sense the mechanical stimuli and formation occurs. That is to say that, as strain contributes to bone formation, it becomes possible to utilise mechanical strain in order to strengthen the bone itself (Skerry et al., 1989; Gluhak-Heinrich et al., 2003).

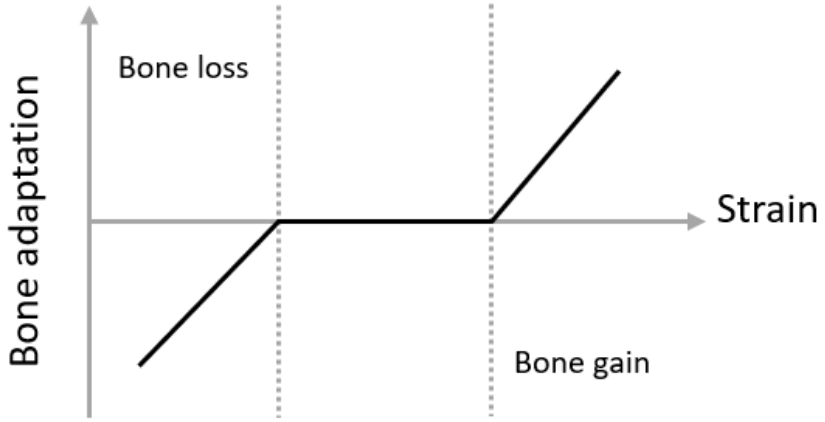

Figure 1.12: *A strain-bone adaptation graph representing Frost's 'mechanostat' theory.*

1.5 Mouse models

1.5.1 Similarities and differences between mouse and human bone

To effectively utilise mouse models for investigating human skeletal diseases and their treatments, it is crucial to understand the similarities and differences between murine and human bone. Both exhibit loss of trabecular bone, thinning of cortical bone, and increased cortical porosity with age (Jilka, 2013). However, the growth plate in humans mineralises after puberty, preventing any further longitudinal growth (Reinwald and Burr, 2008), whilst the mouse skeleton continues longitudinal growth after puberty, albeit at a slower rate than before puberty (Roach et al., 2003; Allen, 2017). In terms of microstructure, human cortical bone has a complex organisation, made up of Haversian systems, which are absent in mouse cortical bone (Parfitt, 1994). This means that humans can undergo intra-cortical remodelling (remodelling within the cortical bone matrix), whilst mouse cortical bone undergo remodelling on the periosteum and endosteum surfaces. Yet, both humans and mice undergo similar remodelling of the trabecular bone.

1.5.2 Mouse models for osteoporosis

Due to osteoporosis not occurring naturally in mice (Laib et al., 2001), the ovariectomised mouse model can be applied for investigations into osteoporosis and related interventions (Waarsing et al., 2004; Boyd et al., 2006; Roberts et al., 2020). This is because ovariectomy leads to an oestrogen deficiency, which results in accelerated bone resorption, a phenotype observed in postmenopausal

osteoporosis (Figure 1.13) (Roberts et al., 2019). The mouse tibia is often used in investigations into osteoporosis and its related treatments (as seen in the following chapter), as it is a weight-bearing bone, making it a relevant model for studying osteoporosis in humans.

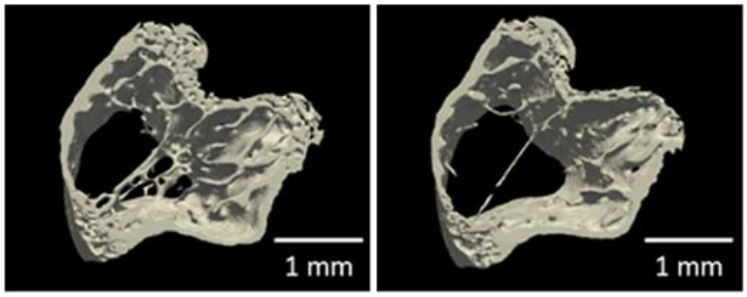

Figure 1.13: *Examples of cross-sections of trabecular bone in the C57BL/6 mouse proximal tibia. Left: Control (healthy) case. Right: Ovariectomy case (ovariectomy leads to hormonal imbalance that replicates an accelerated bone resorption phenotype similar to postmenopausal osteoporosis (Section 4)). Adapted from Roberts et al. (2019).*

1.5.3 Mouse models for multiple myeloma

Different types of mouse models exist for investigations into MM (Rossi et al., 2018). One example is the moderately aggressive MM model which takes human myeloma cell lines and injects them intravenously into mice (Paton-Hough et al., 2019). This is known as a xenograft model. Around 10 weeks post-inoculation, the mice can develop MBD (Figure 1.14). Similar to humans, this results in a loss of trabecular bone, a decrease in BMD, and the formation of lytic lesions (Evans et al., 2024).

For both diseases, to gain a deeper understanding of the mechanical properties of the bone, different imaging and computational modelling tools have been developed.

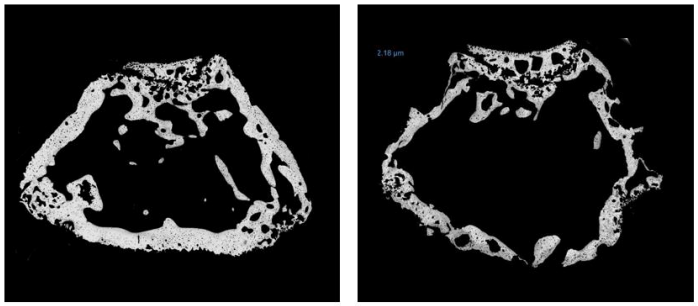

Figure 1.14: *Examples of cross-sections of cortical bone in the NOD scid gamma mouse distal femur. Left: Control (healthy) case. Right: Myeloma bone disease model case (injection of U266-GFP-luc cells from a human myeloma patient leads to myeloma bone disease model). Images courtesy of Evans et al. (2024).*

1.6 References

Allen, M. R. (2017). Preclinical models for skeletal research: how commonly used species mimic (or don't) aspects of human bone. Toxicol. Pathol. 45, 851–854. doi: 10.1177/0192623317733925

Andersen, T. L., Sondergaard, T. E., Skorzynska, K. E., Dagnaes-Hansen, F., Plesner, T. L., Hauge, E. M., et al. (2009). A physical mechanism for coupling bone resorption and formation in adult human bone. Am. J. Pathol. 174, 239–247. doi: 10.2353/ajpath.2009.080627

Bakker, A. D., Da Silva, V. C., Krishnan, R., Bacabac, R. G., Blaauboer, M. E., Lin, Y. C., et al. (2009). Tumor necrosis factor alpha and interleukin-1beta modulate calcium and nitric oxide signaling in mechanically stimulated osteocytes. Arthritis Rheum. 60, 3336–3345. doi: 10.1002/art.24920

Baron, R., and Rawadi, G. (2007). Targeting the Wnt/beta-catenin pathway to regulate bone formation in the adult skeleton. Endocrinology 148, 2635–2643. doi: 10.1210/en.2007-0270

Betts, J. G., Desaix, P., Johnson, E., Johnson, J. E., Korol, O., Kruse, D., et al. (2013). Anatomy and Physiology.

Bilezikian, J. P., Raisz, L. G., and Martin, T. J. (2008). Principles of bone biology.

Blanco, A., and Blanco, G. (2022). Essential minerals. Med. Biochem., 779–810. doi: 10.1016/b978-0-323-91599-1.00006-7

Bonewald, L. F. (2011). The amazing osteocyte. J. Bone Miner. Res. 26, 229–238. doi: 10.1002/jbmr.320

Boyd, S. K., Davison, P., Müller, R., and Gasser, J. A. (2006). Monitoring individual morphological changes over time in ovariectomized rats by in vivo micro-computed tomography. Bone 39, 854–862. doi: 10.1016/j.bone.2006.04.017

Chen, H., Senda, T., and Kubo, K. ya (2015). The osteocyte plays multiple roles in bone remodeling and mineral homeostasis. Med. Mol. Morphol. 48, 61–68. doi: 10.1007/s00795-015-0099-y

Clarke, B. (2008). Normal Bone Anatomy and Physiology. Clin. J. Am. Soc. Nephrol. 3, S131. doi: 10.2215/cjn.04151206

Coleman, R. E. (1997). Skeletal Complications of Malignancy. Cancer 80, 1588–1594. doi: 10.1002/(sici)1097-0142(19971015)80:8

Cowin, S., and Telega, J. (2003). Bone Mechanics Handbook, 2nd Edition. Appl. Mech. Rev. 56, B61–B63. doi: 10.1115/1.1579463

Crockett, J. C., Rogers, M. J., Coxon, F. P., Hocking, L. J., and Helfrich, M. H. (2011). Bone remodelling at

a glance. J. Cell Sci. 124, 991–998. doi: 10.1242/jcs.063032

Currey, J. D. (2006). Bones. Princeton university press.

Diem, K., and Lentner, C. (1970). Scientific tables, documenta Geigy. Ciba-Geigy Pharm. New York.

Dore, R. K. (2011). The RANKL pathway and denosumab. Rheum. Dis. Clin. North Am. 37, 433–452. doi: 10.1016/j.rdc.2011.07.004

Du, Q., Zhang, X., Liu, Q., Zhang, X., Bartels, C. E., and Geller, D. A. (2013). Nitric oxide production upregulates Wnt/β-catenin signaling by inhibiting Dickkopf-1. Cancer Res. 73, 6526–6537. doi: 10.1158/0008-5472.can-13-1620

Eriksen, E. F. (1994). Bone histology and histomorphometry. Bone histomorphometry, 33–48.

European Foundation for Osteoporosis (1993). Consensus development conference: diagnosis, prophylaxis, and treatment of osteoporosis. Am. J. Med. 94, 646–650. doi: 10.1016/0002-9343(93)90218-e

Evans, H., Andrews, R., Abedi, F. A., Sprules, A., Trend, J., Lovric, G., et al. (2024). Evidence for peri-lacunar remodeling and altered osteocyte lacuno-canalicular network in mouse models of myeloma-induced bone disease. JBMR Plus. doi: 10.1093/jbmrpl/ziae093

Fabre, S., Funck-Brentano, T., and Cohen-Solal, M. (2020). Anti-sclerostin antibodies in osteoporosis and other bone diseases. J. Clin. Med. 9, 1–16. doi: 10.3390/jcm9113439

Ferguson, S. J., and Steffen, T. (2003). Biomechanics of the aging spine. Eur. Spine J. 12, S97–S103. doi: 10.1007/s00586-003-0621-0

Fraser, W. D., Ahmad, A. M., and Vora, J. P. (2004). The physiology of the circadian rhythm of parathyroid hormone and its potential as a treatment for osteoporosis. Curr. Opin. Nephrol. Hypertens. 13, 437–444. doi: 10.1097/01.mnh.0000133985.29880.34

Frolik, C. A., Black, E. C., Cain, R. L., Satterwhite, J. H., Brown-Augsburger, P. L., Sato, M., et al. (2003). Anabolic and catabolic bone effects of human parathyroid hormone (1-34) are predicted by duration of hormone exposure. Bone 33, 372–379. doi: 10.1016/S8756-3282(03)00202-3

Frost, H. M. (2003). Bone's mechanostat: a 2003 update. Anat. Rec. A. Discov. Mol. Cell. Evol. Biol. 275, 1081–1101. doi: 10.1002/ar.a.10119

Gaillard, F. (2016). Normal thoracolumbar spine. Radiopaedia.org. doi: 10.53347/rid-43822

Gasser, J. A. (2006). The relative merits of anabolics versus anti-resorptive compounds: where our

targets should be, and whether we are addressing them. Curr. Opin. Pharmacol. 6, 313–318. doi: 10.1016/j.coph.2006.03.004

Gluhak-Heinrich, J., Ye, L., Bonewald, L. F., Feng, J. Q., MacDougall, M., Harris, S. E., et al. (2003). Mechanical loading stimulates dentin matrix protein 1 (DMP1) expression in osteocytes in vivo. J. Bone Miner. Res. 18, 807–817. doi: 10.1359/jbmr.2003.18.5.807

Gould, S. E., Junttila, M. R., and De Sauvage, F. J. (2015). Translational value of mouse models in oncology drug development. Nat. Med. 21, 431–439. doi: 10.1038/nm.3853

Gray, H., and Lewis, W. H. (1918). Anatomy of the human body., 20th Edn. Philadelphia: Lea & Febiger.

Grey, A. (2007). Emerging pharmacologic therapies for osteoporosis. Expert Opin. Emerg. Drugs 12, 493–508. doi: 10.1517/14728214.12.3.493

Hadjidakis, D. J., and Androulakis, I. I. (2006). Bone remodeling. Ann. N. Y. Acad. Sci. 1092, 385–396. doi: 10.1196/annals.1365.035

Healy, C. F., Murray, J. G., Eustace, S. J., Madewell, J., O'Gorman, P. J., and O'Sullivan, P. (2011). Multiple myeloma: a review of imaging features and radiological techniques. Bone Marrow Res. 2011, 583439. doi: 10.1155/2011/583439

Hofbauer, L. C., Khosla, S., Dunstan, C. R., Lacey, D. L., Boyle, W. J., and Riggs, B. L. (2000). The roles of osteoprotegerin and osteoprotegerin ligand in the paracrine regulation of bone resorption. J. Bone Miner. Res. 15, 2–12. doi: 10.1359/jbmr.2000.15.1.2

Jilka, R. L. (2013). The relevance of mouse models for investigating age-related bone loss in humans. Journals Gerontol. Ser. A 68, 1209–1217. doi: 10.1093/gerona/glt046

Jin, Z., Kho, J., Dawson, B., Jiang, M. M., Chen, Y., Ali, S., et al. (2021). Nitric oxide modulates bone anabolism through regulation of osteoblast glycolysis and differentiation. J. Clin. Invest. 131. doi: 10.1172/jci138935

Kanis, J. A., Norton, N., Harvey, N. C., Jacobson, T., Johansson, H., Lorentzon, M., et al. (2021). SCOPE 2021: a new scorecard for osteoporosis in Europe. Arch. Osteoporos. 16, 1–82. doi: 10.1007/s11657-020-00871-9

Kanis, J. A., Norton, N., Harvey, N. C., Jacobson, T., Johansson, H., Lorentzon, M., et al. (2022). SCOPE 2021: Epidemiology, burden, and treatment of osteoporosis in the United Kingdom. Available at: https://www.osteoporosis.foundation/scope-2021 (Accessed May 11, 2024).

Kenkre, J. S., and Bassett, J. H. D. (2018). The bone remodelling cycle. Ann. Clin. Biochem. 55, 308–327.

doi: 10.1177/0004563218759371

Kini, U., and Nandeesh, B. N. (2012). Physiology of bone formation, remodeling, and metabolism, in Radionuclide and hybrid bone imaging. Springer, 29–57

Kyle, R. A., Gertz, M. A., Witzig, T. E., Lust, J. A., Lacy, M. Q., Dispenzieri, A., et al. (2003). Review of 1027 patients with newly diagnosed multiple myeloma. Mayo Clin. Proc. 78, 21–33. doi: 10.4065/78.1.21

Lacey, D. L., Timms, E., Tan, H. L., Kelley, M. J., Dunstan, C. R., Burgess, T., et al. (1998). Osteoprotegerin ligand is a cytokine that regulates osteoclast differentiation and activation. Cell 93, 165–176. doi: 10.1016/s0092-8674(00)81569-x

Laib, A., Kumer, J. L., Majumdar, S., and Lane, N. E. (2001). The temporal changes of trabecular architecture in ovariectomized rats assessed by microCT. Osteoporos. Int. 12, 936–941. doi: 10.1007/s001980170022

Lavaill, M., Trichilo, S., Scheiner, S., Forwood, M. R., Cooper, D. M. L., and Pivonka, P. (2020). Study of the combined effects of PTH treatment and mechanical loading in postmenopausal osteoporosis using a new mechanistic PK-PD model. Biomech. Model. Mechanobiol. 19, 1765–1780. doi: 10.1007/s10237-020-01307-6

Le, B. Q., Nurcombe, V., Cool, S. M. K., van Blitterswijk, C. A., de Boer, J., and LaPointe, V. L. S. (2018). The components of bone and what they can teach us about regeneration. Materials (Basel). 11. doi: 10.3390/ma11010014

Li, X., Zhang, Y., Kang, H., Liu, W., Liu, P., Zhang, J., et al. (2005). Sclerostin binds to LRP5/6 and antagonizes canonical Wnt signaling. J. Biol. Chem. 280, 19883–19887. doi: 10.1074/jbc.m413274200

Martin, J. T. (2016). Parathyroid hormone-related protein, its regulation of cartilage and bone development, and role in treating bone diseases. Physiol. Rev. 96, 831–871. doi: 10.1152/physrev.00031.2015

Matic, I., Matthews, B. G., Wang, X., Dyment, N. A., Worthley, D. L., Rowe, D. W., et al. (2016). Quiescent bone lining cells are a major source of osteoblasts during adulthood. Stem Cells 34, 2930–2942. doi: 10.1002/stem.2474

Mekhemar, M., Mohamed Fawzy El-Sayed, K., Liu, H., Liu, L., and Rosen, C. J. (2024). PTH and the regulation of mesenchymal cells within the bone marrow niche. Cells 2024, Vol. 13, Page 406 13, 406. doi: 10.3390/cells13050406

Morgan, E. F., Unnikrisnan, G. U., and Hussein, A. I. (2018). Bone mechanical properties in healthy and diseased states. Annu. Rev. Biomed. Eng. 20, 119. doi: 10.1146/annurev-bioeng-062117-121139

NC3Rs (2021). The 3Rs | NC3Rs. Available at: https://nc3rs.org.uk/who-we-are/3rs (Accessed April 5, 2024).

NHS England (2023). National Disease Registration Service (NDRS) database.

Northern Ireland Cancer Registry (2021). Northern Ireland Cancer Registry (NICR) database.

Ominsky, M. S., Brown, D. L., Van, G., Cordover, D., Pacheco, E., Frazier, E., et al. (2015). Differential temporal effects of sclerostin antibody and parathyroid hormone on cancellous and cortical bone and quantitative differences in effects on the osteoblast lineage in young intact rats. Bone 81, 380–391. doi: 10.1016/j.bone.2015.08.007

Osagie-Clouard, L., Sanghani, A., Coathup, M., Briggs, T., Bostrom, M., and Blunn, G. (2017). Parathyroid hormone 1-34 and skeletal anabolic action: The use of parathyroid hormone in bone formation. Bone Jt. Res. 6, 14–21. doi: 10.1302/2046-3758.61.bjr-2016-0085.r1

Owen, R., and Reilly, G. C. (2018). In vitro models of bone remodelling and associated disorders. Front. Bioeng. Biotechnol. 6. doi: 10.3389/fbioe.2018.00134

Palumbo, C., and Ferretti, M. (2021). The osteocyte: from “prisoner” to “orchestrator.” J. Funct. Morphol. Kinesiol. 6, 28. doi: 10.3390/jfmk6010028

Parfitt, A. M. (1994). Osteonal and hemi-osteonal remodeling: The spatial and temporal framework for signal traffic in adult human bone. J. Cell. Biochem. 55, 273–286. doi: 10.1002/jcb.240550303

Paton-Hough, J., Tazzyman, S., Evans, H., Lath, D., Down, J. M., Green, A. C., et al. (2019). Preventing and repairing myeloma bone disease by combining conventional antiresorptive treatment with a bone anabolic agent in murine models. J. Bone Miner. Res. 34, 783. doi: 10.1002/jbmr.3606

Potter, L. K., Greller, L. D., Cho, C. R., Nuttall, M. E., Stroup, G. B., Suva, L. J., et al. (2005). Response to continuous and pulsatile PTH dosing: A mathematical model for parathyroid hormone receptor kinetics. Bone 37, 159–169. doi: 10.1016/j.bone.2005.04.011

Prideaux, M., Findlay, D. M., and Atkins, G. J. (2016). Osteocytes: The master cells in bone remodelling. Curr. Opin. Pharmacol. 28, 24–30. doi: 10.1016/j.coph.2016.02.003

Public Health Scotland (2021). Scottish Cancer Registry database.

Rachner, T. D., Khosla, S., and Hofbauer, L. C. (2011). Osteoporosis: now and the future. Lancet (London,

England) 377, 1276–1287. doi: 10.1016/s0140-6736(10)62349-5

Raggatt, L. J., and Partridge, N. C. (2010). Cellular and molecular mechanisms of bone remodeling. J. Biol. Chem. 285, 25103. doi: 10.1074/jbc.r109.041087

Reinwald, S., and Burr, D. (2008). Review of nonprimate, large animal models for osteoporosis research. J. Bone Miner. Res. 23, 1353–1368. doi: 10.1359/jbmr.080516

Ren, Q., Chen, J., and Liu, Y. (2021). LRP5 and LRP6 in Wnt signaling: similarity and divergence. Front. Cell Dev. Biol. 9, 670960. doi: 10.3389/fcell.2021.670960

Rho, J. Y., Kuhn-Spearing, L., and Zioupos, P. (1998). Mechanical properties and the hierarchical structure of bone. Med. Eng. Phys. 20, 92–102. doi: 10.1016/s1350-4533(98)00007-1

Roach, H. I., Mehta, G., Oreffo, R. O. C., Clarke, N. M. P., and Cooper, C. (2003). Temporal analysis of rat growth plates: cessation of growth with age despite presence of a physis. J. Histochem. Cytochem. 51, 373–383. doi: 10.1177/002215540305100312

Roberts, B. C., Arredondo Carrera, H. M., Zanjani-pour, S., Boudiffa, M., Wang, N., Gartland, A., et al. (2020). PTH(1–34) treatment and/or mechanical loading have different osteogenic effects on the trabecular and cortical bone in the ovariectomized C57BL/6 mouse. Sci. Reports, 101 10, 1–16. doi: 10.1038/s41598-020-65921-1

Roberts, B. C., Giorgi, M., Oliviero, S., Wang, N., Boudiffa, M., and Dall'Ara, E. (2019). The longitudinal effects of ovariectomy on the morphometric, densitometric and mechanical properties in the murine tibia: A comparison between two mouse strains. Bone 127, 260–270. doi: 10.1016/j.bone.2019.06.024

Robling, A. G., and Bonewald, L. F. (2020). The osteocyte: new insights. Annu. Rev. Physiol. 82, 485–506. doi: 10.1146/annurev-physiol-021119-034332

Rosko, A. E., Hade, E. M., Li, W., Ing, S., Jackson, R. D., Paskett, E. D., et al. (2018). Bone health and survival in women with multiple myeloma. Clin. Lymphoma. Myeloma Leuk. 18, 597. doi: 10.1016/j.clml.2018.06.002

Rossi, M., Botta, C., Arbitrio, M., Grembiale, R. D., Tagliaferri, P., and Tassone, P. (2018). Mouse models of multiple myeloma: technologic platforms and perspectives. Oncotarget 9, 20119. doi: 10.18632/oncotarget.24614

Rubin, M. R., and Bilezikian, J. P. (2005). Parathyroid hormone as an anabolic skeletal therapy. Drugs 65, 2481–2498. doi: 10.2165/00003495-200565170-00005

Ryan, J., and Premanandan, C. (2017). Veterinary Histology. The Ohio State University. Available at:

https://ohiostate.pressbooks.pub/vethisto/chapter/5-bone-microanatomy/ (Accessed June 14, 2024).

Saad, A. A., Sharma, M., and Higa, G. M. (2009). Oncology: treatment of multiple myeloma in the targeted therapy era. doi: 10.1345/aph.1l428

Saad, F., Lipton, A., Cook, R., Chen, Y. M., Smith, M., and Coleman, R. (2007). Pathologic fractures correlate with reduced survival in patients with malignant bone disease. Cancer 110, 1860–1867. doi: 10.1002/cncr.22991

Scheiner, S., Pivonka, P., and Hellmich, C. (2013). Coupling systems biology with multiscale mechanics, for computer simulations of bone remodeling. Comput. Methods Appl. Mech. Eng. 254, 181–196. doi: 10.1016/j.cma.2012.10.015

Shaker, B., Ahmad, S., Lee, J., Jung, C., and Na, D. (2021). In silico methods and tools for drug discovery. Comput. Biol. Med. 137, 104851. doi: 10.1016/j.compbiomed.2021.104851

Shane, E., Burr, D., Abrahamsen, B., Adler, R. A., Brown, T. D., Cheung, A. M., et al. (2014). Atypical subtrochanteric and diaphyseal femoral fractures: second report of a task force of the American Society for Bone and Mineral Research. J. Bone Miner. Res. 29, 1–23. doi: 10.1002/jbmr.1998

Silva, B. C., and Bilezikian, J. P. (2015). Parathyroid hormone: Anabolic and catabolic actions on the skeleton. Curr. Opin. Pharmacol. 22, 41–50. doi: 10.1016/j.coph.2015.03.005

Skerry, T. M., Lanyon, L. E., Bitensky, L., and Chayen, J. (1989). Early strain-related changes in enzyme activity in osteocytes following bone loading in vivo. J. Bone Miner. Res. 4, 783–788. doi: 10.1002/jbmr.5650040519

Streicher, C., Heyny, A., Andrukhova, O., Haigl, B., Slavic, S., Schüler, C., et al. (2017). Estrogen regulates bone turnover by targeting RANKL expression in bone lining cells. Sci. Rep. 7. doi: 10.1038/s41598-017-06614-0

Tay, D., Cremers, S., and Bilezikian, J. P. (2018). Optimal dosing and delivery of parathyroid hormone and its analogues for osteoporosis and hypoparathyroidism – translating the pharmacology. Br. J. Clin. Pharmacol. 84, 252. doi: 10.1111/bcp.13455

Tournis, S., and Makris, K. (2018). Clinical use of bone turnover markers in osteoporosis. Ref. Modul. Biomed. Sci. doi: 10.1016/b978-0-12-801238-3.99538-2

Trichilo, S., Scheiner, S., Forwood, M., Cooper, D. M. L., and Pivonka, P. (2019). Computational model of the dual action of PTH — application to a rat model of osteoporosis. J. Theor. Biol. 473, 67–79. doi: 10.1016/j.jtbi.2019.04.020

Turesson, I., Velez, R., Kristinsson, S. Y., and Landgren, O. L. A. (2010). Patterns of multiple myeloma during the past 5 decades: stable incidence rates for all age groups in the population but rapidly changing age distribution in the clinic. Mayo Clin. Proc. 85, 225–230. doi: 10.4065/mcp.2009.0426

Vatsa, A., Smit, T. H., and Klein-Nulend, J. (2007). Extracellular NO signalling from a mechanically stimulated osteocyte. J. Biomech. 40 Suppl 1. doi: 10.1016/j.jbiomech.2007.02.015

Viguet-Carrin, S., Garnero, P., and Delmas, P. D. (2006). The role of collagen in bone strength. Osteoporos. Int. 17, 319–336. doi: 10.1007/s00198-005-2035-9

Waarsing, J. H., Day, J. S., Van Der Linden, J. C., Ederveen, A. G., Spanjers, C., De Clerck, N., et al. (2004). Detecting and tracking local changes in the tibiae of individual rats: a novel method to analyse longitudinal in vivo micro-CT data. Bone 34, 163–169. doi: 10.1016/j.bone.2003.08.012

Wang, J. S., and Wein, M. N. (2022). Pathways controlling formation and maintenance of the osteocyte dendrite network. Curr. Osteoporos. Rep. 20, 493. doi: 10.1007/s11914-022-00753-8

Welsh Cancer Intelligence and Surveillance Unit (2022). Welsh Cancer Intelligence and Surveillance Unit (WCISU) database.

WHO (1992). Assessment of fracture risk and its application to screening for postmenopausal osteoporosis : report of a WHO study group [meeting held in Rome from 22 to 25 June 1992]. Available at: https://iris.who.int/handle/10665/39142 (Accessed March 28, 2024).

Wolff, J. (1892). Das gesetz der transformation der knochen. Berlin: Hirschwald.

Wu, M., Chen, G., and Li, Y. P. (2016). TGF-β and BMP signaling in osteoblast, skeletal development, and bone formation, homeostasis and disease. Bone Res. 4, 16009. doi: 10.1038/boneres.2016.9

Wu, M., Wu, S., Chen, W., and Li, Y. P. (2024). The roles and regulatory mechanisms of TGF-β and BMP signaling in bone and cartilage development, homeostasis and disease. Cell Res. 2024 342 34, 101–123. doi: 10.1038/s41422-023-00918-9

Yap, K., Sharma, R., and Campos, A. (2010). Multiple myeloma. Radiopaedia.org. doi: https://doi.org/10.53347/rid-9555

Yee, C. S., Schurman, C. A., White, C. R., and Alliston, T. (2019). Investigating osteocytic perilacunar/canalicular remodeling. Curr. Osteoporos. Rep. 17, 157–168. doi: 10.1007/s11914-019-00514-0

Young, N., Mikhalkevich, N., Yan, Y., Chen, D., and Zheng, W. (2005). Differential regulation of osteoblast activity by th cell subsets mediated by parathyroid hormone and IFN-γ. J. Immunol. 175, 8287. doi:

10.4049/jimmunol.175.12.8287

Yu, B., Pacureanu, A., Olivier, C., Cloetens, P., and Peyrin, F. (2021). Quantification of the bone lacunocanalicular network from 3D X-ray phase nanotomography images. J. Microsc. 282, 30–44. doi: 10.1111/jmi.12973

Zhao, W., Byrne, M. H., Boyce, B. F., and Krane, S. M. (1999). Bone resorption induced by parathyroid hormone is strikingly diminished in collagenase-resistant mutant mice. J. Clin. Invest. 103, 517. doi: 10.1172/jci5481

Chapter 2: Literature review

2.1 Introduction

Skeletal diseases, such as osteoporosis and myeloma bone disease (MBD), significantly impact bone properties, and hence patient's quality of life. *In silico* models offer a valuable tool to investigate bone adaptation under disease conditions. This chapter reviews existing computational approaches used to study bone. It will explore methods for acquiring data on bone properties, including high-resolution imaging techniques used to capture bone geometry and microstructure. Subsequently, it will delve into the different types of biomechanical models, examining their applications and limitations. This will be followed by a review of available biochemical models and combined biomechanical and biochemical models, focusing on their strengths and weaknesses. By the end of the chapter, the existing literature gaps related to the limitations of the *in silico* models for skeletal diseases will be identified, and any new understanding of the diseases and/or related treatments which could result by resolving these gaps is highlighted. This will provide the context for and justify the specific aims and objectives of this project, highlighting the need for further development and application of these valuable tools.

2.2 Bone imaging

2.2.1 Micro-Computed Tomography

Micro-computed tomography (micro-CT) is a high-resolution 3D imaging technique used to study the inner microstructure of samples and is considered the gold standard for assessing the bone morphology in rodents (Bouxsein et al., 2010). Micro-CT works by emitting X-rays that are transmitted through the sample and acquired onto a detector in a (two-dimensional) 2D image called a "projection" (Figure 2.1). Either the sample, or the X-ray source and detector, is rotated, which allows for a multitude of projections to be captured, which are then reconstructed into a 3D image.

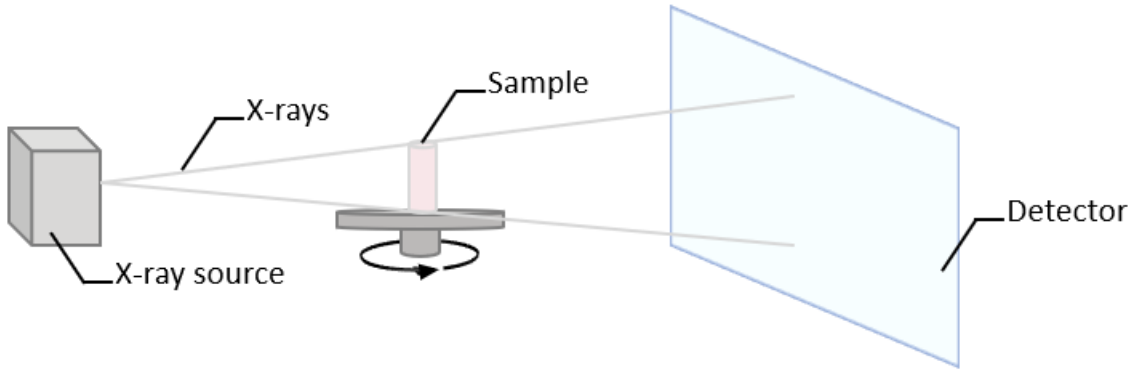

Figure 2.1: *A schematic of a micro-computer tomography scanner, illustrating the X-ray source, the X-rays, the sample and its turntable, and the detector.*

A great deal of information can be gleaned from a micro-CT image (Figure 2.2). A grey level is associated to each voxel (3D pixel) that, if the micro-CT scanner has been calibrated properly, reveals the local tissue mineral density (TMD) of the sample. Morphometric parameters can also be obtained in order to describe the microarchitecture of the bone tissue, for example the cortical thickness (Ct.Th) which describes the average thickness of the cortical bone defined as the distance from the endosteum to the periosteum (Bouxsein et al., 2010).

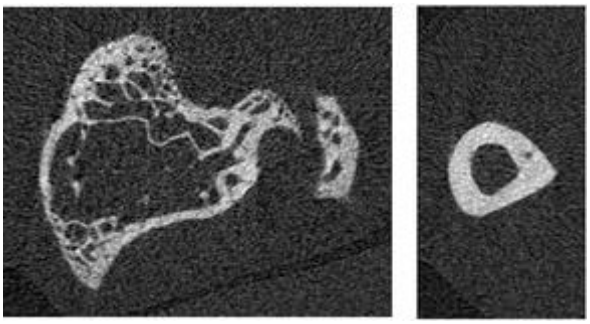

Figure 2.2: *Examples of micro-CT cross-sections of trabecular (left) and cortical (right) bone from the BALB/c mice proximal tibiae. Adapted from Oliviero et al. (2019).*

While micro-CT scanning allows for *in vivo* or *ex vivo* analysis of mouse bones, *ex vivo* scans offer significantly higher spatial resolution. *In vivo* scans require balancing scanning time with image quality due to ionizing radiation exposure (Oliviero et al., 2017). It has been found that micro-CT scans of the

whole mouse tibia can be achieved at 10 µm voxel size with minimal effects on the bone adaptation (Oliviero et al., 2019). Regardless of the scanning method, reliable measurements require a spatial resolution roughly four times larger than the smallest feature of interest (Christiansen, 2016). For instance, when imaging trabeculae (40-70 µm) in the mouse tibia *in vivo*, a 10 µm resolution is sufficient.

2.2.2 Synchrotron radiation computed tomography

Synchrotron radiation computed tomography (SR-micro-CT) is an advanced imaging technique that utilises synchrotron light to achieve high resolution images, with a low scanning time compared to traditional micro-CT (Paul Scherrer Institut, 2019). Synchrotron light is a highly intense and focused beam generated through the acceleration of electrons to near-light speed within an electron accelerator. It is produced via the emission of electromagnetic radiation from electrons travelling in circular orbits under the influence of magnetic fields. As the electrons circulate, the synchrotron light is concentrated into discrete wavelengths (Paul Scherrer Institut, 2019). The synchrotron light is tangentially directed away from the course through beamlines towards the sample. These beamlines allow for the utilisation of different wavelengths. The synchrotron light passes through the sample, and the interaction between the light and the sample results in attenuation and scattering. Detectors positioned opposite the sample capture the transmitted synchrotron light, recording its intensity and spatial distribution. As in micro-CT, the sample is rotated, which allows for a multitude of projections to be captured, which are then reconstructed into a 3D image.

Two main types of X-ray beams are commonly used for synchrotron imaging: pink beam and monochromatic beam. Synchrotron imaging with a monochromatic beam tends to be slower compared to using a pink beam, however, some information such as the TMD can only be obtained from the grey level when using a monochromatic beam (Meganck et al., 2009). Unlike traditional micro-CT, synchrotron imaging is usually performed *ex vivo*. This is due to the high levels of radiation exposure: the synchrotron X-rays are highly intense and will cause harm to living tissues. On the contrary, the image resolution can be much higher than traditional micro-CT (Figure 2.3), allowing for additional morphometric parameters to describe the microarchitecture of the osteocyte lacunae within the bone tissue (Hemmatian et al., 2021; Evans et al., 2024). These parameters include the osteocyte lacunae density (Ocy.L/BV), which define the number of osteocyte lacunae with a volume of bone tissue, and the osteocyte lacunae volume (Ocy.L V), which defines the average or individual volume of the osteocyte lacunae within the bone tissue.

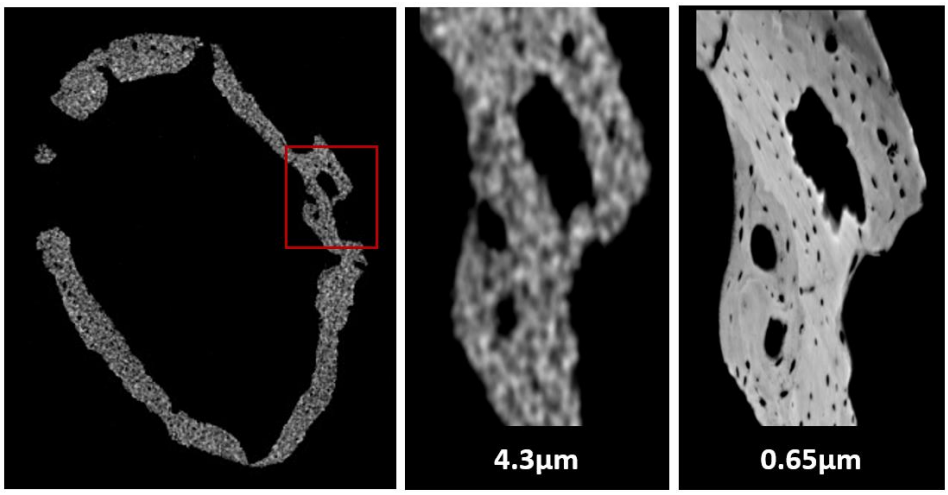

Figure 2.3: *Examples of the cortical bone in the distal mouse femur, comparing a micro-CT image with a resolution of 4.3µm (middle) and a synchrotron image with a resolution of 0.65µm (right). Image courtesy of Evans et al.* (2024).

2.2.3 3D geometrical reconstructions from high-resolution images

Micro-CT and SR-micro-CT imaging, as discussed previously, generates a series of 2D slices of the region of interest (e.g., the whole bone or a section of the bone). These individual slices, however, only provide a limited view of the internal structure. To create a comprehensive understanding of the 3D organisation within the sample, these 2D slices need to be computationally processed and combined. This process, known as 3D reconstruction, allows for the generation of a digital representation of the entire 3D object. In the context of bone analysis, this object would be the whole bone structure or the bone structure of a region of interest.

Several reconstruction algorithms are employed by micro-CT and SR-micro-CT analysis software to achieve this 3D representation. Common examples include filtered back projection (Bouxsein et al., 2010) and the Feldkamp algorithm (Feldkamp et al., 1989).

Generating 3D reconstructions from 2D images enables visualisation of the bone sample's structure, offering a comprehensive view of the complex trabecular network and cortical shell compared to analysing individual 2D slices, thus providing a deeper understanding of bone morphology. Furthermore, quantitative analysis on the bone structure can be done. For example, the trabecular thickness or porosity can be quantified, or the overall bone volume (Bouxsein et al., 2010).

2.3 Biomechanical computational models

2.3.1 Models for the prediction of bone mechanical properties

2.3.1.1 Finite element models

Finite element (FE) analysis is a computational modelling method extensively utilised in engineering, notably in the design processes of structures such as bridges and aeroplane wings, providing their structural mechanical properties. Generating a FE model typically requires three key inputs: the object's geometry, material properties, and loading conditions. These inputs define the specific scenario the model will simulate. The FE model simulations then solve for the resulting displacements, deformations, and stress and strain distributions throughout the structure, and ultimately, its overall stiffness and strength.

2.3.1.1.1 Clinical applications of FE models

This methodology has evolved into other applications, such as bone research. For instance, the CT2FE pipeline (Figure 2.4) (Qasim et al., 2016) proves useful when estimating femoral fracture risks among osteoporosis patients. CT-based FE models have been used to predict bone properties, estimate fracture risk, and evaluate the effect of treatments at a certain time point in humans (Bessho et al., 2007; Keaveny et al., 2007; Zysset et al., 2013; Qasim et al., 2016; Kawabata et al., 2017). These models have been validated against experimental or clinical data, to improve the credibility of their outcomes (Zysset et al., 2013; Qasim et al., 2016) and have been shown to be better predictors of bone strength compared to standard clinical tools, such as CT- or Dual-energy X-ray absorptiometry-based measurements (Cody et al., 1999).

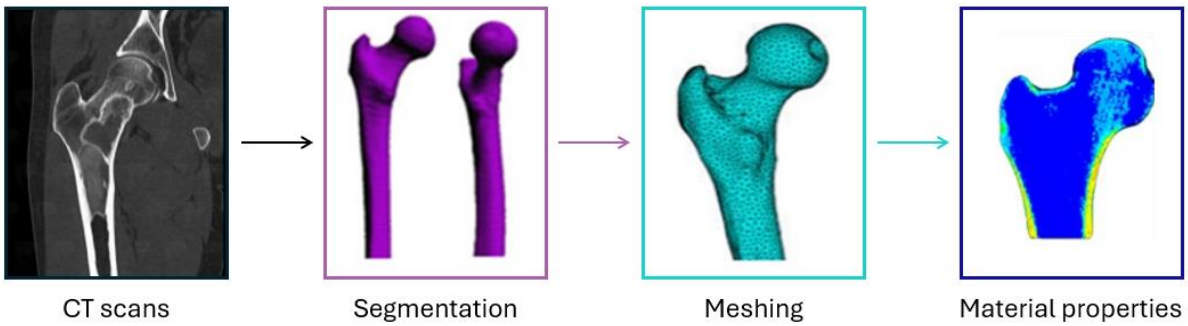

Figure 2.4: *An example of the CT2FE pipeline, showing the CT image, manual segmentation of the image, meshing to generate the FE model, and the application of the heterogeneous material properties. Image courtesy of Dr Xinshan Li.*

2.3.1.1.2 Micro-FE models of mouse bone

High-resolution biomedical imaging has allowed for the generation of micro-FE models. In contrast to traditional CT-based FE models used for clinical applications, high-resolution micro-CT images can be used to create highly detailed models which also consider the microstructure of the modelled specimen. The high-resolution of the images allows for the bone tissue to be separated from the background through a process called segmentation, typically done by using a global threshold. This threshold is a specific value chosen between the two peaks observed in the TMD frequency plot of the micro-CT image. These peaks represent the high-density bone tissue and the low-density background. Each bone voxel can then be converted into a finite element.

Micro-FE models developed in this manner incorporate intricate features such as the trabecular network and cortical porosities, providing a more comprehensive representation of the bone's microstructure. This detailed information allows micro-FE simulations to output localised predictions of bone's mechanical properties, such as the local stiffness. The following sub-sections show various approaches which have been used to analyse whole animal bones. They capture the intricate microstructure, which plays a crucial role in understanding the bone's local mechanical behaviour.

2.3.1.1.2.1 Micro-FE models of in vivo *micro-CT images*

The µCT2µFE pipeline (Oliviero et al., 2022) offers a valuable tool for preclinical studies in bone mechanics. It leverages *in vivo* micro-CT scans (Figure 2.5), similar to the established CT2FE pipeline which uses CT images. This approach allows for the non-invasive, longitudinal assessment of the same mouse tibia over multiple time points, enabling the tracking of changes in bone structure over time.

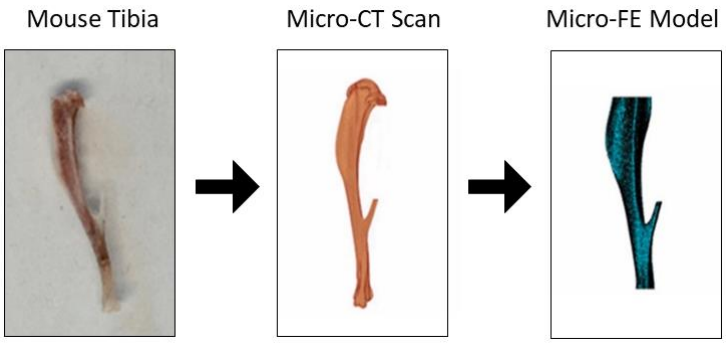

Figure 2.5: *A schematic illustrating the pipeline from tibia to micro-FE model. From left to right: mouse tibia, micro-CT scan of entire tibia, micro-FE model of 80% length of tibia. Adapted from Oliviero et al. (2021b).*

Here, linear finite element models were used. These models used the principles of scaling and superposition of the effects to output variables which can be calculated through combinations of existing model outputs instead of re-running multiple simulations, saving both time and computational resources (Oliviero et al., 2021b). Scaling techniques enable the adjustment of loading parameters, such as magnitude or direction, to simulate the effects of varying loading conditions. By systematically scaling the applied loads, multiple loading scenarios can be investigated without the need for exhaustive computational simulations.

The pipeline's utility has been demonstrated in evaluating novel treatments for osteoporosis. Roberts et al. (2023) used the µCT2µFE pipeline to assess the effectiveness of combined PTH and mechanical loading. Their study found that micro-FE models of the tibia from mice receiving combined therapy exhibited higher stiffness and strength compared to those receiving either PTH or mechanical loading alone (Roberts et al., 2023).

However, limitations exist. When applying mechanical loading, experimentally, there is the inherent assumption of axial loading. However, considering the transmission of the applied load through the knee and ankle joints, compounded by the potential for the leg to be repositioned within the loading device during longitudinal studies, uncertainty arises over the true loading direction and the effect that this may have on bone adaptation. Future refinements of the pipeline could be conducted through a sensitivity analysis of the loading direction on the effect of the bone's mechanical properties.

Additionally, while PTH may improve some mechanical properties, studies have shown it can also increase cortical bone porosity (Meakin et al., 2017). Increased porosity is generally associated with decreased bone strength (Schneider et al., 2013; Carriero et al., 2014b). Capturing these subtle structural changes requires higher resolution micro-CT scans with a smaller voxel size.

2.3.1.1.2.2 Micro-FE models of SR-micro-CT images

SR-micro-CT, offering superior resolution compared to conventional micro-CT, allows for the creation of micro-FE models that capture intricate bone microstructures, such as osteocyte lacunae.

To date, only one study exists which shows the use of SR-micro-CT based micro-FE models to study the effect of the osteocyte lacunae on the strains within the bone matrix (Hemmatian et al., 2021). The study focused on age-related changes in these strains, revealing how lacunae morphology might affect bone mechanical properties across different age groups. This was done by using micro-FE models based on images of the mid-section of the fibula, with a resolution of 0.7µm (Figure 2.6). The micro-FE models of the 0.35mm section of the fibula included the cortical bone matrix, the pericellular matrix

(the bone matrix immediately around the lacunae) and the osteocyte lacunae. Each were assigned their own material properties (16 GPa, 40 kPa, and 4.47 kPa, respectively and all a Poisson ratio of 0.3). This inclusion of the osteocyte lacunae in the micro-FE models, led to a more comprehensive understanding of the local bone mechanical properties. However, the images were acquired *ex vivo*, limiting the investigation to a single time point. Additionally, validating such high-resolution micro-FE models with experimental data remains an ongoing challenge.

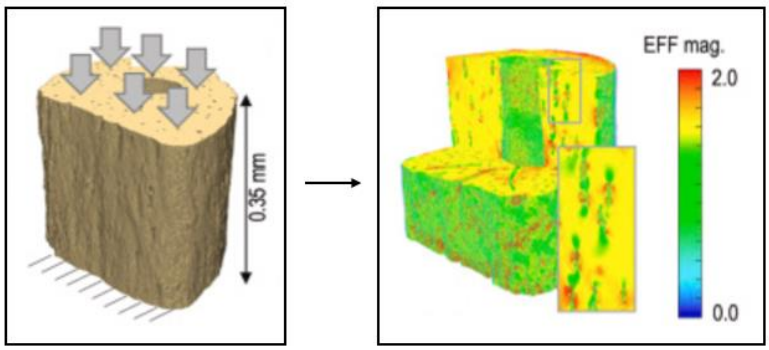

Figure 2.6: *Left: A representation of the micro-FE model of a midfibula diaphysis with the applied loading and boundary conditions. Right: The effective strain distribution (EFF mag.) over the micro-FE model. Adapted from Hemmatian et al. (2021).*

It's important to note that studies using this approach are currently limited. While Hemmatian et al. (2021) focused on age-related changes, further research is needed to explore the use of micro-FE models from SR-micro-CT across different bone regions, interventions, and disease states.

2.3.1.1.2.3 Validation of micro-FE models based on in vivo *micro-CT images of the mouse tibia*

2.3.1.1.2.3.1 Validation techniques

The ability to create micro-FE models from *in vivo* micro-CT scans offers a significant advantage for preclinical studies in bone mechanics. However, the model outputs need to be validated with experimental measurements.

Various techniques can be used to obtain these experimental measurements. For example, strain gauge measurements (Figure 2.7) have previously been used to validate micro-FE models of the mouse tibia (Stadelmann et al., 2009; Patel et al., 2014; Yang et al., 2014). These studies showed varying success, with errors ranging from 8-48%. The application of the strain gauge on small bones, such as those found in the mouse, may cause a local stiffening of the bone (Begonia et al., 2017). Furthermore,

strain gauge measurements can only be acquired in a limited number of spatial locations over the bone. Digital image correlation (DIC) improves upon this limitation by allowing for the evaluation of the displacement and strain distributions across the surface of the bone (Figure 2.8) (Pereira et al., 2015; Begonia et al., 2017). The results vary across studies and bones: Begonia et al. (2017) reported errors ranging from 3-14% in the mouse ulna but higher errors (31-38%) in the mouse radius, highlighting potential limitations of the technique for certain bone geometries and size.

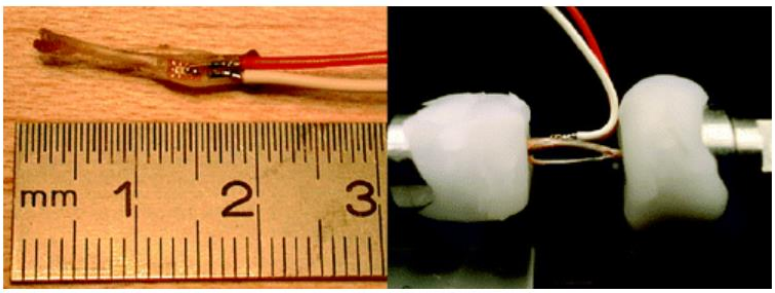

Figure 2.7: *Left: A mouse tibia with strain gauges attached. Right: Mouse tibia, with strain gauges attached, placed in the loading device (Stadelmann et al., 2009).*

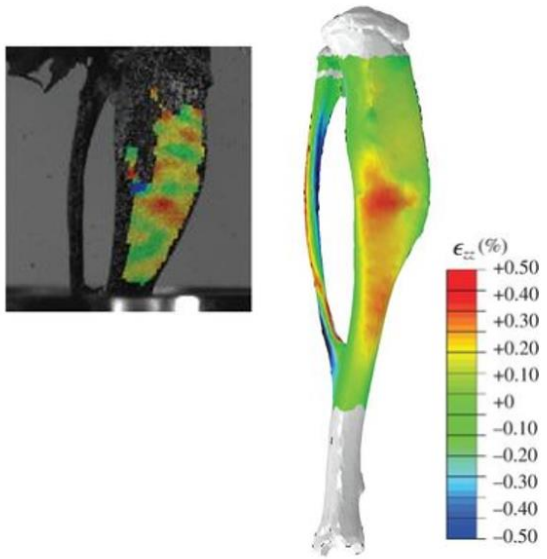

Figure 2.8: *An example of a comparison between the contour plots of the longitudinal strains (ϵ_{zz}) calculated using digital image correlation (DIC) and micro-FE modelling. Adapted from Pereira et al. (2015).*

Digital volume correlation (DVC) is another technique which has been used to validate micro-FE models of the mouse tibia (Oliviero et al., 2018). DVC can be used to compare the deformation of the model with *ex vivo* experimental measurements taken from across the whole specimen, allowing for the calculation of both the internal and the external strains (Figure 2.9). Oliviero et al. (2018) showed that hexahedral homogenous micro-FE models can predict well the local displacements across the tibia (R^2 > 0.82), the apparent stiffness (errors of 14 ± 11%) and the strength (errors of 9 ± 9%). Although DVC offers a comprehensive validation approach (due to its ability to calculate the 3D deformation and strain maps throughout the bone structure), careful consideration of factors throughout the pipeline – from image acquisition to failure criteria – is essential for ensuring model accuracy.

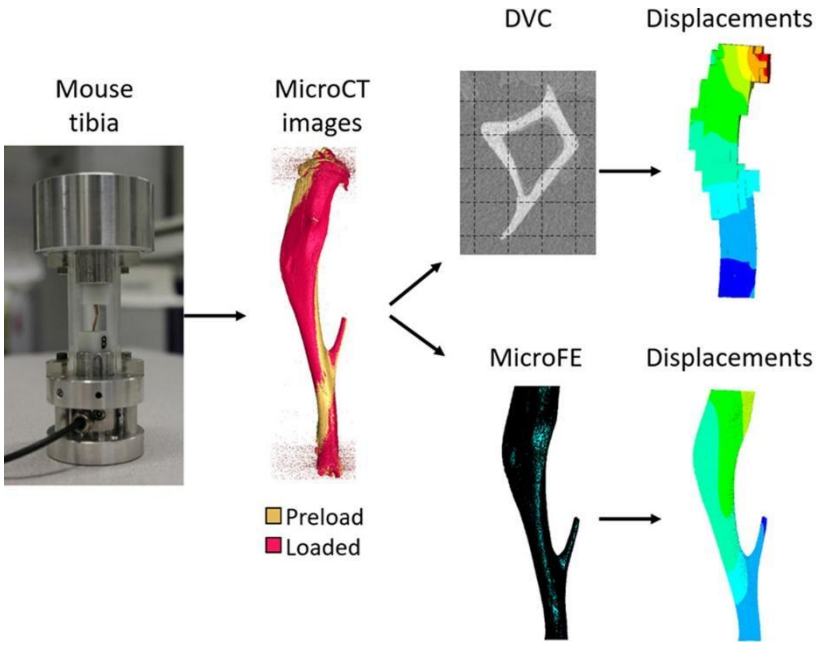

Figure 2.9: *Example of the pipeline used to validate micro-FE models using digital volume correlation (DVC). Left to right: The sample (mouse tibia) was placed within a loading jig and micro-CT scanned in an unloaded configuration. The tibia was then loaded and scanned again. The DVC was applied: the loaded scan was registered to the unloaded scan to calculate the displacement field. The micro-FE model was generated from the unloaded scan. The displacements outputted by the DVC and the micro-FE model were compared. Adapted from Oliviero et al. (2018).*

2.3.1.1.2.3.2 Factors affecting model accuracy

Several factors may influence the accuracy of these micro-FE models. Each part of the pipeline to generate such models needs to be examined. Beginning with the process by which the micro-CT images

are acquired: a compromise between image quality and radiation dose is required. Factors which increase image quality, such as a decrease in voxel size, and an increase in the number of projections (number of images taken across the different angles), frame averaging (the number of times each projection is repeated) and integration time (the time spent on each projection), are related with an increase in radiation dose. Furthermore, a higher number of scans over time increases the radiation affects, though they provide temporal information about the bone properties.

Radiation dose has a significant effect on trabecular and cortical morphometric parameters in the mouse tibia (Klinck et al., 2008; Laperre et al., 2011; Oliviero et al., 2019). Significant reductions in trabecular bone volume fraction (Tb.BV/TV, 8–20%) and trabecular number (Tb.N, 9–16%) have been found with a scanning protocol associated with a 846 mGy radiation dose (200 ms integration time, five weekly scans) (Klinck et al., 2008). Similarly, significant reductions in Tb.BV/TV (-30%) and Tb.N (-35%) have been found with a scanning protocol associated with a 776 mGy radiation dose (3300 ms exposure time, three scans every two weeks) (Laperre et al., 2011). Additionally, significant reductions in Tb.BV/TV (20–38%) and increases in trabecular spacing (Tb.Sp, 29–39%) have been found with a scanning protocol associated with 600 ms integration time, four scans every five days (no radiation dose was recorded) (Willie et al., 2013). One method to decrease the radiation dose, is to decrease the integration time. This was investigated by Oliviero et al. (2017), who found that by varying the integration time from 200 ms to 50 ms, the radiation dose decreased from 513 mGy to 128 mGy. This had the largest effect on trabecular morphometric parameters (7–28%), whilst lower effects were found for cortical parameters (1–3%). This information on the effect of integration time allowed for the development of an appropriate scanning protocol for repeated *in vivo* micro-CT scans (256 mGy, 100 ms integration time, 5 scans every two weeks), which found a reduction in Tb.BV/TV (-14.9%) and Tb.N (-14.2%) and an increase in Tb.Th (+3.3%) and Tb.Sp (+11.6%), allowing for the micro-CT scans to be done on the mouse tibia *in vivo*, without affecting the bone remodelling (Oliviero et al., 2019).

Next, the image processing steps within the pipeline require operator-dependant methods, such as image alignment, selection of region of interest, selection of the threshold value used for segmentation, and hence the reproducibility of these measurements should be assessed. Lu et al. (Lu et al., 2016) evaluated the reproducibility of the bone mineral content (BMC) in growing C57BL/6 mouse tibia of eight mice, each scanned four times. They showed that by dividing the tibia into 40 partitions (10 divisions along the longitudinal axis and 4 cross-sections), the BMC could be calculated with precision errors lower than 3.5% for all partitions. Additionally, Oliviero et al. (2022) evaluated the intra- and inter-operator reproducibility of several bone parameters (morphometric, densitometric and mechanical properties). The lowest reproducibility was found for stiffness estimated with micro-FE

models (precision error = 3.71% intra-operator, 4.09% inter-operator), which was five times lower than the measured effect of the interventions applied to the mice, and therefore, it was deemed that the method could measure the variations between interventions adequately. Furthermore, Razi et al. (2014) evaluated the effect of the longitudinal alignment in FE models of C57BL/6 mouse tibiae. They varied the orientation of the inferior-superior axis of the tibia between a range of 0-20° and loaded the model in compression. The local strains varied up to 40% due to the tibial misalignments, demonstrating the importance of maintaining tibial alignment.

For the modelling parameters, an investigation into the appropriate element shape (hexahedral or tetrahedral) and material properties (homogenous or heterogenous) concluded that using micro-FE models with hexahedral homogenous material properties showed best correlations between experimental and predicted mechanical properties, with lowest errors (apparent stiffness: R^2 = 0.65, error: 14 ± 8%; apparent strength: R^2 = 0.48, error: 9 ± 6%; normalised stiffness: R^2 = 0.80, error: 14 ± 8%; normalised strength: R^2 = 0.81, error: 9 ± 6%; NB: normalised by total bone mass) (Oliviero et al., 2021b). The estimation of the bone strength, used the failure criterion defined for the mouse tibia, proposed by Oliviero et al. (2021a) (based on a previous approach, by Pistoia et al. (2002), for the human distal radius). This was defined by evaluating multiple failure criteria and selecting the optimised parameters by minimising the errors with respect to experimental measurements. Razi et al. (2014) conducted sensitivity analyses on the effect of the boundary conditions and mesh refinement on the strains predicted by micro-FE models of the mouse tibia. The boundary conditions were found to have the largest effect on the local strains, increasing the longitudinal strains by up to 150% compared to strain gauge measurements. This highlighted the importance of the choice in the boundary conditions used in such models. Furthermore, Cheong et al. (2021a) investigated the effect of the loading conditions on the mouse tibia. The effects of physiological, axial, and combined loads on bone adaptation using micro-FE models were evaluated. Strain distributions varied significantly between the loading conditions. However, the overall accuracy of bone remodelling predictions was similar. All predicted densitometric properties were significantly different between the axial and the combined loading conditions. Therefore, the loading conditions of such models should be well defined to accurately predict densitometric properties of the mouse tibia.

These combined studies demonstrate the importance in the selection of scanning parameters, image pre-processing steps, and modelling parameters to create accurate micro-FE models. Furthermore, the validity of the pipeline which creates micro-FE models based on *in vivo* micro-CT scans for the mouse tibia under compressive loading has been presented (Oliviero et al., 2017, 2018, 2019, 2021a, 2021b, 2022).

2.3.1.2 Beam theory

Similar to FE analysis, Euler-Bernoulli beam theory (BT) can be used to determine strains within a bone. BT has been used in bone adaptation studies to estimate stresses, strains, and the strain energy density (SED) in both mice and human samples (Buenzli et al., 2013; Lerebours et al., 2016; Trichilo, 2018; Pickering et al., 2022). In comparison to FE analysis, the time taken for analysis in BT studies is notably shorter. However, modelling of an axial loading scenario may not be accurate regarding SED estimates, as it relies upon the assumption that there are no shear strains present. Furthermore, BT requires the complex geometry of bone to be assumed to be slender beams (Figure 2.10). In the case of the tibia, BT may not capture the geometry as well as a FE model, due to the curvature and changes in cross-sectional area of the bone. Table 2.1 shows the advantages and disadvantages of FE modelling and BT.

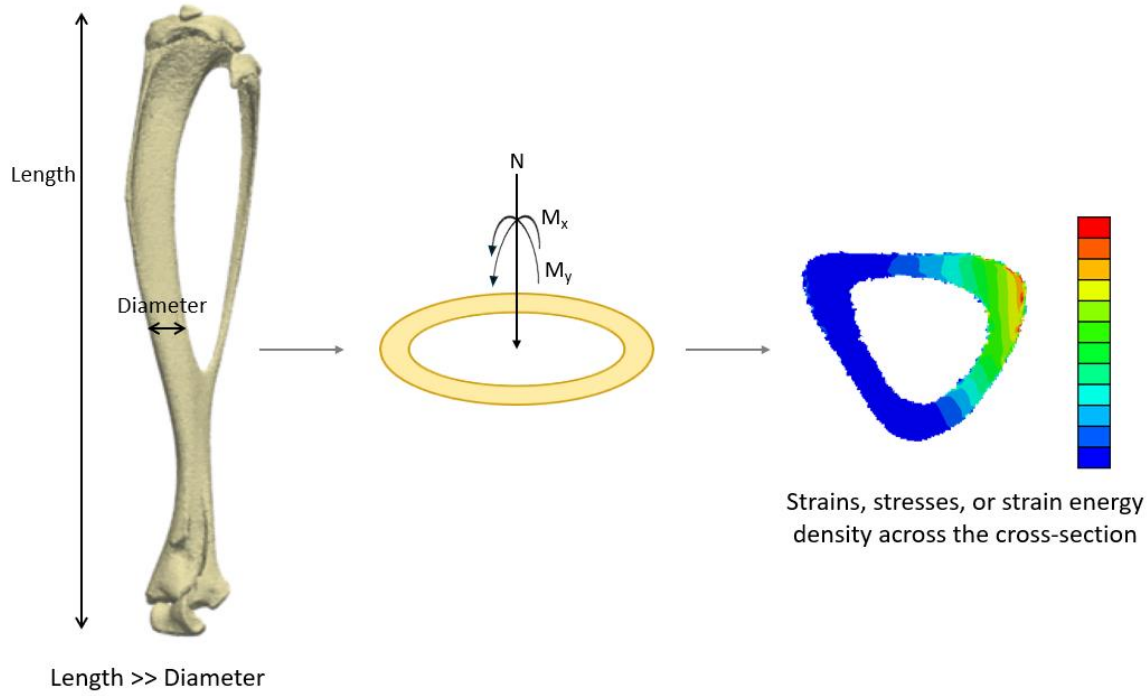

Figure 2.10: *Beam theory is used to compute the normal force (N) and bending moments (M_x, M_y) at a cross-section of the mouse tibia, which is used to compute the strains, stresses, or strain energy density across the mouse tibia.*

Table 2.1: *The advantages and disadvantages of finite element (FE) modelling and beam theory (BT) methods for calculating the local mechanical properties of bone.*

	Finite element models (FE) models	**Beam theory (BT)**
Advantages	● Can handle a wide range of geometries, materials, and loading conditions. It can also account for complex interactions between different parts of a structure. ● Can capture micro-structural deformations, especially when using refined meshes.	● Involves well-defined equations and requires minimal computational resources. This makes it a quick and efficient approach.
Disadvantages	● Requires specialised software and expertise for setting up the model, defining material properties, and interpreting the results. ● Running FE simulations can be computationally expensive, especially for complex models.	● Assumes the bone is a slender beam and experiences small deflections. It cannot account for complex geometries, non-uniform loads, or material nonlinearities. ● Assumes that no shear strains are present.

Studies by Miller et al. (2024a, 2024b) use BT to provide valuable insights into the mechanisms underlying cortical bone adaptation in response to mechanical loading and/or PTH. Miller et al. (2024b) explored the link between the load magnitude and the adaptive response around the periosteum of the tibia at a cross-section level. By quantifying cortical thickness changes, a quasi-linear relationship between load magnitude and bone formation was shown, highlighting the importance of considering local adaptive responses compared to global metrics (Miller et al., 2024b). Miller et al. (2024a) focused on the coupled effect of combined PTH and mechanical loading treatments within two cross-sections of the tibia – a slice located at 37% of the tibial length (0% equated to the proximal end and 100% equated to the distal end of the tibia) and a slice located at 50% of the tibial length. The findings highlighted the non-uniform and region-specific nature of cortical thickness changes in response to treatments, emphasising the importance of understanding their interaction for optimising bone formation strategies (Miller et al., 2024a). Although these studies contribute to the understanding of

cortical bone adaptation mechanisms, they are all based on cross-sectional images of the mouse tibia, the results cannot be generalised across the tibia. Furthermore, due to the cross-sectional analysis, information may be missed, such as the effect of shear strains from the applied loads.

2.3.2 Computational models for predicting bone adaptation over time

2.3.2.1 Mechanoregulation models for predicting bone adaptation

Bone adaptation is the dynamic process by which bone models and remodels itself in response to mechanical stimuli. This allows the bone to maintain its internal structure and density in response to biomechanical or biochemical stimuli. Mechanoregulation models aim to predict this adaptation process by incorporating these mechanical stimuli into computational frameworks.

2.3.2.1.1 Mechanical stimuli

While the exact mechanisms of bone remodelling are still being unravelled, two main theories explain the initiation of mechanically induced bone remodelling (see Section 1.4.2 for more details). One theory suggests that mechanical stimulus directly deforms the bone matrix. Osteocytes, embedded in the matrix, sense these deformations and trigger bone remodelling (Scheiner et al., 2013). The second theory proposes that the mechanical stimulus alters the fluid pressure within the lacunae canalicular network (LCN). Osteocytes within this network sense changes in fluid pressure and initiate bone remodelling accordingly (Scheiner et al., 2013).

Both theories are triggered by mechanical stimuli, which can be represented in various ways within computational models of bone adaptation. Models which focus on the direct deformation of the bone matrix often utilise parameters such as longitudinal stress or strain (Pereira et al., 2015; Pickering et al., 2021; Miller et al., 2024a), principal strains (Pereira et al., 2015; Birkhold et al., 2016; Cheong et al., 2020a), effective strain (Marques et al., 2023), or SED (Adachi et al., 2009; Scheiner et al., 2013; Pereira et al., 2015; Carriero et al., 2018; Trichilo, 2018; Cheong et al., 2020a, 2020b; Scheuren et al., 2020; Cheong et al., 2021a; Marques et al., 2023). Models which focus on fluid dynamics within the LCN might incorporate parameters such as fluid flow (Tan et al., 2007; Adachi et al., 2009; Pereira et al., 2015; Scheiner et al., 2016; Carriero et al., 2018). There is no clear consensus as to which stimuli best predicts bone remodelling. Some studies suggest that through combining multiple stimuli, a more accurate prediction of bone adaptation may be achieved (Cheong et al., 2020a, 2020b). However, strain calculations remain essential for the model due to the dependence of flow on channel deformation.

2.3.2.1.2 Mechanoregulation models of human bone

There exist some initial attempts to that used of FE models in conjunction with Wolff's Law (bone remodels in response to stress) to predict bone adaptation in humans (Tsubota et al., 2009; Boyle and Kim, 2011). A promising avenue for human bone remodelling lies in the potential of poroelastic and micromechanical theories. Scheiner et al. (2016) explored the application of these theories within a multiscale mechanobiological model of bone remodelling (Figure 2.11). These theories offer the ability to model bone as a hierarchical material with porosities of various sizes at different scales, incorporating microstructural features such as pore shape and volume. This approach has the potential to provide a more comprehensive understanding of bone mechanics and remodelling compared to traditional models. However, it is hard to validate the outputs of such bone remodelling models and therefore comparisons have been done in mice using *ex vivo* micro-CT (Boyle and Kim, 2011).

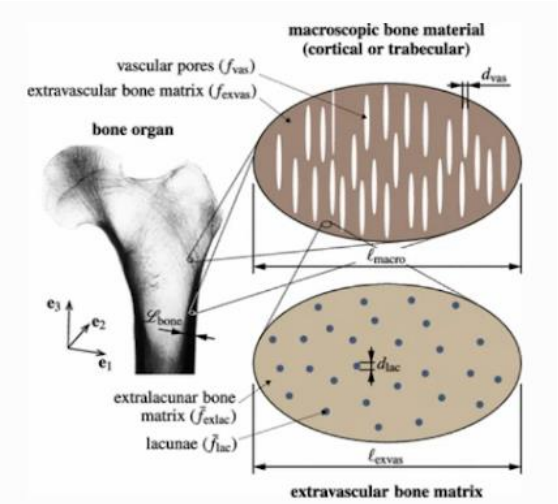

Figure 2.11: *Micromechanical representation of cortical bone, based on a poromicromechanical model (a model which contains microstructural features, for determining the mechanical interactions between pore pressures and stresses acting on the porous bone) (Scheiner et al., 2016).*

2.3.2.1.3 Preclinical applications of mechanoregulation models

A combination of micro-FE models and mechanoregulation algorithms, predominantly based on Frost's 'mechanostat' theory, have been created for the prediction of bone adaptation over time. The micro-FE model gives the strain distribution over the area of interest and the mechanoregulation algorithm relates the strain distribution to the bone adaptation. The relation of these two concepts is based on combinations of the rates of remodelling (formation and resorption, independently) and the

thresholds of adaptation. Experimental studies are increasingly revealing a continuous response to mechanical stimuli, negating the idea of a 'lazy zone' where remodelling does not occur, and that the rates of remodelling can both be described linearly (De Souza et al., 2005; Sugiyama et al., 2012; Schulte et al., 2013a; Razi et al., 2015a; Cheong et al., 2020a). Additionally, existing models typically apply uniform thresholds for remodelling across the bone, assuming a constant response to mechanical stimuli within all regions.

The murine model has been adopted within much preclinical research relating to bone disease. Within bone remodelling studies, the mouse tibia or caudal vertebra, in an axial loading configuration, are often used.

2.3.2.1.3.1 Mechanoregulation models of the mouse tibia

Cheong et al. (2020a) developed a mechanistic model to predict bone adaptation over time. This model was based on an iterative process (Figure 2.12) which combined a micro-CT based micro-FE model with a mechanoregulation algorithm. The micro-FE model had hexahedral elements with isotropic homogenous material properties and has been previously validated (Oliviero et al., 2018, 2021b). The mechanoregulation algorithm assumed the same linear rate of remodelling for both formation and resorption. This rate and threshold of remodelling was calculated for each mouse by optimising the volumetric second moment between the experimental scans at the next time point and the predicted bone, and was applied across the whole bone i.e., mechanosensation (distribution of the osteocytes) was not included in this model. A sensitivity analysis conducted on the inclusion of a 'lazy zone' concluded that it did not significantly improve the predictions of bone adaptation.

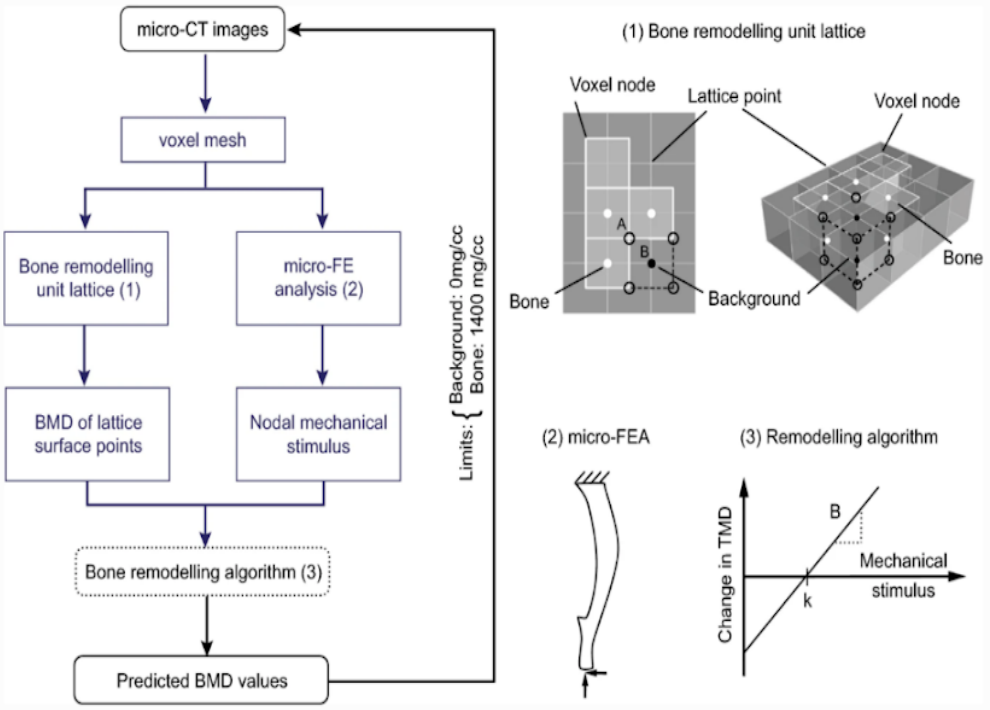

Figure 2.12: *The bone remodelling algorithm flow chart (left), used in the study by Cheong et al. (2020a), showing the generation of the pseudo-micro-CT images and the optimisation algorithm (in blue-grey) to compute the parameters for bone remodelling. (1) The remodelling unit lattice. (2) Boundary conditions of the micro-FE model. (3) Remodelling algorithm with formation limit k and rate of remodelling B (Cheong et al., 2020a).*

No statistically significant differences were observed between the experimentally measured and model-predicted densitometric properties (bone volume, bone volume fraction (BV/TV), BMC, and the bone mineral density (BMD)). However, the highest errors in densitometric properties were located at the proximal end, which could be due to the amount of remodelling differing from the rest of the bone as this region is composed of mainly trabecular bone. A spatial match between the model and experimental results found that 59% of the predicted voxels matched with the experimental sites in formation. Moreover, it was higher on the periosteal than the endosteal surface. The model captured a spatial match of 47% of the predicted voxels for resorption. Although the model was able to predict regions of formation of above 70% on both the periosteal and endosteal surfaces, it also under predicted regions of resorption by over 85%. This underprediction in resorption may be due to the algorithm being unable to predict bone adaptation driven by biochemical stimuli.

Multiple parametric studies were conducted. Comparisons of predictions based on two different mechanical stimuli, SED and maximum principal strain, showed that although the choice of the stimulus did not affect the shape of the errors in predicting densitometric properties, SED captured better the formation. Maximum principal strain captured resorption better, but this was at the expense of formation. It was also shown that subject-specific remodelling thresholds and rates decreased the densitometric errors compared to averaged population values, highlighting the advantage of subject-specific parameters.

Furthermore, the mechanoregulation model was later applied to investigate the effect of passive mechanical loading on the mouse tibia (Cheong et al., 2021a). The mechanoregulation parameters were optimised for a different group of mice, which provided different remodelling rates for formation and resorption. Predictions of the densitometric properties were calculated separately for models loaded with a 12 N load, a daily physiologically relevant load, and a combination of both these loads. The combined loading densitometric properties were most similar to the experimental data, highlighting the importance of including the daily physiological load when investigating the bone's adaptive response to passive mechanical loading.

This mechanoregulation model has since been applied to multiple sets of mice to investigate the effect of mechanical loading, PTH, and combinations of mechanical loading and PTH in ovariectomised mice, over time (Cheong et al., 2020b, 2021b). These studies have shown a linear bone formation response to load-induced changes, which, as expected, was higher during mechanical loading than during ovariectomy. However, the results also showed that resorption was independent of strain at the organ level, alluding to the fact that resorption may be regulated locally or biologically determined (Cheong et al., 2020b). Furthermore, the model was applied to investigate the efficacy of combined mechanical loading and PTH treatments. This showed that the proximal region of the tibia had the greatest gain from positive interactions of combined therapies. Periosteal formation greatly benefited from combined treatments, especially in the proximal region, highlighting the positive benefits of the combined treatments (Cheong et al., 2021b). This study serves as an example of how such models can be used to optimise dosage and treatment duration in preclinical mouse studies. For example, these models could be used to investigate the effects of different dosages, optimal treatment timing, the efficacy of combined therapies, or to identify the most effective treatment windows to maximise bone remodelling.

2.3.2.1.3.2 Mechanoregulation models of the mouse caudal vertebra

Combinations of micro-FE and mechanoregulation models have also been applied to the trabecular bone in the mouse caudal vertebra to non-invasively investigate the effects of osteoporosis and related interventions (Schulte et al., 2013a, 2013b; Scheuren et al., 2020; Marques et al., 2023).

The study by Schulte et al. (2013b) validates a computational model for predicting bone adaptation using *in vivo* micro-CT data. This model incorporates a local mechanical feedback loop, optimising bone remodelling rates for improved accuracy. Tuning resulted in a prediction error ranging from 2.39% to 8.44% for bone morphometric parameters (BV/TV and Tb.Sp, respectively) under mechanical loading. This demonstrates the model's ability to capture bone formation trends, particularly the spatial distribution with an accuracy of 55.4% (a voxel-based comparison was used between experimental and model predictions) (Figure 2.13). However, the model's accuracy for bone loss scenarios remained lower, with a maximum error of 12.1% in BV/TV observed during simulations of ovariectomy-induced bone loss. This suggests the model might be better suited for predicting bone formation under loading conditions. Interestingly, the local mechanical feedback loop appears to play a role in capturing the slowdown of bone loss observed after a certain point, potentially by predicting increased bone formation when bone mass becomes critically low. It is important to note that the model's accuracy in predicting the spatial distribution of bone resorption remains limited, reaching only 47.6% for ovariectomy simulations.

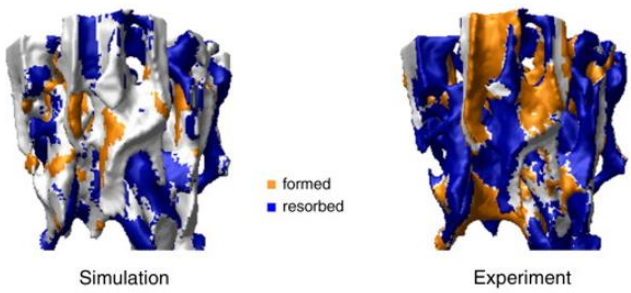

Figure 2.13: *Visual comparison of the spatial distribution between in silico (left) and in vivo (right) models of bone adaptation within the trabecular bone in the mouse caudal vertebra (Schulte et al., 2013b).*

Marques et al. (2023) investigated the relationship between mechanical loading frequency and bone remodelling parameters using *in vivo* micro-CT data of the mouse vertebrae. They estimated remodelling velocity curves from the micro-CT images. These curves were then fitted with

mathematical functions, allowing for the extraction of key parameters such as the remodelling rates. The study revealed a logarithmic dependence of these remodelling parameters on loading frequency, suggesting a more nuanced response of bone adaptation to mechanical stimuli than previously understood.

However, a limitation of using the caudal vertebrae in such studies is that they cannot be investigated under physiological loading conditions, limiting their applicability to real-world scenarios. This is because the physiological loading pattern in the mouse tail is not fully understood. The unknown mechanical stimuli the caudal vertebrae are exposed to makes it difficult to interpret how the observed remodelling response under applied loads translates to other weight-bearing bones that experience distinct physiological loading conditions.

Mechanoregulation models have emerged as valuable tools for investigating bone adaptation and predicting its response to various stimuli. Studies utilising the mouse tibia and caudal vertebra have provided insights into the effects of mechanical loading, PTH treatment, and osteoporosis on bone remodelling. These models offer advantages such as non-invasive investigation and the ability to optimise treatment regimes in preclinical studies. However, the challenge remains in capturing all biological factors influencing bone remodelling.

2.4 Cell & molecular level models

2.4.1 Bone cell population models

Bone cell population models (BCPMs) are typically represented as a system of ordinary differential equations (ODEs). The ODEs aim to capture the biological phenomena that is involved in bone adaptation. Instead of having a mechanical stimulus, in the same way as the models seen above, these models incorporate the biochemical aspects which affect bone remodelling. Pivonka et al. (2008) built upon the work of Lemaire et al. (2004) and formulated an extended bone-cell dynamics model. The system of ODEs (Eqs. 2.1, 2.2 & 2.3) represent the behaviour of the BMUs during bone resorption and formation by modelling the changes of each cell population: osteoblast precursors (OBp), active osteoblasts (OBa), and active osteoclasts (OCa). These changes in cell populations are constructed by the differentiation rates (D) and removal of cells through apoptosis rates (A) within the corresponding lineage. Additionally, activator and repressor functions ($\pi_{act/rep,cell}^{molecule}$) are also included to model transforming growth factor beta ($TGF\text{-}\beta$) and $RANKL$ binding with their receptors (Lemaire et al., 2004; Pivonka et al., 2008).

$$\frac{dOBp}{dt} = D_{OBu} \cdot OBu \cdot \pi_{act,OBu}^{TGF-\beta} - D_{OBp} \cdot OBp \cdot \pi_{rep,OBp}^{TGF-\beta}$$

(2.1)

$$\frac{dOBa}{dt} = D_{OBp} \cdot OBp \cdot \pi_{rep,OBp}^{TGF-\beta} - A_{OBa} \cdot OBa$$

(2.2)

$$\frac{dOCa}{dt} = D_{OCp} \cdot OCp \cdot \pi_{act,OCp}^{RANKL} - A_{OCa} \cdot OCa \cdot \pi_{act,OCa}^{TGF-\beta}$$

(2.3)

Furthermore, an equation representing the change of bone volume over time is shown below (Eq. 2.4) which links the cell numbers obtained from Eqs. 2.1, 2.2 & 2.3 to changes in bone volume (BV).

$$\frac{dBV}{dt} = -k_{res}\widetilde{OCa} + k_{form}\widetilde{OBa}$$

(2.4)

where $\widetilde{OCa}(t) = OCa(t) - OCa(t_0)$, $\widetilde{OBa} = OBa(t) - OBa(t_0)$, and k_{res} and k_{form} are the relative bone resorption and formation rates, respectively (Pivonka et al., 2008).

The above model incorporates the RANK/RANKL/OPG signalling pathway and the regulating action of $TGF\text{-}\beta$, but neglects the role of the Wnt/β-catenin/Scl signalling pathway. This was incorporated by Martin et al. (2019) by extending Eq. 2.1, as shown in Eq. 2.5 below. The additional term includes new variables representing the proliferation rate (P) of the osteoblast precursor cells in response to the concentration of Scl and an activator function to model Wnt binding with its receptors (Martin et al., 2019).

$$\frac{dOBp}{dt} = D_{OBu} \cdot \pi_{act,OBu}^{TGF-\beta} - D_{OBp} \cdot OBp \cdot \pi_{rep,OBp}^{TGF-\beta} + P_{OBp} \cdot OBp \cdot \pi_{act,OBp}^{Wnt}$$

(2.5)

The inclusion of both the RANK/RANKL/OPG and Wnt/β-catenin/Scl signalling pathways allows for the indirect modelling of the catabolic and anabolic effect of mechanical loading on the bone (more details in Section 2.5.1). However, the influence of the lining cells on bone remodelling has still been neglected.

These cell population models have been combined with pharmacokinetic/pharmacodynamic (PK/PD) models to investigate the effect of osteoporosis treatments such as romosozumab (Martin et al., 2020), denosumab (Scheiner et al., 2014; Martínez-Reina and Pivonka, 2019; Martínez-Reina et al., 2021) and PTH (teriparatide) (Trichilo et al., 2019; Lavaill et al., 2020). PK/PD modelling combines pharmacological and mathematical approaches to analyse how a drug is absorbed, distributed, metabolised, and excreted by the body (pharmacokinetics, PK) and how these processes relate to the drug's effects on the body (pharmacodynamics, PD).

A sigmoidal H function is used to capture the non-linear effects of PTH on cellular activity and is shown in generic form in Eqs. 2.6 and 2.7 (Lavaill et al., 2020). The function either upregulates (H^+) or downregulates (H^-) actions with respect to an increase in stimulus L.

$$H_{L,j}^{+} = \rho_j + \frac{(\alpha_j - \rho_j).L^{\gamma_j}}{\delta_j^{\gamma_j} + L^{\gamma_j}} \tag{2.6}$$

$$H_{L,j}^{-} = \alpha_j - \frac{(\alpha_j - \rho_j).L^{\gamma_j}}{\delta_j^{\gamma_j} + L^{\gamma_j}} \tag{2.7}$$

where α is the minimum effective response, ρ is the maximum effective response, δ is the homeostatic value and γ is the response steepness. These parameters are specific to the affected process j (e.g., osteoblast apoptosis) and must be optimised per implementation of the H function.

Trichilo's et al. (2019) development of the step-function within the PK/PD model allowed for the representation of the on/off response of drug dosages which allowed for the investigation into different administrations of drug injections. The comparisons of this study against experimental data of PTH permitted the accurate investigation into different administrations of drug injections.

A major limitation of these cell population models lies in their reliance on a representative volume element (RVE): a region where cell concentrations are assumed to be uniform. The spatial resolution of the model's predictions is inherently limited by the size of the RVE. For example, if the RVE encompasses a large portion of bone tissue, the model may not accurately capture localised variations in bone adaptation, such as those occurring at the level of individual trabeculae. Conversely, if the RVE is too small, it may not be able to accommodate a sufficient number of cells for meaningful analysis.

2.4.2 Agent-based models

Agent-based models (ABMs) have been used to investigate bone remodelling and associated pathologies such as osteoporosis and its treatments (Paoletti et al., 2012; Schutte, 2012; Liu et al., 2015; Truesdell and Saunders, 2019). These models explore the intricate interplay between biomechanical and biochemical stimuli, within a single cell. These single cell models can be combined, which increases the model's complexity: cells can each be modelled as a single agent, with signalling pathways modelled to regulate the cell behaviour (Boaretti et al., 2023; Kendall et al., 2023).

However, it is essential to acknowledge that the accuracy of ABMs heavily relies on the input parameters and the underlying assumptions made about cellular behaviour. Parameters can be determined experimentally, obtained from existing literature, or assumed. These assumed parameters can be optimised, for example, through the comparison of *in silico* and *in vivo* data (Boaretti et al., 2023). Model validation against experimental data is crucial to establish the reliability of ABM predictions (Paoletti et al., 2012). Although this is not currently presented in all ABM studies (Boaretti et al., 2023; Kendall et al., 2023).

While ABMs offer a high degree of detail, through the discrete modelling of cells, their computational demands limit their application to large-scale bone adaptation studies over time. Despite their limitations, ABMs remain a valuable tool for exploring bone biology at a microscopic level. Future advancements in computational power and model refinement may expand the applicability of ABMs to larger-scale bone modelling.

2.5 Combined approaches

In the current literature there are a limited number of models (Table 2.2) that aim to take a combined biomechanical and biochemical approach to simulate bone remodelling. The approach varies according to the authors. Most frequently, the biochemical aspect is modelled by a bone cell population model, represented by a system of ODEs, which is then combined, in some manner, with a mechanical stimulus. Table 2.2 provides an overview of the studies that have used a combined biomechanical and biochemical approach to simulate bone remodelling. As can be seen from the table, this is a limited number of studies.

Table 2.2: *An overview of the studies included in this literature review that use a combined biomechanical and biochemical approach to simulate bone remodelling. For each study the approach, species and site the model is based on, the disease and intervention, and the advantages and disadvantages of each model is listed.*

Reference	Approach	Species & Anatomical Site	Disease & Intervention	Advantages	Disadvantages
Ashrafi et al. (2020)	FE + BCPM	Human proximal femur	Mechanical loading Total hip replacement	Considers two mechanical stimuli: strain and micro-damage Includes a preliminary extension to the model: the inclusion of describing the bone as an anisotropic material	Lack of validation against experimental data Limited in number of pathways/ molecules which are affected by the mechanical stimulus e.g., no Wnt or nitric oxide modelled No specific mechano-sensing model considered, i.e., assumed that the number and location of osteocytes is uniform
Lerebours et al. (2016)	BT + BCPM	Human midshaft femur	Osteoporosis	Outputs site specific bone loss	Assumes periosteal surface is fixed

			Mechanical disuse	Utilises a localised mechanical stimulus (microscopic and tissue level stress/strains used)	No validation against experimental data Assumes constant activity BT assumes no shear strains are present
Pastrama et al. (2018)	Poromicromechanics + BCPM	Human proximal femur + mouse tibia	Mechanical loading	Represents the hierarchical organisation of bone tissue Pore pressure as mechanical stimulus	Validation for rat model relies on similar mechanical sensitivity and cell activity between rats and mice Mechanosensation not taken into account physiologically
Pivonka et al. (2013)	Micromechanics + BCPM	Human cortical + trabecular bone	Mechanical loading + pharmacological Osteoporosis	Model considers various stages of osteoblast and osteoclast development, allowing for a more detailed representation of cellular regulation Improves upon previous bone cell population models through the	Limited understanding and inclusion of pre-osteoblast proliferation (sclerostin)

				inclusion of a mechanical stimulus (SED)	
Scheiner et al. (2013)	Micromechanics + BCPM	Mouse femur	Mechanical loading + pharmacological	Alignment of results with previous findings Inclusion of the effect of microcracks	Limited understanding and inclusion of pre-osteoblast proliferation (sclerostin)

2.5.1 Micromechanics & BCPMs

A cell population model has been coupled with a micromechanical model of bone stiffness through a SED-based feedback loop (Pivonka et al., 2013; Scheiner et al., 2013). Both models included "pre-osteoblast proliferation," later known to be the response to the concentration of Scl, which made the coupling of the ODEs to a mechanical stimulus possible. This was later built upon through the inclusion of Wnt signalling (and its interactions with Scl) and nitric oxide. This modelled the effect of mechanical loading and showed that they could calibrate the anabolic and catabolic regulatory mechanisms so that they were mutually exclusive (Martin et al., 2019).

2.5.2 Beam theory & BCPMs

A combination of BT and micromechanics can be used to determine the tissue-scale and the microscopic strain distributions (Lerebours et al., 2016). This information allows for the SED to be incorporated into the cell population model. Bone remodelling can change the microstructural parameters, inducing changes in the load distribution. The geometrical feedback was, therefore, included in the cell population model (Figure 2.14). The model outputs site specific bone loss. However, it assumes the periosteal surface is fixed and the model outputs have not been validated against experimental data. Furthermore, the analysis is based on BT assumptions. This means that the model inherently excludes shear strains and treats the tibia as a slender beam.

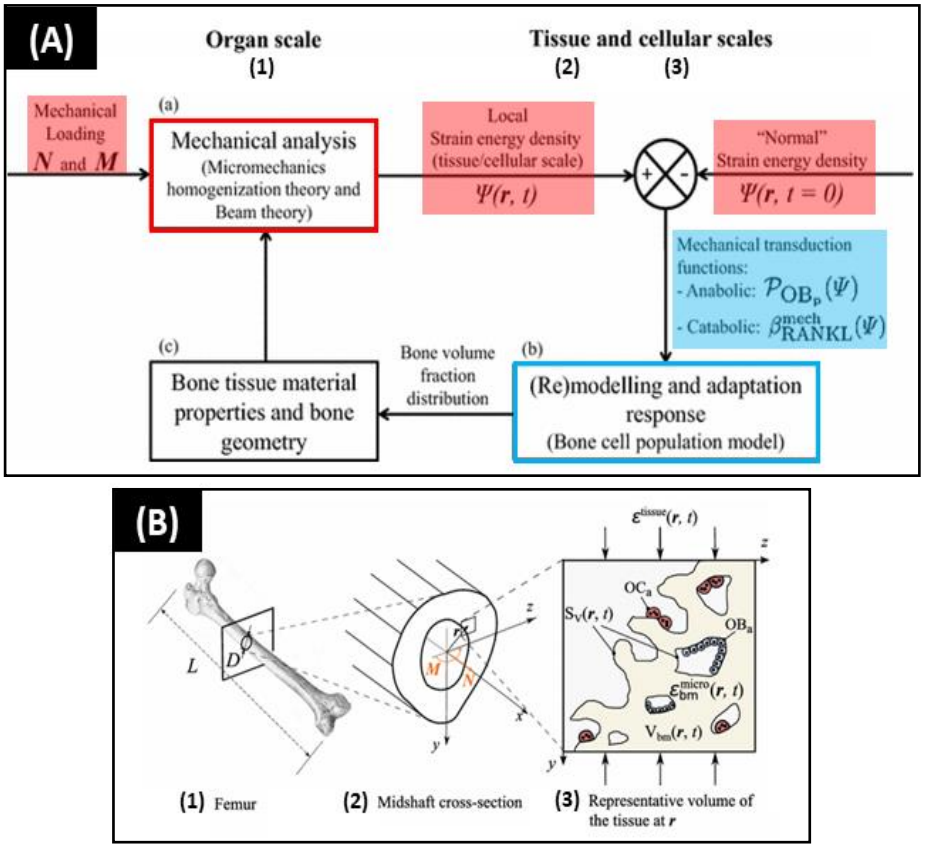

Figure 2.14: *(A) Flowchart of the bone remodelling simulations used by Lerebours et al. (2016), taking into account (a) the global mechanical loading, (b) the bone cell population model, and (c) the bone material and geometry adaptations. The mechanical components of the model are outlined in red, and the coloured red boxes show the mechanical stimuli used in the model. The biochemical components of the model are outlined in blue, and the coloured blue boxes show the biochemical stimuli used in the model. (B) The multiscale representation of bone, used in the study by Lerebours et al. (2016), illustrating (1) the organ scale (femur bone geometry), (2) the tissue scale (midshaft cross section), and (3) the cellular level (representative volume element of cortical bone). Adapted from Lerebours et al. (2016).*

2.5.3 FE & BCPMs

Both pore pressure (Pastrama et al., 2018) and strain-dependent mechanical stimuli (Ashrafi et al., 2020) have been used in combination with cell population models. Pastrama et al. (2018) created a poromicromechanical model which was coupled with a cell population model. Within their model, they included pore space-specific terms, considered concentration changes of cells, and investigated factors that are contained in the pore fluid due to porosity changes. By incorporating mechanical stimuli at multiple scales, they reached a good agreement (a difference of 10-11%) between model

predicted extravascular bone matrix volume fraction and experimental results from Laib et al. (2000). Although their model is able to be applied to both human and rodent bone, it has only been validated against experimental data collected from the trabecular proximal tibiae of tail-suspended rats (Laib et al., 2000). This method of validation involved assuming that the mechanical sensitivity and the cell activities are the same between mice and rats. Additionally, the inclusion of structural analysis of bone at the organ scale is neglected in this study.

Ashrafi et al. (2020) created a mechano-chemo-biological model (Figure 2.15) by combining a FE model with a cell population model. They considered concentration changes of cells, the effects of strains on the bonding-unbonding rate of RANK/RANKL/OPG receptor-ligand reactions, and microdamage to control the mechanical stimulus (Ashrafi et al., 2020). They applied the model to the human femur and attempted to validate their model by comparing results against previous models. However, the sufficient lack of experimental data prevented a proper validation from being conducted.

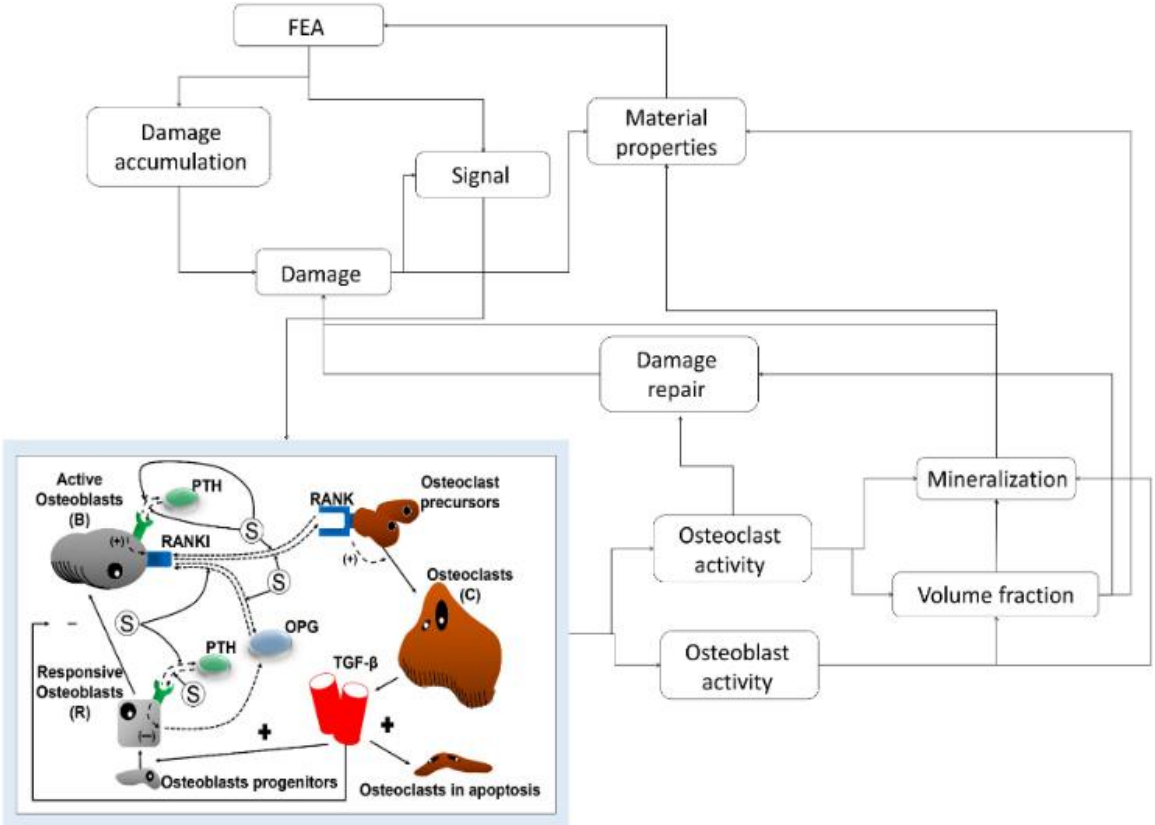

Figure 2.15: *A flowchart of the bone remodelling model used in the study by Ashrafi et al. (2020).*

2.6 Gaps in the literature

Throughout this literature review, numerous gaps within the body of models described have presented themselves. Firstly, the review revealed that the biomechanical micro-FE models usually only investigate one loading condition, assuming that any load applied is axial to the bone and hence ignoring the uncertainties in the loading direction and magnitude from the experimental measurements (physiological loads and/ or the *in vivo* tibia loading model) (Oliviero et al., 2021b). In this thesis this gap will be addressed by conducting a sensitivity analysis of the loading direction on the prediction of the mechanical properties (apparent strength and stiffness) (Objective 1, Chapter 3) and strain distributions (Objective 2, Chapter 4) of the mouse tibia. The importance of controlling this loading direction will be further demonstrated through the relationship between the mouse tibia midshaft cortical thickness and the bone strength, across the investigated range of loading directions (Objective 1, Chapter 3). Evaluating the effect of the loading direction on the strain distributions provides a link to the bone remodelling.

However, we have seen that the biomechanical models alone cannot accurately predict bone changes over time. The mechanoregulation models presented in the literature are limited in their predictions of resorption (Cheong et al., 2020a, 2020b). Therefore, there has been some initial attempts to combine biomechanical models with biochemical models, with varying approaches and limitations (Pivonka et al., 2013; Scheiner et al., 2013; Lerebours et al., 2016; Pastrama et al., 2018; Ashrafi et al., 2020). Those studies which used the BT approach to calculate their strain distributions were also subjected to the BT assumptions – the exclusion of shear strain components and modelling the tibia as a slender beam (Lerebours et al., 2016). The resulting predicted strain distributions, therefore, may not be as accurate as they would have been using another technique. Therefore, this gap will be addressed through an exploratory study, which utilises combinations of validated micro-FE models and a BCPM model to create a multiscale biomechano-chemo model for bone adaptation over time and use this model to measure the sensitivity of biochemical stimuli on the bone remodelling (Objective 3, Chapter 5).

Finally, there is a limited amount of literature on micro-FE models based on high-resolution images, which show the osteocyte lacunae. To address this gap, the tools developed when fulfilling Objectives 1 and 2 will be adapted, to create a micro-FE model of the bone tissue, investigating the effect of the osteocyte lacunae on the local bone stiffness (Objective 4, Chapter 6).

2.7 References

Adachi, T., Aonuma, Y., Tanaka, M., Hojo, M., Takano-Yamamoto, T., and Kamioka, H. (2009). Calcium response in single osteocytes to locally applied mechanical stimulus: differences in cell process and cell body. J. Biomech. 42, 1989–1995. doi: 10.1016/j.jbiomech.2009.04.034

Ashrafi, M., Gubaua, J. E., Pereira, J. T., Gahlichi, F., and Doblaré, M. (2020). A mechano-chemo-biological model for bone remodeling with a new mechano-chemo-transduction approach. Biomech. Model. Mechanobiol. 19, 2499–2523. doi: 10.1007/s10237-020-01353-0

Begonia, M., Dallas, M., Johnson, M. L., and Thiagarajan, G. (2017). Comparison of strain measurement in the mouse forearm using subject specific finite element models, strain gaging, and digital image correlation. Biomech. Model. Mechanobiol. 16, 1243. doi: 10.1007/s10237-017-0885-7

Bessho, M., Ohnishi, I., Matsuyama, J., Matsumoto, T., Imai, K., and Nakamura, K. (2007). Prediction of strength and strain of the proximal femur by a CT-based finite element method. J. Biomech. 40, 1745–1753. doi: 10.1016/j.jbiomech.2006.08.003

Birkhold, A. I., Razi, H., Duda, G. N., Weinkamer, R., Checa, S., and Willie, B. M. (2016). The periosteal bone surface is less mechano-responsive than the endocortical. Sci. Reports 2016 61 6, 1–11. doi: 10.1038/srep23480

Boaretti, D., Marques, F. C., Ledoux, C., Singh, A., Kendall, J. J., Wehrle, E., et al. (2023). Trabecular bone remodeling in the aging mouse: a micro-multiphysics agent-based in silico model using single-cell mechanomics. Front. Bioeng. Biotechnol. 11, 1091294. doi: 10.3389/fbioe.2023.1091294

Bouxsein, M. L., Boyd, S. K., Christiansen, B. A., Guldberg, R. E., Jepsen, K. J., and Müller, R. (2010). Guidelines for assessment of bone microstructure in rodents using micro-computed tomography. J. Bone Miner. Res. 25, 1468–1486. doi: 10.1002/jbmr.141

Boyle, C., and Kim, I. Y. (2011). Three-dimensional micro-level computational study of Wolff's law via trabecular bone remodeling in the human proximal femur using design space topology optimization. J. Biomech. 44, 935–942. doi: 10.1016/j.jbiomech.2010.11.029

Buenzli, P. R., Thomas, C. D. L., Clement, J. G., and Pivonka, P. (2013). Endocortical bone loss in osteoporosis: the role of bone surface availability. Int. J. Numer. Method. Biomed. Eng. 29, 1307–1322. doi: 10.1002/cnm.2567

Carriero, A., Doube, M., Vogt, M., Busse, B., Zustin, J., Levchuk, A., et al. (2014). Altered lacunar and vascular porosity in osteogenesis imperfecta mouse bone as revealed by synchrotron tomography contributes to bone fragility. Bone, 61, 116–124. doi: 10.1016/j.bone.2013.12.020

Carriero, A., Pereira, A. F., Wilson, A. J., Castagno, S., Javaheri, B., Pitsillides, A. A., et al. (2018). Spatial relationship between bone formation and mechanical stimulus within cortical bone: Combining 3D fluorochrome mapping and poroelastic finite element modelling. Bone Reports 8, 72. doi: 10.1016/j.bonr.2018.02.003

Cheong, V. S., Campos Marin, A., Lacroix, D., and Dall'Ara, E. (2020a). A novel algorithm to predict bone changes in the mouse tibia properties under physiological conditions. Biomech. Model. Mechanobiol. 19, 985–1001. doi: 10.1007/s10237-019-01266-7

Cheong, V. S., Kadirkamanathan, V., and Dall'Ara, E. (2021a). The role of the loading condition in predictions of bone adaptation in a mouse tibial loading model. Front. Bioeng. Biotechnol. 9, 676867. doi: 10.3389/fbioe.2021.676867

Cheong, V. S., Roberts, B. C., Kadirkamanathan, V., and Dall'Ara, E. (2020b). Bone remodelling in the mouse tibia is spatio-temporally modulated by oestrogen deficiency and external mechanical loading: A combined in vivo/in silico study. Acta Biomater. 116, 302–317. doi: 10.1016/j.actbio.2020.09.011

Cheong, V. S., Roberts, B. C., Kadirkamanathan, V., and Dall'Ara, E. (2021b). Positive interactions of mechanical loading and PTH treatments on spatio-temporal bone remodelling. Acta Biomater. 136, 291–305. doi: 10.1016/j.actbio.2021.09.035

Christiansen, B. A. (2016). Effect of micro-computed tomography voxel size and segmentation method on trabecular bone microstructure measures in mice. Bone Reports 5, 136. doi: 10.1016/j.bonr.2016.05.006

Cody, D. D., Gross, G. J., J. Hou, F., Spencer, H. J., Goldstein, S. A., and P. Fyhrie, D. (1999). Femoral strength is better predicted by finite element models than QCT and DXA. J. Biomech. 32, 1013–1020. doi: 10.1016/s0021-9290(99)00099-8

De Souza, R. L., Matsuura, M., Eckstein, F., Rawlinson, S. C. F., Lanyon, L. E., and Pitsillides, A. A. (2005). Non-invasive axial loading of mouse tibiae increases cortical bone formation and modifies trabecular organization: A new model to study cortical and cancellous compartments in a single loaded element. Bone, 37, 810–818. doi: 10.1016/j.bone.2005.07.022

Evans, H., Andrews, R., Abedi, F. A., Sprules, A., Trend, J., Lovric, G., et al. (2024). Evidence for peri-lacunar remodeling and altered osteocyte lacuno-canalicular network in mouse models of myeloma-induced bone disease. JBMR Plus. doi: 10.1093/jbmrpl/ziae093

Feldkamp, L. A., Goldstein, S. A., Parfitt, M. A., Jesion, G., and Kleerekoper, M. (1989). The direct examination of three-dimensional bone architecture in vitro by computed tomography. J. Bone Miner. Res. 4, 3–11. doi: 10.1002/jbmr.5650040103

Hemmatian, H., Bakker, A. D., Klein-Nulend, J., and van Lenthe, G. H. (2021). Alterations in osteocyte lacunar morphology affect local bone tissue strains. J. Mech. Behav. Biomed. Mater. 123. doi: 10.1016/j.jmbbm.2021.104730

Kawabata, Y., Matsuo, K., Nezu, Y., Kamiishi, T., Inaba, Y., and Saito, T. (2017). The risk assessment of pathological fracture in the proximal femur using a CT-based finite element method. J. Orthop. Sci. 22, 931–937. doi: 10.1016/j.jos.2017.05.015

Keaveny, T. M., Donley, D. W., Hoffmann, P. F., Mitlak, B. H., Glass, E. V., and San Martin, J. A. (2007). Effects of teriparatide and alendronate on vertebral strength as assessed by finite element modeling of QCT scans in women with osteoporosis. J. Bone Miner. Res. 22, 149–157. doi: 10.1359/jbmr.061011

Kendall, J. J., Ledoux, C., Marques, F. C., Boaretti, D., Schulte, F. A., Morgan, E. F., et al. (2023). An in silico micro-multiphysics agent-based approach for simulating bone regeneration in a mouse femur defect model. Front. Bioeng. Biotechnol. 11, 1289127. doi: 10.3389/fbioe.2023.1289127

Klinck, R. J., Campbell, G. M., and Boyd, S. K. (2008). Radiation effects on bone architecture in mice and rats resulting from in vivo micro-computed tomography scanning. Med. Eng. Phys. 30, 888–895. doi: 10.1016/j.medengphy.2007.11.004

Laib, A., Barou, O., Vico, L., Lafage-Proust, M. H., Alexandre, C., and Rügsegger, P. (2000). 3D micro-computed tomography of trabecular and cortical bone architecture with application to a rat model of immobilisation osteoporosis. Med. Biol. Eng. Comput. 38, 326–332. doi: 10.1007/bf02347054

Laperre, K., Depypere, M., van Gastel, N., Torrekens, S., Moermans, K., Bogaerts, R., et al. (2011). Development of micro-CT protocols for in vivo follow-up of mouse bone architecture without major radiation side effects. Bone 49, 613–622. doi: 10.1016/j.bone.2011.06.031

Lavaill, M., Trichilo, S., Scheiner, S., Forwood, M. R., Cooper, D. M. L., and Pivonka, P. (2020). Study of the combined effects of PTH treatment and mechanical loading in postmenopausal osteoporosis using

a new mechanistic PK-PD model. Biomech. Model. Mechanobiol. 19, 1765–1780. doi: 10.1007/s10237-020-01307-6

Lemaire, V., Tobin, F. L., Greller, L. D., Cho, C. R., and Suva, L. J. (2004). Modeling the interactions between osteoblast and osteoclast activities in bone remodeling. J. Theor. Biol. 229, 293–309. doi: 10.1016/j.jtbi.2004.03.023

Lerebours, C., Buenzli, P. R., Scheiner, S., and Pivonka, P. (2016). A multiscale mechanobiological model of bone remodelling predicts site-specific bone loss in the femur during osteoporosis and mechanical disuse. Biomech. Model. Mechanobiol. 15, 43–67. doi: 10.1007/s10237-015-0705-x

Li, X. (n.d.). CT2S pipeline. Available at: https://ct2s.insigneo.org/ct2s/

Liu, Y. Q., Han, X. F., Liu, T., Cheng, M. C., and Xiao, H. Bin (2015). A cell-based model of bone remodeling for identifying activity of icarrin in the treatment of osteoporosis. Biotechnol. Lett. 37, 219–226. doi: 10.1007/s10529-014-1661-8

Lu, Y., Boudiffa, M., Dall'Ara, E., Bellantuono, I., and Viceconti, M. (2016). Development of a protocol to quantify local bone adaptation over space and time: Quantification of reproducibility. J. Biomech. 49, 2095–2099. doi: 10.1016/j.jbiomech.2016.05.022

Marques, F. C., Boaretti, D., Walle, M., Scheuren, A. C., Schulte, F. A., and Müller, R. (2023). Mechanostat parameters estimated from time-lapsed in vivo micro-computed tomography data of mechanically driven bone adaptation are logarithmically dependent on loading frequency. Front. Bioeng. Biotechnol. 11, 1140673. doi: 10.3389/fbioe.2023.1140673

Martin, M., Sansalone, V., Cooper, D. M. L., Forwood, M. R., and Pivonka, P. (2019). Mechanobiological osteocyte feedback drives mechanostat regulation of bone in a multiscale computational model. Biomech. Model. Mechanobiol. 18, 1475–1496. doi: 10.1007/s10237-019-01158-w

Martin, M., Sansalone, V., Cooper, D. M. L., Forwood, M. R., and Pivonka, P. (2020). Assessment of romosozumab efficacy in the treatment of postmenopausal osteoporosis: Results from a mechanistic PK-PD mechanostat model of bone remodeling. Bone 133, 115223. doi: 10.1016/j.bone.2020.115223

Martínez-Reina, J., Calvo-Gallego, J. L., and Pivonka, P. (2021). Are drug holidays a safe option in treatment of osteoporosis? — Insights from an in silico mechanistic PK–PD model of denosumab treatment of postmenopausal osteoporosis. J. Mech. Behav. Biomed. Mater. 113. doi: 10.1016/j.jmbbm.2020.104140

Martínez-Reina, J., and Pivonka, P. (2019). Effects of long-term treatment of denosumab on bone mineral density: insights from an in-silico model of bone mineralization. Bone 125. doi: 10.1016/j.bone.2019.04.022

Meakin, L. B., Todd, H., Delisser, P. J., Galea, G. L., Moustafa, A., Lanyon, L. E., et al. (2017). Parathyroid hormone's enhancement of bones' osteogenic response to loading is affected by ageing in a dose- and time-dependent manner. Bone 98, 59–67. doi: 10.1016/j.bone.2017.02.009

Meganck, J. A., Kozloff, K. M., Thornton, M. M., Broski, S. M., and Goldstein, S. A. (2009). Beam hardening artifacts in micro-computed tomography scanning can be reduced by x-ray beam filtration and the resulting images can be used to accurately measure BMD. Bone 45, 1104. doi: 10.1016/j.bone.2009.07.078

Miller, C. J., Pickering, E., Martelli, S., Dall'Ara, E., Delisser, P., and Pivonka, P. (2024a). Cortical bone adaptation response is region specific, but not peak load dependent: insights from μ CT image analysis and mechanostat simulations of the mouse tibia loading model. Biomech. Model. Mechanobiol. 23, 287–304. doi: 10.1007/s10237-023-01775-6

Miller, C. J., Trichilo, S., Pickering, E., Martelli, S., Dall'Ara, E., Delisser, P., et al. (2024b). Cortical thickness adaptation to combined mechanical loading and parathyroid hormone treatments is site specific and synergistic in the mouse tibia model. Bone 180, 116994. doi: 10.1016/j.bone.2023.116994

Oliviero, S., Cheong, V. S., Roberts, B. C., Orozco Diaz, C. A., Griffiths, W., Bellantuono, I., et al. (2022). Reproducibility of densitometric and biomechanical assessment of the mouse tibia from in vivo micro-CT images. Front. Endocrinol. (Lausanne). 13, 915938. doi: 10.3389/fendo.2022.915938

Oliviero, S., Giorgi, M., and Dall'Ara, E. (2018). Validation of finite element models of the mouse tibia using digital volume correlation. J. Mech. Behav. Biomed. Mater. 86, 172–184. doi: 10.1016/j.jmbbm.2018.06.022

Oliviero, S., Giorgi, M., Laud, P. J., and Dall'Ara, E. (2019). Effect of repeated in vivo microCT imaging on the properties of the mouse tibia. PLoS One 14, e0225127. doi: 10.1371/journal.pone.0225127

Oliviero, S., Lu, Y., Viceconti, M., and Dall'Ara, E. (2017). Effect of integration time on the morphometric, densitometric and mechanical properties of the mouse tibia. J. Biomech. 65, 203–211. doi: 10.1016/j.jbiomech.2017.10.026

Oliviero, S., Owen, R., Reilly, G. C., Bellantuono, I., and Dall'Ara, E. (2021a). Optimization of the failure

criterion in micro-Finite Element models of the mouse tibia for the non-invasive prediction of its failure load in preclinical applications. J. Mech. Behav. Biomed. Mater. 113, 104190. doi: 10.1016/j.jmbbm.2020.104190

Oliviero, S., Roberts, M., Owen, R., Reilly, G. C., Bellantuono, I., and Dall'Ara, E. (2021b). Non-invasive prediction of the mouse tibia mechanical properties from microCT images: comparison between different finite element models. Biomech. Model. Mechanobiol. 20, 941–955. doi: 10.1007/s10237-021-01422-y

Paoletti, N., Liò, P., Merelli, E., and Viceconti, M. (2012). Multilevel computational modeling and quantitative analysis of bone remodeling. IEEE/ACM Trans. Comput. Biol. Bioinforma. 9, 1366–1378. doi: 10.1109/tcbb.2012.51

Pastrama, M. I., Scheiner, S., Pivonka, P., and Hellmich, C. (2018). A mathematical multiscale model of bone remodeling, accounting for pore space-specific mechanosensation. Bone 107, 208–221. doi: 10.1016/j.bone.2017.11.009

Patel, T. K., Brodt, M. D., and Silva, M. J. (2014). Experimental and finite element analysis of strains induced by axial tibial compression in young-adult and old female C57Bl/6 mice. J. Biomech. 47, 451–457. doi: 10.1016/j.jbiomech.2013.10.052

Paul Scherrer Institut (2019). Synchrotron Light | SLS | Paul Scherrer Institut (PSI). Available at: https://www.psi.ch/en/sls/synchrotron-light (Accessed April 7, 2024).

Pereira, A. F., Javaheri, B., Pitsillides, A. A., and Shefelbine, S. J. (2015). Predicting cortical bone adaptation to axial loading in the mouse tibia. J. R. Soc. Interface 12. doi: 10.1098/rsif.2015.0590

Pickering, E., Silva, M. J., Delisser, P., Brodt, M. D., Gu, Y. T., and Pivonka, P. (2021). Estimation of load conditions and strain distribution for in vivo murine tibia compression loading using experimentally informed finite element models. J. Biomech. 115, 110140. doi: 10.1016/j.jbiomech.2020.110140

Pickering, E., Trichilo, S., Delisser, P., and Pivonka, P. (2022). Beam theory for rapid strain estimation in the mouse tibia compression model. Biomech. Model. Mechanobiol. 21, 513–525. doi: 10.1007/s10237-021-01546-1

Pistoia, W., Van Rietbergen, B., Lochmüller, E. M., Lill, C. A., Eckstein, F., and Rüegsegger, P. (2002). Estimation of distal radius failure load with micro-finite element analysis models based on three-dimensional peripheral quantitative computed tomography images. Bone 30, 842–848. doi:

10.1016/s8756-3282(02)00736-6

Pivonka, P., Buenzli, P. R., Scheiner, S., Hellmich, C., and Dunstan, C. R. (2013). The influence of bone surface availability in bone remodelling—A mathematical model including coupled geometrical and biomechanical regulations of bone cells. Eng. Struct. 47, 134–147. doi: 10.1016/j.engstruct.2012.09.006

Pivonka, P., Zimak, J., Smith, D. W., Gardiner, B. S., Dunstan, C. R., Sims, N. A., et al. (2008). Model structure and control of bone remodeling: a theoretical study. Bone 43, 249–263. doi: 10.1016/j.bone.2008.03.025

Qasim, M., Farinella, G., Zhang, J., Li, X., Yang, L., Eastell, R., et al. (2016). Patient-specific finite element estimated femur strength as a predictor of the risk of hip fracture: the effect of methodological determinants. Osteoporos. Int. 27, 2815–2822. doi: 10.1007/s00198-016-3597-4

Razi, H., Birkhold, A. I., Weinkamer, R., Duda, G. N., Willie, B. M., and Checa, S. (2015). Aging leads to a dysregulation in mechanically driven bone formation and resorption. J. Bone Miner. Res. 30, 1864–1873. doi: 10.1002/jbmr.2528

Razi, H., Birkhold, A. I., Zehn, M., Duda, G. N., Willie, B. M., and Checa, S. (2014). A finite element model of in vivo mouse tibial compression loading: influence of boundary conditions. Facta Univ. Ser. Mech. Eng. 12, 195–207. Available at: https://casopisi.junis.ni.ac.rs/index.php/FUMechEng/article/view/624 (Accessed July 28, 2024).

Roberts, B. C., Cheong, V. S., Oliviero, S., Carrera, H. M. A., Wang, N., Gartland, A., et al. (2023). Combining PTH(1-34) and mechanical loading has increased benefit to tibia bone mechanics in ovariectomised mice. J. Orthop. Res. doi: 10.1002/jor.25777

Scheiner, S., Pivonka, P., and Hellmich, C. (2013). Coupling systems biology with multiscale mechanics, for computer simulations of bone remodeling. Comput. Methods Appl. Mech. Eng. 254, 181–196. doi: 10.1016/j.cma.2012.10.015

Scheiner, S., Pivonka, P., and Hellmich, C. (2016). Poromicromechanics reveals that physiological bone strains induce osteocyte-stimulating lacunar pressure. Biomech. Model. Mechanobiol. 15, 9. doi: 10.1007/s10237-015-0704-y

Scheiner, S., Pivonka, P., Smith, D. W., Dunstan, C. R., and Hellmich, C. (2014). Mathematical modeling of postmenopausal osteoporosis and its treatment by the anti-catabolic drug denosumab. Int. J. Numer.

Method. Biomed. Eng. 30, 1. doi: 10.1002/cnm.2584

Scheuren, A. C., Vallaster, P., Kuhn, G. A., Paul, G. R., Malhotra, A., Kameo, Y., et al. (2020). Mechano-Regulation of Trabecular Bone Adaptation Is Controlled by the Local in vivo Environment and Logarithmically Dependent on Loading Frequency. Front. Bioeng. Biotechnol. 8, 566346. doi: 10.3389/fbioe.2020.566346

Schneider, P., Voide, R., Stampanoni, M., Donahue, L. R., and Müller, R. (2013). The importance of the intracortical canal network for murine bone mechanics. Bone 53, 120–128. doi: 10.1016/j.bone.2012.11.024

Schulte, F. A., Ruffoni, D., Lambers, F. M., Christen, D., Webster, D. J., Kuhn, G., et al. (2013a). Local mechanical stimuli regulate bone formation and resorption in mice at the tissue level. PLoS One 8, e62172. doi: 10.1371/journal.pone.0062172

Schulte, F. A., Zwahlen, A., Lambers, F. M., Kuhn, G., Ruffoni, D., Betts, D., et al. (2013b). Strain-adaptive in silico modeling of bone adaptation--a computer simulation validated by in vivo micro-computed tomography data. Bone 52, 485–492. doi: 10.1016/j.bone.2012.09.008

Schutte, L. J. (2012). An agent-based model for evaluating cellular mechanisms of bone remodeling. Carnegie Mellon University. doi: 10.1184/r1/6714668.v1

Stadelmann, V. A., Hocke, J., Verhelle, J., Forster, V., Merlini, F., Terrier, A., et al. (2009). 3D strain map of axially loaded mouse tibia: a numerical analysis validated by experimental measurements. Comput. Methods Biomech. Biomed. Engin. 12, 95–96. doi: 10.1080/10255840903077287

Sugiyama, T., Meakin, L. B., Browne, W. J., Galea, G. L., Price, J. S., and Lanyon, L. E. (2012). Bones' adaptive response to mechanical loading is essentially linear between the low strains associated with disuse and the high strains associated with the lamellar/woven bone transition. J. Bone Miner. Res. 27, 1784–1793. doi: 10.1002/jbmr.1599

Tan, S. D., de Vries, T. J., Kuijpers-Jagtman, A. M., Semeins, C. M., Everts, V., and Klein-Nulend, J. (2007). Osteocytes subjected to fluid flow inhibit osteoclast formation and bone resorption. Bone 41, 745–751. doi: 10.1016/j.bone.2007.07.019

Trichilo, S. (2018). Assessment of the anabolic effects of PTH drug treatment and mechanical loading on bone using high-resolution imaging and in silico modelling. The University of Melbourne.

Trichilo, S., Scheiner, S., Forwood, M., Cooper, D. M. L., and Pivonka, P. (2019). Computational model

of the dual action of PTH — application to a rat model of osteoporosis. J. Theor. Biol. 473, 67–79. doi: 10.1016/j.jtbi.2019.04.020

Truesdell, S. L., and Saunders, M. M. (2019). Bone remodeling platforms: understanding the need for multicellular lab-on-a-chip systems and predictive agent-based models. Math. Biosci. Eng. 17, 1233–1252. doi: 10.3934/mbe.2020063

Tsubota, K. ichi, Suzuki, Y., Yamada, T., Hojo, M., Makinouchi, A., and Adachi, T. (2009). Computer simulation of trabecular remodeling in human proximal femur using large-scale voxel FE models: Approach to understanding Wolff's law. J. Biomech. 42, 1088–1094. doi: 10.1016/j.jbiomech.2009.02.030

Willie, B. M., Birkhold, A. I., Razi, H., Thiele, T., Aido, M., Kruck, B., et al. (2013). Diminished response to in vivo mechanical loading in trabecular and not cortical bone in adulthood of female C57Bl/6 mice coincides with a reduction in deformation to load. Bone 55, 335–346. doi: 10.1016/j.bone.2013.04.023

Yang, H., Butz, K. D., Duffy, D., Niebur, G. L., Nauman, E. A., and Main, R. P. (2014). Characterization of cancellous and cortical bone strain in the in vivo mouse tibial loading model using microCT-based finite element analysis. Bone 66, 131–139. doi: 10.1016/j.bone.2014.05.019

Zysset, P. K., Dall'Ara, E., Varga, P., and Pahr, D. H. (2013). Finite element analysis for prediction of bone strength. Bonekey Rep. 2, 386. doi: 10.1038/bonekey.2013.120

Chapter 3: The loading direction dramatically affects the mechanical properties of the mouse tibia

The main body of this chapter is based on the peer-reviewed and published research article:

Farage-O'Reilly S.M., Cheong V.S., Pickering E., Pivonka P., Bellantuono I., Kadirkamanathan V. and Dall'Ara E., 2024. The loading direction dramatically affects the mechanical properties of the mouse tibia. Frontiers in Bioengineering and Biotechnology, 12, p.1335955.
https://doi.org/10.3389/fbioe.2024.1335955

The contents of this chapter investigate the effect of the loading direction on the mechanical properties of the mouse tibia, when using the *in vivo* tibial loading model. The study investigates 504 different loading directions through the use of micro-CT based micro-FE models. The models were based on two groups of mice: a group which were ovariectomised, to simulate post-menopausal osteoporosis, and a group which underwent mechanical loading after ovariectomy. It was shown that the loading direction significantly impacts the failure load within the mouse tibia. The chapter goes on to show that the cortical thickness is better related to the failure load at a different loading direction than at the nominal axial case.

Abstract

Introduction: The *in vivo* tibial loading mouse model has been extensively used to evaluate bone adaptation in the tibia after mechanical loading treatment. However, there is a prevailing assumption that the load is applied axially to the tibia. Additionally, the tibia midshaft structural property, cortical thickness (Ct.Th), is a good predictor of the failure load (R^2: 84.5%, $p < 0.001$), numerically predicted in C57BL/6 mice which have undergone ovariectomy and subsequently been treated with related interventions (Roberts et al., 2023). The aim of this *in silico* study was to evaluate how much the apparent mechanical properties of the mouse tibia are affected by the loading direction and to investigate if the midshaft Ct.Th is better related to the failure load at a different loading direction to the nominal axial case, by using a validated micro-finite element (micro-FE) model of mice which have been ovariectomised and exposed to external mechanical loading over a two-week period.

Methods: Longitudinal micro-computed tomography (micro-CT) images were taken of the tibiae of eleven ovariectomised mice at ages 18 and 20 weeks. Six of the mice underwent a mechanical loading treatment at age 19 weeks. Micro-FE models were generated, based on the segmented micro-CT images. Three models using unitary loads were linearly combined to simulate a range of loading directions, generated as a function of the angle from the inferior-superior axis (θ, 0°–30° range, 5° steps) and the angle from the anterior-posterior axis (ϕ, 0°: anterior axis, positive anticlockwise (inferior-superior view), 0°–355° range, 5° steps). The minimum principal strain was calculated and used to estimate the failure load, by linearly scaling the strain until 10% of the nodes reached the critical strain level of −14,420 με. The apparent bone stiffness was calculated as the ratio between the axial applied force and the average displacement along the longitudinal direction, for the loaded nodes. A linear regression was carried out between the Ct.Th and the failure load at each loading direction.

Results: The results demonstrated a high sensitivity of the mouse tibia to the loading direction across all groups and time points. Higher failure loads were found for several loading directions (θ = 10°, ϕ 205°–210°) than for the nominal axial case (θ = 0°, ϕ = 0°), highlighting adaptation of the bone for loading directions far from the nominal axial one. The midshaft Ct.Th was a modest to good predictor of the failure load across all loading directions (R^2-range: 67.8-87.9%, all $p < 0.001$). For the loading conditions θ = 5°, ϕ = 215-280° and θ = 10°, ϕ = 225-290°, the R^2 values were all greater than that of the nominal axial case, with the maximum occurring at θ = 5°, ϕ = 240°. Above θ = 10°, the R^2 values were generally smaller than that of the nominal axial case.

Conclusion: These results suggest that the loading direction significantly impacts the failure load of the mouse tibia. Thus, the magnitude and direction of the applied load should be well controlled during the experiments. Specifically, the loading range must be controlled within a θ value of 10°, if the failure

load is to be predicted from the midshaft Ct.Th. Beyond this, the midshaft Ct.Th loses its predictive ability.

3.1 Introduction

Bone is a dynamic tissue that adapts over time due to biomechanical and biochemical stimuli (Martin et al., 1998; Frost, 2003; Bonewald, 2011). It is the balance between these adaptations which keeps bone healthy, through bone cells which continuously maintain and remodel the bone tissue. However, musculoskeletal diseases, such as osteoporosis, can disrupt this balance. Osteoporosis affects bone remodelling, reducing the bone mineral density (BMD) by reducing the number or thickness of trabeculae, reducing the cortical thickness, increasing the cortical porosity and/or decreasing the local mineralisation and consequently the tissue mineral density (TMD). These changes deteriorate the mechanical properties, leading to a decrease in bone strength, and hence, an increase in fracture risk (Birkhold et al., 2014; Razi et al., 2015a; Roberts et al., 2019).

Various treatments exist for osteoporosis, including antiresorptive treatments (targeting osteoclasts, i.e., bone resorbing cells) or bone anabolic treatments (targeting both osteoclasts and osteoblasts, i.e., bone forming cells). However, these treatments have side effects, for example, long term use of bisphosphonates (antiresorptive drugs) is associated with atypical femoral fractures (Shane et al., 2014). On the other hand, anabolic treatments such as Parathyroid Hormone (PTH) are associated with poor cost effectiveness (Yeam et al., 2018). Therefore, new and improved treatments for osteoporotic patients are needed. New treatments must be tested in animals preclinically before being assessed in clinical trials, with the mouse model being the most commonly used animal model in drug development (Gould et al., 2015). Osteoporosis treatments are usually tested in adult mice after ovariectomy, a model of oestrogen deficiency that induces accelerated bone resorption and with a phenotype similar to that observed in postmenopausal osteoporotic patients (Bouxsein et al., 2005; Roberts et al., 2019). Mechanical loading affects bone adaptation responses (Frost, 2003). Low levels of mechanical loading (including complete unloading) can cause bone resorption, whilst high levels of mechanical loading can stimulate bone formation, hence, increasing bone density and bone strength (Frost, 2003). As a result, mechanical loading in the form of exercise has been suggested as an anabolic treatment against osteoporotic fractures (Martelli et al., 2020; Du et al., 2021; O'Rourke et al., 2021). Additionally, mouse models have been used to study the combined effects of mechanical loading and pharmacological treatments on bone remodelling and mechanical properties (Levchuk et al., 2014; Scheuren et al., 2020).

Several rodent models are available to evaluate the effect of mechanical loading on the bone in a controlled way (Nepal et al., 2023). Among them, the *in vivo* tibial loading model has been extensively used to evaluate bone adaptation in the tibia after the application of external mechanical loads through the knee and the ankle joints, aiming at loading the tibia predominantly along its axial

direction. This model has been used to investigate bone adaptation in various ways, such as: in disuse models (Moustafa et al., 2012); under different peak loads, by mimicking impact exercises (De Souza et al., 2005; Sugiyama et al., 2010; Main et al., 2020; Miller et al., 2021); varying loading type (static vs static and dynamic) (Sugiyama et al., 2010); and varying the load frequency (Holguin et al., 2013; Yang et al., 2017). Furthermore, this model has been used to investigate bone changes over time (Lynch et al., 2011; Birkhold et al., 2014; Melville et al., 2014; Razi et al., 2015a, 2015b; Roberts et al., 2020), showing that mechanical loading generally led to increased bone formation and improved some aspects of bone architecture.

Although the *in vivo* tibial loading model is widely used, there is a prevailing assumption that the load is applied axially to the tibia. However, considering the transmission of the applied load through the knee and ankle joints, compounded by the potential for the leg to be repositioned within the loading device during longitudinal studies, uncertainty arises over the true loading direction and the effect that this may have on bone adaptation. Digital image correlation measurements have highlighted the sensitivity of the mouse tibia superficial strain as a function of the loading conditions (Carriero et al., 2014). Moreover, a previous study that used digital volume correlation (DVC) showed that repositioning of the bone when using the *in vivo* tibial loading model affected the internal strain distribution across the tibia, inducing areas of higher strain, particularly at the distal end of the bone (Giorgi and Dall'Ara, 2018).

The gold standard for evaluating the effect of mechanical loading and combined treatments on bone densitometric and morphometric properties is using *ex vivo* or *in vivo* micro-computed tomography (micro-CT) (Bouxsein et al., 2010). Recently, micro-CT based micro-finite element (micro-FE) models have been developed to non-invasively evaluate the mechanical properties of bone. Micro-FE models not only have the potential to dramatically reduce and partially replace the use of mice in skeletal research (Viceconti and Dall'Ara, 2019), but also to evaluate the sensitivity of different parameters on the biomechanical properties of the bone; something that could not be achieved with experiments. Nevertheless, prior to their application in preclinical studies, the models should be validated against biomechanical experiments. Recent validation studies showed that hexahedral homogeneous micro-FE models can accurately predict local displacements ($R^2 > 0.82$, against displacements measured with DVC), apparent stiffness (errors of 14 ± 11%), and failure load (errors of 9 ± 9%) (Oliviero et al., 2018). Following that study, an optimisation of the failure criterion in the mouse tibia was conducted. Hexahedral homogeneous micro-FE models were found to accurately predict normalised stiffness ($R^2 = 0.80$, error of 14 ± 8%) and normalised failure load ($R^2 = 0.81$, errors of 9 ± 6%) (Oliviero et al., 2021a). Different material properties (homogenous and heterogeneous) and different mesh types (hexahedral and tetrahedral) were also investigated. The micro-FE models with homogeneous material properties

and hexahedral meshes were found to be the best predictors of the tibial mechanical properties. In fact, heterogeneous material properties based on the local or average values of TMD calculated from the micro-CT images did not improve the predictive ability of the micro-FE models (Oliviero et al., 2021b). This pipeline has previously been used to predict mechanical properties of the bone from the structural properties (Oliviero et al., 2021a; Roberts et al., 2023). It has been shown that the tibia midshaft structural property, cortical thickness (Ct.Th [µm]), is not a good predictor of the failure load (R^2: 22%, $p = 0.035$) in pooled data of BALB/c and C57BL/6 mice ages of 16 and 24 weeks, half of which had been ovariectomised (Oliviero et al., 2021a). However, the Ct.Th is a good predictor of the failure load (R^2: 84.5%, $p < 0.001$) in pooled data of C57BL/6 mice between the ages of 18-24 weeks, which have been ovariectomised and some have subsequently been treated with mechanical loading, PTH, or a combination of mechanical loading and PTH (Roberts et al., 2023).

Additionally, strain gauges have been used to compare local experimental strain measurements to the predictions of micro-FE models within the same locations (Stadelmann et al., 2009; Patel et al., 2014; Yang et al., 2014; Razi et al., 2015b). The accuracy of the micro-FE models for the estimation of the local strains varied ($0.40 < R^2 < 0.99$, errors between 5-20%). It should be considered that several factors contribute to the comparison between experimental and computational strain assessments, including the number and location of strain gauges, differences in the ages of the mice used, and variations in micro-FE input parameters.

Micro-FE models combined with strain gauges placed on the lateral, posterior and antero-medial surfaces of the bone have been used to inversely identify the point of application of the external load. It was found that the load location varied among mice, and the strains in the tibia were highly sensitive to the load location (Pickering et al., 2021). Micro-FE models have also been used to investigate the loading conditions when predicting bone adaptation during application of the *in vivo* tibial loading model, highlighting the importance of the load direction (i.e., the magnitude of the three Cartesian components of the load), through the inclusion of both the external axial load and the daily physiological axial and transverse loads (Cheong et al., 2021a). Nevertheless, the extent to which the mechanical properties of the mouse tibia are affected by the loading direction associated with the tibial loading model is still unknown.

The aim of this study was to evaluate how much the apparent mechanical properties of the mouse tibia are affected by the loading direction and to investigate if the midshaft Ct.Th is better related to the failure load at a different loading direction to the nominal axial case, by using a validated micro-FE model, of ovariectomised mice subjected to external mechanical loading over a two-week period.

3.2 Materials and methods

3.2.1 Experimental *in vivo* data

The experimental data used in this study were acquired from a previous study by Roberts et al. (2020), wherein it was determined that a sample size of six mice per group was sufficient to attain 80% statistical power, considering morphometric parameters such as trabecular bone volume fraction and cortical thickness. Eleven female C57BL/6 mice from two separate generations were subjected to ovariectomy at age 14 weeks (Figure 3.1). Every other week, from week 14 to 24, the body weight of each mouse was recorded (Table 3.1), and *in vivo* micro-CT images were taken of the right tibiae, while the mice were anesthetised (VivaCT80, Scanco Medical Brütisellen, Switzerland). The scanning protocol used (55 kVp, 145 µA, 10.4 µm isotropic voxel size, 32 mm field of view, 100 ms integration time and 1500/750 samples/projections) allowed for minimal effects of radiation on the tibia whilst still allowing for scanning of the whole bone at high resolution (Oliviero et al., 2017, 2019). The images were reconstructed using a third-order polynomial beam hardening correction algorithm based on a 1200 mgHA/cm3 wedge phantom, which was provided by the manufacturer.

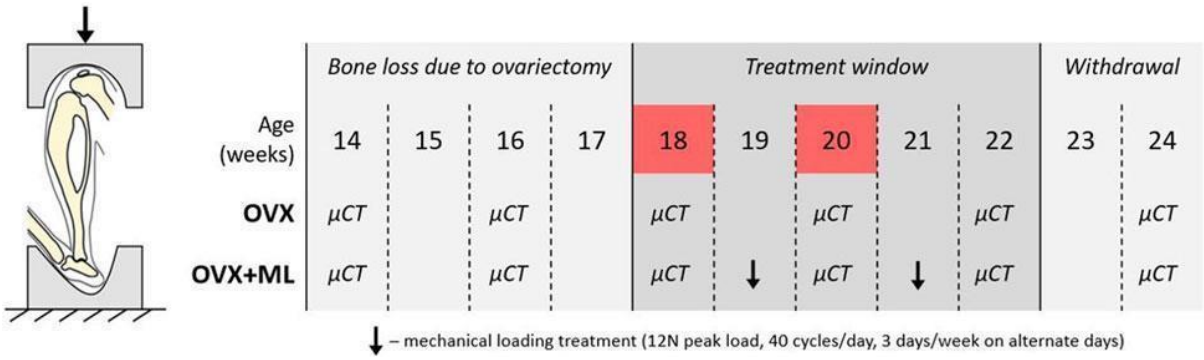

Figure 3.1: *Left: Schematic of the in vivo tibial loading model. Right: Overview of the data collection timeline in C57BL/6 mice, acquired from a previous study (Roberts et al., 2020). OVX: ovariectomy, OVX+ML: ovariectomy and mechanical loading. Ovariectomy was performed at age 14 weeks, micro-CT images were taken every two weeks throughout the duration of the study, treatment window commenced at week 18 and was withdrawn by week 23. Images from weeks 18 and 20 were used in this study (highlighted in red).*

Group	Mouse	Weight (g)					
		W14	W16	W18	W20	W22	W24
OVX	1	18	20	22	22	24	28
	2	20	22	22	24	26	26
	3	20	24	24	26	28	28
	5	16	18	22	22	26	26
	6	20	24	22	26	28	30
	mean ± SD	*18.8 ± 1.789*	*21.6 ± 2.608*	*22.4 ± 0.894*	*24.0 ± 2.000*	*26.4 ± 1.673*	*27.6 ± 1.673*
OVX+ML	1	20	24	21.4	21.3	21.8	-
	2	20	22	22.2	20.1	20.2	-
	3	18	22	20.2	18.9	19.8	-
	4	20	22	20.1	18.1	18.4	-
	5	20	24	21.8	21	22	-
	6	22	24	24.2	23.6	22.6	-
	mean ± SD	*20.0 ± 1.265*	*23.0 ± 1.095*	*21.7 ± 1.510*	*20.5 ± 1.948*	*20.8 ± 1.600*	-

Table 3.1: *The individual and grouped (mean ± SD) mouse weights in grams, reported for both groups and time points. SD – standard deviation, OVX – ovariectomy, OVX+ML – ovariectomy and mechanical loading, W14 – week 14, W16 – week 16, W18 – week 18, W20 – week 20, W22 – week 22 and W24 – week 24.*

In this study the micro-CT images acquired both for the ovariectomised mice (OVX group, N=5) and for mice ovariectomised and subsequently subjected to external mechanical loading (OVX+ML group, N=6) were considered. Only images acquired at weeks 18 and 20 were used, *as this period exhibited the largest differences in bone remodelling (Cheong et al., 2020a).* Briefly, mice in the OVX+ML group underwent external mechanical loading treatment at weeks 19 and 21, while anesthetised, using the *in vivo* tibial loading model (Figure 3.1). Each right tibia was fixed in between two soft caps and mechanically loaded using a 12 N peak load (2 N static preload superimposed with a 10 N high-strain dynamic load at a rate of 160,000 N/s (maximal nominal speed of the machine), 40 cycles/day, 3 days/week on alternate days; ElectroForce BioDynamics 5100, TA instruments, USA). The applied nominal load was assumed to be along the axial direction of the tibia. This procedure has been shown to induce cortical and trabecular lamellar bone adaptation without inducing micro-damage (De Souza et al., 2005). All the procedures were performed under a British Home Office licence (PPL 40/3499 and PF61050A3), were in compliance with the Animal (Scientific Procedures) Act 1986 and were reviewed and approved by the local Research Ethics Committee of The University of Sheffield (Sheffield, UK).

3.2.2 Image processing and micro-FE models

The main steps of the image processing, creation of the micro-FE models, and post-processing to calculate the apparent mechanical properties of each tibia are reported in Figure 3.2. The modelling pipeline has been previously validated for predictions of apparent structural properties using

compressive tests (Oliviero et al., 2021b) and prediction of local displacements using DVC (Oliviero et al., 2018).

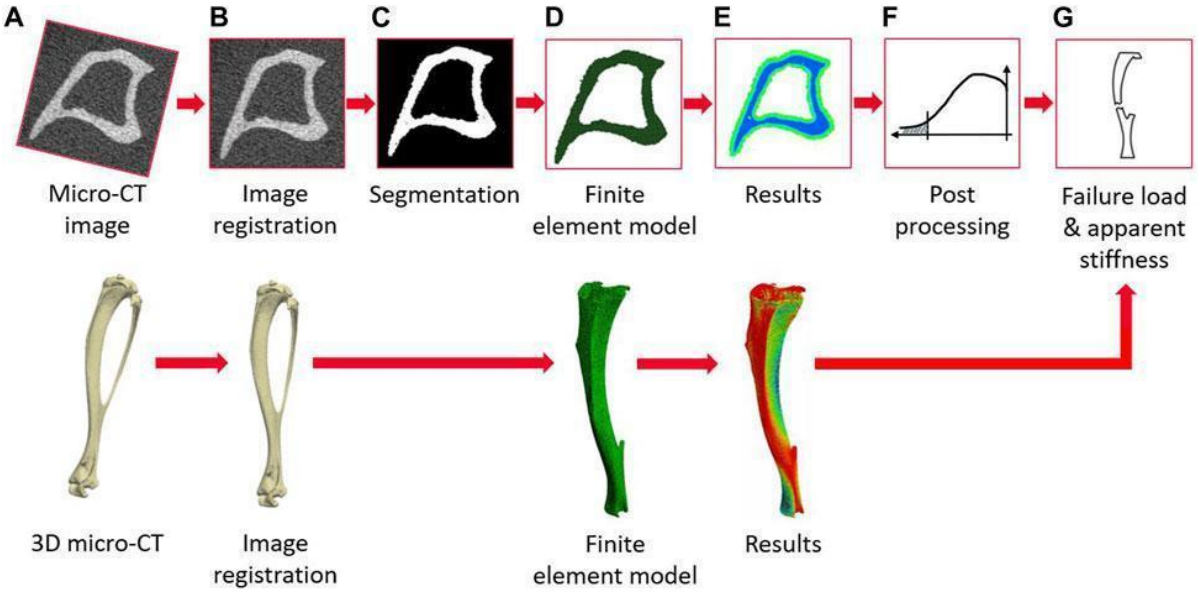

Figure 3.2: *Flowchart illustrating the main steps of the pipeline to create the micro-FE models from the micro-CT images and to evaluate the apparent mechanical properties: (from A to G) micro-CT acquisition, image registration, image segmentation (binarisation), creation of the micro-FE models, results generation, post-processing of the local displacements and strains, calculation of failure load and apparent stiffness.*

To align the micro-CT images across the time points, one reference tibia was roughly aligned such that the axis of the bone was aligned to the z-axis of the image, and the sagittal plane bisected the midpoint of the line joining the centres of the articular surfaces of the medial and lateral condyles (Lu et al., 2016). This orientation is referred to as the "nominal axial" orientation within this study. The images were then rigidly registered to the reference image taken at week 14 (Amira 6.3.0, Thermo Fisher Scientific, France), as detailed in Lu et al. (2016, 2017). After alignment, the fibula was virtually removed from all the images and the images were cropped from the slice below the proximal growth plate towards the distal end of the tibia, resulting in 80% of the total tibia length (MATLAB, 2018A, The MathWorks Inc., Natick MA, USA) (Cheong et al., 2020b, 2021b). This procedure was associated with reproducibility errors in estimating local bone mineral content (BMC) lower than 4.25% (Oliviero et al., 2022). The midshaft Ct.Th for the mice were calculated by Roberts et al. (2023), as the same mice were used in this study. Briefly, a 1 mm thick region was centred at the tibial 50% of the tibia bone length,

and the region of interest was manually marked and the midshaft Ct.Th was computed (CT Analyser v1.18.4.0, Skyscan-Bruker, Kontich, Belgium).

The images were segmented by applying a single-level threshold, defined as the midpoint between the background and bone peaks of the grey value histogram of the images (Oliviero et al., 2018; Cheong et al., 2021b). All segmented images were converted into micro-FE models by converting each bone voxel into a finite element (linear 8-node hexahedral elements). Larger elements were not used as they would not enable a proper description of the geometry of the trabecular bone in the proximal portion of the tibia (average trabecular thickness of approximately 45 μm (Roberts et al., 2020)). Tetrahedral elements were not found to improve the prediction of the bone mechanical properties (Oliviero et al., 2021b). Each model contained approximately 10 million nodes and 9 million elements. Isotropic, homogeneous, linear elastic material properties were used (E = 14.8 GPa, v = 0.3), which is in line with previous validation studies which showed good agreement with experimental measurements (Oliviero et al., 2018, 2021a, 2021b). The boundary conditions were set to simulate the *in vivo* tibial loading model: the nodes in the proximal end were fully constrained, and the nodes in the distal end were connected via kinematic coupling to a control node which was located at the centroid of the distal surface with a small offset in the superior direction. This was done to avoid over-constraining the tibia (Cheong et al., 2020a). Three independent unitary load cases (Figure 3.3) were applied along the inferior-superior, medio-lateral or anterior-posterior directions for each mouse at each time point. The minimum principal strain was calculated at the nodes. All input files for the models were generated using MATLAB. The models were solved in Abaqus 2018 (Dassault Systèmes Simulia, RI, USA) using the University of Sheffield High Performance Computing Clusters (ShARC).

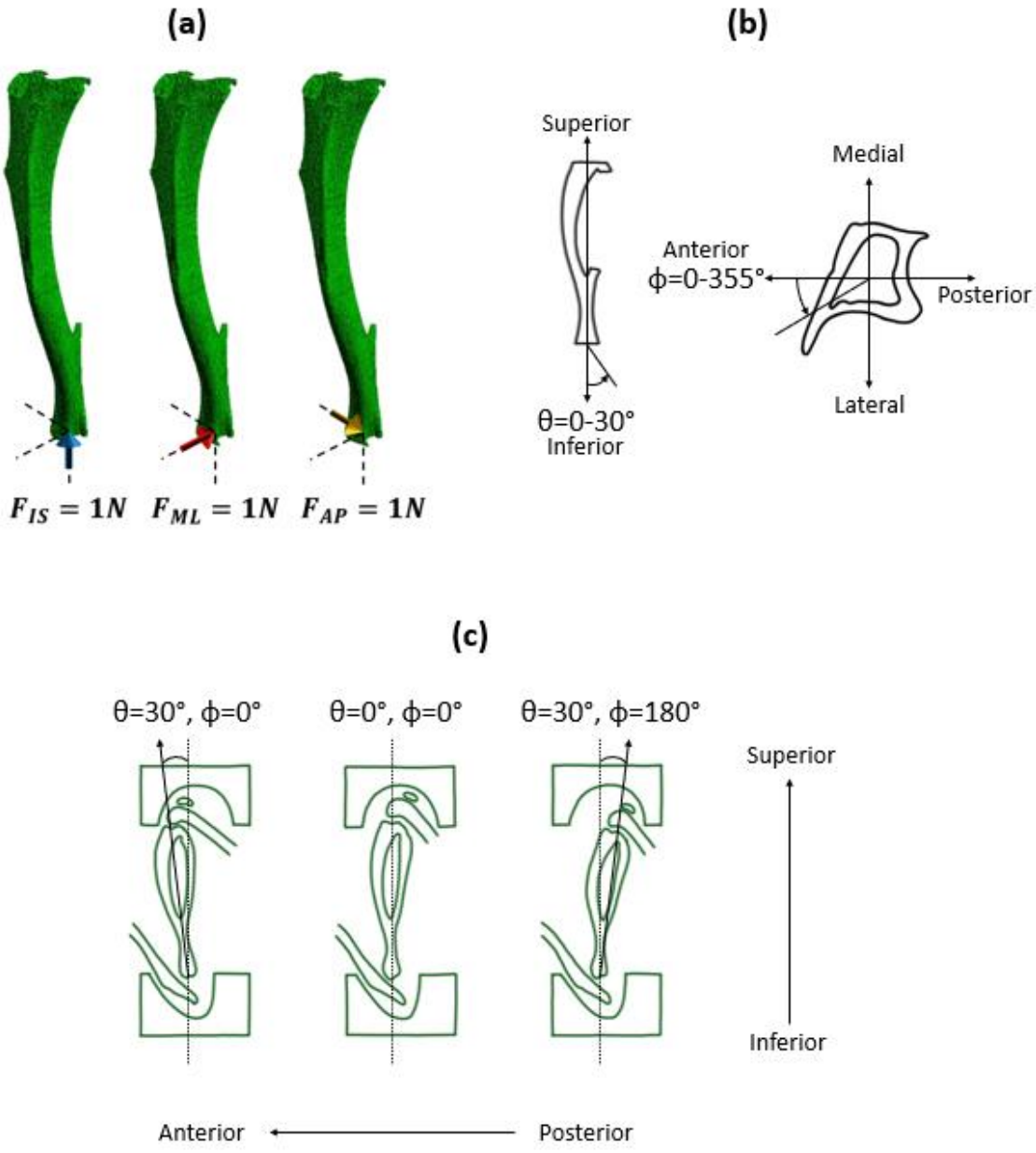

Figure 3.3: *(a) Three independent unitary load cases (1N in the inferior-superior direction (F_{IS}), 1N in the medio-lateral direction (F_{ML}), and 1N in the anterior-posterior direction (F_{AP}) for each mouse at each time point) were used to calculate the failure load along the different loading directions. (b) Schematic representation of the loading directions as a function of the two angles ϑ and ϕ. The angle from the inferior-superior axis is describes by ϑ and ranges from 0° to 30° in steps of 5°. The angle from the anterior-posterior axis, going anticlockwise (inferior-superior view) is described by ϕ, and ranges from 0° to 355° in steps of 5°. (c) Example of three loading directions (from left to right): ϑ=30°, ϕ=0°; ϑ=0°, ϕ=0° (i.e., nominal axial case); and ϑ=30°, ϕ=180°.*

3.2.3 Post processing

Due to the linear nature of the models, scaling and superposition of the effects were used to combine the results from the unitary load models during post-processing. This scaling and superposition were tested for two loading conditions (Case 1: a force of 18.9N at an angle of θ = 45°, ϕ = 45° i.e. 12 N applied along each Cartesian direction; Case 2: a moment of 1 Nm in each Cartesian direction), in two section models of the tibia (a proximal section and a midshaft section). The results of the maximum and minimum principal strains, the effective strain, and the strain energy density (SED) obtained from the section model run with the specific loading conditions (direction and magnitude) were compared against the results obtained from scaling and superimposing the outputs of the unitary section models by conducting a linear regression analysis. For more details on the testing of the scaling and superposition, please see Appendix A).

These methods were then applied to the whole bone model to calculate the minimum principal strain for a resultant of 1 N with different combinations of loading directions (Eqs. 3.1 – 3.4). Calculations were performed as a function of the angle from the inferior-superior axis (θ, 0-30° range, 5° steps) and the angle from the anterior-posterior axis (ϕ, 0°: anterior axis, positive anticlockwise (inferior-superior view), 0-355° range, 5° steps) (Figure 3.3).

$$\varepsilon_{min}^{\theta,\phi} = F^{IS}\left[\varepsilon_{min}^{IS}\right] + F^{ML}\left[\varepsilon_{min}^{ML}\right] + F^{AP}\left[\varepsilon_{min}^{AP}\right] \quad (3.1)$$

where, $\varepsilon_{min}^{\theta,\phi}$ is the minimum principal strain value calculated in each node for the loading direction defined by the angles θ and ϕ, $\varepsilon_{min}^{IS}, \varepsilon_{min}^{ML}, and\ \varepsilon_{min}^{AP}$ are the minimum principal strain values calculated in each node for each of the three unitary cases, and F^{IS} , F^{ML} , and F^{AP} are scaling coefficients, such that:

$$F^{IS} = F cos\ \theta \quad (3.2)$$

$$F^{ML} = F sin\ \theta\ sin\ \phi \quad (3.3)$$

$$F^{AP} = F sin\ \theta\ cos\ \phi \quad (3.4)$$

where, F is the applied force in the model, i.e., F = 1 N.

The bone strength (failure load; FL_FE, N) for each loading direction (Figure 3.2 F&G) was estimated using a previously validated modelling pipeline (Oliviero et al., 2021a). The bone was assumed to fail when 10% of the nodes of the model reached a critical third principal strain value equal to -14,420 με (Oliviero et al., 2021a). Therefore, the tenth percentile value of the minimum principal strain was calculated and used to rescale the applied unitary load in order to calculate the failure load (Eqs. 3.5 – 3.6).

Let $X = \{x_1, x_2, \dots, x_n\}$ be the ordered set of minimum principal strain values, where n is the number of nodes in the micro-FE model.

$$FL\_FE = \frac{-14420}{x_k \times 10^6} \times F$$

(3.5)

where, F is the force applied to the micro-FE model (in this case 1N) and

$$k = \lceil 0.1n \rceil$$

(3.6)

i.e., k is the smallest integer greater than or equal to 10% of n.

To enable comparison across loading directions, the FL_FE for each loading direction was normalised (NFL_FE, %) by the FL_FE calculated for the nominal axial loading direction (θ = 0°, φ = 0°) for each mouse at each time point (Eq. 3.7).

$$NFL\_FE^{\theta,\phi} = \frac{FL\_FE^{\theta,\phi} - FL\_FE^{0,0}}{FL\_FE^{0,0}} \times 100$$

(3.7)

where, $NFL\_FE^{\theta,\phi}$ is the normalised failure load at the loading direction defined by ϑ and ϕ, with respect to the nominal axial case, $FL\_FE^{\theta,\phi}$ is the failure load at the loading direction defined by ϑ and ϕ, and $FL\_FE^{0,0}$ is the failure load of the nominal axial case. Note: If a loading direction has a positive NFL_FE then the FL_FE of that loading direction is higher than the nominal axial case, and a negative NFL_FE refers to a FL_FE which is lower than the nominal axial case.

To evaluate the effect of the time point (week 18 vs week 20), and of the group (OVX vs OVX+ML), the following quantities were calculated for all loading directions (θ in range 0-30°, ϕ in range 0-355°): the absolute difference in failure load (absΔFLt_FE, N) between the time points (week 18 vs week 20) for OVX and OVX+ML groups, percentage differences in failure load (ΔFLt_FE, %) between time points

(week 18 vs week 20) for OVX and OVX+ML groups (Eq. 3.8), and the percentage points (difference between the percentage changes) of the failure load (ΔFLg_FE, %pt) from week 18 to week 20 calculated between the two groups (OVX vs OVX+ML).

$$\Delta\mathrm{FLt\_FE}^{\theta,\phi} = \frac{FL\_FE_{W20}^{\theta,\phi} - FL\_FE_{W18}^{\theta,\phi}}{FL\_FE_{W18}^{\theta,\phi}} \times 100$$

(3.8)

where, $\Delta\mathrm{FLt\_FE}^{\theta,\phi}$ is the percentage difference in failure load between time points at the loading direction defined by ϑ and ϕ, $FL\_FE_{W18}^{\theta,\phi}$ and $FL\_FE_{W20}^{\theta,\phi}$ are the failure loads at week 18 and week 20, respectively at the same loading direction (defined by ϑ and ϕ).

A safety factor (SF) was calculated for each loading direction by dividing the calculated FL_FE by the applied load in the *in vivo* tibial loading model (12 N). This was to identify the loading directions for which the tibia was at risk of fracture.

The apparent bone stiffness (S_FE, N/mm) was calculated as the ratio between the axial applied force (i.e., when θ = 0°) and the average displacement along the longitudinal direction calculated for the loaded nodes.

3.2.4 Statistical analysis

The mean, standard deviation (SD) and coefficient of variation (CV) of the apparent bone stiffness was calculated for the nominal axial loading direction for each group of mice, at each time point. The mean, SD and CV of the bone strengths were calculated for each loading direction for each group of mice, at each time point.

Non-parametric tests were chosen due to the results not being normally distributed (Shapiro-Wilks test) and the small sample size. The difference in stiffness between time points was assessed using the non-parametric two-tailed Wilcoxon test. The difference in mean stiffness between groups was assessed using the non-parametric two-tailed Mann-Whitney U test. The effect of the loading direction on the strength between time points was assessed using the non-parametric two-tailed Wilcoxon test. The effect of the loading direction on the mean strength between groups was assessed using the non-parametric two-tailed Mann-Whitney U test, as was the comparison between the nominal axial loading direction and every other loading direction. The statistical significance level was set at α = 0.05 for all tests.

The FL_FE for every mouse in both groups and both time points were pooled for each loading direction (N=22). The p-value was computed to check if the midshaft Ct.Th and the FL_FE were correlated for each loading direction. The null hypothesis was that the coefficient of determination (R^2 value) between the two variables was not statistically different from zero. If the null hypothesis was rejected, the R^2 value and the equation of the linear regression line were calculated for the regression analysis corresponding to that loading direction. The range of the failure load across the pooled data, for each loading direction, was calculated and normalised by the mean strength for that loading direction i.e., the normalised range for a loading direction was calculated as the difference between the maximum and minimum values of the pooled failure loads for that loading direction, divided by the mean pooled failure load for that loading direction, and multiplied by 100 to obtain the normalised range (MATLAB, 2023A, The MathWorks Inc., Natick MA, USA).

3.3 Results

In total, 504 loading directions were evaluated for each mouse, for both mouse groups (OVX and OVX+ML) and for two time points (week 18 and week 20) (Table 3.2).

Table 3.2: *For both groups and time points: loading directions associated with the minimum (ϑ = 30°, ϕ = 30-50°) and maximum failure loads (ϑ = 10°, ϕ = 205-210°), mean minimum and maximum failure loads (FL_FE), and mean apparent stiffness (S_FE) calculated for the nominal axial direction (ϑ = 0°, ϕ = 0°). SD – standard deviation, OVX – ovariectomy, OVX+ML – ovariectomy and mechanical loading, W18 – week 18, and W20 – week 20.*

	Loading direction for minimum FL_FE (θ, range of φ) [°]	Minimum FL_FE (mean ± SD) [N]	Loading direction for maximum FL_FE (θ, range of φ) [°]	Maximum FL_FE (mean ± SD) [N]	S_FE (mean ± SD) [N/mm]
OVX-W18	30, [30–45]	12.6 ± 0.772	10, [205–210]	65.7 ± 4.78	243.2 ± 27.1
OVX-W20	30, [35–45]	12.5 ± 0.691	10, [205–210]	66.3 ± 4.40	237.0 ± 22.8
OVX + ML-W18	30, [40–45]	13.3 ± 0.606	10, [205–210]	69.5 ± 2.15	273.7 ± 8.0
OVX_ML-W20	30, [45–50]	15.1 ± 0.659	10, [205–210]	78.0 ± 3.34	293.0 ± 15.4

SD, standard deviation; OVX, ovariectomy; OVX + ML, ovariectomy and mechanical loading; W18, week 18; and W20, week 20.

The apparent bone stiffness (S_FE) in the OVX group was not significantly different between week 18 (243.2 ± 27.1 N/mm) and week 20 (237.0 ± 22.8 N/mm; p = 0.188). The S_FE in the OVX+ML group at week 18 (273.7 ± 8.0 N/mm) was significantly different from the S_FE at week 20 (293.0 ± 15.4 N/mm, p = 0.031). The difference in the change of S_FE from week 18 to 20 was significantly higher for the OVX+ML (7.03 ± 2.66%) group compared to the OVX group (-2.55 ± 3.70%, p = 0.009).

Large variation in the failure load (FL_FE) of the mouse tibiae across the tested loading directions was observed (Figure 3.4). Similar trends were found across all groups and time points. For the OVX group, at week 18, the FL_FE ranged from 12.6 N (θ = 30°, ϕ = 30-45°) to 65.7 N (θ = 10°, ϕ = 205-210°). At week 20, the FL_FE within the OVX group ranged from 12.5 N (θ = 30°, ϕ = 35-45°) to 66.3 N (θ = 10°, ϕ = 205-210°). For the OVX+ML group at week 18, the FL_FE ranged from 13.3 N (θ = 30°, ϕ = 40-45°) to 69.5 N (θ = 10°, ϕ = 205-210°). At week 20, the FL_FE in the OVX+ML group increased and ranged from 15.1 N (θ = 30°, ϕ = 45-50°) to 78.0 N (similar angle for maximum FL_FE as for week 18; θ = 10°, ϕ = 205-210°). The CV for the FL_FE for all groups and time points ranged between 2.49% and 8.54%, with the OVX group generally having larger coefficients of variation than the OVX+ML group.

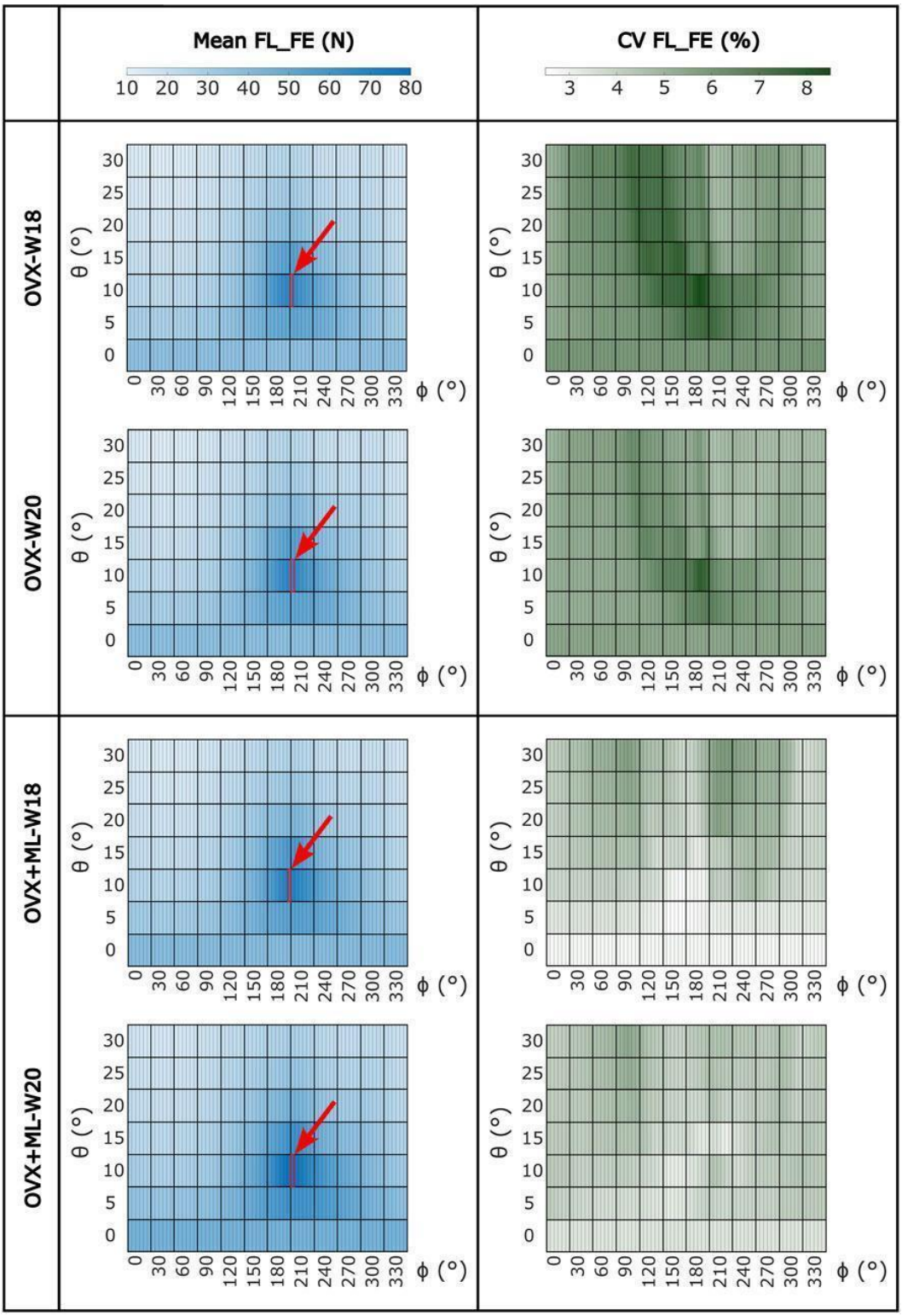

Figure 3.4: *Heatmaps of the mean values of FL_FE and coefficients of variation (CV) across all loading directions (ϑ in range 0-30°, ϕ in range 0-355°) for both groups (OVX and OVX+ML) and time points (W18 and W20). The red square and arrow highlight the loading direction for which the maximum FL_FE was found. OVX – ovariectomy, OVX+ML – ovariectomy and mechanical loading, W18 – week 18, W20 – week 20.*

Similar trends were found for the normalised failure load (NFL_FE) across all groups and time points (Figure 3.5). NFL_FE nearly doubled for loading directions with θ approximately 10° and ϕ between 205 and 210°.

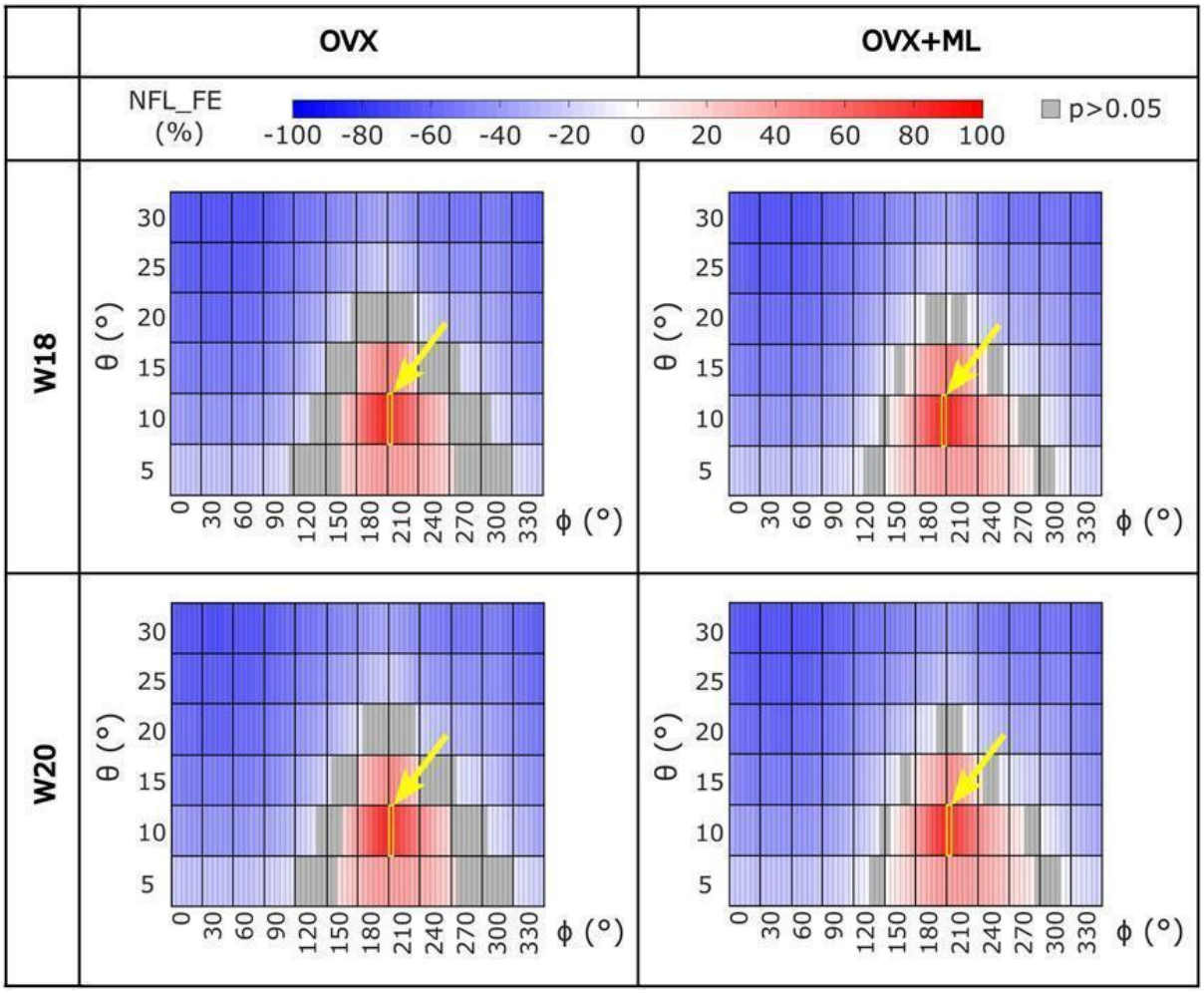

Figure 3.5: *Heatmaps of the mean normalised failure load (NFL_FE) across all loading directions (ϑ in range 5-30°, ϕ in range 0-355°) for both groups (OVX and OVX+ML) and time points (W18 and W20). The values in grey show the loading directions associated with FL_FE to be not significantly different to the FL_FE obtained for the nominal axial loading direction. The yellow square and arrow highlight the loading direction for which the maximum mean NFL_FE was found. The failure loads have been normalised by the nominal axial case, hence why the ϑ = 0° is omitted. OVX – ovariectomy, OVX+ML – ovariectomy and mechanical loading, W18 – week 18, W20 – week 20.*

Typical distributions of the minimum principal strain obtained for loads along the nominal axial loading direction (θ = 0°, ϕ = 0°), and in the direction associated with the maximum FL_FE, are reported in

Figure 3.6. For both the nominal axial loading direction and the loading direction associated with the minimum FL_FE and NFL_FE, high absolute values of the minimum principal strain were localised in the medial distal and lateral portions of the tibia. High strains were found proximally to the distal tibiofibular junction in the posterior portion of the bone, across all groups and time points. Lower strains were found at the anterior crest for all groups and time points. Additionally, for the loading direction associated with maximum FL_FE and NFL_FE, high absolute values of the minimum principal strain were also localised in the medial proximal portion of the tibia. As expected, small differences were found for models at week 18 between the two groups (both groups scanned before treatment started), and significant differences induced by the mechanical loading could be observed at week 20. Typical internal distributions of the minimum principal strain calculated for models loaded along the nominal axial loading direction (θ = 0°, ϕ = 0°), along the direction associated with the minimum FL_FE, and along the direction associated with the maximum FL_FE, are reported in Figure 3.7. High absolute values of the minimum principal strain bridge the periosteal and endosteal surfaces of the cortical bone, for these three loading directions.

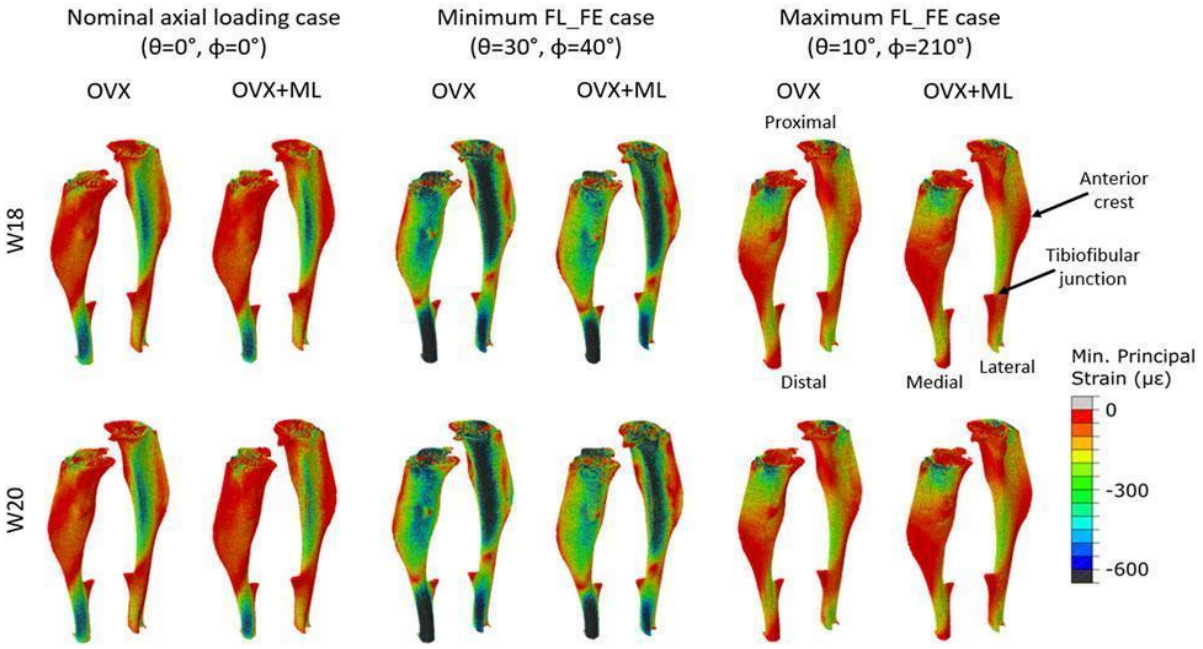

Figure 3.6: *Minimum principal strain distribution of two representative tibiae (OVX – mouse 3, OVX+ML – mouse 5) obtained using a load of magnitude 1N at W18 and W20. It should be noted that at W18 both groups were untreated, so observed differences are associated mainly with different animals. Left: Load applied along the nominal axial loading direction (ϑ = 0°, ϕ = 0°). Middle: Load applied along the loading direction associated with the minimum FL_FE (ϑ = 30°, ϕ = 40°). Right: Load applied along the loading direction associated with the maximum FL_FE (ϑ = 10°, ϕ = 210°). OVX – ovariectomy, OVX+ML – ovariectomy and mechanical loading, W18 – week 18, W20 – week 20.*

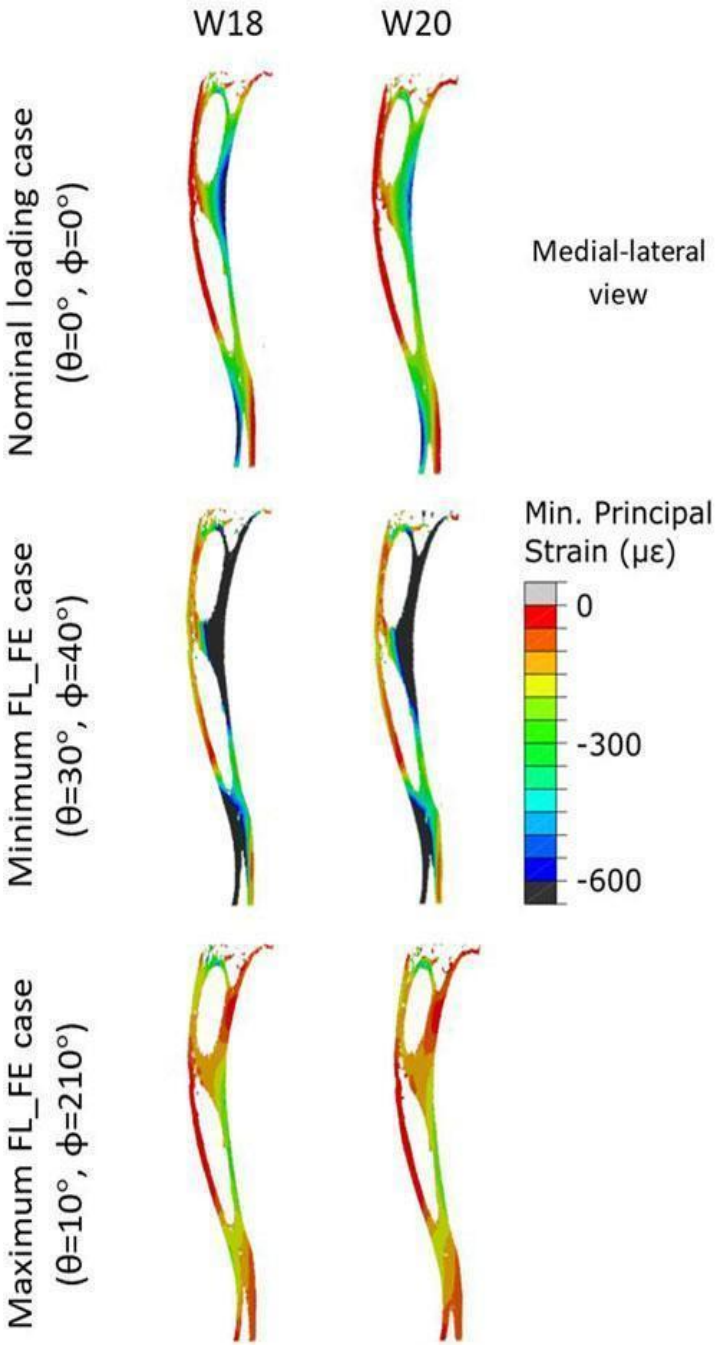

Figure 3.7: *Internal minimum principal strain distribution of a representative tibia (mouse 5) within the OVX+ML group, obtained using a load magnitude 1 N at W18 and W20. For each week three loading directions are shown: the load applied along the nominal axial loading direction (ϑ = 0°, ϕ = 0°), the load applied along the loading direction associated with the minimum FL_FE (ϑ = 30°, ϕ = 40°), and the load applied along the loading direction associated with the maximum FL_FE (ϑ = 10°, ϕ = 210°). OVX – ovariectomy, W18 – week 18, W20 – week 20.*

For the OVX group, the FL_FE between weeks 18 and 20, both absolute difference and percentage difference (absΔFLt_FE and ΔFLt_FE, respectively) were not significantly different for any loading direction (maximum absolute difference 0.80 N (Figure 3.8), maximum absolute percentage difference 1.7% (Figure 3.9), $p > 0.05$). For the OVX+ML group, the FL_FE increased significantly between weeks 18 and 20 ($p < 0.031$) with absΔFLt_FE between 1.6 N (θ = 30°, ϕ = 70°) and 8.6 N (θ = 10°, ϕ = 210°) and ΔFLt_FE between 5.4% (θ = 15°, ϕ = 190°) and 16.0% (θ = 10°, ϕ = 305°). Percentage point differences between ΔFLt_FE for the OVX and the OVX+ML groups were significant for any loading direction ($p < 0.004$), with ΔFLg_FE ranging between 6.2% (θ = 15°, ϕ = 190°) and 14.6% (θ = 10°, ϕ = 310°) (Figure 3.9).

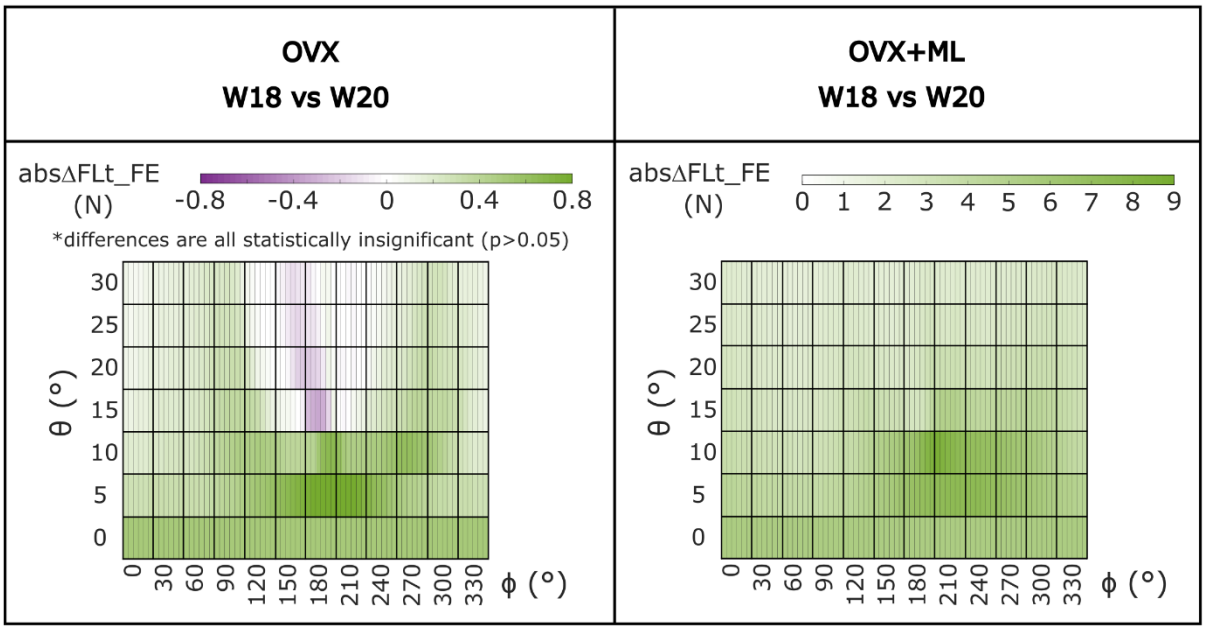

Figure 3.8: *Left: Heatmap of the absolute difference in mean failure load (absΔFLt_FE) between time points (W18 vs W20) for OVX group for all loading directions (ϑ in range 0-30°, ϕ in range 0- 355°). Differences are all statistically insignificant (Wilcoxon test, $p < 0.05$). Right: Heatmap of absΔFLt_FE for the OVX+ML group for all loading directions. All loading directions were statistically significant when the two time points were compared (Wilcoxon test, $p < 0.05$). OVX – ovariectomy, OVX+ML – ovariectomy and mechanical loading, W18 – week 18, W20 – week 20.*

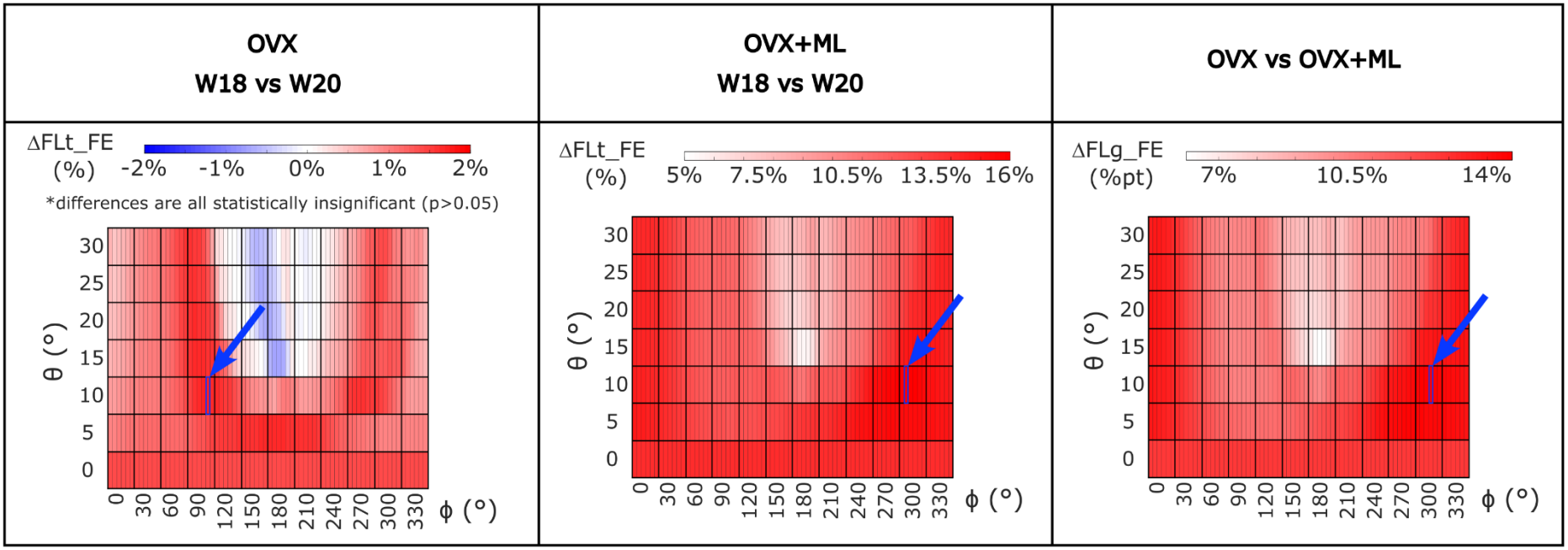

Figure 3.9: *Left: Heatmap of the percentage difference in mean failure load (ΔFLt_FE) between time points (W18 vs W20) for OVX group for all loading directions (ϑ in range 0-30°, ϕ in range 0- 355°). Differences are all statistically insignificant (Wilcoxon test, $p < 0.05$). Middle: Heatmap of ΔFLt_FE for OVX+ML group for all loading directions. Right: Heatmap of the difference between the percentage points between the failure load across the two groups (OVX vs OVX-ML) (ΔFLg_FE) for all loading directions. All loading directions were statistically significant when the two time points were compared (Wilcoxon test, $p < 0.05$). The blue square and arrow highlight the loading direction for which the maximum difference was found. OVX – ovariectomy, OVX+ML – ovariectomy and mechanical loading, W18 – week 18, W20 – week 20.*

The safety factor (SF) across all loading directions ranged from approximately 1 (in most cases for θ = 30° and ϕ between 35° and 50°) to 5-6 (θ = 10°, ϕ between 195° and 215°), in all groups and time points (Figure 3.10).

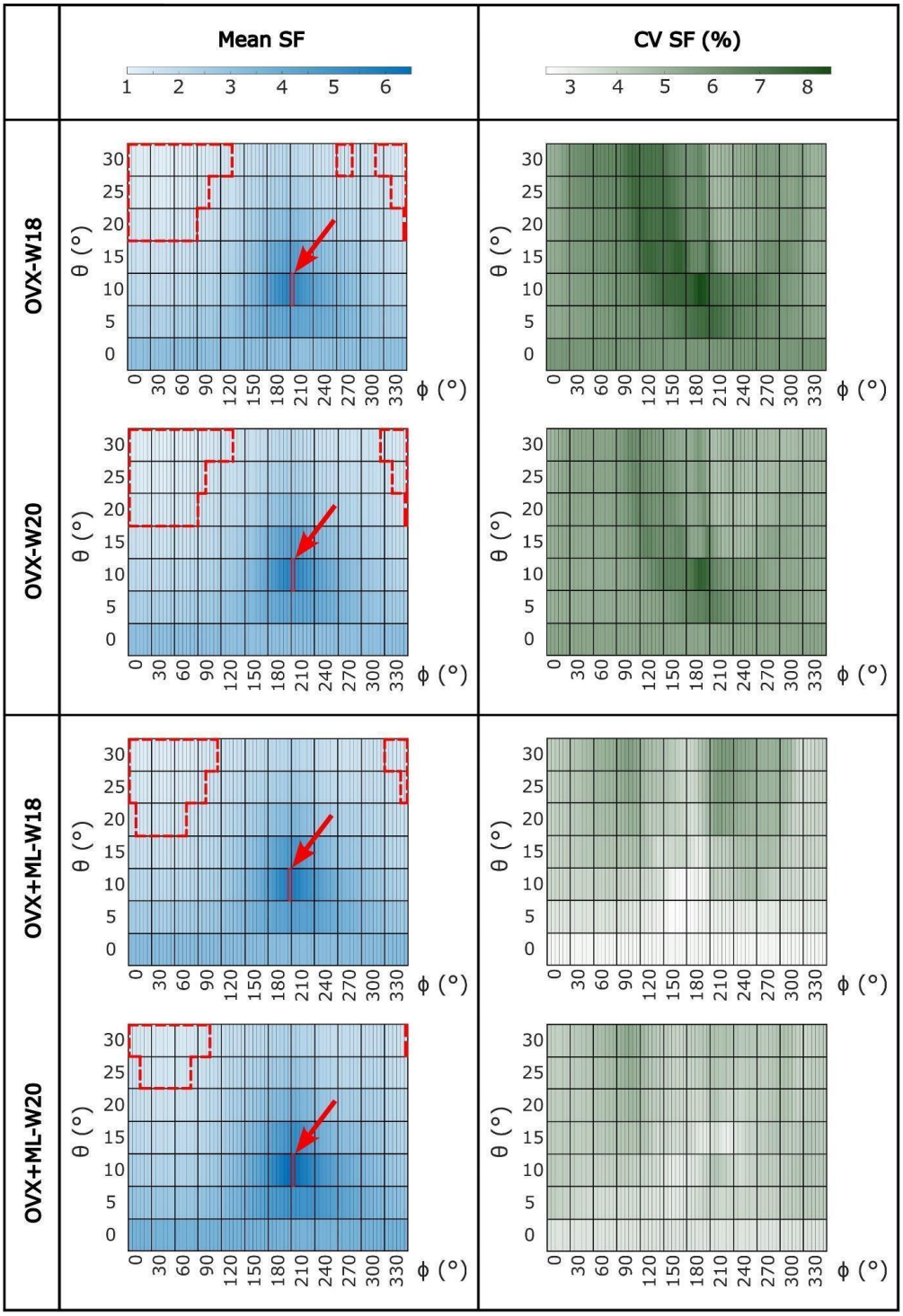

Figure 3.10: *Heatmaps of the mean values of safety factor (SF) and coefficients of variation (CV, %) across all loading directions (ϑ = 0-30°, ϕ = 0-355°) for both groups and time points. The red square and arrow highlight the loading direction for which the maximum safety factor was found, and the dashed red areas highlight the loading directions where the safety factor was between 1 and 1.5 (low safety factor values). OVX – ovariectomy, OVX+ML – ovariectomy and mechanical loading, W18 – week 18, and W20 – week 20.*

In the pooled data (OVX, OVX+ML, W18, W20) the midshaft Ct.Th was a modest to good predictor of the failure load across all loading directions (R^2-range: 67.8-87.9%, all $p < 0.001$) (Figure 3.11). For the loading conditions θ = 5°, ϕ = 215-280° and θ = 10°, ϕ = 225-290°, the R^2 values were all greater than that of the nominal axial case, with the maximum occurring at θ = 5°, ϕ = 240°. Above θ = 10°, the R^2 values were generally smaller than that of the nominal axial case. The normalised range (the range of the failure load across the pooled data, normalised by the mean failure load for that loading direction) (Figure 3.11) ranged from 23.3 – 39.5%, with the maximum occurring at θ = 30°, ϕ = 105° and the minimum occurring at θ = 15°, ϕ = 195°. For the nominal axial case, the normalised range was 33.3%. Above θ = 10°, and ϕ = 150°, the normalised range values were generally smaller than that of the nominal axial case.

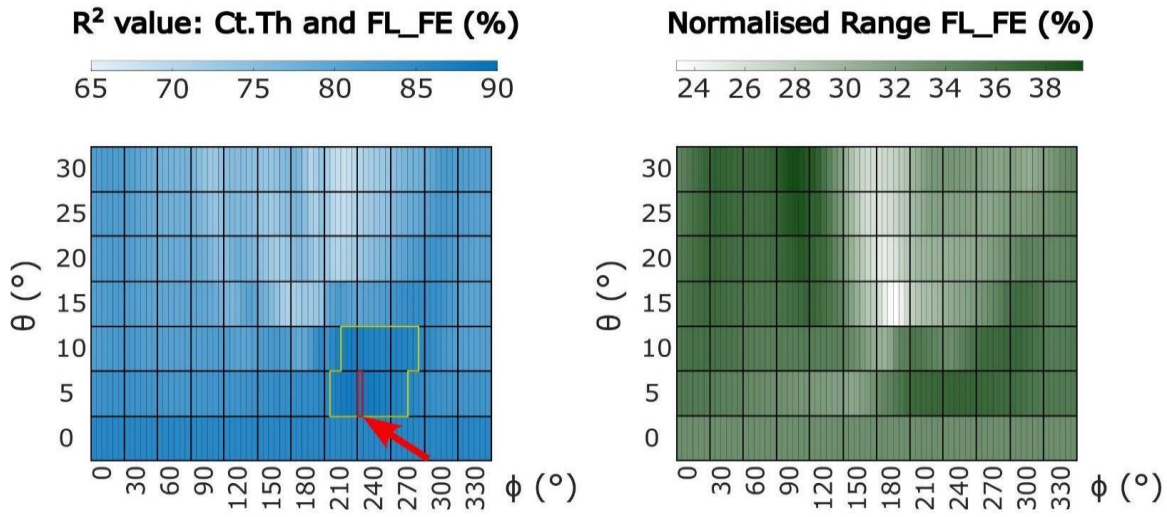

Figure 3.11: *Left: Heatmap of the R^2 values when conducting a linear regression analysis between the midshaft cortical thickness (Ct.Th) and the predicted failure load (FL_FE), across all mice in both groups (OVX and OVX+ML) and at both time points (weeks 18 and 20), for all loading directions (ϑ in range 0-30°, ϕ in range 0-355°). The yellow area highlights the loading directions which have an R^2 value which is greater than the R^2 value of the nominal axial case (ϑ = 0°, ϕ = 0°). The red square and arrow highlight the maximum R^2 value. Right: Heatmap of the normalised range, across all mice in both groups (OVX and OVX+ML) and at both time points (weeks 18 and 20), for all loading directions (ϑ in range 0-30°, ϕ in range 0-355°).*

3.4 Discussion

The overall goal of the study was to investigate the effect of the loading direction on the apparent mechanical properties of the mouse tibia and to evaluate how the apparent mechanical properties are sensitive to the load after the treatment with external mechanical loading.

Using validated micro-CT based micro-FE models, the apparent mechanical properties of the tibiae under different loading directions were calculated. The change over time of the apparent stiffness of the bone was higher for the OVX+ML group than the OVX group. A previous study, in which the experimental axial stiffness was measured from the load-displacement curves, showed the stiffness of C57BL/6 mice at ages 16 and 24 weeks to be in the range 188-307 N/mm for ovariectomised mice and in the range 234-366 N/mm for ovariectomised mice treated with PTH (Oliviero et al., 2021b). The high variability could be due to the heterogeneous effect of ovariectomy and PTH, but could also be due to experimental variables such as the bone alignment and fixation in the testing machine. Nevertheless, even though the age range of the mice in that study was larger (weeks 16-24) than that of this study (weeks 18-20) and the treatments vary between the two studies, the apparent stiffness values obtained in this study fit within the range of previously reported experimental stiffness values.

The values of the failure load for the different loading directions showed that the bone is stronger for a different loading direction to the nominal axial case ($\theta = 0°$, $\phi = 0°$), with the maximum occurring at θ equal to 10° and ϕ equal to 205° or 210°, suggesting that the bone is optimised for this loading direction, ignoring any contribution of the fibula. The loading direction for which the tibia-fibula component (lower leg) is loaded *in vivo* is not currently known. It could be assumed that the loading direction associated with the maximum failure load is the component of the knee force that loads the tibia. The fibula is located roughly at a ϕ angle between 170° and 220°; including the fibula in the model may change the loading direction associated with the maximum failure load as the fibula may share some of the load and reduce the deformation of the tibia if loaded along these directions. The low coefficients of variation (range: 2.5-8.5%) associated with the FL_FE estimations at each loading direction per time point, per group, could be due to small intrinsic differences between mice and could suggest the reproducibility of the results, in line with the low errors associated with the generation of the micro-FE models, as recently reported by Oliviero et al. (2022). The mouse tibia has been shown to be very sensitive to the loading direction, with some loading directions resulting in a FL_FE ranging from half to double that of the nominal axial case. This result expands on those of a previous study, which showed that small variations of the load direction (effect of transverse load due to physiological loading on top of axial external mechanical loading) affect the local deformation and strain energy density (Cheong et al., 2021a). This result highlights the importance of controlling the loading direction

when using the *in vivo* tibial loading model; a problem already demonstrated in a repositioning study for the *in vivo* tibial loading model (Giorgi and Dall'Ara, 2018) and in a misalignment study for the rodent tail loading model (Goff et al., 2014). The loading direction during this kind of experiment could be partially accounted for by integrating a tri-axial load cell in the experimental setup or using advanced 3D printed loading caps. It should be noted that the variability of the loading direction could be critical when developing multiscale models to predict bone adaptation driven by mechanoregulation (Pereira et al., 2015; Cheong et al., 2020b, 2021b), and accounting for it may improve the accuracy of the predictions.

It should also be noted that the safety factor calculated in this study identified the loading directions with $\theta = 30°$ as critically close to 1, and therefore at risk of bone failure during the *in vivo* tibial loading experiments (Figure 3.10), a problem which has been previously reported (Yang et al., 2017). While further studies should be performed to understand the load sharing between the different musculoskeletal components of the mouse leg, this risk should be considered to maximise animal welfare during the experimental studies. Furthermore, the risks of inducing bone fractures during the tests would be reduced by incorporating features in the loading rigs that minimise potential misalignment errors, ensuring that they stay below 20° with respect to the longitudinal axis of the tibia.

When making comparisons between time points for the OVX group, the differences in FL_FE were within the limits of the inter-operator reproducibility error of the FE pipeline (precision error below 1.96%) (Oliviero et al., 2022), and in fact were not statistically different. This result confirms that the potential changes in bone geometry, trabecular bone volume fraction and cortical porosity (calculated for each of the ten longitudinal partitions of the tibia), and microstructure due to ovariectomy and growth between week 18 and week 20 do not affect the failure load, as previously reported by Roberts et al. (2019). However, this study extends the findings by confirming that this is valid for several loading directions. On the contrary, for the OVX+ML group, a statistically significant difference between the time points for all loading directions was found, with an increase of FL_FE between 5.4% and 16.0% (1.6 – 8.6 N). This was also confirmed by comparing longitudinally the OVX and OVX+ML groups, which highlighted differences in longitudinal changes of failure load between 6.2% and 14.6%. These results confirmed that the changes in morphometric and densitometric properties of the trabecular and cortical bone induced by the external mechanical loading (Roberts et al., 2020) translate into changes to the FL_FE for the different loading directions included in this study. Furthermore, the direction of the optimal load remains relatively constant (within 5°) across groups and time points (Figure 3.4). This result suggests that the mechanical loading increases the tibia FL_FE for all loading directions. However, when longitudinally comparing the two groups (OVX and OVX+ML), the largest difference was found for different loading directions (Figure 3.9), suggesting that the external mechanical loading may

induce bone remodelling that leads to an improvement in FL_FE at non-optimised locations. Furthermore, the absolute difference in the failure load between weeks 18 and 20 (Figure 3.8) suggests that this improvement is heterogeneous across loading directions. Nevertheless, the orientation of the optimal load remains similar across the two considered time points.

The relationship between the midshaft Ct.Th and the FL_FE, predicted across various loading directions, was investigated. This was in order to see the potential usage of the Ct.Th as a surrogate of the FL_FE at different loading directions. It was found that for loading directions with a θ value greater than 10°, the predictions of FL_FE by using the midshaft Ct.Th are not accurate. As the θ value increased from 10-30°, the range of ϕ values which resulted in poor R^2 values increased. For angles with a θ value greater than 10°, more bending is induced to the tibia. Given that the tibia is optimised for compressive loads, where Ct.Th significantly contributes to load-bearing, the increasing influence of bending at loading directions which correlate with higher θ values likely explains this reduced predictive accuracy. The maximum value of FL_FE across all loading directions was found at θ = 10°, ϕ = 205-210°. The R^2 value corresponding to these loading directions (R^2: 83.1-84.9%) were within 3% of the R^2 value of the nominal axial case (R^2: 85.4%). It was also found that for the loading directions θ = 5°, ϕ = 215-280° and θ = 10°, ϕ = 225-290°, the R^2 values were all greater than that of the nominal axial case. This suggests that the loading direction the mouse tibia is mainly subjected to during physiological activities may be within this range.

The main limitation of the study is that the model of the tibio-fibular complex has been simplified. Firstly, the fibula has not been included in the model. It is known that small differences in repositioning can lead to large transverse loads at the knee and ankle, which induce bending in the tibia (Giorgi and Dall'Ara, 2018). This is modelled by increasing θ, which results in an increase in the transverse loads, and this would in part be transferred through the fibula (Prasad et al., 2010; Cheong et al., 2021a). However, the inclusion of the fibula in the model would induce further assumptions, as the tibiofibular joint material properties are currently not known. Additionally, the growth plate has not been included in the model. The main reason for this design choice is that currently little is known about the material properties of the growth plate. Nevertheless, this feature is likely to affect the transmission of the load in the proximal portion of the tibia, and may therefore affect the local deformation, and consequently the failure load, differently for the different loading directions. It remains to be demonstrated to what extent the contribution of the fibula, proximal tibio-fibular joint, and soft tissues around the two bones, would affect the deformation of the tibia.

In conclusion, this study has highlighted the importance of the loading direction on the failure load of the mouse tibia. The results of this study will be important to optimise the protocols for *in vivo* tibial

loading experiments on mice. Moreover, external mechanical loading has been found to increase the bone strength across all loading directions, providing more insights on the effect of this intervention on the bone's apparent mechanical properties.

3.5 Funding

The study was partially funded by the UK National Centre for the Replacement, Refinement and Reduction of Animals in Research (NC3Rs, Grant number: NC/R001073/1), by the Engineering and Physical Sciences Research Council (EPSRC) Frontier Multisim Grant (EP/K03877X/1 and EP/S032940/1) and by the University of Sheffield EPSRC Doctoral Training Partnership (DTP) Scholarship (X/013991-12).

3.6 Acknowledgements

We thank Dr. B. Roberts, Dr. N. Wang, and Mr. H. Arredondo Carrera for sharing the experimental data, Dr. S Oliviero for the original mouse tibia failure load script, and the Skelet.Al laboratory for access to the imaging facilities (http://skeletal.group.shef.ac.uk/).

3.7 Conflict of interest

The authors declare that the research was conducted in the absence of any commercial or financial relationships that could be construed as a potential conflict of interest.

3.8 Ethics statement

The animal study was reviewed and approved by the Research Ethics Committee of the University of Sheffield.

3.9 References

Birkhold, A. I., Razi, H., Duda, G. N., Weinkamer, R., Checa, S., and Willie, B. M. (2014). The influence of age on adaptive bone formation and bone resorption. Biomaterials 35, 9290–9301. doi: 10.1016/j.biomaterials.2014.07.051

Bonewald, L. F. (2011). The amazing osteocyte. J. Bone Miner. Res. 26, 229–238. doi: 10.1002/jbmr.320

Bouxsein, M. L., Boyd, S. K., Christiansen, B. A., Guldberg, R. E., Jepsen, K. J., and Müller, R. (2010). Guidelines for assessment of bone microstructure in rodents using micro-computed tomography. J. Bone Miner. Res. 25, 1468–1486. doi: 10.1002/jbmr.141

Bouxsein, M. L., Myers, K. S., Shultz, K. L., Donahue, L. R., Rosen, C. J., and Beamer, W. G. (2005). Ovariectomy-induced bone loss varies among inbred strains of mice. J. Bone Miner. Res. 20, 1085–1092. doi: 10.1359/jbmr.050307

Carriero, A., Abela, L., Pitsillides, A. A., and Shefelbine, S. J. (2014). Ex vivo determination of bone tissue strains for an in vivo mouse tibial loading model. J. Biomech. 47, 2490–2497. doi: 10.1016/j.jbiomech.2014.03.035

Cheong, V. S., Campos Marin, A., Lacroix, D., and Dall'Ara, E. (2020a). A novel algorithm to predict bone changes in the mouse tibia properties under physiological conditions. Biomech. Model. Mechanobiol. 19, 985–1001. doi: 10.1007/s10237-019-01266-7

Cheong, V. S., Kadirkamanathan, V., and Dall'Ara, E. (2021a). The Role of the Loading Condition in Predictions of Bone Adaptation in a Mouse Tibial Loading Model. Front. Bioeng. Biotechnol. 9, 676867. doi: 10.3389/fbioe.2021.676867

Cheong, V. S., Roberts, B. C., Kadirkamanathan, V., and Dall'Ara, E. (2020b). Bone remodelling in the mouse tibia is spatio-temporally modulated by oestrogen deficiency and external mechanical loading: A combined in vivo/in silico study. Acta Biomater. 116, 302–317. doi: 10.1016/j.actbio.2020.09.011

Cheong, V. S., Roberts, B. C., Kadirkamanathan, V., and Dall'Ara, E. (2021b). Positive interactions of mechanical loading and PTH treatments on spatio-temporal bone remodelling. Acta Biomater. 136, 291–305. doi: 10.1016/j.actbio.2021.09.035

De Souza, R. L., Matsuura, M., Eckstein, F., Rawlinson, S. C. F., Lanyon, L. E., and Pitsillides, A. A. (2005). Non-invasive axial loading of mouse tibiae increases cortical bone formation and modifies trabecular organization: A new model to study cortical and cancellous compartments in a single loaded element. Bone 37, 810–818. doi: 10.1016/j.bone.2005.07.022

Du, J., Hartley, C., Brooke-Wavell, K., Paggiosi, M. A., Walsh, J. S., Li, S., et al. (2021). High-impact exercise stimulated localised adaptation of microarchitecture across distal tibia in postmenopausal women. Osteoporos. Int. 32, 907–919. doi: 10.1007/s00198-020-05714-4

Frost, H. M. (2003). Bone's mechanostat: a 2003 update. Anat. Rec. A. Discov. Mol. Cell. Evol. Biol. 275, 1081–1101. doi: 10.1002/ar.a.10119

Giorgi, M., and Dall'Ara, E. (2018). Variability in strain distribution in the mice tibia loading model: A preliminary study using digital volume correlation. Med. Eng. Phys. 62, 7–16. doi: 10.1016/j.medengphy.2018.09.001

Goff, M. G., Chang, K. L., Litts, E. N., and Hernandez, C. J. (2014). The effects of misalignment during in vivo loading of bone: techniques to detect the proximity of objects in three-dimensional models. J. Biomech. 47, 3156–3161. doi: 10.1016/j.jbiomech.2014.06.016

Gould, S. E., Junttila, M. R., and De Sauvage, F. J. (2015). Translational value of mouse models in oncology drug development. Nat. Med. 21, 431–439. doi: 10.1038/nm.3853

Holguin, N., Brodt, M. D., Sanchez, M. E., Kotiya, A. A., and Silva, M. J. (2013). Adaptation of tibial structure and strength to axial compression depends on loading history in both C57BL/6 and BALB/c mice. Calcif. Tissue Int. 93, 211–221. doi: 10.1007/s00223-013-9744-4

Levchuk, A., Zwahlen, A., Weigt, C., Lambers, F. M., Badilatti, S. D., Schulte, F. A., et al. (2014). The Clinical Biomechanics Award 2012 - presented by the European Society of Biomechanics: large scale simulations of trabecular bone adaptation to loading and treatment. Clin. Biomech. (Bristol, Avon) 29, 355–362. doi: 10.1016/j.clinbiomech.2013.12.019

Lu, Y., Boudiffa, M., Dall'Ara, E., Bellantuono, I., and Viceconti, M. (2016). Development of a protocol to quantify local bone adaptation over space and time: quantification of reproducibility. J. Biomech. 49, 2095–2099. doi: 10.1016/j.jbiomech.2016.05.022

Lu, Y., Boudiffa, M., Dall'Ara, E., Liu, Y., Bellantuono, I., and Viceconti, M. (2017). Longitudinal effects of Parathyroid Hormone treatment on morphological, densitometric and mechanical properties of mouse tibia. J. Mech. Behav. Biomed. Mater. 75, 244–251. doi: 10.1016/j.jmbbm.2017.07.034

Lynch, M. E., Main, R. P., Xu, Q., Schmicker, T. L., Schaffler, M. B., Wright, T. M., et al. (2011). Tibial compression is anabolic in the adult mouse skeleton despite reduced responsiveness with aging. Bone 49, 439–446. doi: 10.1016/j.bone.2011.05.017

Main, R. P., Shefelbine, S. J., Meakin, L. B., Silva, M. J., van der Meulen, M. C. H., and Willie, B. M. (2020). Murine axial compression tibial loading model to study bone mechanobiology: implementing

the model and reporting results. J. Orthop. Res. 38, 233–252. doi: 10.1002/jor.24466

Martelli, S., Beck, B., Saxby, D., Lloyd, D., Pivonka, P., and Taylor, M. (2020). Modelling human locomotion to inform exercise prescription for osteoporosis. Curr. Osteoporos. Rep. 18, 301–311. doi: 10.1007/s11914-020-00592-5

Martin, R. B., Burr, D. B., and Sharkey, N. A. (1998). Skeletal tissue mechanics. Skelet. Tissue Mech. doi: 10.1007/978-1-4757-2968-9

Melville, K. M., Kelly, N. H., Khan, S. A., Schimenti, J. C., Ross, F. P., Main, R. P., et al. (2014). Female mice lacking estrogen receptor-alpha in osteoblasts have compromised bone mass and strength. J. Bone Miner. Res. 29, 370–379. doi: 10.1002/jbmr.2082

Miller, C. J., Trichilo, S., Pickering, E., Martelli, S., Delisser, P., Meakin, L. B., et al. (2021). Cortical thickness adaptive response to mechanical loading depends on periosteal position and varies linearly with loading magnitude. Front. Bioeng. Biotechnol. 9, 671606. doi: 10.3389/fbioe.2021.671606

Moustafa, A., Sugiyama, T., Prasad, J., Zaman, G., Gross, T. S., Lanyon, L. E., et al. (2012). Mechanical loading-related changes in osteocyte sclerostin expression in mice are more closely associated with the subsequent osteogenic response than the peak strains engendered. Osteoporos. Int. 23, 1225–1234. doi: 10.1007/s00198-011-1656-4

Nepal, A. K., Essen, H. W. van, Jongh, R. T. de, Schoor, N. M. van, Otten, R. H. J., Vanderschueren, D., et al. (2023). Methodological aspects of in vivo axial loading in rodents: a systematic review. J. Musculoskelet. Neuronal Interact. 23, 236. Available at: /pmc/articles/pmc10233220/ (Accessed October 3, 2023).

O'Rourke, D., Beck, B. R., Harding, A. T., Watson, S. L., Pivonka, P., and Martelli, S. (2021). Assessment of femoral neck strength and bone mineral density changes following exercise using 3D-DXA images. J. Biomech. 119, 110315. doi: 10.1016/j.jbiomech.2021.110315

Oliviero, S., Cheong, V. S., Roberts, B. C., Orozco Diaz, C. A., Griffiths, W., Bellantuono, I., et al. (2022). Reproducibility of densitometric and biomechanical assessment of the mouse tibia from in vivo micro-CT images. Front. Endocrinol. (Lausanne). 13, 915938. doi: 10.3389/fendo.2022.915938

Oliviero, S., Giorgi, M., and Dall'Ara, E. (2018). Validation of finite element models of the mouse tibia using digital volume correlation. J. Mech. Behav. Biomed. Mater. 86, 172–184. doi: 10.1016/j.jmbbm.2018.06.022

Oliviero, S., Giorgi, M., Laud, P. J., and Dall'Ara, E. (2019). Effect of repeated in vivo microCT imaging on the properties of the mouse tibia. PLoS One 14, e0225127. doi: 10.1371/journal.pone.0225127

Oliviero, S., Lu, Y., Viceconti, M., and Dall'Ara, E. (2017). Effect of integration time on the morphometric, densitometric and mechanical properties of the mouse tibia. J. Biomech. 65, 203–211. doi: 10.1016/j.jbiomech.2017.10.026

Oliviero, S., Owen, R., Reilly, G. C., Bellantuono, I., and Dall'Ara, E. (2021a). Optimization of the failure criterion in micro-Finite Element models of the mouse tibia for the non-invasive prediction of its failure load in preclinical applications. J. Mech. Behav. Biomed. Mater. 113, 104190. doi: 10.1016/j.jmbbm.2020.104190

Oliviero, S., Roberts, M., Owen, R., Reilly, G. C., Bellantuono, I., and Dall'Ara, E. (2021b). Non-invasive prediction of the mouse tibia mechanical properties from microCT images: comparison between different finite element models. Biomech. Model. Mechanobiol. 20, 941–955. doi: 10.1007/s10237-021-01422-y

Patel, T. K., Brodt, M. D., and Silva, M. J. (2014). Experimental and finite element analysis of strains induced by axial tibial compression in young-adult and old female C57Bl/6 mice. J. Biomech. 47, 451–457. doi: 10.1016/j.jbiomech.2013.10.052

Pereira, A. F., Javaheri, B., Pitsillides, A. A., and Shefelbine, S. J. (2015). Predicting cortical bone adaptation to axial loading in the mouse tibia. J. R. Soc. Interface 12. doi: 10.1098/rsif.2015.0590

Pickering, E., Silva, M. J., Delisser, P., Brodt, M. D., Gu, Y. T., and Pivonka, P. (2021). Estimation of load conditions and strain distribution for in vivo murine tibia compression loading using experimentally informed finite element models. J. Biomech. 115, 110140. doi: 10.1016/j.jbiomech.2020.110140

Prasad, J., Wiater, B. P., Nork, S. E., Bain, S. D., and Gross, T. S. (2010). Characterizing gait induced normal strains in a murine tibia cortical bone defect model. J. Biomech. 43, 2765–2770. doi: 10.1016/j.jbiomech.2010.06.030

Razi, H., Birkhold, A. I., Weinkamer, R., Duda, G. N., Willie, B. M., and Checa, S. (2015a). Aging leads to a dysregulation in mechanically driven bone formation and resorption. J. Bone Miner. Res. 30, 1864–1873. doi: 10.1002/jbmr.2528

Razi, H., Birkhold, A. I., Zaslansky, P., Weinkamer, R., Duda, G. N., Willie, B. M., et al. (2015b). Skeletal maturity leads to a reduction in the strain magnitudes induced within the bone: a murine tibia study. Acta Biomater. 13, 301–310. doi: 10.1016/j.actbio.2014.11.021

Roberts, B. C., Arredondo Carrera, H. M., Zanjani-pour, S., Boudiffa, M., Wang, N., Gartland, A., et al. (2020). PTH(1–34) treatment and/or mechanical loading have different osteogenic effects on the trabecular and cortical bone in the ovariectomized C57BL/6 mouse. Sci. Reports 2020 101 10, 1–16.

doi: 10.1038/s41598-020-65921-1

Roberts, B. C., Cheong, V. S., Oliviero, S., Arredondo Carrera, H. M., Wang, N., Gartland, A., et al. (2023). Combining PTH(1-34) and mechanical loading has increased benefit to tibia bone mechanics in ovariectomised mice. J. Orthop. Res. doi: 10.1002/jor.25777

Roberts, B. C., Giorgi, M., Oliviero, S., Wang, N., Boudiffa, M., and Dall'Ara, E. (2019). The longitudinal effects of ovariectomy on the morphometric, densitometric and mechanical properties in the murine tibia: a comparison between two mouse strains. Bone 127, 260–270. doi: 10.1016/j.bone.2019.06.024

Scheuren, A. C., Vallaster, P., Kuhn, G. A., Paul, G. R., Malhotra, A., Kameo, Y., et al. (2020). Mechano-regulation of trabecular bone adaptation is controlled by the local in vivo environment and logarithmically dependent on loading frequency. Front. Bioeng. Biotechnol. 8, 566346. doi: 10.3389/fbioe.2020.566346/bibtex

Shane, E., Burr, D., Abrahamsen, B., Adler, R. A., Brown, T. D., Cheung, A. M., et al. (2014). Atypical subtrochanteric and diaphyseal femoral fractures: second report of a task force of the American Society for Bone and Mineral Research. J. Bone Miner. Res. 29, 1–23. doi: 10.1002/jbmr.1998

Stadelmann, V. A., Hocke, J., Verhelle, J., Forster, V., Merlini, F., Terrier, A., et al. (2009). 3D strain map of axially loaded mouse tibia: a numerical analysis validated by experimental measurements. Comput. Methods Biomech. Biomed. Engin. 12, 95–96. doi: 10.1080/10255840903077287

Sugiyama, T., Price, J. S., and Lanyon, L. E. (2010). Functional adaptation to mechanical loading in both cortical and cancellous bone is controlled locally and is confined to the loaded bones. Bone 46, 314–321. doi: 10.1016/j.bone.2009.08.054

Viceconti, M., and Dall'Ara, E. (2019). From bed to bench: How in silico medicine can help ageing research. Mech. Ageing Dev. 177, 103–108. doi: 10.1016/j.mad.2018.07.001

Yang, H., Butz, K. D., Duffy, D., Niebur, G. L., Nauman, E. A., and Main, R. P. (2014). Characterization of cancellous and cortical bone strain in the in vivo mouse tibial loading model using microCT-based finite element analysis. Bone 66, 131–139. doi: 10.1016/j.bone.2014.05.019

Yang, H., Embry, R. E., and Main, R. P. (2017). Effects of loading duration and short rest insertion on cancellous and cortical bone adaptation in the mouse tibia. PLoS One 12, e0169519. doi: 10.1371/journal.pone.0169519

Yeam, C. T., Chia, S., Tan, H. C. C., Kwan, Y. H., Fong, W., and Seng, J. J. B. (2018). A systematic review of factors affecting medication adherence among patients with osteoporosis. Osteoporos. Int. 2018 2912 29, 2623–2637. doi: 10.1007/s00198-018-4759-3

Chapter 4: Quantifying the local strain energy density distribution in the mouse tibia: the critical role of the loading direction

This chapter is based on the following manuscript in preparation:

Quantifying the local strain energy density distribution in the mouse tibia: the critical role of the loading direction

Farage-O'Reilly, S.M., Cheong, V.S., Pickering, E., Pivonka, P., Bellantuono, I., Kadirkamanathan, V. and Dall'Ara, E.

To be submitted to Biomechanics and Modeling in Mechanobiology.

The contents of this chapter investigate the effect of the loading direction on the strain energy density (SED) distributions across the mouse tibia, when using the *in vivo* tibial loading model. The study investigates all the 504 different loading directions studied in chapter 3, through the use of micro-CT based micro-FE models. The models were based on two groups of mice: a group which were ovariectomised, to simulate post-menopausal osteoporosis, and a group which underwent mechanical loading after ovariectomy. It was shown that the loading direction changes the SED distribution across the mouse tibia. The highest SED values changed significantly, varying from half to double the amount seen when the load was applied directly along the bone's axis. These high SED values were found across the posterior side and at the distal portion of the tibia. This finding is important as the SED is considered as the main driver of mechanoregulated bone remodelling.

Abstract

Introduction: The *in vivo* tibial loading mouse model has been extensively used to evaluate bone adaptation in the tibia after mechanical loading. However, there is a prevailing assumption that the load is applied axially to the tibia. Mechanoregulated bone remodelling models often utilises strain energy density (SED) as an input parameter to predict bone adaptation, though other mechanical stimuli, such as principal strains can also be used. The aim of this study was to quantify the effect of the loading direction on the SED distribution within the mouse tibia, by using validated micro-FE models of mice which have been ovariectomised and exposed to external mechanical loading over a two-week period.

Methods: Longitudinal micro-computed tomography (micro-CT) images were taken of the tibiae of eleven ovariectomised mice at ages 18 and 20 weeks. Six of the mice underwent mechanical loading treatment at age 19 weeks. Micro-FE models were generated, based on the segmented micro-CT images. Three models using unitary loads were linearly combined to simulate a range of loading directions, generated as a function of the angle from the inferior-superior axis (θ, 0°–30° range, 5° steps) and the angle from the anterior-posterior axis (ϕ, 0°: anterior axis, positive anticlockwise, (inferior-superior view), 0°–355° range, 5° steps). The SED was calculated and the median 95^{th}-100^{th} percentile of the SED was obtained (95P_SED).

Results: The results demonstrated a high sensitivity of the mouse tibia to the loading direction across all groups and time points. Lower values of the 95P_SED were found for several loading directions (θ = 10°, ϕ = 205-210°) than for the nominal axial case (θ = 0°, ϕ = 0°). Higher values of the 95P_SED were found at different loading directions (θ = 30°, ϕ = 35-50°) to the nominal axial case. These results stress the high sensitivity to the loading direction.

Conclusion: These results demonstrate that the loading direction significantly impacts the SED distribution across the mouse tibia. Thus, the magnitude and direction of the applied load should be well controlled during the experiments and taken into account in predictive models of bone adaptation using mechanoregulation theories. For example, the findings suggest that in order to decrease the risk of local micro-damage the value of θ should be kept below 15° and the value of ϕ should be in the range 175° and 245°. Conversely, higher values of θ and specific values of ϕ would lead to high values of local SED that may lead to an increase in mechanoregulated bone formation.

4.1 Introduction

Bone is a constantly changing tissue, adapting to the demands placed upon it. This adaptation is driven by a complex interplay of both biomechanical and biochemical factors (Bonewald, 2011; Martin et al., 2019). One of the key theories explaining the biomechanical influence on bone adaptation is Frost's 'mechanostat' theory (Frost, 2003). This proposes that bone tissue responds and adapts to the level of mechanical strain it experiences. When subjected to appropriate levels of strain, bone responds by initiating a process called mechanoregulated bone remodelling. This adaptation of the bone is undertaken by the bone cells: osteocytes sense the mechanical stimulus, osteoblasts add bone where needed (for values of strain above a remodelling threshold and below bone yield), and osteoclasts remove bone where it is not needed (for values of strain below a certain threshold). Understanding and utilising the principles of this 'mechanostat' theory hold significant potential for promoting bone formation and preventing or treating skeletal diseases such as osteoporosis.

Ovariectomised mice are the most common experimental model for simulating postmenopausal osteoporosis caused by an oestrogen deficiency, which triggers accelerated bone resorption (Bouxsein et al., 2005; Roberts et al., 2019). Investigations into the effect of external mechanical loading on mouse bones (which can induce appropriate strain levels for bone adaptation) using axial loading models have been conducted. This loading model, first introduced by De Souza (2005) for the mouse tibia, has become a widely adopted approach in investigations of bone adaptation. In the past 15 years, it has been utilised in at least 58 studies involving the tibia (Meakin et al., 2014; Nepal et al., 2023). Moreover, this model has been applied to other murine anatomical sites, including the ulna (at least 10 studies) and caudal vertebra (at least 8 studies) (Nepal et al., 2023)). However, the majority of these studies investigate the effect of loading on the morphometric parameters, such as the cortical thickness and trabecular number, or the structural mechanical properties, such as the stiffness and strength of the bone (Nepal et al., 2023). Yet, information on the strain and strain energy density (SED) distributions across the bone can provide useful insights to predict mechanoregulated bone adaptation. These strains can be recorded experimentally through the use of strain gauges in portions of the external surface of the bone (Sugiyama et al., 2008; Moustafa et al., 2009, 2012; Stadelmann et al., 2009; Li et al., 2013; Patel et al., 2014; Yang et al., 2014; Norman et al., 2015; Razi et al., 2015), digital image correlation (DIC) on the external surface of the bone (Carriero et al., 2014; Begonia et al., 2017) and digital volume correlation (DVC) within the bone loaded in a stepwise manner (Giorgi and Dall'Ara, 2018; Oliviero et al., 2018). Strain gauges can be used to measure local strain values of the bone during loading, either *ex vivo* or *in vivo* (although, if done *in vivo*, applications of the strain gauges is extremely invasive). However, they only output strains in limited locations on the bone surface. Additionally, they

have been associated with stiffening effects due to their relative size compared to the mouse bone (Begonia et al., 2017). In comparison, DIC outputs the strain distribution across the surface of the bone. This technique is sensitive to different parameters required for calculating the strain distribution, such as speckle size and density (Carriero et al., 2014). Additionally, due to the nature of the technique, it must be conducted *ex vivo*. DVC offers a more detailed output of the strain distribution, measuring both internal (with higher accuracy) and surface (with lower accuracy) strains. Again, this technique must be carried out *ex vivo.* To mitigate these limitations, *in silico* (computational) models can be used to provide an alternative method for predicting the strains across the internal and surface of the mouse bone under loading (Birkhold et al., 2016; Carriero et al., 2018; Cheong et al., 2020a, 2021a, 2021b).

Micro-computed tomography (micro-CT) based micro-finite element (micro-FE) models allow for the non-invasive prediction of the strain distribution across the mouse bone when externally mechanically loaded (Razi et al., 2014; Yang et al., 2014; Birkhold et al., 2016; Cheong et al., 2021b, 2021a; Roberts et al., 2023). They also allow for an evaluation of the sensitivity of different parameters on the biomechanical properties of the bone, where it was found that the loading direction has a significant impact on the bone's failure load (Farage-O'Reilly et al., 2024); something that could not be achieved with experiments. Nevertheless, to ensure their accuracy and reliability in preclinical settings, these models require validation against experimental data. The displacement and mechanical properties (stiffness and failure load) of the mouse tibia under compression were accurately predicted by hexahedral homogeneous micro-finite element (micro-FE) models, as demonstrated in previous studies (Oliviero et al., 2018, 2021).

These models have been integrated with mechanoregulation algorithms, based on the SED outputs of the micro-FE models, to predict local bone adaptation (Schulte et al., 2013; Levchuk et al., 2014; Pereira et al., 2015; Carriero et al., 2018; Cheong et al., 2020a, 2021a). These models have been applied to investigate the effect of individual and combined treatments for osteoporosis, specifically parathyroid hormone (PTH) and external mechanical loading, applied using the *in vivo* tibial loading model (Cheong et al., 2020b, 2021b). When compared to longitudinal *in vivo* micro-CT images, the models were shown to predict bone formation well (a spatial match of above 59% on both the periosteal and endosteal surfaces) but did not capture resorption well (a spatial match of 47% of the predicted voxels) (Cheong et al., 2020a). Additionally, this model was used to identify the strain energy density (SED) as the most suitable mechanical stimulus for driving that mechanoregulation algorithm. However, this finding, and the overall model outputs, depend on the correctness of the underlying assumptions used to generate the models.

A key assumption commonly made in studies simulating the loading direction experimentally induced by the *in vivo* tibial loading model is that the load is applied axially to the bone. However, the load is applied through the knee and ankle joints, introducing uncertainty to the direction of the force applied to the tibia. Furthermore, as this procedure is repeated several times, repositioning may also have an effect on the local bone strains (Giorgi and Dall'Ara, 2018). Recent research suggests that the loading direction can significantly impact the bone's mechanical properties (Farage-O'Reilly et al., 2024). The predicted failure load ranged from half to double of that of the assumed axial case, depending on the loading direction. Nevertheless, it is still unknown how the loading direction affects the local mechanical properties of the mouse tibia, which would impact the mechanoregulated bone adaptation. Therefore, the aim of this study was to quantify the effect of the loading direction on the SED distribution within the mouse tibia, by using a validated micro-FE model of mice which have been ovariectomised and exposed to external mechanical loading over a two-week period.

4.2 Materials and methods

4.2.1 Experimental *in vivo* data

The same experimental data was used as in Chapter 3. Imaging data was acquired from a previous study by Roberts et al. (2020) where eleven female C57BL/6 mice were ovariectomised at age 14 weeks (Figure 3.1) and the right tibiae of the mice were scanned every other week, from week 14 to 24, using *in vivo* micro-CT (VivaCT80, Scanco Medical Brütisellen, Switzerland). The scanning protocol has been previously defined by Oliviero et al. (2017), to allow for the scanning of the whole bone at a high resolution, with minimal effects of radiation (scanning parameters: 55 kVp, 145 µA, 10.4 µm isotropic voxel size, 32 mm field of view, 100 ms integration time and 1500/750 samples/projections). The images were reconstructed using a third-order polynomial beam hardening correction algorithm based on a 1200 mgHA/cm^3 wedge phantom, which was provided by the manufacturer.

In this study the micro-CT images acquired at weeks 18 and 20 for both for the ovariectomised mice (OVX group, N=5) and for mice ovariectomised and subsequently subjected to external mechanical loading (OVX+ML group, N=6) were used. This external mechanical loading was applied using the *in vivo* tibial loading model, at weeks 19 and 21 (Figure 3.1).

Each right tibia was secured between two soft caps and subjected to a mechanically loading regime. The regime consisted of a peak load of 12 N, comprising of a static preload of 2 N followed by a dynamic load of 10 N. The dynamic load was applied at a high-strain rate of 160,000 N/s (reaching the machines

maximum nominal speed) for 40 cycles per day, repeated three times per week on alternate days (ElectroForce BioDynamics 5100, TA instruments, USA). The applied nominal load was assumed to be along the axial direction of the tibia. This established protocol has been shown to induce adaptations in both cortical and trabecular lamellar bone without inducing micro-damage (De Souza et al., 2005). All the experimental procedures complied with the UK Animals (Scientific Procedures) Act 1986 and were approved by the local Research Ethics Committee of the University of Sheffield.

4.2.2 Image processing and micro-FE models

This study utilises the same validated modelling approach detailed in Chapter 3 (Figure 3.2). The sole modification to the model involves adjusting the boundary conditions: the load magnitude is scaled from 1 N to 12 N to simulate the load used in the *in vivo* tibial loading model (Roberts et al., 2020).

4.2.3 Post processing

The principals of superposition of the effects and scaling were employed during post-processing, due to the linearity of the models (Figure 3.2 F). This allowed for the unitary load models generated in Chapter 3 to be combined to output the SED distributions for the resultant load of 12 N acting within a code of uncertainty (Chapter 3, Equations 1-4, where F = 12 N). This cone was defined in function of the angle from the inferior-superior axis (θ, 0-30° range, 5° steps) and the angle from the anterior-posterior axis (ϕ, 0°: anterior axis, positive anticlockwise (inferior-superior view), 0-355° range, 5° steps) (Figure 3.3).

The frequency plots for the SED values across the tibia were plotted for each loading direction, for 10-90% of the cropped tibial length (to exclude any effects due to the boundary conditions) (Figure 4.1). Based on the mechanostat theory, bone formation is anticipated in response to the higher range of SED values experienced by the tibia, in particular in the OVX+ML group, as due to the mechanical loading these values are likely to exceed the bone formation threshold (Frost, 2003; Cheong et al., 2021b). Therefore, the median of the 95th-100th percentiles of the SED (95P_SED, MPa) were investigated further. This approach was used to evaluate the highest level of SED for each model, removing isolated SED peaks in the distributions which are likely artifacts of local stress-strain concentrations. These concentrations may be due to local issues with the geometry or mesh. The 95P_SED was calculated as the median of the top 5% SED values for each mouse at each loading direction, to consider all the points without being dependent on the peaks. (Note that this is not equivalent to the 97.5th percentile due to the non-symmetric distribution of the data.) These medians were then averaged across mice within each group and time point to obtain the group-level 95P_SED. To enable comparison across loading directions, the 95P_SED for each loading direction was

normalised (N95P_SED, %) by the 95P_SED calculated for the nominal axial loading direction (ϑ = 0°, ϕ = 0°) for each mouse at each time point (Eq. 4.1).

$$N95P\_SED^{\theta,\phi} = \frac{95P\_SED^{\theta,\phi} - 95P\_SED^{0,0}}{95P\_SED^{0,0}} \times 100 \quad (4.1)$$

where, $N95P\_SED^{\theta,\phi}$ is the normalised median of the 95th-100th percentiles of the SED at the loading direction defined by ϑ and ϕ, with respect to the nominal axial case, $95P\_SED^{\theta,\phi}$ is the median of the 95th-100th percentiles of the SED at the loading direction defined by ϑ and ϕ, and $95P\_SED^{0,0}$ is the median of the 95th-100th percentiles of the SED of the nominal axial case. Note: If a loading direction has a positive N95P_SED then the 95P_SED of that loading direction is higher than the nominal axial case, and a negative N95P_SED refers to a 95P_SED which is lower than the nominal axial case.

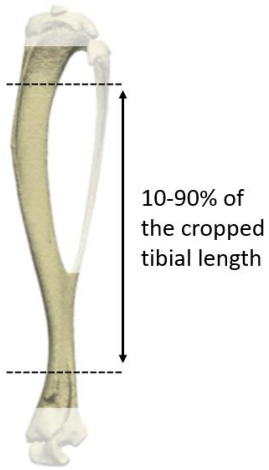

Figure 4.1: *Location of the region comprising 10-90% of the cropped tibial length.*

To evaluate the effect of the time point (week 18 vs week 20), and of the group (OVX vs OVX+ML), the following quantities were calculated for all loading directions (θ in range 0-30°, ϕ in range 0-355°): the absolute difference in the 95P_SED (absΔ95t_SED, MPa) between the time points (week 18 vs week 20) for OVX and OVX+ML groups, percentage differences in the 95P_SED (Δ95Pt_SED, %) between time points (week 18 vs week 20) for OVX and OVX+ML groups, and the percentage point difference from week 18 to 20 calculated between the two groups (OVX vs OVX+ML) (Δ95Pg_SED, %pt).

4.2.4 Statistical analysis

The mean, standard deviation (SD) and coefficient of variation (CV) of the 95P_SED was calculated for the nominal axial loading direction for each group of mice, at each time point.

Non-parametric tests were chosen due to the results not being normally distributed (Shapiro-Wilks test) and the small sample size. The effect of the loading direction on the 95P_SED between time points (Δ95Pt_SED) was assessed independently, using the non-parametric two-tailed Wilcoxon test. The effect of the loading direction on the 95P_SED between groups (Δ95Pg_SED) was assessed using the non-parametric two-tailed Mann-Whitney U test, as was the comparison between the nominal axial loading direction and every other loading direction (N95P_SED). The statistical significance level was set at $\alpha = 0.05$ for all tests.

4.3 Results

In total, 504 loading directions were evaluated for each mouse in both mouse groups (OVX and OVX+ML) and for the two time points (week 18 and week 20).

When comparing between loading directions, large variation in the SED distribution across the mouse tibia were observed. As θ increased (i.e., as the angle from the inferior-superior axis increased), the SED distribution deviated from the nominal axial case: the SED consistently increased, for all values of ϕ (Figure 4.2). This was a consistent trend across all groups and time points. However, the change in SED distribution fluctuated as ϕ increased (Figure 4.3). This fluctuation was dependent on the specific loading direction, with the lowest SED fluctuation observed at loading directions associated with $\phi = 45°$ and the largest SED fluctuation observed at loading directions associated with $\phi = 135°$. The SED distribution for the loading directions applied in the anterior-posterior ($\phi = 0°$) and medial-lateral ($\phi = 90°$) directions were similar and were distributed between the range of those applied at $\phi = 45°$ and $\phi = 135°$. This pattern was consistent across groups and time points.

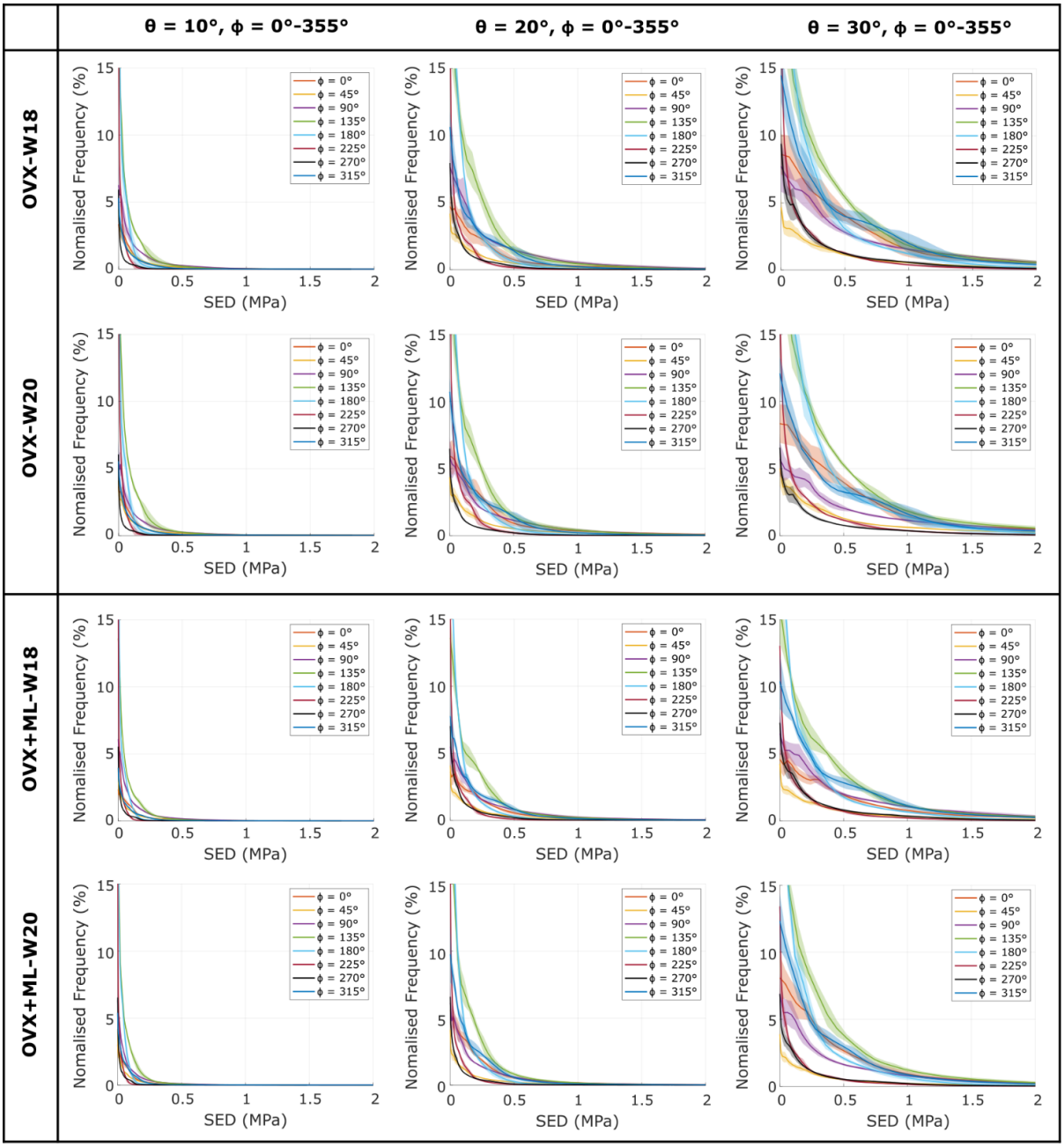

Figure 4.2: *The frequency plots for strain energy density (SED; mean ± standard deviation) between 0-2 MPa, for the loading directions associated with ϑ = 10°, 20°, 30° and ϕ = 0-355°, for both groups at both time points. OVX, ovariectomy; OVX+ML, ovariectomy and mechanical loading; W18, week 18; W20, week 20.*

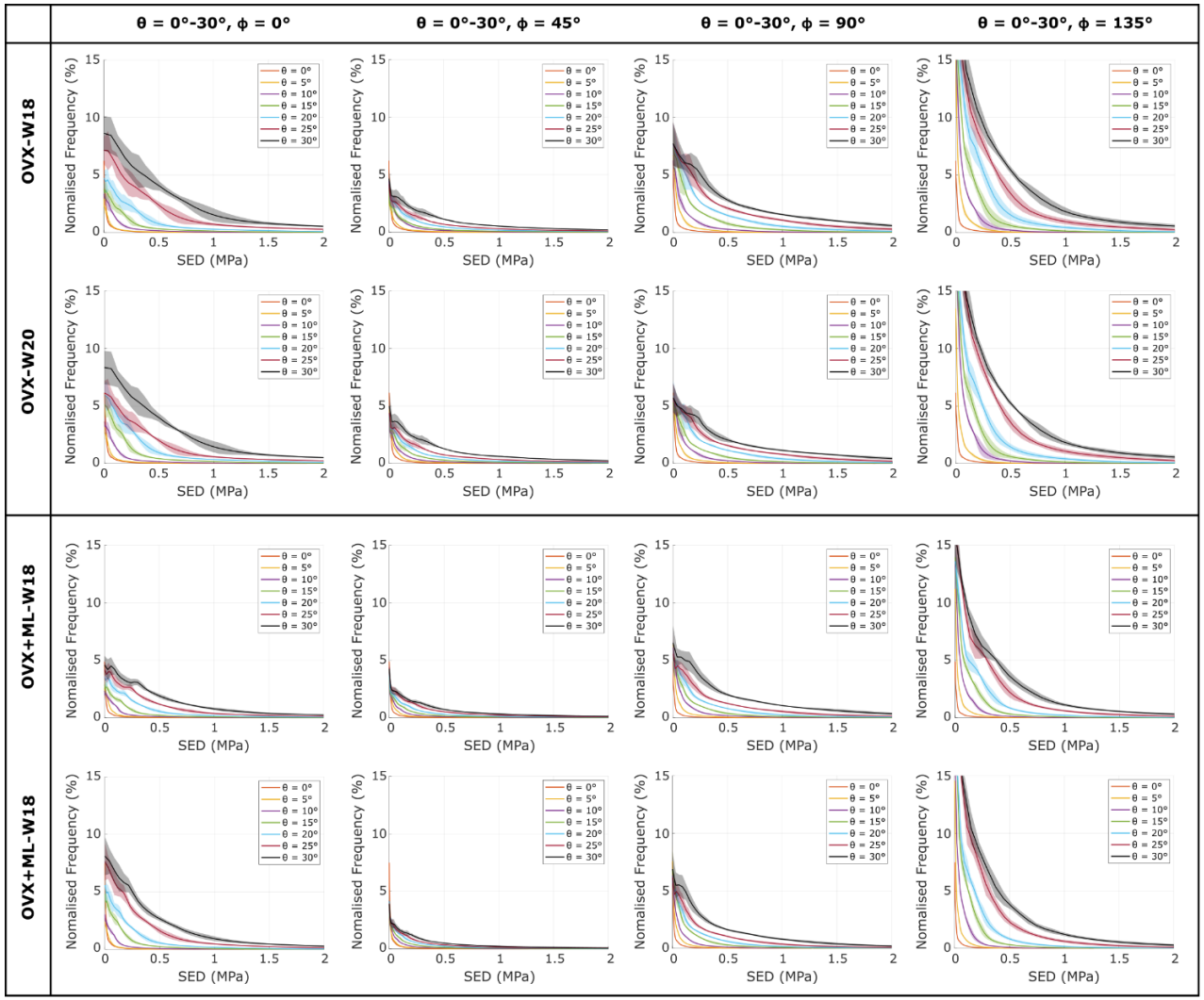

Figure 4.3: *The frequency plots for strain energy density (SED; mean ± standard deviation) between 0-2 MPa, for the loading directions associated with ϑ = 0-30° and ϕ = 0°, 45°, 90°, 135°, for both groups at both time points. OVX, ovariectomy; OVX+ML, ovariectomy and mechanical loading; W18, week 18; W20, week 20.*

The largest changes in the SED distribution were found for loading directions θ = 0-30°, ϕ = 135° and θ = 30°, ϕ = 0-355° (Figure 4.4). The change in the distributions for both sets of loading directions (a change in θ compared to a change in ϕ) were similar: the SED was sensitive to both θ and ϕ in their considered ranges (θ = 0-30° and ϕ = 0-355°). Again, this pattern was consistent across groups and time points.

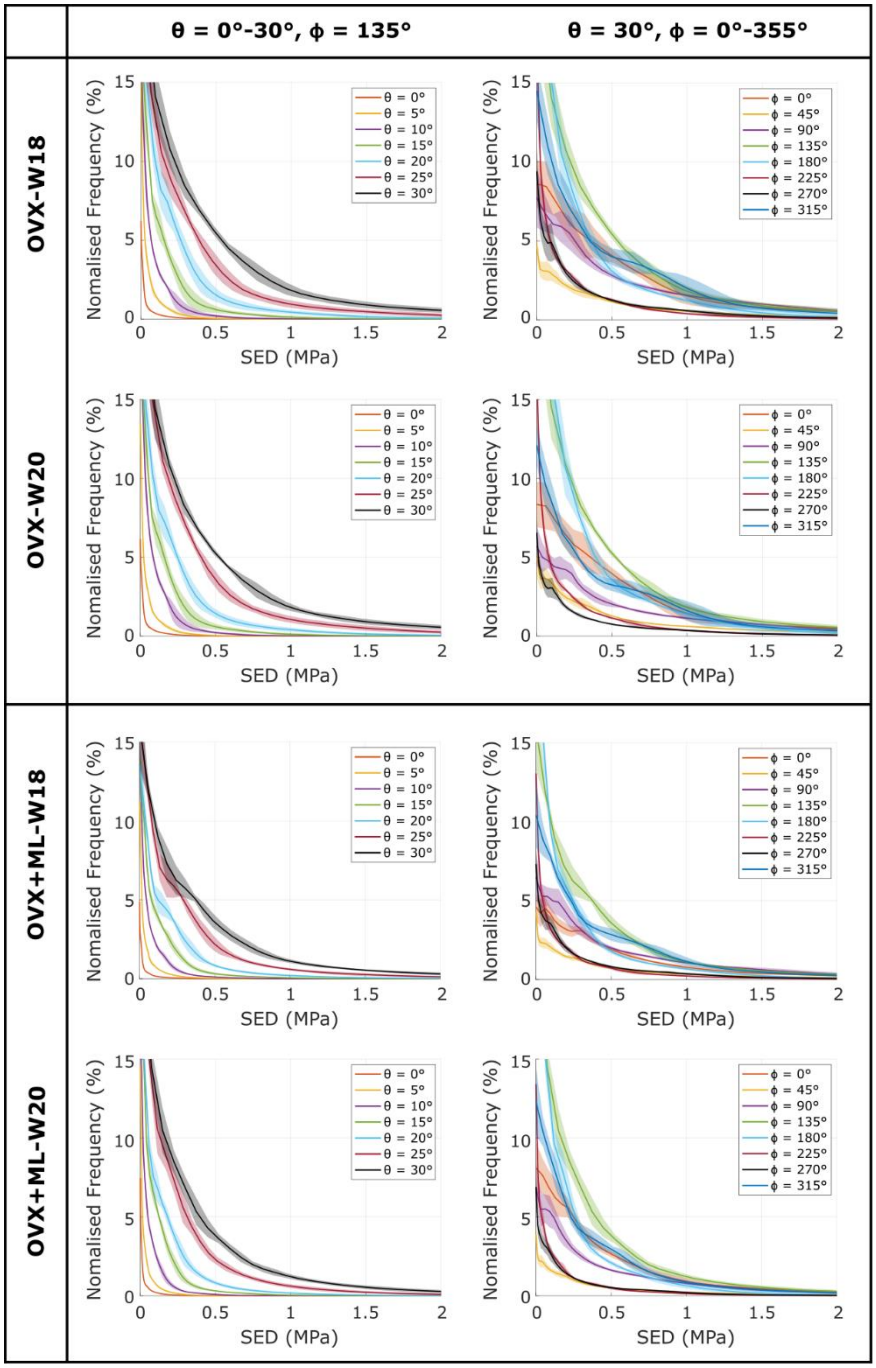

Figure 4.4: *The frequency plots for strain energy density (SED; mean ± standard deviation) between 0-2 MPa, for the loading directions associated with the largest changes in distribution (ϑ = 0-30° and ϕ = 135°; ϑ = 30° and ϕ = 0-355°) compared to the nominal axial case, for both groups at both time points. OVX, ovariectomy; OVX+ML, ovariectomy and mechanical loading; W18, week 18; W20, week 20.*

The minimum and maximum values of the median of the 95th-100th percentiles of the SED (95P_SED) were calculated, and their associated loading directions are reported in Table 4.1. The minimum

95P_SED (Figure 4.5, highlighted by the blue arrow) was found at θ = 10°, ϕ = 205° for the both the OVX and OVX+ML groups at both time points. The maximum 95P_SED (Figure 4.5, highlighted by the yellow arrow) was found at θ = 30°, ϕ = 40° for the OVX group at both time points and at θ = 30°, ϕ = 45° for the OVX+ML group at both time points. The 95P_SED ranged from 0.08-4.79 MPa for the OVX-W18 group, 0.08-4.70 MPa for the OVX-W20 group, 0.07-4.44 MPa for the OVX+ML-W18 group, 0.06-3.52 MPa for the OVX+ML-W20 group. All the groups and time points show similar patterns. However, OVX+ML-W20 exhibited a lower 95P_SED compared to the other groups and time points. The CV ranged from 10.00-21.78% for the OVX-W18 group, from 9.03-18.79% for the OVX-W20 group, from 4.44-11.34% for the OVX+ML-W18 group, and from 5.41-11.18% for the OVX+ML-W20 group. There was greater variation in the OVX group compared to the OVX+ML group. Furthermore, week 20 had marginally lower variability than week 18.

	Loading direction for minimum 95P_SED (θ, range of ϕ) [°]	Minimum 95P_SED (mean ± SD) [MPa]	Loading direction for maximum 95P_SED (θ, range of ϕ) [°]	Maximum 95P_SED (mean ± SD) [MPa]
OVX-W18	10, 205	0.08 ± 0.02	30, 35-45	4.79 ± 0.60
OVX-W20	10, 205	0.08 ± 0.02	30, 35-45	4.70 ± 0.50
OVX+ML-W18	10, 205-210	0.07 ± 0.01	30, 40-50	4.44 ± 0.30
OVX+ML-W20	10, 205-210	0.06 ± 0.01	30, 45-50	3.52 ± 0.31

Table 4.1: *For both groups and time points: the loading directions associated with the minimum (ϑ = 10°, ϕ = 205-210°) and maximum (ϑ = 30°, ϕ = 35-50°) median 95th-100th percentile of the SED (95P_SED), and the corresponding mean ± standard deviation (SD). It should be noted that at W18 both groups were untreated, so observed differences are associated mainly with different animals (the differences between OVX-W18 and OVX+ML-W18 for the maximum and minimum 95P_SED are both not significant (p > 0.05). OVX, ovariectomy; OVX+ML, ovariectomy and mechanical loading; W18, week 18; W20, week 20.*

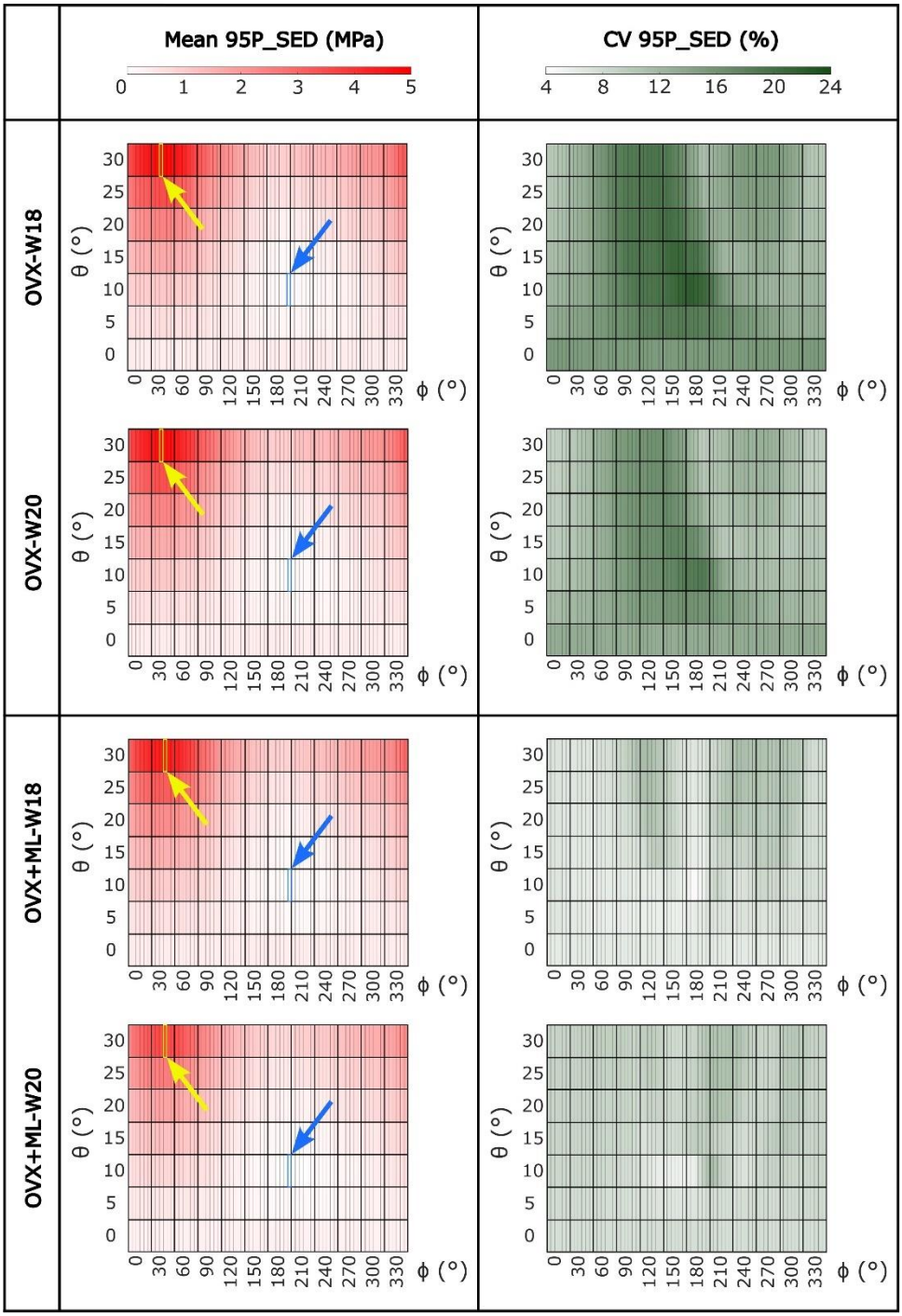

Figure 4.5: *Heatmaps of the mean values of the median 95th-100th percentile of the SED (95P_SED) and the coefficient of variation (CV) across all loading directions (ϑ in range 0-30°, ϕ in range 0-355°) for both groups (OVX and OVX+ML) and time points (W18 and W20). The blue square and arrow highlight the loading direction for which the minimum 95P_SED was found, and the yellow square and arrow highlight the loading direction for which the maximum 95P_SED was found. OVX, ovariectomy; OVX+ML, ovariectomy and mechanical loading; W18, week 18; W20, week 20.*

The 95P_SED normalised for each loading direction (N95P_SED) ranged from half to double of that of the nominal axial case (Figure 4.6). Similar trends were found to the 95P_SED: the maximum N95P_SED was at θ = 10°, ϕ = 205° for all groups and time points. The minimum N95P_SED was at the loading direction θ = 30°, ϕ = 40° for the OVX group and at θ = 30°, ϕ = 45° for the OVX+ML group. For all groups and time points, loading directions less than θ = 15° and ϕ = 175-245°, a reduction in the N95P_SED was found compared to the nominal axial case.

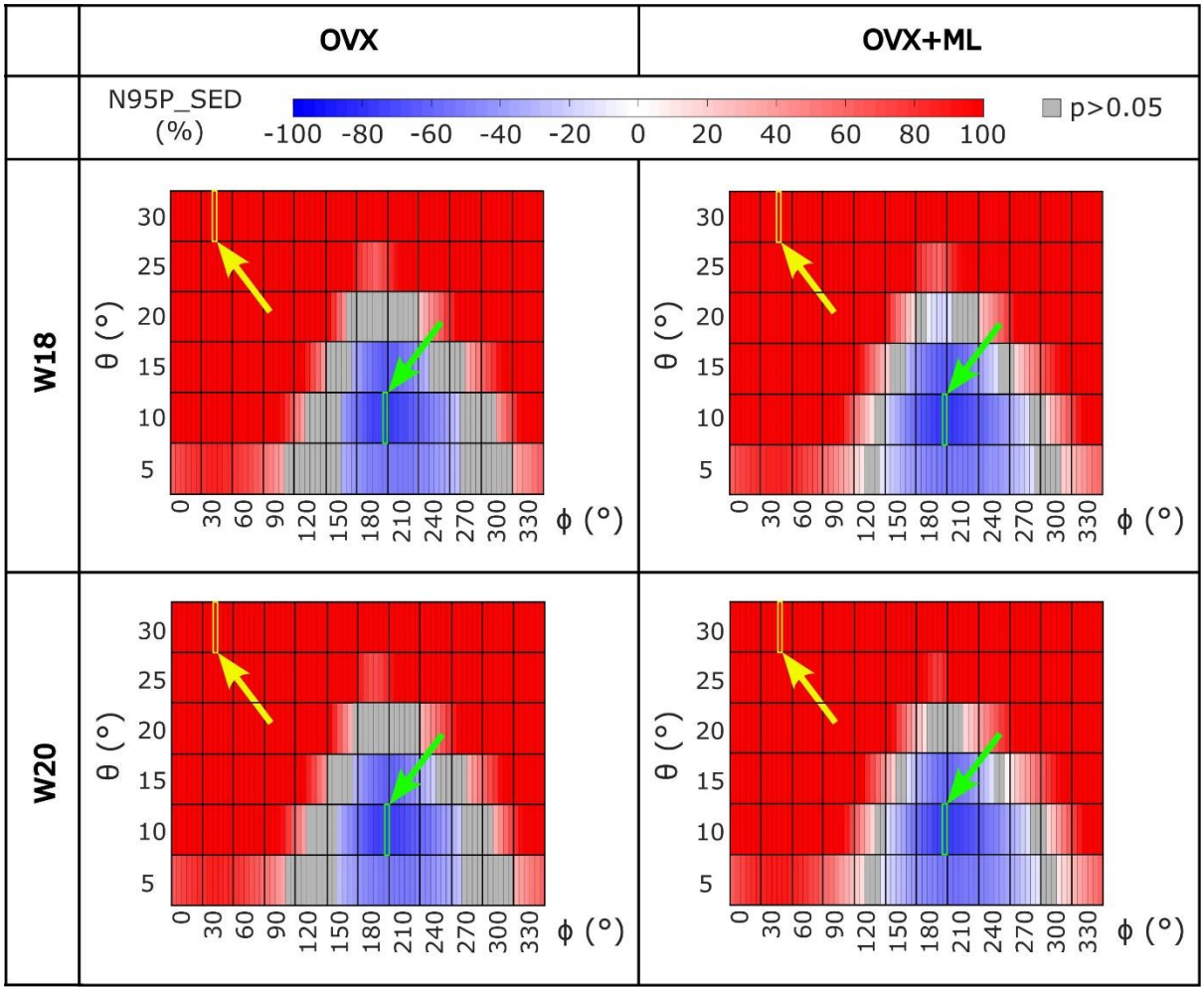

Figure 4.6: *Heatmaps of the normalised median 95th-100th percentile of the SED (N95P_SED) across all loading directions (ϑ in range 5-30°, ϕ in range 0-355°) for both groups (OVX and OVX+ML) and time points (W18 and W20). The values in grey show the loading directions associated with a 95P_SED to be not significantly different to the 95P_SED obtained for the nominal axial loading direction. The green square and arrow highlight the loading direction for which the minimum N95P_SED was found, and the yellow square and arrow highlight the loading direction for which the maximum 95P_SED was found. OVX, ovariectomy; OVX+ML, ovariectomy and mechanical loading; W18, week 18; W20, week 20.*

Typical distributions of the SED obtained for loads along the nominal axial loading direction (θ = 0°, ϕ = 0°), and in the direction associated with the maximum and the minimum 95P_SED, are reported in Figure 4.7. The loading direction associated with the minimum 95P_SED (θ = 10°, ϕ = 205°) had a higher frequency of values close to 0 MPa compared to the nominal axial case (Figure 4.7 Minimum 95P_SED case). This was confirmed by the SED frequency plots (Figure 4.8). Similarly, the loading directions associated with the maximum 95P_SED (θ = 30°, ϕ = 40-45°) had higher SED values compared to the nominal axial case (Figure 4.7 Maximum 95P_SED case). This was also confirmed by the SED frequency plots, which show a higher frequency of larger SED values than the nominal axial case (Figure 4.8). For the nominal axial loading direction, high values of the SED were found mainly in the distal portion of the tibia and across the posterior side of the tibia. These SED values were higher in the maximum 95P_SED case and lower in the minimum 95P_SED case. Lower SED values were found at the anterior crest for all groups and time points. However, the anterior crest SED was increased in the maximum 95P_SED case, compared to the nominal axial case. High SED values were found proximally to the distal tibiofibular junction in the posterior portion of the bone, across all groups and time points. As expected, small differences were found for models at week 18 between the two groups (both groups untreated), and larger differences induced by the mechanical loading could be observed at week 20.

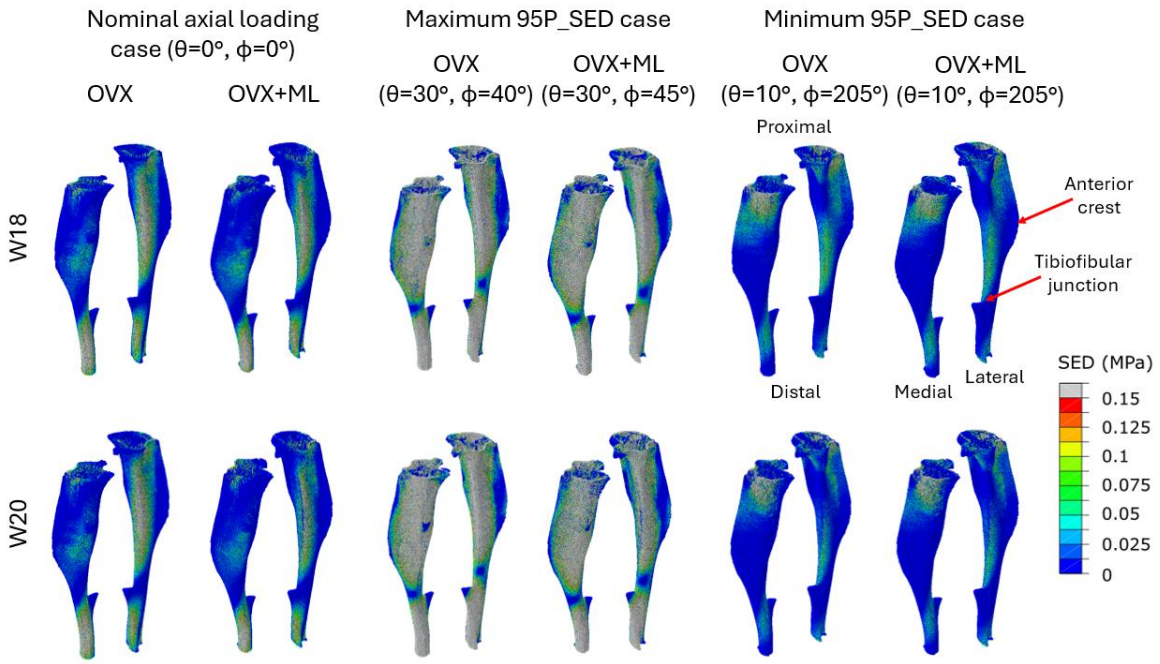

Figure 4.7: *Strain energy density (SED) distributions of two representative tibiae (OVX–mouse 2, OVX+ML–mouse 5) obtained using a load of magnitude 12 N at W18 and W20. It should be noted that at W18 both groups were untreated, so observed differences are associated mainly with different animals. Left: Load applied along the nominal axial loading direction (ϑ = 0°, ϕ = 0°). Middle: Load applied along the loading directions associated with the maximum median 95th-100th percentile of the SED (95P_SED) (ϑ = 30°, ϕ = 40-45°). Right: Load applied along the loading direction associated with the minimum 95P_SED (ϑ = 10°, ϕ = 205°). OVX, ovariectomy; OVX+ML, ovariectomy and mechanical loading; W18, week 18; W20, week 20.*

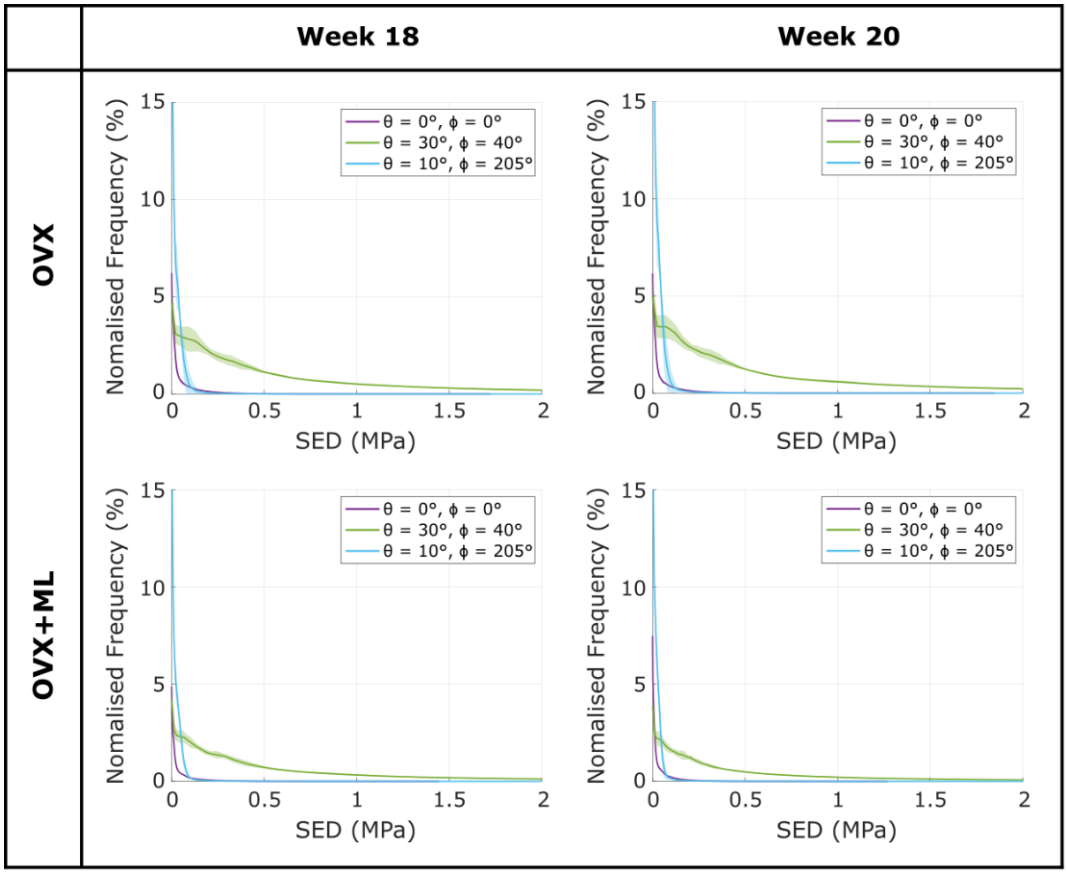

Figure 4.8: *The frequency plots for strain energy density (SED; mean ± standard deviation) between 0-2 MPa, for the loading directions associated with the minimum median 95th-100th percentile of the SED (ϑ = 10°, ϕ = 205°), the maximum median 95th-100th percentile of the SED (ϑ = 30°, ϕ = 40-45°), and the nominal axial case (ϑ = 0°, ϕ = 0°), for both groups at both time points. OVX, ovariectomy; OVX+ML, ovariectomy and mechanical loading; W18, week 18; W20, week 20.*

For the OVX group, the 95P_SED between weeks 18 and 20, both absolute difference and percentage difference (absΔ95t_SED and Δ95t_SED, respectively) were not significantly different for any loading direction (maximum absolute difference 0.12 MPa (Figure 4.9), maximum absolute percentage difference 4.24% (Figure 4.10), $p > 0.05$). For the OVX+ML group, the 95P_SED decreased significantly between weeks 18 and 20 for majority of the loading directions, not including the nominal axial case. The range of the OVX+ML absΔ95t_SED was between -0.92 MPa (θ = 30°, ϕ = 40°) and -0.01 MPa (θ = 15°, ϕ = 210°). While the Δ95t_SED range was between -25.62% (θ = 5°, ϕ = 245°) and -9.81% (θ = 15°, ϕ = 195°) (Figure 4.10). Percentage point differences between Δ95t_SED for the OVX and the OVX+ML groups were significant for every loading direction ($p < 0.030$), with Δ95g_SED ranging between -22.46% (θ = 5°, ϕ = 255°) and -10.83% (θ = 15°, ϕ = 190°) (Figure 4.10).

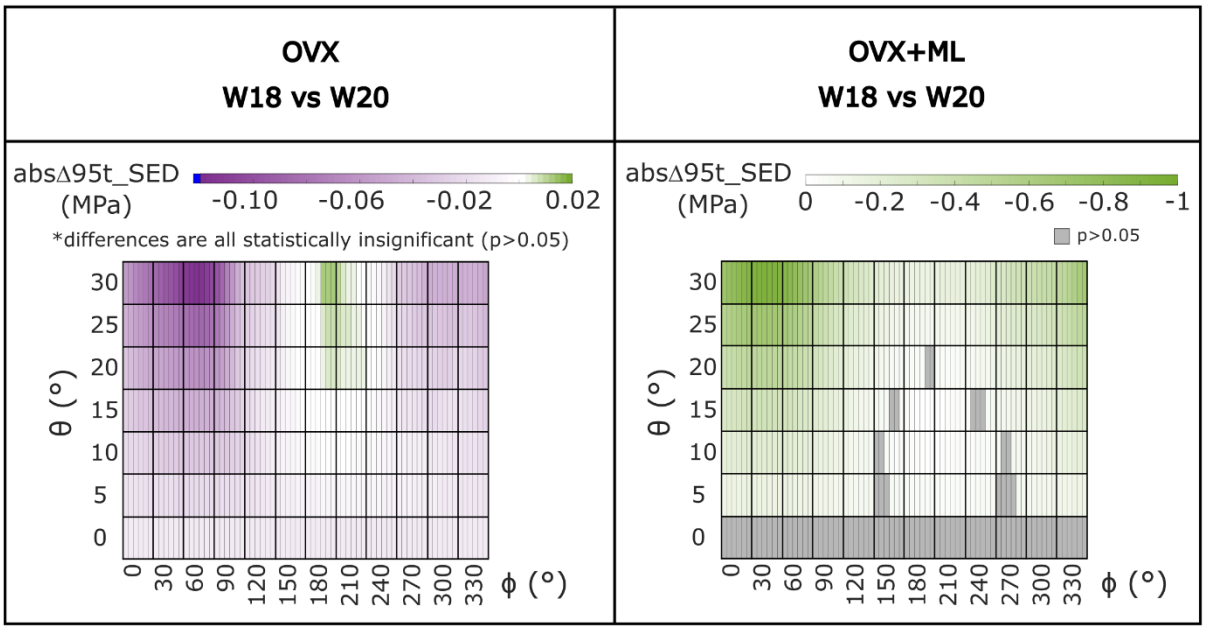

Figure 4.9: *Left: Heatmap of the absolute difference in mean 95P_SED (absΔ95t_SED) between time points (W18 vs W20) for OVX group for all loading directions (ϑ in range 0-30°, ϕ in range 0- 355°). Differences are all statistically insignificant (Wilcoxon test, p < 0.05). Right: Heatmap of absΔ95t_SED for the OVX+ML group for all loading directions. The values in grey show the loading directions associated with non-significant differences between time points (Wilcoxon test, α = 0.05). OVX – ovariectomy, OVX+ML – ovariectomy and mechanical loading, W18 – week 18, W20 – week 20.*

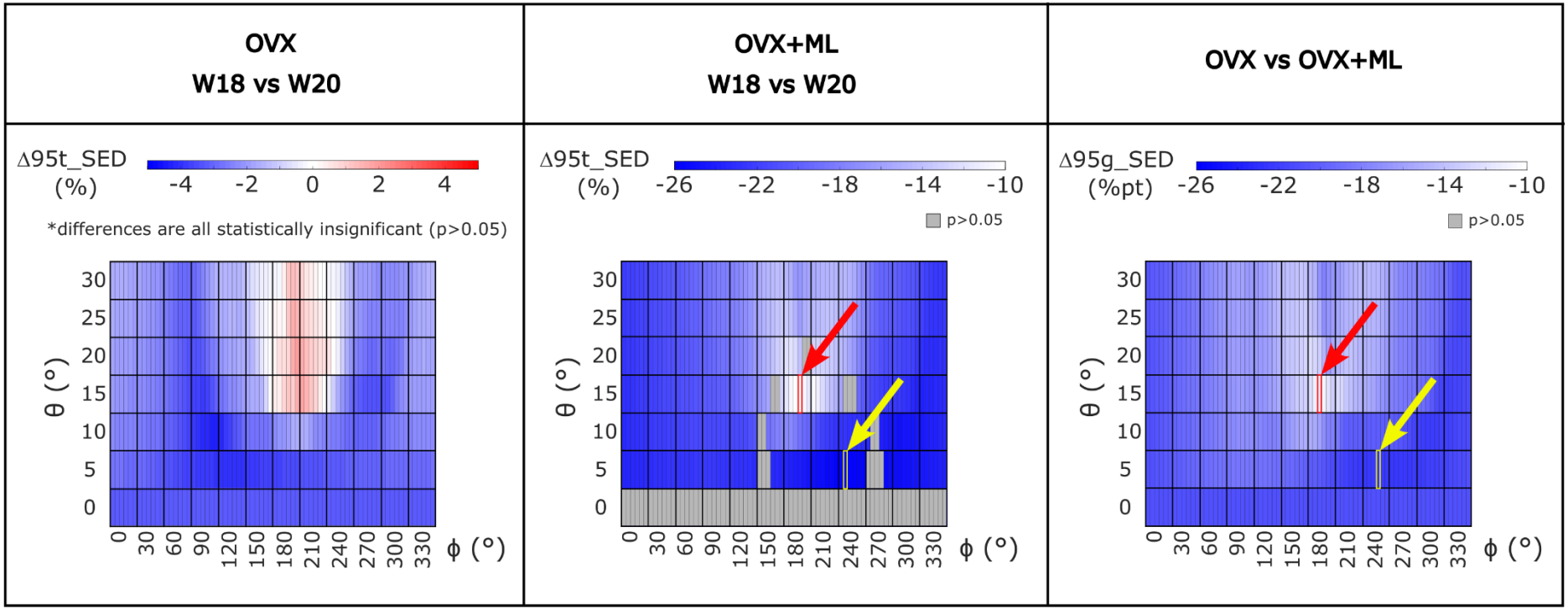

Figure 4.10: *Left: Heatmap of the percentage difference in the median 95th-100th percentile of the SED (Δ95t_SED) between time points (W18 vs W20) for the OVX group for all loading directions (ϑ in range 0-30°, ϕ in range 0-355°). Differences are all statistically insignificant (Wilcoxon test, α = 0.05). Middle: Heatmaps of (Δ95t_SED) between time points (W18 vs W20) for the OVX+ML group for all loading directions. The values in grey show the loading directions associated with non-significant differences between time points (Wilcoxon test, α = 0.05). Right: Heatmaps of the percentage point differences in Δ95t_SED for the OVX and OVX+ML groups (Δ95g_SED) for all loading directions. Differences are all statistically significant (Mann-Whitney U test, α = 0.05). The red square and arrow highlight the loading direction for which the smallest difference was found, and the yellow square and arrow highlight the loading direction for which the largest difference was found. OVX, ovariectomy; OVX+ML, ovariectomy and mechanical loading; W18, week 18; W20, week 20.*

4.4 Discussion

The purpose of this study was to quantify the effect of the loading direction on the SED distribution within the mouse tibia after applying external mechanical loading. Using validated micro-CT based micro-FE models, the SED distributions across the tibiae were calculated for different loading directions.

The frequency plots showed that the SED experienced by the bone is sensitive to both a change in the load direction in the inferior-superior direction (defined by θ) and a change in the load direction in the anterior-posterior and medial-lateral directions (defined by ϕ). The loads investigated fell within a cone of uncertainty centred at the assumed nominal axial loading direction (θ = 0°, ϕ = 0°; θ ranged from 0-30° and ϕ from 0-355°, where the foot would be oriented along ϕ = 0°). As θ increased, larger transverse loads were applied to the model, resulting in an increase of higher SED values compared to the nominal axial case. The difference caused by a change in ϕ determined the direction of the transverse load. Inclusion of the fibula in the model is expected to result in lower SED values for loading directions which have larger transverse load components, as suggested by Yang et al. (2014). However, further investigation is needed to quantify the extent to which the fibula contributes to mitigating high tibial SED values.

The SED distributions across the tibiae for the nominal axial case were in line with those from a previous study, which applied the same load magnitude (Cheong et al., 2021a). Furthermore, similar SED distributions were found to those in another study, which applied physiological loads to the tibia (linearly scaling the SED values results in a comparable range for the nominal axial case) (Cheong et al., 2020b). Additionally, the high SED values, found proximally to the distal tibiofibular junction, in the posterior portion of the bone for all groups and time points, are consistent with reported experimental bone formation after mechanical loading (Sugiyama et al., 2012; Roberts et al., 2020). Furthermore, formation was predicted in this location by a mechanoregulation model (Cheong et al., 2020b). As expected, the values of the maximum 95P_SED for the different loading directions showed that the bone experiences higher SED values when loaded in the direction occurring at θ equal to 30° and ϕ equal to 35-50°. Employing the principles of the ‘mechanostat’ theory, these results suggest that the bone may undergo more formation if loaded at in this direction compared to the nominal axial case (Frost, 2003). Higher strains are associated with increased woven bone formation (Sugiyama et al., 2012). However, as the bone experiences higher SED values, it is also more likely to fracture when loaded in this direction, compared to the nominal axial case. This is in line with a recent study performed within the group, which showed that the failure load of the mouse tibia was lowest for a load in the direction occurring at θ equal to 30° and ϕ equal to 30-50° (Farage-O’Reilly et al., 2024). The loading directions corresponding to the maximum SED values fall within this range. Therefore,

although loading directions associated with θ equal to 30° and ϕ equal to 30-50° may induce more bone formation, it is not advised to load the bone in this direction due to the predicted failure load, or if the bone does not yield, the induction of micro-damage.

Conversely, the loading directions associated with the minimum 95P_SED occur when θ equal to 10° and ϕ equal to 205-210°. These results are in line with the previously mentioned study, which showed that the loading direction associated with the lowest failure load was also θ equal to 10° and ϕ equal to 205-210° (Farage-O'Reilly et al., 2024). Due to this reduction in high SED values, it could be assumed that less mechanoregulated bone formation could be occurring if loaded in this direction compared to the nominal axial case. This could be because the bone is optimised for this loading direction: given that the fibula's typical orientation is at a ϕ angle ranging from 170° to 220°. The standard deviations for each loading direction between 0-2 MPa are low for every loading direction. This highlights the reproducibility of the results and could suggest a good registration between tibiae, although does not guarantee it. Poor registration would likely result in greater variation in results due to misalignment of the loading directions. However, the coefficient of variation for the 95P_SED ranges from 4.44% to 21.78% across the groups and time points. This suggests that the larger SED values experienced by each mouse across the loading directions varied. This could be due to the individual geometries and micro-structures of each mouse.

The mouse tibia has been shown to be very sensitive to the loading direction, with some loading directions resulting in a 95P_SED ranging from half to double of that of the nominal axial case. This is in line with the previous study, which showed the inverse results for the failure load (Farage-O'Reilly et al., 2024). Furthermore, these results expand on those of a previous study, which showed that a small increase in the transverse loading direction affects the local deformation and SED (Cheong et al., 2021a). Similar concerns regarding loading direction have been identified in previous studies, including a repositioning investigation for the *in vivo* tibial model (Giorgi and Dall'Ara, 2018) and a misalignment study for the rodent tail loading model (Goff et al., 2014). It has been suggested that the loading direction could be controlled through the use of a tri-axial load cell during the loading procedure, or through the use of mouse-specific 3D printed loading caps (Meakin et al., 2014; Main et al., 2020; Farage-O'Reilly et al., 2024). Controlling well the variability of the loading direction could improve predictions of bone adaptation when using mechanoregulation models, as it would limit the transference of errors in the strain distributions being carried forward though the model pipeline (Pereira et al., 2015b; Cheong et al., 2020b, 2021b).

When comparing the 95P_SED between time points, the OVX group showed no statistically significant differences for all loading directions. This is corroborated by Farage-O'Reilly et al. (2024), where it was

shown that the failure load for the OVX group between week 18 and 20 were not statistically different for all the loading directions (an extension on a study by Roberts et at. (2019), who showed no change in the failure load between weeks 18 and 20 for the assumed nominal axial case for the OVX group). In contrast, the OVX+ML group showed a statistically significant difference in the 95P_SED between the time points for most loading directions (a decrease between 9.81 % and 25.62%). Surprisingly, no significant difference was found for the nominal axial case. When comparing the differences between the groups, no significant difference was found at week 18. However, when comparing the groups across time points, a statistically significant decrease was found for all loading directions (a decrease between 10.83% and 22.46%). These results suggest that the external mechanical loading changed the morphometric and densitometric properties of the bone, as previously reported by Roberts et al. (2020). Interestingly, the direction of the optimal load exhibited minimal variation (within 5°) across groups and time points (Figure 4.5). However, the absolute difference in the 95P_SED between weeks 18 and 20 (Figure 4.9) suggests that this improvement is heterogeneous across loading directions. This suggests a relatively uniform increase in the 95P_SED throughout the tibia regardless of loading direction during mechanical loading.

This study is limited by the removal of the fibula from the model. An increase in θ, increases the transverse load applied to the tibia. These loads would in part be shared with the fibula (Prasad et al., 2010; Cheong et al., 2021a). However, the tibiofibular joint properties are currently unknown, introducing additional assumptions to the modelling pipeline. Similarly, the growth plate has been removed from the model, as including this would introduce additional assumptions of the unknown growth plate material properties. Instead, it was assumed that the load is uniformly applied to the proximal slice of the model. However, it has recently been found that the strains in the tibia are highly sensitive to the load location (a study done using micro-FE models and strain gauges, to inversely identify the location of the load applied) (Pickering et al., 2021). Therefore, it would be of value to model a range of loading applications in future iterations of the model. This could allow for a more accurate assessment of load distribution and its influence on the SED experienced by the bone.

In conclusion, this study has highlighted the importance of the loading direction on the SED distributions across the mouse tibia. The results of this study will be important to minimise errors carried forward in multiscale models of mechanoregulated bone adaptation, potentially increasing the accuracy of such models.

4.5 References

Begonia, M., Dallas, M., Johnson, M. L., and Thiagarajan, G. (2017). comparison of strain measurement in the mouse forearm using subject specific finite element models, strain gaging, and digital image correlation. Biomech. Model. Mechanobiol. 16, 1243. doi: 10.1007/s10237-017-0885-7

Birkhold, A. I., Razi, H., Duda, G. N., Weinkamer, R., Checa, S., and Willie, B. M. (2016). The periosteal bone surface is less mechano-responsive than the endocortical. Sci. Reports 2016 61 6, 1–11. doi: 10.1038/srep23480

Bonewald, L. F. (2011). The amazing osteocyte. J. Bone Miner. Res. 26, 229–238. doi: 10.1002/jbmr.320

Bouxsein, M. L., Myers, K. S., Shultz, K. L., Donahue, L. R., Rosen, C. J., and Beamer, W. G. (2005). Ovariectomy-induced bone loss varies among inbred strains of mice. J. Bone Miner. Res. 20, 1085–1092. doi: 10.1359/jbmr.050307

Carriero, A., Abela, L., Pitsillides, A. A., and Shefelbine, S. J. (2014). Ex vivo determination of bone tissue strains for an in vivo mouse tibial loading model. J. Biomech. 47, 2490–2497. doi: 10.1016/j.jbiomech.2014.03.035

Carriero, A., Pereira, A. F., Wilson, A. J., Castagno, S., Javaheri, B., Pitsillides, A. A., et al. (2018). Spatial relationship between bone formation and mechanical stimulus within cortical bone: Combining 3D fluorochrome mapping and poroelastic finite element modelling. Bone Reports 8, 72. doi: 10.1016/j.bonr.2018.02.003

Cheong, V. S., Campos Marin, A., Lacroix, D., and Dall'Ara, E. (2020a). A novel algorithm to predict bone changes in the mouse tibia properties under physiological conditions. Biomech. Model. Mechanobiol. 19, 985–1001. doi: 10.1007/s10237-019-01266-7

Cheong, V. S., Kadirkamanathan, V., and Dall'Ara, E. (2021a). The role of the loading condition in predictions of bone adaptation in a mouse tibial loading model. Front. Bioeng. Biotechnol. 9, 676867. doi: 10.3389/fbioe.2021.676867

Cheong, V. S., Roberts, B. C., Kadirkamanathan, V., and Dall'Ara, E. (2020b). Bone remodelling in the mouse tibia is spatio-temporally modulated by oestrogen deficiency and external mechanical loading: A combined in vivo/in silico study. Acta Biomater. 116, 302–317. doi: 10.1016/j.actbio.2020.09.011

Cheong, V. S., Roberts, B. C., Kadirkamanathan, V., and Dall'Ara, E. (2021b). Positive interactions of mechanical loading and PTH treatments on spatio-temporal bone remodelling. Acta Biomater. 136, 291–305. doi: 10.1016/j.actbio.2021.09.035

De Souza, R. L., Matsuura, M., Eckstein, F., Rawlinson, S. C. F., Lanyon, L. E., and Pitsillides, A. A. (2005). Non-invasive axial loading of mouse tibiae increases cortical bone formation and modifies trabecular organization: a new model to study cortical and cancellous compartments in a single loaded element. Bone 37, 810–818. doi: 10.1016/j.bone.2005.07.022

Farage-O'Reilly, S. M., Cheong, V. S., Pickering, E., Pivonka, P., Bellantuono, I., Kadirkamanathan, V., et al. (2024). The loading direction dramatically affects the mechanical properties of the mouse tibia. Front. Bioeng. Biotechnol. 12, 1335955. doi: 10.3389/fbioe.2024.1335955

Frost, H. M. (2003). Bone's mechanostat: a 2003 update. Anat. Rec. A. Discov. Mol. Cell. Evol. Biol. 275, 1081–1101. doi: 10.1002/ar.a.10119

Giorgi, M., and Dall'Ara, E. (2018). Variability in strain distribution in the mice tibia loading model: A preliminary study using digital volume correlation. Med. Eng. Phys. 62, 7–16. doi: 10.1016/j.medengphy.2018.09.001

Goff, M. G., Chang, K. L., Litts, E. N., and Hernandez, C. J. (2014). The effects of misalignment during in vivo loading of bone: techniques to detect the proximity of objects in three-dimensional models. J. Biomech. 47, 3156–3161. doi: 10.1016/j.jbiomech.2014.06.016

Levchuk, A., Zwahlen, A., Weigt, C., Lambers, F. M., Badilatti, S. D., Schulte, F. A., et al. (2014). The Clinical Biomechanics Award 2012 - presented by the European Society of Biomechanics: large scale simulations of trabecular bone adaptation to loading and treatment. Clin. Biomech. (Bristol, Avon) 29, 355–362. doi: 10.1016/j.clinbiomech.2013.12.019

Li, H., Li, R. X., Wan, Z. M., Xu, C., Li, J. Y., Hao, Q. X., et al. (2013). Counter-effect of constrained dynamic loading on osteoporosis in ovariectomized mice. J. Biomech. 46, 1242–1247. doi: 10.1016/j.jbiomech.2013.02.016

Main, R. P., Shefelbine, S. J., Meakin, L. B., Silva, M. J., van der Meulen, M. C. H., and Willie, B. M. (2020). Murine axial compression tibial loading model to study bone mechanobiology: implementing the model and reporting results. J. Orthop. Res. 38, 233–252. doi: 10.1002/jor.24466

Martin, M., Sansalone, V., Cooper, D. M. L., Forwood, M. R., and Pivonka, P. (2019). Mechanobiological osteocyte feedback drives mechanostat regulation of bone in a multiscale computational model. Biomech. Model. Mechanobiol. 18, 1475–1496. doi: 10.1007/s10237-019-01158-W

Meakin, L. B., Price, J. S., and Lanyon, L. E. (2014). The contribution of experimental in vivo models to understanding the mechanisms of adaptation to mechanical loading in bone. Front. Endocrinol. (Lausanne). 5, 111548. doi: 10.3389/fendo.2014.00154

Moustafa, A., Sugiyama, T., Prasad, J., Zaman, G., Gross, T. S., Lanyon, L. E., et al. (2012). Mechanical loading-related changes in osteocyte sclerostin expression in mice are more closely associated with the subsequent osteogenic response than the peak strains engendered. Osteoporos. Int. 23, 1225–1234. doi: 10.1007/s00198-011-1656-4

Moustafa, A., Sugiyama, T., Saxon, L. K., Zaman, G., Sunters, A., Armstrong, V. J., et al. (2009). The mouse fibula as a suitable bone for the study of functional adaptation to mechanical loading. Bone 44, 930. doi: 10.1016/j.bone.2008.12.026

Nepal, A. K., Essen, H. W. van, Jongh, R. T. de, Schoor, N. M. van, Otten, R. H. J., Vanderschueren, D., et al. (2023). Methodological aspects of in vivo axial loading in rodents: a systematic review. J. Musculoskelet. Neuronal Interact. 23, 236. Available at: /pmc/articles/pmc10233220/ (Accessed October 3, 2023).

Norman, S. C., Wagner, D. W., Beaupre, G. S., and Castillo, A. B. (2015). Comparison of three methods of calculating strain in the mouse ulna in exogenous loading studies. J. Biomech. 48, 53–58. doi: 10.1016/j.jbiomech.2014.11.004

Oliviero, S., Giorgi, M., and Dall'Ara, E. (2018). Validation of finite element models of the mouse tibia using digital volume correlation. J. Mech. Behav. Biomed. Mater. 86, 172–184. doi: 10.1016/j.jmbbm.2018.06.022

Oliviero, S., Lu, Y., Viceconti, M., and Dall'Ara, E. (2017). Effect of integration time on the morphometric, densitometric and mechanical properties of the mouse tibia. J. Biomech. 65, 203–211. doi: 10.1016/j.jbiomech.2017.10.026

Patel, T. K., Brodt, M. D., and Silva, M. J. (2014). Experimental and finite element analysis of strains induced by axial tibial compression in young-adult and old female C57Bl/6 mice. J. Biomech. 47, 451–457. doi: 10.1016/j.jbiomech.2013.10.052

Pereira, A. F., Javaheri, B., Pitsillides, A. A., and Shefelbine, S. J. (2015). Predicting cortical bone adaptation to axial loading in the mouse tibia. J. R. Soc. Interface 12. doi: 10.1098/rsif.2015.0590

Pickering, E., Silva, M. J., Delisser, P., Brodt, M. D., Gu, Y. T., and Pivonka, P. (2021). Estimation of load conditions and strain distribution for in vivo murine tibia compression loading using experimentally informed finite element models. J. Biomech. 115, 110140. doi: 10.1016/j.jbiomech.2020.110140

Prasad, J., Wiater, B. P., Nork, S. E., Bain, S. D., and Gross, T. S. (2010). Characterizing gait induced normal strains in a murine tibia cortical bone defect model. J. Biomech. 43, 2765–2770. doi: 10.1016/j.jbiomech.2010.06.030

Razi, H., Birkhold, A. I., Zaslansky, P., Weinkamer, R., Duda, G. N., Willie, B. M., et al. (2015). Skeletal maturity leads to a reduction in the strain magnitudes induced within the bone: A murine tibia study. Acta Biomater. 13, 301–310. doi: 10.1016/j.actbio.2014.11.021

Razi, H., Birkhold, A. I., Zehn, M., Duda, G. N., Willie, B. M., and Checa, S. (2014). A finite element model of in vivo mouse tibial compression loading: influence of boundary conditions. Facta Univ. Ser. Mech. Eng. 12, 195–207. Available at: https://casopisi.junis.ni.ac.rs/index.php/FUMechEng/article/view/624 (Accessed July 28, 2024).

Roberts, B. C., Arredondo Carrera, H. M., Zanjani-pour, S., Boudiffa, M., Wang, N., Gartland, A., et al. (2020). PTH(1–34) treatment and/or mechanical loading have different osteogenic effects on the trabecular and cortical bone in the ovariectomized C57BL/6 mouse. Sci. Reports 2020 101 10, 1–16. doi: 10.1038/s41598-020-65921-1

Roberts, B. C., Cheong, V. S., Oliviero, S., Arredondo Carrera, H. M., Wang, N., Gartland, A., et al. (2023). Combining PTH(1-34) and mechanical loading has increased benefit to tibia bone mechanics in ovariectomised mice. J. Orthop. Res. doi: 10.1002/JOR.25777

Roberts, B. C., Giorgi, M., Oliviero, S., Wang, N., Boudiffa, M., and Dall'Ara, E. (2019). The longitudinal effects of ovariectomy on the morphometric, densitometric and mechanical properties in the murine tibia: a comparison between two mouse strains. Bone 127, 260–270. doi: 10.1016/j.bone.2019.06.024

Schulte, F. A., Ruffoni, D., Lambers, F. M., Christen, D., Webster, D. J., Kuhn, G., et al. (2013). Local mechanical stimuli regulate bone formation and resorption in mice at the tissue level. PLoS One 8, e62172. doi: 10.1371/journal.pone.0062172

Stadelmann, V. A., Hocke, J., Verhelle, J., Forster, V., Merlini, F., Terrier, A., et al. (2009). 3D strain map of axially loaded mouse tibia: a numerical analysis validated by experimental measurements. Comput. Methods Biomech. Biomed. Engin. 12, 95–96. doi: 10.1080/10255840903077287

Sugiyama, T., Meakin, L. B., Browne, W. J., Galea, G. L., Price, J. S., and Lanyon, L. E. (2012). Bones' adaptive response to mechanical loading is essentially linear between the low strains associated with disuse and the high strains associated with the lamellar/woven bone transition. J. Bone Miner. Res. 27, 1784–1793. doi: 10.1002/jbmr.1599

Sugiyama, T., Saxon, L. K., Zaman, G., Moustafa, A., Sunters, A., Price, J. S., et al. (2008). Mechanical loading enhances the anabolic effects of intermittent parathyroid hormone (1–34) on trabecular and cortical bone in mice. Bone 43, 238–248. doi: 10.1016/j.bone.2008.04.012

Yang, H., Butz, K. D., Duffy, D., Niebur, G. L., Nauman, E. A., and Main, R. P. (2014). Characterization of cancellous and cortical bone strain in the in vivo mouse tibial loading model using microCT-based finite element analysis. Bone 66, 131–139. doi: 10.1016/j.bone.2014.05.019

Chapter 5: Assessing the heterogeneity of biomechanical and biochemical influence in a multiscale biomechano-chemo model of bone adaptation within a cortical section of the mouse tibia

This chapter is based on the following short communication in preparation:

Assessing the heterogeneity of biomechanical and biochemical influence in a multiscale biomechano-chemo model of bone adaptation within a cortical section of the mouse tibia

Farage-O'Reilly S.M., Miller C., Cheong V.S., Pivonka P., Dall'Ara E.

To be submitted to a methodological journal as a short communication or to be later integrated as part of a larger paper.

This chapter explores the development of a pipeline which integrates a micro-FE model with a bone cell population model (BCPM; an ODE based model) to predict bone adaptation over a two-week period in an ovariectomised mouse subjected to external mechanical loading, through the *in vivo* tibial loading model. This multiscale approach enables a comprehensive understanding of bone adaptation, encompassing various dimensional levels from the cellular and molecular level to the organ level. Therefore, allowing for the adjustment of parameters influencing different aspects of the bone remodelling process across the different scales. This study investigates the heterogeneity of biomechanical, biochemical and bone adaptation parameters within a midshaft cortical section of the mouse tibia. Given the substantial changes in bone geometry observed after the initial two-day simulation period, the micro-FE model should be re-meshed and re-run to ensure accurate estimation of the local mechanical parameter (strain energy density).

Abstract

Introduction: Understanding how bone adapts to biomechanical and biochemical stimuli is fundamental for optimising preclinical investigations of osteoporosis treatments. Micro-finite element (micro-FE) models paired with mechanoregulation algorithms predict the formation well, but under-predict resorption, suggesting that resorption is not only mechanically regulated, but also biochemically regulated. On the other hand, bone cell population models (BMPCs) predict bone remodelling by calculating the cellular and molecular concentrations within a volume of the bone. Combined micro-FE models and BCPMs have provided a possible avenue for coupling biomechanical and biochemical stimuli within the bone. The aims of this study were to (1) develop a pipeline which integrates a micro-FE model with a bone cell population model (BCPM) to predict bone adaptation over a two-week period in an ovariectomised mouse subjected to external mechanical loading, and (2) use this combined model to investigate the heterogeneity of biomechanical, biochemical and bone adaptation parameters within a midshaft cortical section of the mouse tibia.

Methods: Longitudinal micro-computed tomography (micro-CT) images were taken of the tibia of an ovariectomised mouse, every two weeks from age 14 to 24 weeks. The mouse underwent external mechanical loading at age 19 weeks. A micro-FE model was generated, based on the week 18 segmented micro-CT images, and the strain energy density (SED) was calculated. The segmented images were cropped to a midshaft section of the tibia to reduce computational costs. The images were mapped to obtain the periosteal and endosteal surfaces for each 2D slice within the section. The surfaces were sampled to obtain representative surface elements (RSEs) which lined both the periosteal and endosteal surfaces across each 2D slice. A BCPM, based on a system of ordinary differential equations (ODEs), was run at each RSE daily, between weeks 18 to 20. The SED was used to regulate biochemical interactions within the BCPM. Bone adaptation was predicted for both surfaces, at the end of each day. The daily geometrical changes and cellular and molecular concentrations were recorded.

Results: The results demonstrated a fair prediction of bone adaptation for the periosteum (54 ± 6%) and endosteum (51 ± 17%) across all slices, when compared to the corresponding week 20 experimental data. Daily surface adaptation predictions show substantial changes in bone geometry after two days of simulation, suggesting that the micro-FE model should be re-meshed and re-run to ensure accurate estimation of the biomechanical stimulus.

Conclusion: These results show that a combined micro-FE and BCPM can be used to predict bone changes over time. However, optimisation of the model parameters and significant developments to the model are required to increase the predictive accuracy.

5.1 Introduction

Bone is a highly adaptive tissue which responds to biomechanical and biochemical stimuli. These stimuli are interlinked through complex pathways that regulate the bone remodelling process. Osteoporosis is a skeletal disease which disrupts the healthy remodelling which occurs in bone. It reduces the bone mineral density (BMD) and causes cortical thinning, increasing the patient's risk of fracture, which can lead to a decrease in mobility and quality of life (Rachner et al., 2011). Current treatments for osteoporosis include pharmacological interventions, such as parathyroid hormone (PTH) (Graeff et al., 2009; Borggrefe et al., 2010). However, PTH is associated with high costs and poor treatment adherence (Yeam et al., 2018). Given bone's adaptive response to mechanical stimuli, biomechanical interventions have been proposed to enhance bone formation in osteopenic and osteoporotic patients (Zhao et al., 2015; Watson et al., 2018). Nonetheless, these mechanical interventions often yield modest bone responses (Zhao et al., 2015).

Preclinical experimental studies using ovariectomised mouse models and either *ex vivo* or *in vivo* micro-computed tomography (micro-CT) imaging have demonstrated that PTH increases bone formation within the mouse tibia, increasing bone strength (Alexander et al., 2001; Iida-Klein et al., 2007; Zhao et al., 2015; Roberts et al., 2020). Similarly, compressive mechanical loading, through the use of the *in vivo* tibial loading model, has also been shown to increase bone formation (De Souza et al., 2005; Fritton et al., 2005; Birkhold et al., 2014; Razi et al., 2015a; Roberts et al., 2019; Main et al., 2020). Furthermore, combined mechanical loading and PTH treatments elicit an increased osteogenic response when compared to the respective individual treatments (Sugiyama et al., 2008; Meakin et al., 2017; Roberts et al., 2020). Therefore, understanding the independent and combined effects of mechanical loading and PTH treatments on the bone remodelling processes in preclinical studies can aid in the investigation of new and improved osteoporosis treatments. However, when using preclinical mouse models, it's essential to consider the differences between human and mouse bone. Unlike humans, mice lack Haversian canals, indicating a lack of intracortical remodelling (Jilka, 2013).

Although *in vivo* micro-CT imaging enables the assessment of the bone microstructure over time, the mechanisms underlying bone remodelling and biomechanics cannot be investigated. To overcome this, micro-CT based micro-finite element (micro-FE) models have been used (Stadelmann et al., 2009; Patel et al., 2014; Yang et al., 2014; Razi et al., 2015b; Oliviero et al., 2021b). Micro-FE models provide a non-invasive method to extract the bone's mechanical properties, such as the stiffness and failure load, so that the effect of treatments on the bone can be investigated longitudinally (Oliviero et al., 2021a). Furthermore, they allow for the prediction of local mechanical properties across the bone to be made, providing a deeper understanding of the role of local mechanics in bone remodelling (Meakin et al.,

2017; Oliviero et al., 2021a; Roberts et al., 2023). Building upon this, micro-CT based micro-FE models coupled with mechanoregulation algorithms have been employed to predict local bone changes over time, enabling investigations into the temporal dynamics of mechanoregulated bone adaptation (Schulte et al., 2013a, 2013b; Cheong et al., 2020a, 2020b; Scheuren et al., 2020; Cheong et al., 2021b; Marques et al., 2023). These mechanoregulated models have been shown to predict well formation but under-predict resorption (Schulte et al., 2013b; Cheong et al., 2021b). Highlighting that bone is not only mechanically regulated, but also biochemically regulated.

A neighbouring avenue to investigate bone changes over time is the development of bone cell population models (Lemaire et al., 2004; Pivonka et al., 2008; Martínez-Reina and Pivonka, 2019; Trichilo et al., 2019; Lavaill et al., 2020). These models, known as bone cell population models (BCPMs), rely on information about the bone cells and biochemical pathways which underlie bone remodelling and are usually represented by a system of ordinary differential equations (ODEs). BCPMs model bone remodelling by calculating the concentration of bone cells (osteoblast precursors (OBp), active osteoblasts (OBa), and active osteoclasts (OCa)) within a specific volume of bone and at a specific time point. The ODE outputs are then combined to determine the change in bone volume. These BCPMs have been used to investigate bone adaptation in humans due to PTH and mechanical loading (Martin et al., 2019; Lavaill et al., 2020) and different PTH administration regimes in a rat model (Trichilo et al., 2019). With appropriate tuning, these models could predict the mean trends observed in experimental data. However, localised mechanical input is neglected. Given that bone adapts in response to biomechanical stimuli, which can vary across the bone, incorporating these localised biomechanical variations may impact the local cellular and molecular concentrations and hence the local bone adaptation.

To overcome this limitation, multiscale models have been developed which combine biomechanical models with BCPM models. Beam theory provides one approach for calculating biomechanical stimuli which can be combined with BCPMs (Lerebours et al., 2016; Miller, 2023). This has allowed for investigations into osteoporosis and related treatments. However, beam theory relies on the assumptions that the bone is modelled as a long beam, and that no shear strains are present. An alternative to this is to combine micro-FE models with BCPMs. This approach has been used to model osteoporotic conditions in the human proximal femur (Ashrafi et al., 2020). However, this combined model was not validated.

The objectives of this study were to (1) develop of pipeline which integrates a micro-FE model with a bone cell population model (BCPM) to predict bone adaptation over a two-week period in an ovariectomised mouse subjected to external mechanical loading, and (2) use this combined model to

investigate the heterogeneity of biomechanical, biochemical and bone adaptation parameters within a midshaft cortical section of the mouse tibia.

5.2 Materials and methods

The model described in this chapter builds upon a hybrid model developed by Miller (2023). Miller's hybrid model predicts bone adaptation in a 2D slice of the mouse tibia by combining a mechanical beam theory model with a BCPM developed by the QUT Centre for Biomechanics research group (Martin et al., 2019; Trichilo et al., 2019; Lavaill et al., 2020). The model described in this chapter differs from that developed by Miller (2023) in two significant ways: (1) by using the SED, obtained from a micro-FE model, as the biomechanical input, and (2) by predicting bone adaptation across a section of the mouse tibia. These modifications allow for the inclusion of shear strains in the calculation of the of biomechanical stimulus. Additionally, extending the model to a larger section of the tibia will enhance its ability to capture the spatial variability of bone adaptation. As a feasibility study, this analysis utilised data from a single mouse. However, future investigations can extend this approach to larger datasets to validate and refine the model's predictive capabilities. All the experimental procedures complied with the UK Animals (Scientific Procedures) Act 1986 and were approved by the local Research Ethics Committee of the University of Sheffield.

5.2.1 Experimental *in vivo* data

One mouse from the OVX-ML group was used from the experimental data described in Chapters 3 and 4, which was collected by Roberts et al. (2020). The mouse was ovariectomised at week 14 of age and underwent external mechanical loading at weeks 19 and 21, using the *in vivo* tibial loading model (Figure 3.1; 12 N peak load, 2 N static preload superimposed with a 10 N high-strain dynamic load, at a rate of 160,000 N/s (maximal nominal speed of the machine), 40 cycles/day, 3 days/week on alternate days; ElectroForce BioDynamics 5100, TA instruments, USA). The entire right tibia was imaged every two weeks from weeks 14 to 24 using *in vivo* micro-CT (VivaCT80, Scanco Medical Brütisellen, Switzerland). The scanning protocol was previously defined by Oliviero et al. (2017, 2019) (scanning parameters: 55 kVp, 145 µA, 10.4 µm isotropic voxel size, 32 mm field of view, 100 ms integration time and 1500/750 samples/projections). The images were reconstructed using a third-order polynomial beam hardening correction algorithm based on a 1200 mgHA/cm^3 wedge phantom, which was provided by the manufacturer. In this study, the week 18 and 20 images were used.

5.2.2 Image pre-processing

The main steps of the image pre-processing and the generation of the micro-FE model to calculate the SED are reported in Figure 5.1. The modelling pipeline was previously validated for predictions of apparent structural properties using compressive tests (Oliviero et al., 2021b) and predictions of local displacements using Digital Volume Correlation (Oliviero et al., 2018).

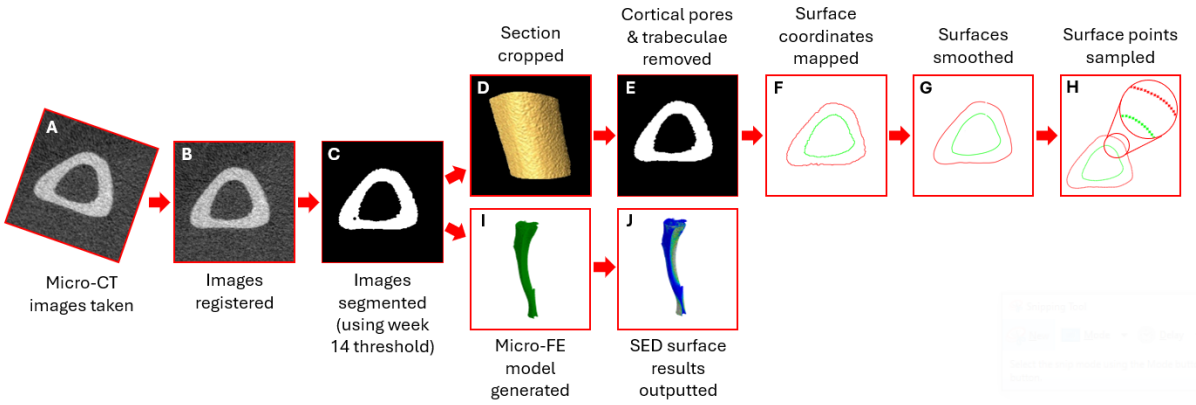

Figure 5.1: *Pre-processing pipeline for input into the biomechano-chemo model. (A) Micro-CT images are taken, (B) Images are registered, (C) Images are segmented using the week 14 threshold, (D) Section of interest is cropped, (E) Cortical pores are automatically filled and trabeculae are manually removed, (F) Surface coordinates for each slice are mapped, (G) Surface maps are smoothed, (H) Surface points are sampled, (I) Micro-finite element (micro-FE) model is generated from the segmented images, (J) Micro-FE model is run and the strain energy density (SED) is outputted.*

One reference tibia from week 14 was repositioned such that the longitudinal axis of the bone was aligned to the z-axis of the image, and the sagittal plane bisected the midpoint of the line joining the centres of the articular surfaces of the medial and lateral condyles (Lu et al., 2016). This reference image was then used to rigidly register all other images (Figure 5.1 B; Amira 6.3.0, Thermo Fisher Scientific, France), as detailed in Lu et al. (2016, 2017). The fibula was virtually removed from all the registered images and were then cropped from the slice below the proximal growth plate towards the distal end of the tibia, resulting in 80% of the total tibia length (Cheong et al., 2020b, 2021b) and the fibula was virtually removed from all the images (MATLAB, 2018A, The MathWorks Inc., Natick MA, USA) (Oliviero et al., 2022). This procedure was associated with low reproducibility errors (less than 3.94% when estimating the stiffness and less than 1.96% when estimating the failure load) (Oliviero et al., 2022).

The week 14 images of the mouse used in this study were automatically segmented by applying a single-level threshold, defined as the midpoint between the background and bone peaks of the grey value histogram of the images (Oliviero et al., 2018; Cheong et al., 2021b). This threshold (529 mgHA/cc) was then used to segment the week 18 and 20 images of the same mouse (Figure 5.1 C).

The week 18 images were then cropped (Figures 5.1 D and 5.2) to a 10% section of interest within the tibia midshaft (resulting in a section equating to 135 image slices), a section which undergoes significant adaptation due to combined mechanical loading and PTH treatment (Roberts et al., 2020). The cortical pores and trabeculae were removed from the section of interest (Figure 5.1 E), so that the mapping of the periosteal and endosteal surfaces could later be done. This was carried out using the procedure defined by Moraiti et al. (2024). Briefly, for each 2D image slice, all pores with a perimeter smaller than 52 pixels were automatically identified and artificially filled by applying simultaneous dilation and erosion algorithms (MATLAB, 2020B, The MathWorks Inc., Natick MA, USA). For the remaining hole-like features, images from weeks 18 and 20 were analysed to determine the number of consecutive slices containing the feature. Features present in fewer than seven consecutive slices at both ages were identified as trabeculae and manually removed from all slices in the images. Given that the typical size of trabeculae in mice ranges from 40 to 70 µm (Christiansen, 2016), this criterion was used to identify trabeculae. Any remaining features were either classified as early-stage trabeculae (these features resembled notches) or transverse cortical pores (these features resembled transverse cortical gaps). Those identified as trabeculae were removed, and cortical pores were filled.

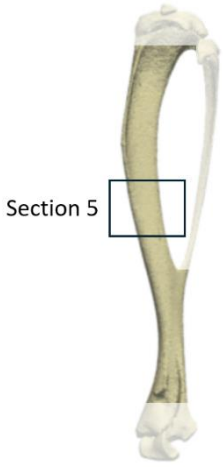

Figure 5.2: *Location of the section of interest (section 5) within the tibia.*

To align with the location of bone adaptation in mice, which is primarily confined to the bone surfaces due to the absence of osteons, the pixels along the periosteal and endosteal surfaces, for each slice,

were identified and mapped to an array (periosteal array: P^P, endosteal array: P^E; Figure 5.1 F). The surfaces of each slice were described using the continuous function

$$\boldsymbol{\eta}^S = (\boldsymbol{\eta}_x^S, \boldsymbol{\eta}_y^S), \qquad \text{where } S \in \{P, E\} \tag{5.1}$$

which represents the (x, y) coordinates of the points on a surface (S), where S can either be P (representing the periosteum) or E (representing the endosteum). The surface functions were smoothed by calculating the mean over a window of 10 surface points on the periosteum and 20 surface points on the endosteum, to mitigate for any partial volume effects (Figure 5.1 G). The smoothed surfaces arrays for each slice were sampled (Figure 5.1 H) evenly such that the periosteum of each slice consisted of 160 points and the endosteum consisted of 100 points, maintaining a periosteum to endosteum perimeter length ratio of 8:5. The sampled surfaces arrays P^P and P^E each define the centre of a representative surface element (RSE). Each RSE is approximately 100 µm in diameter, which was defined as large enough to contain the cells (an osteoclast is approximately 50 µm in diameter), but small enough to capture the bone surface geometry. Although RSEs can overlap with one another, they are assumed to be independent. Each RSE only considers surface elements, but to adapt for the parameters used within the BCPM (Section 5.2.4.3.5), which are mainly related to volumetric estimations, the RSEs were given a constant thickness equivalent to the voxel size (10.4 µm).

5.2.3 Micro-FE model generation

From the segmented week 18 images of the whole tibia, micro-FE models were generated (Figure 5.1 I). This was done by converting each bone voxel into a finite element (linear 8-node hexahedral elements). The element size was equal to the voxel size to minimise partial volume effect. Tetrahedral elements were not found to improve the prediction of the bone mechanical properties (Oliviero et al., 2021b) so hexahedral elements were preferred as the meshing procedure is more efficient. The model contained approximately 10 million nodes and 9 million elements. Isotropic, homogeneous, linear elastic material properties were used (E = 14.8 GPa, ν = 0.3), which is in line with previous validation studies which showed good agreement with experimental measurements (Oliviero et al., 2018, 2021a, 2021b). The boundary conditions were set to simulate the *in vivo* tibial loading model: the nodes in the proximal end were fully constrained, and the nodes in the distal end were connected via kinematic coupling to a control node which was located at the centroid of the distal surface with a small offset in the superior direction (Cheong et al., 2020a). A 12 N load was applied to the control node along the inferior-superior direction. The SED was recorded at the nodes (Figure 5.1 J). All input files for the

models were generated using MATLAB. The model was solved in Abaqus 2021 (Dassault Systèmes Simulia, RI, USA) using the University of Sheffield High Performance Computing Clusters (Stanage).

5.2.4 Biomechano-chemo model

The main steps of the biomechano-chemo model to predict the changes in geometry over time are reported in Figure 5.3. The modelling pipeline has been adapted from that of Miller (2023).

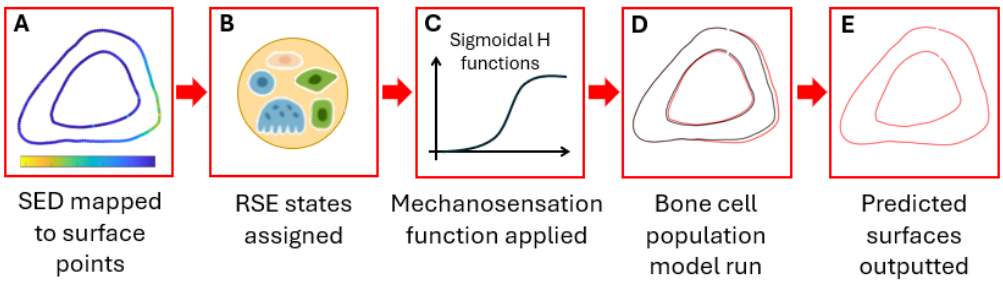

Figure 5.3: *Pipeline for the biomechano-chemo model. (A) External strain energy density (SED) results are mapped to the sampled surface points, (B) Initial conditions for the representative surface elements (RSEs) are assigned, (C) Mechanosensation function is applied, (D) Bone cell population model is run, and the geometry is updated, (E) Predicted surfaces are outputted.*

5.2.4.1 Regulatory functions

BCPMs are based on the interactions of molecules included in the bone remodelling pathways, including ligands and receptors. The binding of ligand-receptor complexes depletes the available ligand and receptor populations while simultaneously increasing related signalling pathway activity (i.e., upregulating downstream signalling pathways), leading to enhanced cellular responses, such as increased cell proliferation or differentiation. Conversely, the unbinding of these ligand-receptor complexes can decrease related signalling pathway activity (i.e., downregulate these downstream functions). There are two main regulatory functions which are employed in this model, affecting the concentration of PTH and RANKL, the differentiation of lining cells and the proliferation of osteoblast precursor cells. First, the logarithmic π function, which activate (π_{act}) or repress (π_{rep}) downstream functions. The general equations for these functions can be seen below.

$$\pi_{act}^{L} = \frac{L}{K_{act,RL} + L} \tag{5.2}$$

$$\pi_{rep}^{L} = \frac{K_{rep,RL}}{K_{rep,RL} + L}$$

(5.3)

where L represents the ligand concentration, $K_{act,RL}$ and $K_{rep,RL}$ represent the activation and repression coefficients of the ligand-receptor complex. Secondly, the sigmoidal H function, which upregulates (H^+) or downregulates (H^-) downstream functions with respect to an increase in stimulus (L). The general equations for these functions can be seen below.

$$H_{L,j}^{+} = \rho_j + \frac{(\alpha_j - \rho_j).L^{\gamma_j}}{\delta_j^{\gamma_j} + L^{\gamma_j}}$$

(5.4)

$$H_{L,j}^{-} = \alpha_j - \frac{(\alpha_j - \rho_j).L^{\gamma_j}}{\delta_j^{\gamma_j} + L^{\gamma_j}}$$

(5.5)

where α is the minimum effect response, ρ is the maximum effect response, δ is the homeostatic value, and γ is the response steepness of a specific affected process j. The resultant of both the logarithmic π functions and the sigmoidal H functions is a scalar, which will scale certain parameters in downstream functions, as will be seen in Sections 5.2.4.2 and 5.2.4.3.

5.2.4.2 Biomechanical model

The biomechanical stimulus (the SED) was obtained from the micro-FE models of the whole tibia. The external surface SED results were outputted by the micro-FE model, cropped to the section of interest, and mapped onto the sampled surface points (i.e., the centroid of each RSE), using the nearest neighbour approach (Figure 5.2 A). These surface point SED values were transformed into daily strain signals through two sigmoidal H functions, one which upregulates functions in the BCPM and one which downregulates functions in the BCPM. These can be described as mechanosensation functions and take the following forms:

$$H_{SED,j}^{-} = \alpha_j - \frac{(\alpha_j - \rho_j).SED^{\gamma_j}}{\delta_j^{\gamma_j} + SED^{\gamma_j}}, \qquad \text{where } j = \beta_{RANKL}$$

(5.6)

$$H_{SED,j}^{+} = \rho_j + \frac{(\alpha_j - \rho_j).SED^{\gamma_j}}{\delta_j^{\gamma_j} + SED^{\gamma_j}}, \qquad \text{where } j = D_{LC}, P_{OB_p}$$

(5.7)

where H is the scalar daily strain stimulus value, α and ρ are the minimum and maximum bounds, respectively, δ is the SED value that induces a 50% response, and γ is the response steepness of the target process j. In the H^- function the target process is RANKL production (β_{RANKL}). Low SED values cause an increase in RANKL production on the endosteal surface. In the H^+ function the target processes are either the bone lining cell differentiation (D_{LC}) or the osteoblast precursor proliferation (P_{OB_p}). High SED values upregulate the differentiation of bone lining cells into active modelling osteoblasts on the periosteum and upregulate the proliferation of osteoblast precursors into active remodelling osteoblasts on the endosteum. All H functions are calculated at the start (day 1) of the simulation, before the BCPM, for each sampled surface point, on both surfaces and across every slice, independently.

5.2.4.3 Bone cell population model

The equations which define the BCPM are taken from Miller et al. (2023), for convenience the equations are listed below, each followed by its description. The BCPM was modified to account for SED in place of longitudinal strains originally considered in the previous model. Additionally, modified parameters within the model have been explicitly stated.

The following sections outline the system of ordinary differential equations (ODEs) that describe the BCPM. The ODEs describe changes in the cellular environments and are solved for each RSE independently. The terminology used within these equations are listed in Table 5.1.

The periosteal and endosteal RSEs contain their respective bone cells (Figure 5.4). Periosteal RSEs contain bone lining cells and active modelling osteoblasts, while endosteal RSEs contain active remodelling osteoblasts and osteoclasts, due to low levels of periosteal resorption previously observed in the mice (Cheong et al., 2021b). Consequently, the periosteal surface can only undergo formation and the endosteal surface can undergo formation and resorption.

Table 5.1: *Terminology and description of the common parameters within the BCPM, where j can represent either a cell or molecule, as outlined by Miller (2023).*

Parameter	Description
β_j	Production rate of j
D_j	Degradation rate of j
inj_j	External dose concentration of j
$k_{f,j}$	Binding rate constant of ligand j
$k_{r,j}$	Unbinding rate of ligand j
P_j	Proliferation rate of cell j
A_j	Apoptosis rate of cell j

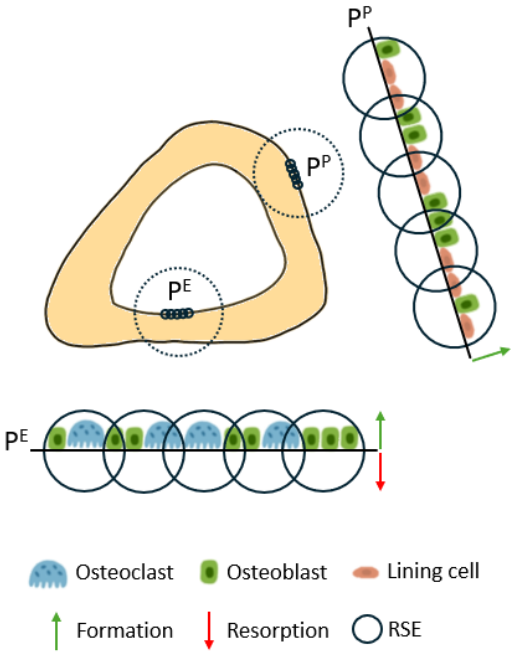

Figure 5.4: *Cell type availability across the representative surface elements (RSEs). RSEs on the periosteum (P^P) can only undergo formation (green arrow) and consists of osteoblasts and bone lining cells. RSEs on the endosteal surface (P^E) can undergo both formation (green arrow) and resorption (red arrow) and consists of osteoblasts and osteoclasts.*

5.2.4.3.1 Ligand-receptor complexes related to periosteal adaptation

On the periosteal, surface PTH in the system affects osteoblast apoptosis. PTH anabolically downregulates active osteoblast apoptosis, increasing the concentration of active osteoblasts, thus increasing formation. The concentration of PTH was modelled over time using the below equation.

$$\frac{dPTH}{dt} = \beta_{PTH} - D_{PTH} \cdot PTH + inj_{PTH}$$

(5.8)

where β_{PTH} represents the production of PTH, $D_{PTH} \cdot PTH$ represents the natural degradation of PTH, and inj_{PTH} represents an external injection of PTH, which in this model was set to 0 as only external mechanical loading was applied.

PTH affects the active osteoblast apoptosis through the regulatory factors Runt-related transcription factor 2 (Runx2), phosphorylation of CREB (pCREB), and B-cell lymphoma 2 (Bcl-2) (Peterson and Riggs, 2010; Martin et al., 2020). Therefore, the following equations are used to model the intracellular mechanics of PTH.

$$\frac{dRunx2}{dt} = \beta_{Runx2} - D_{Runx2} \cdot H^{+}_{PTH,Runx2} \cdot Runx2$$

(5.9)

$$\frac{dpCREB}{dt} = \beta_{pCREB} \cdot H^{+}_{PTH,pCREB} - D_{pCREB} \cdot pCREB$$

(5.10)

$$\frac{dBcl\text{-}2}{dt} = \beta_{Bcl\text{-}2} \cdot Runx2 \cdot pCREB - D_{Bcl\text{-}2} \cdot Bcl\text{-}2$$

(5.11)

Each equation has a production term followed by a degradation term. The two sigmoidal H functions regulate the degradation of Runx2 and the production of pCREB, with respect to PTH. These equations are later integrated into the BCPM as parameters in the periosteal ODEs representing the concentration of active osteoblasts over time.

5.2.4.3.2 Ligand-receptor complexes related to endosteal adaptation

Identically to the periosteal surface, PTH effects the endosteal surface. The same equations are used to model the intracellular mechanics of PTH as described in Eqs. 5.8 – 5.11 and integrated into the BCPM as parameters in the endosteal ODEs representing the concentration of active osteoblasts over time and the concentration of osteoblast precursors over time. Furthermore, endosteal adaptation

also depends on the concentration of TGF-β and RANKL. The concentration of TGF-β is described by the following equation.

$$\frac{dTGF\text{-}\beta}{dt} = \alpha_{TGF\text{-}\beta} \cdot K_{res} \cdot OCa - D_{TGF\text{-}\beta} \cdot TGF\text{-}\beta$$

(5.12)

where $\alpha_{TGF\text{-}\beta}$ represents the concentration of TGF-β stored in the bone matrix, and K_{res} is the resorption constant with respect to the active osteoclast concentration (OCa). Therefore, the first term represents the concentration of TGF-β released from the bone matrix during resorption, followed by a degradation term. TGF-β upregulates the apoptosis of osteoclasts and upregulates the differentiation of osteoblast precursors, but downregulates the differentiation of active osteoblasts (Wu et al., 2016). Therefore, this ligand is integrated into the BCPM as a downregulatory parameter in the endosteal ODEs representing the concentration of active osteoblasts and the concentration of active osteoclasts over time, and as an upregulatory parameter in the ODEs representing the concentration of osteoblast precursors over time.

The RANKL concentration is primarily regulated by the RANK-RANKL-OPG pathway and therefore this dynamic pathway is modelled by the following equations.

$$\frac{dOPG}{dt} = \beta_{OPG} \cdot OBa \cdot \left(1 - \frac{OPG}{OPG_{sat}}\right) \cdot \pi_{rep}^{PTH} - k_{f,OPG} \cdot OPG \cdot RANKL + k_{r,OPG} \cdot OL - D_{OPG} \cdot OPG$$

(5.13)

$$\frac{dRANKL}{dt} = H_{SED,\beta_{RANKL}}^{-} \cdot \beta_{RANKL} \cdot OBp \cdot \pi_{act}^{PTH} \cdot \left(1 - \frac{RANKL + OL + KL}{N_{RANKL,OBp_{max}} \cdot OBp}\right) + inj_{RANKL} - k_{f,OPG} \cdot OPG \cdot RANKL + k_{r,OPG} \cdot OL - k_{f,RANK} \cdot RANK \cdot RANKL + k_{r,RANK} \cdot KL - D_{RANKL} \cdot RANKL$$

(5.14)

$$\frac{dOL}{dt} = k_{f,OPG} \cdot OPG \cdot RANKL - k_{r,OPG} \cdot OL - D_{OL} \cdot OL$$

(5.15)

$$\frac{dKL}{dt} = k_{f,RANK} \cdot RANK \cdot RANKL - k_{r,RANK} \cdot KL - D_{KL} \cdot KL$$

(5.16)

where OL and KL represent the concentrations of bound OPG-RANKL and RANK-RANKL complexes respectively, where OPG_{sat} is the upper limit of OPG concentration and $N_{RANKL,OBp_{max}}$ is the maximum number of RANKL per osteoblast precursor OBp.

Eq. 5.13 represents the change in OPG over time. The equation contains a production term, which is downregulated through the logarithmic $\pi_{\mathrm{rep}}^{\mathrm{PTH}}$ function, an OPG-RANKL binding term, an OPG-RANKL unbinding term, and an OPG degradation term.

Eq. 5.14 represents the changes in RANKL over time. It includes a production term, which is downregulated by the sigmoidal $\mathrm{H}_{\mathrm{SED},\beta_{\mathrm{RANKL}}}^{-}$ and upregulated by the logarithmic $\pi_{\mathrm{act}}^{\mathrm{PTH}}$ function. Low SED values will upregulate RANKL production, leading to an increase in active osteoclasts, whilst high SED values will decrease RANKL production, supressing the number of active osteoclasts (Martin et al., 2019; Galea et al., 2020). Additionally, the change in RANKL is described by an external injection term used to induce bone loss (equivalent to ovariectomy – a mouse model of osteoporosis), an OPG-RANKL binding term, an OPG-RANKL unbinding term, a RANK-RANKL binding term, a RANK-RANKL unbinding term, and a RANKL degradation term. Eqs. 5.15 and 5.16 describe the binding, unbinding and degradation of the receptor-ligand complexes OPG-RANKL (OL) and RANK-RANKL (KL) respectively.

5.2.4.3.3 Governing BCPM equations

Whilst bone resorption and formation are "allowed" by the model, only bone formation is assumed on the periosteum, due to the low levels of periosteal resorption previously observed in the mice (Cheong et al., 2021b). The periosteum is comprised of lining cells (LC) and active modelling osteoblasts (OBa_m). Therefore, either formation can occur, or the current periosteal surface can be maintained. The periosteal concentration of OBa_m is described by the following equation.

$$\frac{dOBa_m}{dt} = D_{LC} \cdot LC \cdot \left(\lambda_{OBa_m,s} \cdot \left(H^{+}_{PTH,D_{LC}} + H^{+}_{SED,D_{LC}}\right) + \lambda_{OBa_m,c} \cdot H^{+}_{PTH,D_{LC}} \cdot H^{+}_{SED,D_{LC}}\right) - A_{OBa_m} \cdot H^{-}_{PTH,A_{OBa_m}} \cdot OBa_m \quad (5.17)$$

where λ serves as a synergism ratio between the effects of PTH and mechanical loading. This first term of the equation describes the interactions of PTH and mechanical loading on lining cell differentiation. The relationship between PTH and mechanical loading is described by the $\lambda_{OBa_m,s} \cdot \left(H^{+}_{PTH,D_{LC}} + H^{+}_{SED,D_{LC}}\right) + \lambda_{OBa_m,c} \cdot H^{+}_{PTH,D_{LC}} \cdot H^{+}_{SED,D_{LC}}$ terms. The term $\lambda_{OBa_m,s} \cdot \left(H^{+}_{PTH,D_{LC}} + H^{+}_{SED,D_{LC}}\right)$ allows PTH and mechanical loading to affect the differentiation of the lining cells into active modelling osteoblasts independently, linearly scaled by a single treatment factor, diminishing its weight in the model. The term $\lambda_{OBa_m,c} \cdot H^{+}_{PTH,D_{LC}} \cdot H^{+}_{SED,D_{LC}}$ allows for the combined interaction of PTH and

mechanical loading to affect the differentiation of the lining cells into active modelling osteoblasts, linearly scaled by a combined treatment factor, increasing its weight in the model. The second term of the equation describes the active modelling osteoblast apoptosis rate. This apoptosis term also accounts for the reversion of OBa_m into inactive lining cells (Matic et al., 2016; Wein, 2017).

The endosteum is comprised of active remodelling osteoblasts (OBa_r) and osteoclasts (OCa) (Jilka, 2013). The concentration of osteoblast precursor cells (OBp) affects the concentration of active remodelling osteoblasts over time. Together these cells allow either formation or resorption to occur on the endosteal surface. This endosteal remodelling is described by the following equations.

$$\frac{dOBp}{dt} = D_{OBu} \cdot \pi_{act,OBu}^{TGF\text{-}\beta} \cdot OBu - D_{OBp} \cdot \pi_{rep,OBu}^{TGF\text{-}\beta} \cdot OBp + P_{OBp} \cdot \left(\lambda_{OBa_r,s} \cdot \left(H_{PTH,P_{OBp}}^{+} + H_{SED,P_{OBp}}^{+}\right) + \lambda_{OBp,c} \cdot H_{PTH,P_{OBp}}^{+} \cdot H_{SED,P_{OBp}}^{+}\right) \cdot OBp \quad (5.18)$$

$$\frac{dOBa_r}{dt} = D_{OBp} \cdot \pi_{rep,OBp}^{TGF\text{-}\beta} \cdot OBp - A_{OBa_r} \cdot H_{PTH,A_{OBa_r}}^{-} \cdot OBa_r \quad (5.19)$$

$$\frac{dOCa}{dt} = D_{OCp} \cdot \pi_{act,OBp}^{RANKL} \cdot OCp - A_{OCa} \cdot \pi_{act,OCa}^{TGF\text{-}\beta} \cdot OCa \quad (5.20)$$

Eq. 5.18 represents the concentration of population of osteoblast precursors on the endosteum, and is described by an uncommitted osteoblast differentiation term, which is upregulated by the logarithmic $\pi_{act,OBu}^{TGF\text{-}\beta}$ function, a reduction term due to the differentiation of osteoblast precursors into active remodelling osteoblasts, which is downregulated by the logarithmic $\pi_{rep,OBu}^{TGF\text{-}\beta}$ function, and an osteoblast precursor proliferation term that is upregulated by the sigmoidal $H_{PTH,P_{OBp}}^{+}$ and $H_{SED,P_{OBp}}^{+}$ functions (i.e., with respect to PTH and mechanical loading). Similarly to Eq. 5.17, Eq. 5.18 contains a term which describes the relationship between PTH and mechanical loading. However, this term instead considers the proliferation of the osteoblast precursors, instead of the differentiation of the lining cells, as described in Eq. 5.17.

Eq. 5.19 represents the concentration of active remodelling osteoblasts on the endosteal surface, and is described by the differentiation of osteoblast precursor cells, which is upregulated by the logarithmic $\pi_{rep,OBp}^{TGF\text{-}\beta}$ function, and the apoptosis of active remodelling osteoblasts, which is downregulated by the sigmoidal $H_{PTH,A_{OBa_r}}^{-}$ function (i.e., with respect to PTH). Eq. 5.20 represents the active osteoclast concentration on the endosteal surface, and is described by the differentiation of osteoclast precursor

cells, which is upregulated by the logarithmic $\pi_{act,OBp}^{RANKL}$ function, and the apoptosis of the active remodelling osteoclasts, which is downregulated by the logarithmic $\pi_{act,OCa}^{TGF\text{-}\beta}$ function.

The ODEs related to the periosteum were solved simultaneously, as were the ODEs related to the endosteum (MATLAB, 2020B, ODE45 solver function, The MathWorks Inc., Natick MA, USA) and were run locally (Intel Core i7-9700 CPU (3.00GHz, 16.0 GB RAM)). Both sets of ODEs are independent from one another and were solved for each RSE and across every slice, independently, between t^d and $t + \Delta t^d$ (days 1 to 14), evaluated at sub-intervals of t^s (every 0.01 hours, i.e., every 36 seconds).

5.2.4.3.4 Initial conditions

The initial conditions of the ODEs were equivalent to that of Miller (2023), with the exception of the parameters relating to the SED (Table 5.2). These were tuned to fit the experimental results to the predicted results from the biomechano-chemo model by finding an appropriate visual match between experimental week 20 results and predicted week 20 (i.e., day 14) results, across three slices (most proximal slice, mid-slice and most distal slice). The same parameters were used for all slices in the model (i.e., no slice specific tuning was done). Miller's (2023) parameters are based on BCPMs of the rat (Trichilo et al., 2019) and of humans (Lavaill et al., 2020). These BCPMs, in turn, rely on literature by Lamaire et al. (2004), Pivonka et al. (2008, 2010), and Buenzli et al. (Buenzli et al., 2012). Parameters that were constant between the rat and human models were assumed to be constant for the mouse. Parameters that varied between species were scaled, by using the assumed mouse to rat representative volume element ratio of 1×10^5 µm^3 : 2×10^9 µm^3 (mouse : rat) (Miller, 2023). Steady state calculations were performed by Miller (2023) on the model as a standalone system (i.e., without mechanical loading or PTH treatments, nor with OVX conditions) until t^d = 1000 days to achieve homeostatic values.

Table 5.2: *The initial conditions of the BCPM, as described by Miller (2023), with the exception of the parameters relating to the SED.*

Parameter	Value	Unit	Description	Literature
			Baseline cell and ligand concentrations	
PTH	10	pM	Parathyroid hormone	Taken from Trichilo et al. (2019), based on experimental data (Stratford et al., 2014)
Runx2	10	-	Runx2	Taken from Trichilo et al. (2019), based on experimental data (Peterson and Riggs, 2010)
pCREB	10	-	Phosphorylation of CREB	Taken from Trichilo et al. (2019), based on experimental data (Peterson and Riggs, 2010)
Bcl-2	100	-	B-cell lymphoma 2	Taken from Trichilo et al. (2019), based on experimental data (Peterson and Riggs, 2010)
TGF-β	$2.7039e^{-4}$	pM	Transforming growth factor β	Taken from Trichilo et al. (2019), based on Lemaire et al. (2004), an estimate from experimental data
OPG	$3.3481e^{-4}$	pM	Osteoprotogenin	Taken from Trichilo et al. (2019), based on Pivonka et al. (2010)
RANK	9.6054	pM	Receptor of activator of nuclear factor κ-B	Taken from Trichilo et al. (2019), based on Lemaire et al. (2004) and Pivonka et al. (2008), an estimate from experimental data
RANKL	1.20401	pM	Receptor of activator of nuclear factor κ-B ligand	Taken from Trichilo et al. (2019), based on Pivonka et al. (2008)

Parameter	Value	Unit	Description	Literature
OL	40.153	pM	Bound OPG-RANKL complex	Taken from Trichilo et al. (2019), based on optimised values from Pivonka et al. (2008)
KL	0.3933	pM	Bound RANK-RANKL complex	Taken from Trichilo et al. (2019), based on optimised values from Pivonka et al. (2008)
OBa_m	0	pM	Active modelling osteoblasts on the periosteum	Taken from Trichilo et al. (2019), based on Pivonka et al. (2008, 2010) and Buenzli et al. (2012)
OBu	$1e^{-3}$	pM	Uncommitted osteoblasts on the endosteum	Taken from Trichilo et al. (2019), based on Pivonka et al. (2008, 2010) and Buenzli et al. (2012)
OBp	$3.4821e^{-3}$	pM	Osteoblast precursor cells on the endosteum	Taken from Trichilo et al. (2019), based on Pivonka et al. (2008, 2010) and Buenzli et al. (2012)
OBa_r	$1.07636e^{-3}$	pM	Active remodelling osteoblasts on the endosteum	Taken from Trichilo et al. (2019), based on Pivonka et al. (2008, 2010) and Buenzli et al. (2012)
OCp	$1e^{-3}$	pM	Osteoclast precursors cells	Taken from Trichilo et al. (2019), based on Pivonka et al. (2008, 2010) and Buenzli et al. (2012)
OCa	$7.7254e^{-5}$	pM	Active osteoclast on the endosteum	Taken from Trichilo et al. (2019), based on Pivonka et al. (2008, 2010) and Buenzli et al. (2012)
			Disassociation and association rate constants	
$k_{PTH,RANK}^{act}$	4	pM	Activating constant of RANKL production with respect to PTH	Taken from Trichilo et al. (2019), recalibrated in that study, based on Pivonka et al. (Pivonka et al., 2012) experimental data (Lemaire et al., 2004)

Parameter	Value	Unit	Description	Literature
$k_{PTH,OPG}^{rep}$	0.7423	pM	Repressing constant of OPG production with respect to PTH	Taken from Trichilo et al. (2019), recalibrated in that study, based on Lemaire et al. (2004), obtained from experimental data
$k_{TGF\text{-}\beta,OB_u}^{act}$	$5.63e^{-4}$	pM	Activating constant of uncommitted osteoblasts with respect to TGF-β	Taken from Trichilo et al. (2019), based on Pivonka et al. (2008, 2010) and Buenzli et al. (2012)
$k_{TGF\text{-}\beta,OC_p}^{act}$	$5.63e^{-4}$	pM	Activating constant of osteoclast precursors with respect to TGF-β	Taken from Trichilo et al. (2019), based on Pivonka et al. (2008, 2010) and Buenzli et al. (2012)
$k_{TGF\text{-}\beta,OB_p}^{rep}$	$1.75e^{-4}$	pM	Repressing constant of osteoblast precursor differentiation with respect to TGF-β	Taken from Trichilo et al. (2019), based on Pivonka et al. (2008, 2010) and Buenzli et al. (2012)
k_{RANKL,OC_p}^{act}	16.65	pM	Activating constant of active osteoclast precursor differentiation with respect to TGF-β	Taken from Trichilo et al. (2019), based on Pivonka et al. (2008, 2010) and Buenzli et al. (2012)
$k_{f,OPG}$	$8.333e^{-4}$	1/h	OPG-RANKL binding rate	Taken from Trichilo et al. (2019), recalibrated in that study, based on Lemaire et al. (2004), obtained from experimental data
$k_{r,OPG}$	0.4167	1/(pM h)	OPG-RANKL unbinding rate	Taken from Trichilo et al. (2019), recalibrated in that study, based on Lemaire et al. (2004), obtained from experimental data

Parameter	Value	Unit	Description	Literature
$k_{f,RANKL}$	$3.009e^{-3}$	1/h	RANK-RANKL binding rate	Taken from Trichilo et al. (2019), recalibrated in that study, based on Lemaire et al. (2004), obtained from experimental data
$k_{r,RANKL}$	$7.083e^{-4}$	1/(pM h)	RANK-RANKL unbinding rate	Taken from Trichilo et al. (2019), recalibrated in that study, based on experimental data (Lemaire et al., 2004)
			Production and degradation rates	
β_{PTH}	83.16	1/h	OPG production rate	Taken from Trichilo et al. (2019), based on PK/PD model of Teriparatide (Danhof et al., 2007)
β_{Runx2}	6.93	1/h	Runx2 production rate	Taken from Trichilo et al. (2019)
β_{pCREB}	0.0999	1/h	pCREB production rate	Taken from Trichilo et al. (2019)
$\beta_{Bcl\text{-}2}$	0.693	1/h	Bcl-2 production rate	Taken from Trichilo et al. (2019)
β_{OPG}	$6.7917e^{6}$	1/h	OPG production rate	Taken from Trichilo et al. (2019), based on an estimate from experimental data (Lemaire et al., 2004)
β_{RANKL}	7000	pM/h	RANKL production rate	Taken from Trichilo et al. (2019), recalibrated in that study, based on experimental data (Lemaire et al., 2004)

Parameter	Value	Unit	Description	Literature
D_{PTH}	8.316	1/h	PTH degradation rate	Taken from Trichilo et al. (2019), recalibrated in that study, based on experimental data (Lemaire et al., 2004)
D_{Runx2}	1	1/h	Runx2 degradation rate	Taken from Trichilo et al. (2019)
D_{pCREB}	$9.6e^{-3}$	1/h	pCREB degradation rate	Taken from Trichilo et al. (2019)
$D_{Bcl\text{-}2}$	0.693	1/h	Bcl-2 degradation rate	Taken from Trichilo et al. (2019)
$D_{TGF\text{-}\beta}$	0.0833	pM/h	TGF-β degradation rate	Taken from Trichilo et al. (2019), based on Pivonka et al. (2008, 2010) and Buenzli et al. (2012)
D_{OPG}	0.01458	1/h	OPG degradation rate	Taken from Trichilo et al. (2019), based on Pivonka et al. (2008, 2010) and Lemaire et al. (2004), from experimental data
D_{RANKL}	0.4167	1/h	RANKL degradation rate	Taken from Trichilo et al. (2019), based on Pivonka et al. (Pivonka et al., 2012) and Lemaire et al. (2004), from experimental data
D_{OL}	0.4167	1/h	OPG-RANKL complex degradation rate	Taken from Trichilo et al. (2019), based on Pivonka et al. (2008, 2010)
D_{KL}	0.0875	1/h	RANK-RANKL complex degradation rate	Taken from Trichilo et al. (2019), based on Pivonka et al. (Pivonka et al., 2012)

Parameter	Value	Unit	Description	Literature
			Differentiation, proliferation and apoptosis rates	
D_{LC}	$6.917e^{-3}$	1/h	Lining cell differentiation rate	Taken from Trichilo et al. (2019), based on
D_{OB_u}	0.0233	1/h	Uncommitted osteoblast differentiation rate	Taken from Trichilo et al. (2019), based on Lemaire et al. (2004), an estimate from experimental data
D_{OB_p}	$6.917e^{-3}$	1/h	Osteoblast precursor differentiation rate	Taken from Trichilo et al. (2019), based on Lemaire et al. (2004) and Pivonka et al. (2008), an estimate from experimental data
D_{OC_p}	0.0875	1/h	Osteoclast precursor differentiation rate	Taken from Trichilo et al. (2019), based on Lemaire et al. (2004), an estimate from experimental data
P_{OB_p}	0.0011	1/h	Osteoblast precursor proliferation rate	Taken from Trichilo et al. (2019), based on
A_{OBa_r}	$8.792e^{-3}$	1/h	Active remodelling osteoblast apoptosis rate	Taken from Trichilo et al. (2019), based on Lemaire et al. (2004)
A_{OBa_m}	$8.792e^{-3}$	1/h	Active modelling osteoblast apoptosis rate	Taken from Trichilo et al. (2019), based on Lemaire et al. (2004)
A_{OC_a}	0.2354	1/h	Active osteoclast apoptosis rate	Taken from Trichilo et al. (2019), based on Lemaire et al. (2004), an estimate from experimental data
			Additional parameters of the BCPM	
$\alpha_{TGF\text{-}\beta}$	0.01	pM	Concentration of TGF-β stored within the bone matrix	Taken from Trichilo et al. (2019), based on Pivonka et al. (2010) and Buenzli et al. (2012)

Parameter	Value	Unit	Description	Literature
inj_{PTH}	0	pM	External PTH dosage term	For main results no treatment was given. For discussion result this parameter was set to 100, based on experimental data (Roberts et al., 2020)
inj_{RANKL}	100	pM	External RANKL dosage term	Taken from Miller (2023)
$N_{RANKL,OBp_{max}}$	$2.7e^6$	-	Maximum number of RANKL per osteoblast precursor cell	Taken from Trichilo et al. (2019), based on Lemaire et al. (2004), an estimate from experimental data
$D_{OPG_{sat}}$	$2e^8$	pM	Maximum concentration of OPG	Taken from Trichilo et al. (2019), based on Pivonka et al. (2008)
$\lambda_{OBa_m,s}$	1	-	Periosteal surface single treatment weighting multiplier	Taken from Miller (2023)
$\lambda_{OBa_m,c}$	0.15	-	Periosteal surface combined treatment weighting multiplier	Taken from Miller (2023)
$\lambda_{OBa_r,s}$	1	-	Endosteal surface single treatment weighting multiplier	Taken from Miller (2023)
$\lambda_{OBa_r,c}$	0.10	-	Endosteal surface combined treatment weighting multiplier	Taken from Miller (2023)
K_{res}	29.1667	1/(pM h)	Volume of bone matrix resorbed per active osteoclast	Taken from Trichilo et al. (2019), recalibrated in that study

Parameter	Value	Unit	Description	Literature
K_{form}	2.0932	1/(pM h)	Volume of bone matrix formed per active remodelling osteoblast	Taken from Miller (2023)
K^P	$1e^{-4}$	µm/pM	Periosteal cell concentration to micrometre conversion factor	Taken from Miller (2023), scaling ratio of mouse to rat
K^E	$1e^{-4}$	µm/pM	Endosteal cell concentration to micrometre conversion factor	Taken from Miller (2023), scaling ratio of mouse to rat
			Parameters of H and π functions	
$\alpha_{PTH,D_{Runx2}}$	2.5625	-	Runx2 maximum degradation response with respect to PTH	Taken from Trichilo et al. (2019)
$\rho_{PTH,D_{Runx2}}$	0.125	-	Runx2 minimum degradation response with respect to PTH	Taken from Trichilo et al. (2019)
$\gamma_{PTH,D_{Runx2}}$	1	-	Runx2 degradation response steepness	Taken from Trichilo et al. (2019)
$\delta_{PTH,D_{Runx2}}$	32.913	pM	PTH concentration to achieve 50% Runx2 degradation potency	Taken from Trichilo et al. (2019)
$\alpha_{PTH,\beta_{pCREB}}$	15.588	-	pCREB maximum production response with respect to PTH	Taken from Trichilo et al. (2019)

Parameter	Value	Unit	Description	Literature
$\rho_{PTH,\beta_{pCREB}}$	0.5	-	pCREB minimum production response with respect to PTH	Taken from Trichilo et al. (2019)
$\gamma_{PTH,\beta_{pCREB}}$	1	-	pCREB production response steepness	Taken from Trichilo et al. (2019)
$\delta_{PTH,\beta_{pCREB}}$	317.317	pM	PTH concentration to achieve 50% pCREB production potency	Taken from Trichilo et al. (2019)
$\alpha_{PTH,P_{OBp}}$	10	-	Osteoblast precursor maximum proliferation rate with respect to PTH	Taken from Trichilo et al. (2019), based on Pivonka et al. (2008)
$\rho_{PTH,P_{OBp}}$	0.9	-	Osteoblast precursor minimum proliferation rate with respect to PTH	Taken from Trichilo et al. (2019), based on Pivonka et al. (2008)
$\gamma_{PTH,P_{OBp}}$	7	-	Osteoblast precursor proliferation response steepness	Taken from Trichilo et al. (2019), based on Pivonka et al. (2008)
$\delta_{PTH,P_{OBp}}$	190.2	pM	PTH concentration to achieve 50% Osteoblast precursor proliferation degradation potency	Taken from Trichilo et al. (2019), based on Pivonka et al. (2008)
$\alpha_{PTH,D_{LC}}$	0.1	-	Lining cell maximum differentiation rate with respect to PTH	Taken from Trichilo et al. (2019), based on Pivonka et al. (2008)
$\rho_{PTH,D_{LC}}$	0	-	Lining cell minimum differentiation rate with respect to PTH	Taken from Trichilo et al. (2019), based on Pivonka et al. (2008)

Parameter	Value	Unit	Description	Literature
$\gamma_{PTH,D_{LC}}$	30	-	Lining cell differentiation rate potency with respect to PTH	Taken from Trichilo et al. (2019), based on Pivonka et al. (2008)
$\delta_{PTH,D_{LC}}$	130	pM	PTH concentration required to achieve a 50% lining cell potency	Taken from Trichilo et al. (2019), based on Pivonka et al. (2008)
$\alpha_{PTH,A_{OBa_{R/m}}}$	1.1	-	Active (re)modelling osteoblast maximum apoptosis rate with respect to PTH	Taken from Trichilo et al. (2019), based on Pivonka et al. (2008)
$\rho_{PTH,A_{OBa_{R/m}}}$	0.1	-	Active (re)modelling osteoblast minimum apoptosis rate with respect to PTH	Taken from Trichilo et al. (2019), based on Pivonka et al. (2008)
$\gamma_{PTH,A_{OBa_{R/m}}}$	5	-	Active (re)modelling osteoblast apoptosis rate steepness	Taken from Trichilo et al. (2019), based on Pivonka et al. (2008)
$\delta_{PTH,A_{OBa_{R/m}}}$	155.2	pM	PTH concentration required to achieve 50% active (re)modelling osteoblast apoptosis potency	Taken from Trichilo et al. (2019), based on Pivonka et al. (2008)
$\alpha_{SED,\beta_{RANKL}}$	1.1	-	RANKL maximum production rate with respect to mechanical strain	Tuned in this model, based on Miller (2023)
$\rho_{SED,\beta_{RANKL}}$	0.9	-	RANKL maximum production rate with respect to mechanical strain	Tuned in this model, based on Miller (2023)
$\gamma_{SED,\beta_{RANKL}}$	0.35	-	RANKL production rate steepness	Tuned in this model

Parameter	Value	Unit	Description	Literature
$\delta_{SED,\beta_{RANKL}}$	0.0025	MPa	Mechanical strain required to achieve a 50% RANKL production potency	Tuned in this model, based on (Cheong et al., 2021) and (Schulte et al., 2013)
$\alpha_{SED,D_{LC}}$	11	-	Lining cell maximum differentiation rate with respect to strain energy density	Tuned in this model, based on Miller (2023)
$\rho_{SED,D_{LC}}$	0.5	-	Lining cell minimum differentiation rate with respect to strain energy density	Tuned in this model, based on Miller (2023)
$\gamma_{SED,D_{LC}}$	7	-	Lining cell differentiation rate potency with respect to strain energy density	Tuned in this model, based on Miller (2023)
$\delta_{SED,D_{LC}}$	0.4	MPa	Strain energy density required to achieve a 50% lining cell differentiation potency	Tuned in this model
$\alpha_{SED,P_{OBp}}$	8	-	Osteoblast precursor maximum proliferation rate with respect to strain energy density	Tuned in this model
$\rho_{SED,P_{OBp}}$	0.5	-	Osteoblast precursor minimum proliferation rate with respect to strain energy density	Tuned in this model, based on Miller (2023)
$\gamma_{SED,P_{OBp}}$	2	-	Osteoblast precursor proliferation rate potency with respect to strain energy density	Tuned in this model

Parameter	Value	Unit	Description	Literature
$\delta_{SED,P_{OBp}}$	0.0025	MPa	Strain energy density required to achieve a 50% osteoblast precursor proliferation potency	Tuned in this model, based on Cheong et al. (2021) and Schulte et al. (2013)

5.2.4.4 Geometrical adaptation algorithm

For every time step (i.e., between days 1 to 14), the changes in cell concentrations were converted into a geometrical net adaptation quantity. These changes are defined by the following equations.

$$M^P = K^P \cdot \left(\frac{dOBa_m}{dt^s}\right)$$

(5.21)

$$M^E = K^E \cdot \left(\frac{k_{form} \cdot OBa_r - k_{res} \cdot OCa}{dt^s}\right)$$

(5.22)

where k_{form} is the volume of bone formed per active remodelling osteoblast, k_{res} is the volume of bone resorbed per active osteoclast, and K^P and K^E are conversion constants to relate cellular concentrations (pM) to geometrical adaptation (µm). Geometrical changes are assumed to occur perpendicular to the surface at the centre of a given RSE and are defined by the following equation.

$$\boldsymbol{\eta}^S_{t^d+\Delta t^d,i} = \boldsymbol{\eta}^S_{t^d,i} + M_i^S\big|_{t^d} \cdot \widehat{\boldsymbol{u}}_i^S\big|_{t^d} \cdot \Delta t^d$$

(5.23)

where $\boldsymbol{\eta}^S_{t^d+\Delta t^d,i}$ represents the updated surface RSE centroid coordinates for the time step, $\boldsymbol{\eta}^S_{t^d,i}$ represents the initial surface RSE centroid coordinates, M_i^S represents the net adaptation evaluated at time t^d, $\widehat{\boldsymbol{u}}_i^S$ is the normal unit vector evaluated at time t^d, calculated by using the coordinates of the neighbouring RSEs.

For each time step (i.e., each day), $\boldsymbol{\eta}^S_{t^d+\Delta t^d,i}$ was recorded and used to quantify the heterogeneity of biomechanical, biochemical and bone adaptation parameters across the section of interest.

5.2.5 Comparison of predicted results against experimental data

The predicted week 18, day 14 (i.e., week 20) surface geometries were compared against the experimental week 20 surface geometries. The experimental week 20 micro-CT images were pre-processed analogously to the week 18 micro-CT images (i.e., mapped, smoothed and sampled as detailed in Section 5.2.2). However, due to the tibial 3D rigid registration not being optimised on a per slice basis, an additional registration was needed between the sections of interest across the two weeks. Corresponding slice percentages were selected from the week 20 images to form the week 20 section of interest (i.e., as the week 18 section of interest corresponds to the 43% - 53% of the tibial length (here, tibial length refers to the 80% length of the tibia, starting from below the proximal growth

plate), then 43% - 53% of the week 20 tibial length were chosen). This assumes that any growth occurs homogenously along the tibial length. The week 20 section of interest was re-registered (rigid image registration) to the week 18 section of interest, to best align the sections, whilst maintaining a uniform orientation across all slices (i.e., all rotations and translations were applied to the whole section of interest, not to individual slices). To evaluate the accuracy of the model, the surface points across the re-registered week 20 experimental data and the week 20 predicted data were compared. A surface point was defined as accurate if the predicted surface measurement was within one voxel of the experimental data (i.e., $\Delta\eta^S$ < 10.4 μm).

5.3 Results

The results in this section demonstrate the development of the biomechano-chemo model pipeline to (1) include biomechanical inputs generated by micro-FE models of the mouse tibia, and (2) output bone adaptation across a section of the mouse tibia. As an example of this, the results are presented for one mouse which has undergone ovariectomy and has been subsequently exposed to external mechanical loading. The model has been run for a mid-shaft cortical section of the mouse tibia. The results have been outputted daily, from age week 18 to week 20 of the mouse (i.e., $t_{d_{max}}$ = 14 days). The micro-FE model took approximately 2 hours 30 minutes to run using the University of Sheffield High Performance Computing Clusters (Stanage) and the BCPM took approximately 10 minutes to run locally (Intel Core i7-9700 CPU (3.00GHz, 16.0 GB RAM)). To visualise the results, three example slices of the section have been selected: the most superior slice, the mid-slice and the most inferior slice. The presented results are preliminary as the model parameters have not undergone significant optimisation and refinement. Therefore, any conclusions drawn from these results are dependent on the current model parameters.

The SED distribution across the tibia was generated by the whole bone micro-FE model at week 18, prior to any external mechanical loading (Figure 5.5). Under a 12 N load, the maximum SED in the section of interest can be seen towards the posterior region of the bone, with the minimum SED found on the anterior region of the bone. These regions have been highlighted with a red cross and green cross, respectively (Figure 5.5). These will be used as reference points when describing the model results.

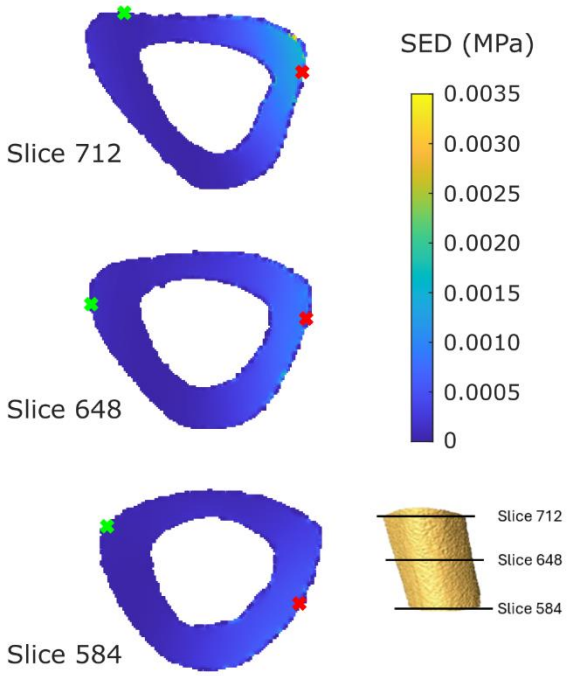

Figure 5.5: *Strain energy density (SED) distribution across three example slices of the section of interest (slice 712 refers to the most superior slice in the section of interest, slice 648 represents the mid-slice and slice 584 represents the most inferior slice of the section of interest). The green crosses signify the location of the minimum SED, and the red crosses signify the location of the maximum SED.*

The biomechanical input to the BCPM is defined by the sigmoidal H functions and can be seen for each slice in Figure 5.6. The only difference between the slice sigmoidal H functions is the SED values for that slice. As each slice experiences different values of SED, which are not normally distributed for both periosteal SED and endosteal SED (Shapiro-Wilks test), the mean and standard deviation is not necessarily representative of the functions and therefore all slices have been graphed together to allow for the difference in sigmoidal H functions across slices to be seen. The maximum differentiation rate of the lining cells is 11, and the maximum proliferation rate of the osteoblast precursors is 8 (note: both rates are dimensionless). The SED thresholds for all functions were chosen to result in a reasonable amount of bone adaptation when compared to experiments (Roberts et al., 2023), and hence as a best match between the experimental week 20 results and the predicted day 14 (i.e., week 20) model outputs. These SED thresholds translate the sigmoidal H functions in the SED axis, determining the biomechanical stimulus needed to invoke a cellular/ molecular response greater than the minimum response. Due to the low SED thresholds chosen for the parameters relating to the proliferation of the osteoblast precursor cells and the production rate of RANKL, the functions appear not to be sigmoidal for the current range of SED.

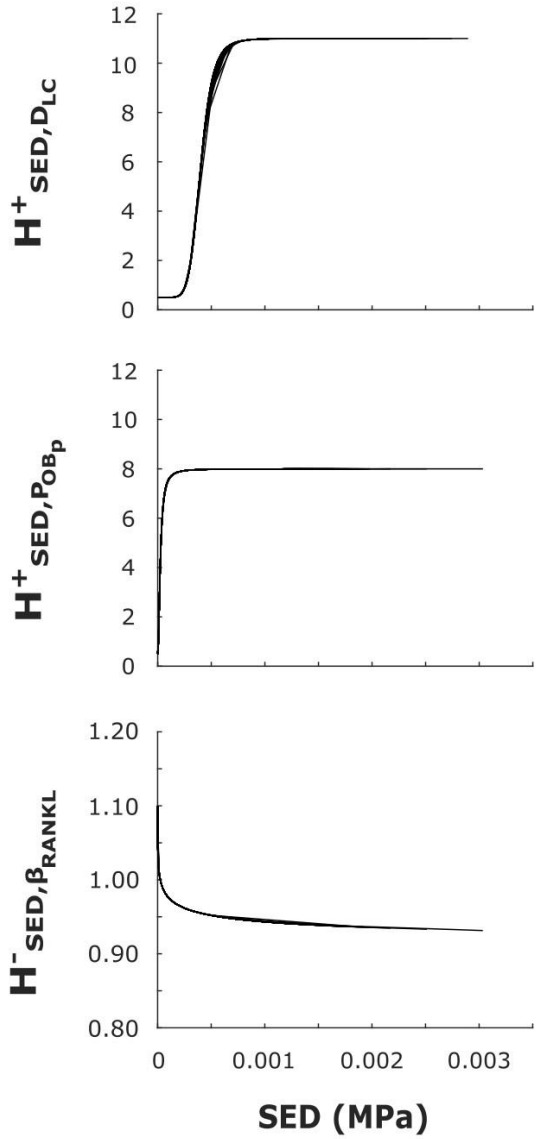

Figure 5.6: *Sigmoidal mechanical H functions: $H^{+}_{SED,D_{LC}}$ represents the upregulation of lining cell differentiation, H^{+}_{SED,POB_p} represents the upregulation of osteoblast precursor proliferation, $H^{-}_{SED,\beta_{RANKL}}$ represents the downregulation of RANKL production, all with respect to the strain energy density (SED). Each plot shows the sigmoidal H functions sensitivity with respect to the SED for each of the slices in the section of interest.*

The cellular and molecular concentrations for the surface points relating to the maximum and minimum values of the SED, for the three example slices can be seen in Figure 5.7. The cellular and molecular concentrations range across the slice, between those relating to the maximum and minimum SED. The parameter relating to the periosteal surface (OBa_m) shows a logarithmic response

for the surface point relating to the maximum value of SED, converging towards day 14. For the surface point associated to the maximum value of SED, the parameters relating to the endosteal surface (OBa_r, OBp, OPG, OL, OCa, TGF-β, RANKL, KL) exhibit either a logarithmic response, converging towards day 14, or an exponential response, diverging as time increases. Their responses are categorised based on their association with either formation or resorption pathways. OCa, TGF-β, RANKL, and KL converge over time, aligning with resorption pathways. Conversely, OBa_r, OBp, OPG, and OL diverge, and are associated with formation pathways. As expected, all parameters for the surface points relating to the minimum SED remain constant at their respective base-line values. As the external injection of PTH has been modelled as 0 (i.e., no external PTH dose was given), the parameters Runx2, pCREB and Bcl-2 remain constant across the time period and have therefore been omitted from Figure 5.7.

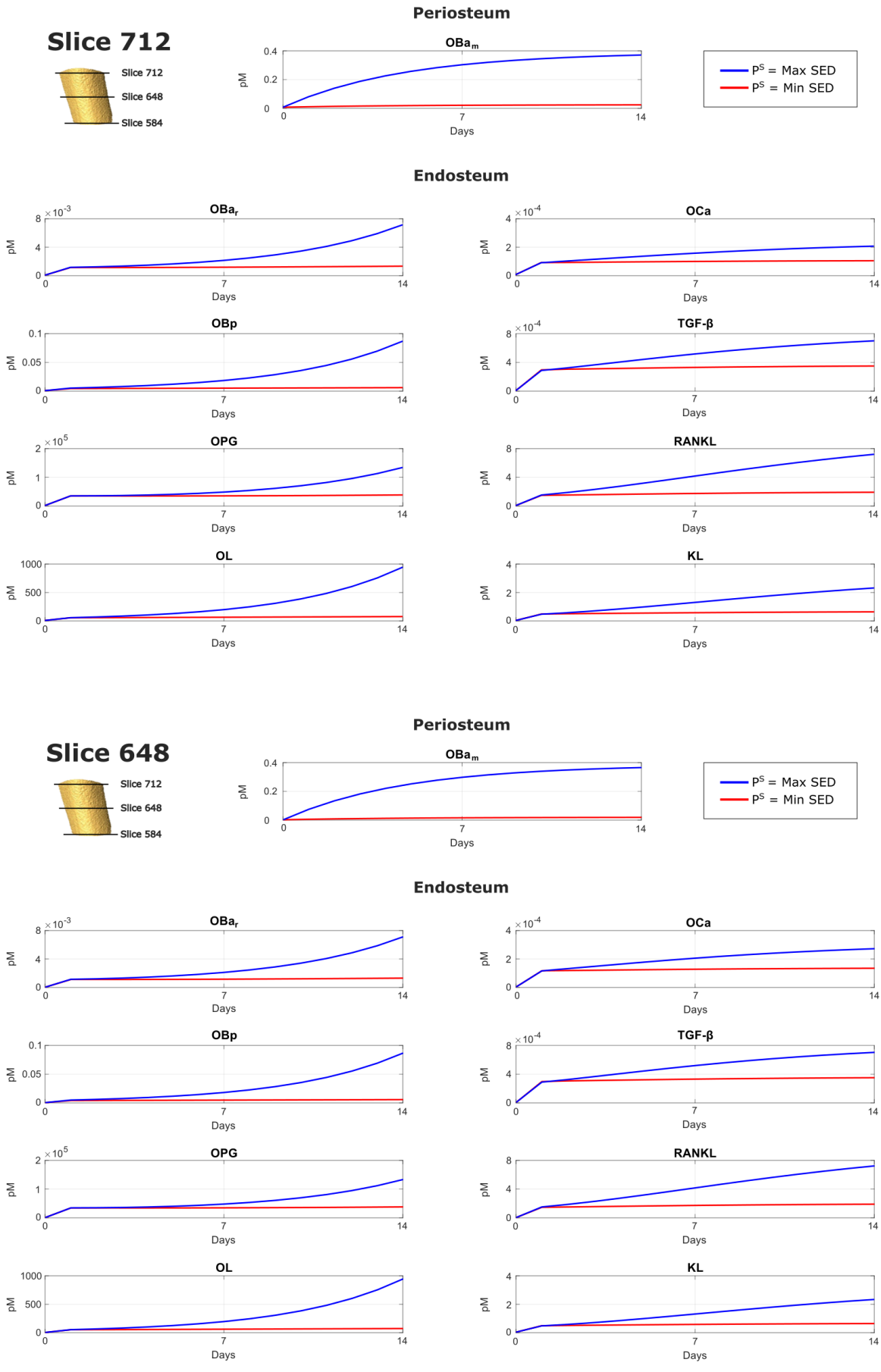
Slice 712
Slice 712
Slice 648
Slice 584
Periosteum
OBa$_m$
pM
Days
P^S = Max SED
P^S = Min SED
Endosteum
OBa$_r$
OCa
OBp
TGF-β
OPG
RANKL
OL
KL
Slice 648
Slice 712
Slice 648
Slice 584
Periosteum
OBa$_m$
Endosteum
OBa$_r$
OCa
OBp
TGF-β
OPG
RANKL
OL
KL

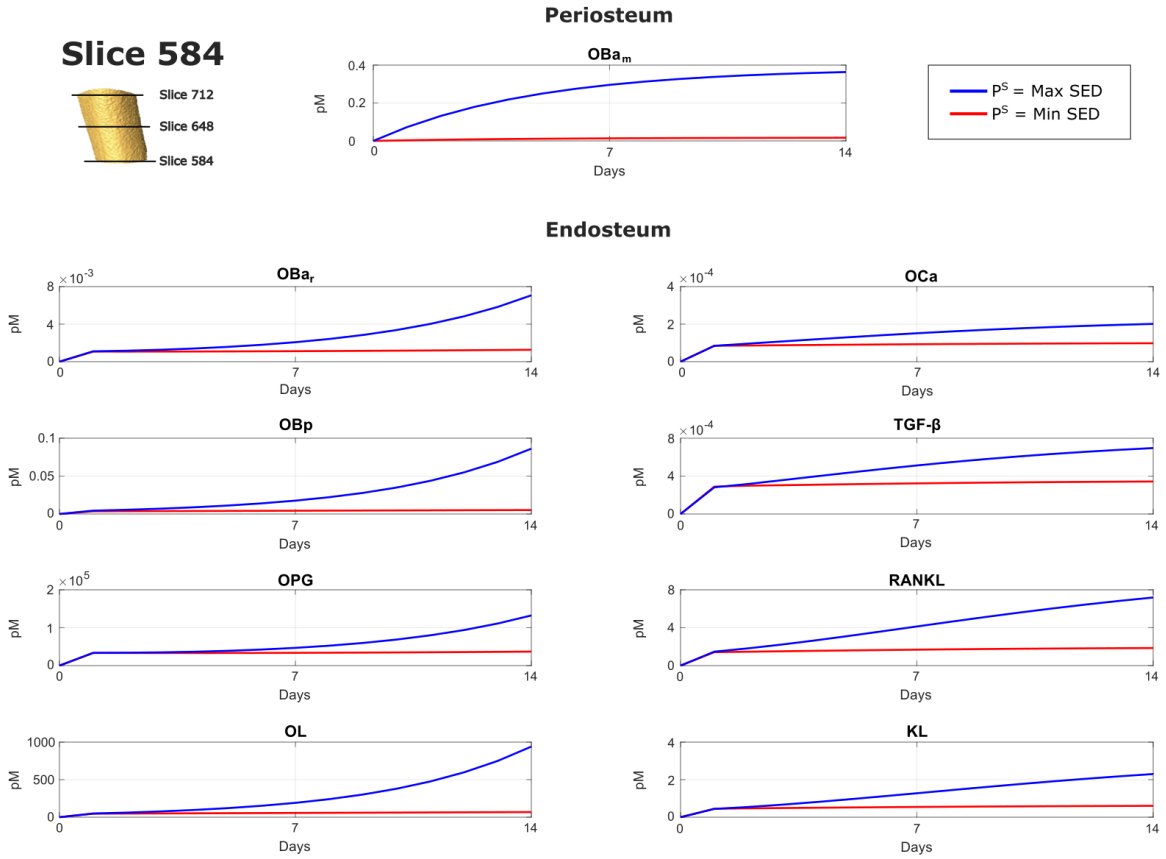

Figure 5.7: *Cell concentrations for days 1 to 14. The periosteal remodelling is defined by the number of osteoblast precursors (OBp), active remodelling osteoblasts (OBa_r), active osteoclasts (OCa), OPG, TGF-β, RANKL, OPG-RANKL compounds (OL), and RANK-RANKL compounds (KL). The endosteal remodelling is defined by the number of active modelling osteoblasts (OBa_m). The results show these values over time for the representative surface elements (P^S) which correspond to the maximum strain energy density (blue line) and the P^S which corresponds for the minimum strain energy density (red line), allowing for the range of the cellular and molecular concentrations across the slice to be seen. The results are shown for three example slices (slice 712, 648 and 584).*

The daily predicted surface adaptation for each of the 14 days can be seen in Figure 5.8 (left). The number of surface points with changes larger than one voxel (i.e., $\Delta\eta^S$ < 10.4 µm), can be seen in Figure 5.8 (right). The regions which experience highest values of SED, undergo the largest amount of adaptation. The adaptation on the periosteum occurs logarithmically between days 1 to 14. The changes occur linearly for the first two days, most likely due to the constant SED values across the days. The adaptation on the endosteum occurs at a later point, increasing dramatically between days 12 and

14. These changes in the surface adaptation can be described by their respective cellular and molecular concentrations.

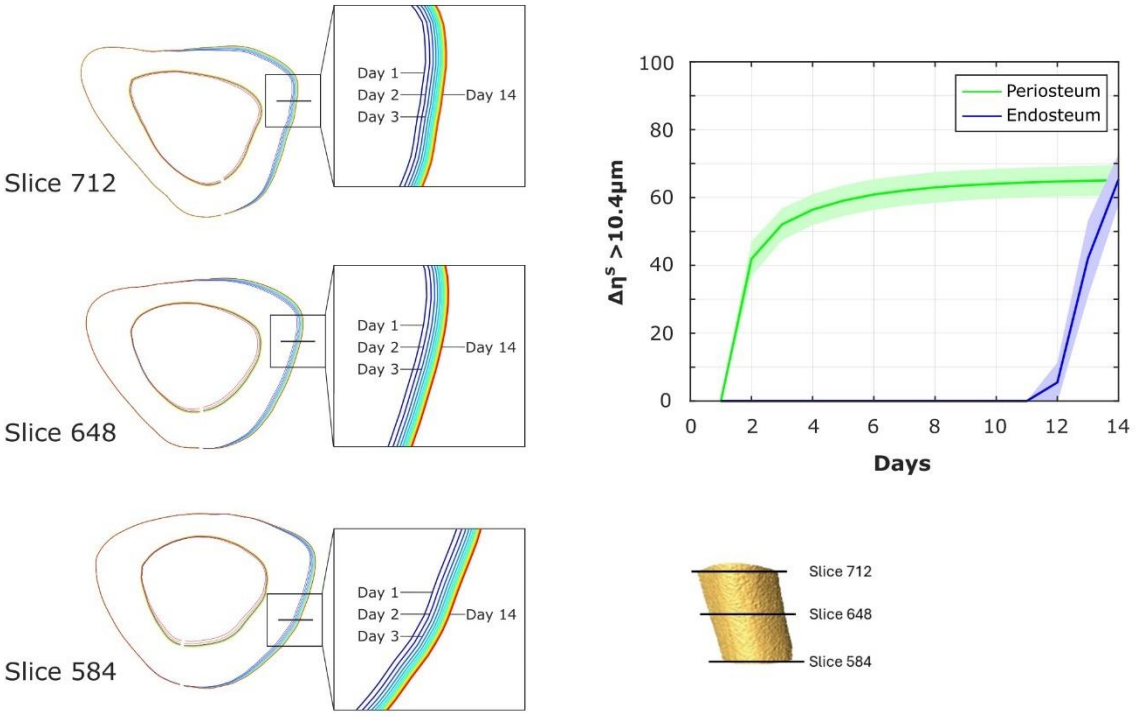

Figure 5.8: *Geometrical changes on the periosteum ($\Delta\eta^P$) and endosteum ($\Delta\eta^E$) across days 1 to 14. Left: Geometrical changes for three example slices, the black line marks the location of maximum strain energy density. Right: $\Delta\eta^S$ changes for points on the surfaces which are greater than the voxel size (10.4μm) across all slices. The plot shows the mean ± standard deviation of $\Delta\eta^P$ and $\Delta\eta^E$ across all slices.*

The predicted surface adaptation after 14 days can be seen in Figure 5.9. Experimental data at week 18 is represented by the thin black lines, the experimental data at week 20 is represented by the blue lines, and the predicted adaptation at day 14 (i.e., week 20) is represented by the red lines. The current parameters were able to accurately predict adaptation at 54 ± 6% of periosteal and 51 ± 17% of endosteal points. For the three example slices shown, slice 712 resulted in an accurate prediction of adaptation at 56% of periosteal and 93% of endosteal points. Slice 684 resulted in an accurate prediction at 51% of periosteal and 42% of endosteal points. Slice 584 resulted in an accurate prediction at 56% of periosteal and 33% of endosteal points. The periosteum had relatively consistent

predictions across slices (Figure 5.10), and the endosteum decreased in predictive ability as the slice became more distal.

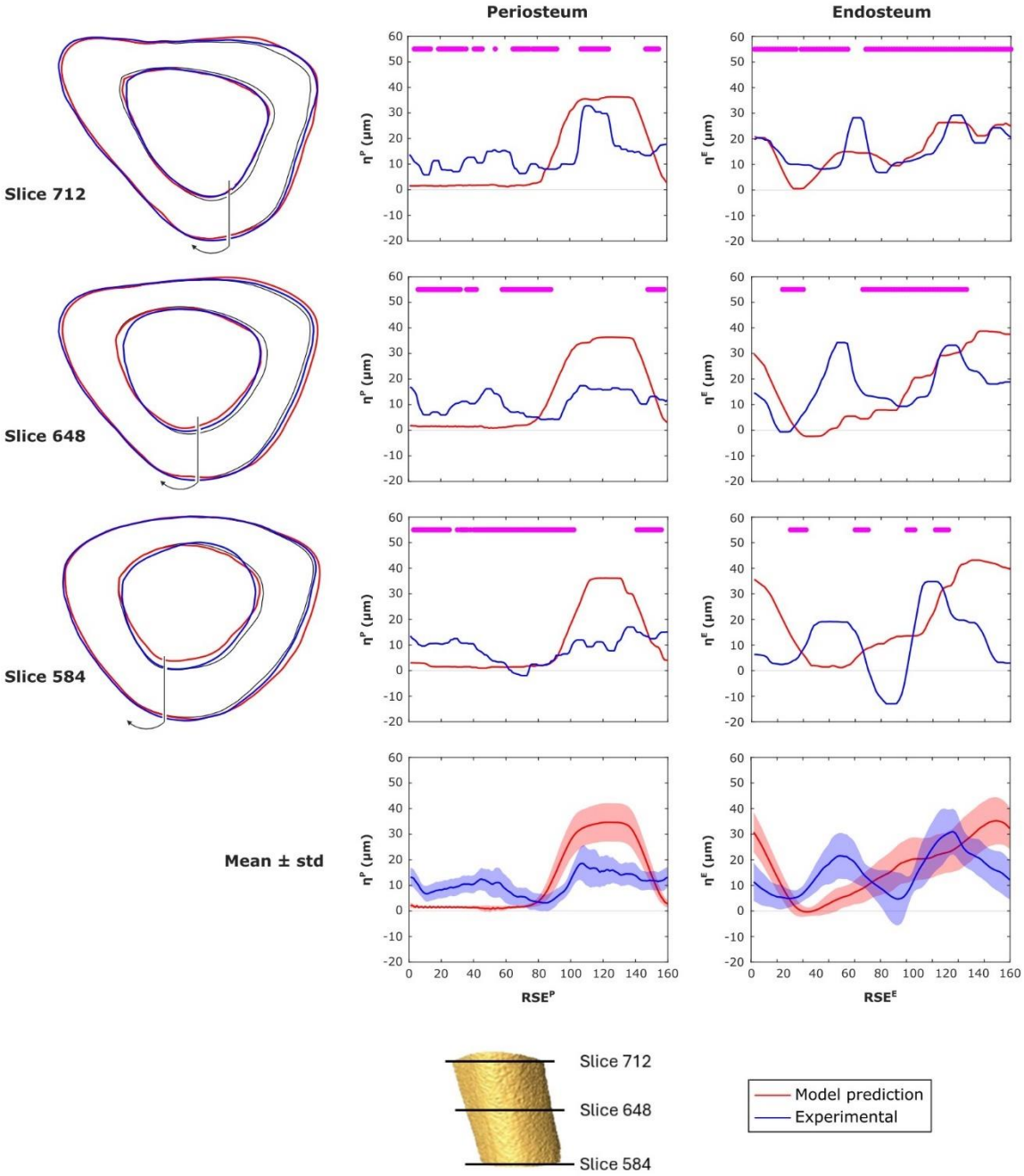

Figure 5.9: *Comparisons of the model predictions and the experimental data for bone adaptation. Three example slices are shown. Model predictions for week 20 (i.e., day 14) are in red, experimental data for week 18 are in a thin black line, and experimental data for week 20 are in blue. The bone adaptation on the periosteum (η^P) can be seen in the centre column, and the bone adaptation for the endosteum (η^E) can be seen to the right. The representative surface elements (RSEs) increase around*

the perimeter surface starting from the black line and arrow and increasing clockwise. Points marked by a pink line denote simulated measurements within ±10.4µm (i.e., one voxel) of the experimental results for the three slice examples. The mean ± std bone adaptation across all slices can be seen at the bottom.

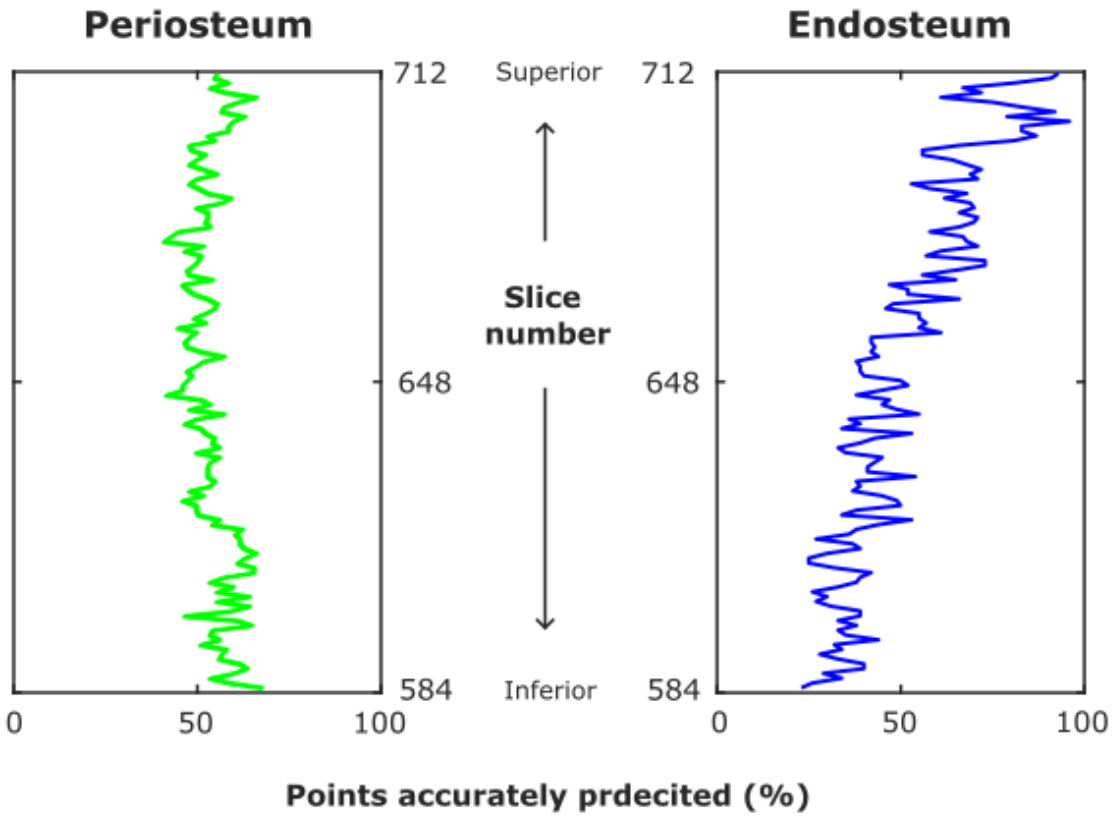

Figure 5.10: *Percentage of points along the periosteum and endosteum which are within 10.4µm (i.e., one voxel) of the experimental results.*

5.4 Discussion and future developments

The purpose of this study was to develop a pipeline to combine a micro-FE model with a BCPM (an ODE based model) to predict bone adaptation over time and to use this multiscale model to evaluate the heterogeneity of the biomechanical, biochemical and hence bone adaptation parameters within a cortical section of the mouse tibia.

The sensitivity analysis (Figure 5.8) of the daily change in bone adaptation (between 1 and 14 days) predicted by the multiscale model in the cortical bone section shows that regions which experience

highest values of SED, undergo the largest amount of adaptation. This is in line with the current literature (Razi et al., 2015a; Roberts et al., 2019; Miller et al., 2024). The sensitivity analysis goes on to show that the adaptation on the periosteal surface, across all slices, occurs logarithmically across days 1 to 14, and appears to be converging, although the simulation needs to be run over a longer time period to determine if it does in fact converge. The changes occur linearly for the first two days, most likely due to the constant SED values across the days (i.e., that the micro-FE model is not re-meshed and re-run in between iterations of the BCPM). In experimental data of C57BL/6 mice, the tibial cortical thickness (Ct.Th) and cortical area (Ct.Ar) both increased significantly after external mechanical loading (approximately 16% ($p = 0.003$) and 14% ($p = 0.010$), respectively) between weeks 18 and 20 of age (Roberts et al., 2023). This sensitivity analysis suggests that after external mechanical loading, the majority of the periosteal formation occurs imminently, stabilising by day 14. However, the adaptation on the endosteal surface occurs at a later point, increasing dramatically between days 12 and 14. The results suggest that the micro-FE model should be re-run after two days of simulation so that the biomechanical stimulus can be updated to account for geometrical changes that may affect the local SED values and therefore the predictions of bone adaptation. However, additional investigation would be needed to assess if the change in geometry is larger enough to warrant re-running the micro-FE model again after this point, and if so, how frequently.

Preliminary results of the multiscale model, based on the current parameters show that localised, daily change in bone adaptation can be modelled. The current sigmoidal H functions, which are related to the mechanosensation, are capable of modulating cellular and molecular concentrations. This allows for the SED to induce heterogeneity within each slice. The current parameters result in a fair prediction of net geometrical adaptation across the periosteal surface (54 ± 6%) and the endosteal surface (51 ± 17%) after 14 days when compared to experimental data. This is most likely largely due to the sigmoidal H function parameters not yet being optimised. The current SED threshold for the sigmoidal H functions related to the endosteum (0.0025 MPa) lies between those reported by Cheong et al. (2021a) (0.0001341 MPa) and Schulte et al. (2013b) (formation: 0.01630 MPa, resorption: 0.0100 MPa). However, the SED threshold related to the periosteum (0.4 MPa) far exceeds both those reported in the literature. Furthermore, cellular and molecular concentrations related to endosteal formation displayed an exponential response, diverging as time increases, most likely contributing to the poor endosteal predictions. Additionally, the endosteum experienced low levels of SED, which would theoretically be more likely to result in resorption, and hence the low SED threshold parameter used within the sigmoidal H function may cause the model to not capture this resorption well. Updating these parameters would also allow for the sigmoidal shape of these H functions to be captured. By increasing the SED threshold, the number of points which invoke higher levels of RANKL concentration

would increase, in turn increasing the amount of resorption. This could partially explain the dramatic range of endosteal predictions across slices. Additionally, these differences in endosteal predictive ability across slices could be mitigated by assigning heterogeneity to the parameters across the section. Current parameters are homogenous across all slices in the section, and no slice-specific tuning has been done. The sigmoidal H function parameters could be linearly scaled in function of the slice location (from proximal to distal), to account for the differences in mechanosensation (number of osteocytes) across the length of the section. However, additional data is required to understand the distribution of the osteocytes and hence correctly implement this scaling.

The spatial predictions obtained from this model are less accurate than that of a previous study, which used a mechanoregulation model, and had a spatial match of approximately 60% on both periosteal and endosteal surfaces in the same section of the mouse tibia (Cheong et al., 2020a). A major difference between the two models is that the mechanoregulated model could undergo formation and resorption on both the periosteal and endosteal surfaces. However, that model included optimised parameters for the SED threshold, and formation and resorption rates. Though that study employed a stricter definition of spatial match, requiring that the correct bone changes in formation and resorption were also made. Furthermore, compared to the results by Miller et al. (2023), which uses the same BCPM equations to this study, periosteal predictions and endosteal predictions were less accurate. A potential explanation for the observed discrepancy is the increased size of the modelled region. This may have also led to higher registration errors between the week 18 and week 20 experimental data, subsequently propagating these errors into the prediction analysis. These errors may have not been evenly distributed, contributing to the differences in endosteal predictive ability across slices. Additionally, the assumption that growth occurs homogeneously across the bone may mean that equivalent sections of the bone across were not being compared, hence increasing the error in predictions.

This multiscale model allows insights into bone adaptation which occur in between the current imaging time points; something which can only be achieved experimentally through daily micro-CT imaging, which would affect the bone due to the increase in radiation doses. However, this multiscale model is not yet complete, nor has it been optimised, and therefore would benefit from the modifications outlined below. The assumptions made in this model have been outlined in Table 5.3. A justification of these assumptions is also given, alongside a suggestion for future development of the model.

Table 5.3: *The current assumptions made in the biomechanical-chemo model, alongside their respective justification and a suggestion for future development of the model.*

Assumption	Experimental/ modelling decision	Justification	Future development
Experimental data assumptions			
-	Ovariectomise the mouse (Roberts et al., 2020)	Ovariectomy leads to an oestrogen deficiency, which results in accelerated bone resorption, a phenotype observed in postmenopausal osteoporosis	-
-	Perform *in vivo* micro-CT imaging every other week using the following scanning parameters: 55 kVp, 145 µA, 10.4 µm isotropic voxel size, 32 mm field of view, 100 ms integration time and 1500/750 samples/projections (Roberts et al., 2020)	The scanning protocol was previously defined by Oliviero et al. (2017, 2019), which allowed for minimal effects of radiation on the tibia whilst still allowing for scanning of the whole bone at high resolution	-

Assumption	Experimental/ modelling decision	Justification	Future development
Image registration accurately aligned the tibia so that the z-axis of the image correlated with the longitudinal axis of the tibia	Manually aligned a reference image such that the axis of the bone was aligned to the z-axis of the image, and the sagittal plane bisected the midpoint of the line joining the centres of the articular surfaces of the medial and lateral condyles, and then rigidly registered the images to this reference image (Lu et al., 2016, 2017)	This procedure was associated with reproducibility errors in estimating local bone mineral content (BMC) lower than 4.25% (Oliviero et al., 2022)	-
External mechanical loading was applied axially along the bone when using the *in vivo* tibial loading model	The tibia was fixed in between two soft caps by an experienced researcher	-	Tri-axial load cells or mouse-specific 3D-printed caps could be used to mitigate errors associated to the loading direction. Alternatively, a sensitivity analysis can be conducted to assess the impact of loading direction on predicted bone adaptation within the biomechano-chemical model

Assumption	Experimental/ modelling decision	Justification	Future development
-	A 12 N peak load (2 N static preload superimposed with a 10 N high-strain dynamic load at a rate of 160,000 N/s	This established protocol has been shown to induce adaptations in both cortical and trabecular lamellar bone without inducing micro-damage (De Souza et al., 2005)	-
Micro-FE model assumptions			
The fibula does not affect the SED distribution across the tibia	The fibula was virtually removed from the images	Although that is has been shown that the fibula does affect the cortical strain adaptation (Yang et al., 2014), including the fibula in the model would require additional assumptions to be made about the tibio-fibular joint material properties. The micro-FE model used has been validated for local displacements and structural properties (Oliviero et al., 2018, 2021b)	The fibula could be included in the micro-FE model, but additional assumptions of the tibio-fibula joint and the growth plate would be needed
The growth plate does not affect the SED distribution	The images were cropped from below the proximal growth plate, resulting in 80% of the total tibial length		

Assumption	Experimental/ modelling decision	Justification	Future development
-	Linear 8-node hexahedral elements were used	The hexahedral micro-FE model has been validated (Oliviero et al., 2018, 2021b)	-
-	Isotropic homogeneous material properties were used (Young's Modulus = 14.8 GPa, Poisson's ratio = 0.3)	Heterogenous material properties based on the TMD obtained from the images have been previously investigated, but homogeneous models have been shown to be better correlated with experimental data (Oliviero et al., 2021b)	-
The soft tissues do not affect the SED distribution	Only the bone matrix has been modelled	Including the soft tissues would significantly increase the complexity of the model and hence would require more computational resources	The forces applied to the bone could be modified to partially account for the soft tissues

Assumption	Experimental/ modelling decision	Justification	Future development
The SED distribution is not affected by small intracortical pores (< 10.4 μm) or the osteocyte lacune	Small intracortical pores and osteocyte lacunae are omitted from the model and modelled as bone tissue	Intracortical pores in C57BL/6 mice are often less than 10 μm, therefore not possible to model with the current image resolution (10.4 μm). Scanning at a resolution high enough to capture these features will affect the bone tissue due to radiation exposure	Micro-FE models based on high resolution images which capture the pores could be generated, although modifications to the BCPM would have to be made to account for the additional surfaces, although longitudinal comparisons (across time) may not be possible

Assumption	Experimental/ modelling decision	Justification	Future development
BCPM model assumptions			
The biomechanical stimulus is constant for an RSE across all time steps	The micro-FE model is run once, at the start of the biomechano-chemo model and hence the SED is not updated daily	Running the micro-FE model when the geometry is not significantly different to a previous time step is not computationally efficient. This was investigated in this study, and it was shown that the daily surface adaptation predictions suggest that the micro-FE model may need to be re-run after two days of simulation.	The micro-FE model could be automatically re-run after 2 days so that the SED is recalculated based on the updated geometry. Additional investigation would be needed to assess if the change in geometry is larger enough to warrant re-running the micro-FE model after this point, and if so, how frequently. A smoothing function between the slices would be required so that the updated 3D geometry does not have sharp transitions between the slices. Additionally, the BCPM could be modified to include physiological loading and to mimic the experimental protocol (external

			mechanical loading 3 days/week on alternate days during week 19)
Bone adaptation is not affected by the cortical pores or the trabeculae	Cortical pores are filled, and trabeculae are manually removed	The current biomechano-chemo model can only identify two surfaces (the periosteum and endosteum). Additional modelling parameters and assumptions would be needed to be able to predict bone adaptation on the cortical pore and trabeculae surfaces	The BCPM could be modified to be able to identify multiple surfaces. However, higher resolution images would be required, which may mean that longitudinal comparisons (across time) are no longer possible
Cellular and molecular concentrations are non-linearly affected by biomechanical and biochemical stimuli	Mechanosensation functions are modelled using sigmoidal functions	Cellular and molecular concentration is non-linearly regulated (Peterson and Riggs, 2010; Martin et al., 2019; Lavaill et al., 2020)	The mechanosensation functions can be modified and a comparison can be done between models. More experimental data is needed for assessing the spatial density and distributions of osteocytes across the tibia

Assumption	Experimental/ modelling decision	Justification	Future development
The current parameters of the sigmoidal H functions and the π functions accurately represent the biological interactions	The current parameters can be seen in Table 5.2	Current parameters were chosen to represent a change in cortical bone adaptation which is similar to experimental data (Roberts et al., 2023)	The mechanosensation parameters should be optimised to reduce the error between the predicted results and the experimental data, considering the heterogeneity of predictive accuracy across the length of the studies section
Bone adaptation occurs independently to its surrounding environment	The BCPM is calculated for each RSE independently, i.e., no interaction is modelled between the RSEs	Modelling interactions between RSEs would require additional parameters to be included which would increase the computational resources required to run the model. More experimental parameters about the distributions of bone cells and molecules involved in bone adaptation would be needed to inform the model.	The model could be adapted to include an array which stores the cellular and molecular availability, so that neighbouring RSEs can be affected by each other. Additionally, surrounding SED could also be used to alter the mechanosensation functions

Assumption	Experimental/ modelling decision	Justification	Future development
The RSEs are an appropriate size to be able to accurately model bone adaptation	The periosteum consisted of 160 RSEs and the endosteum consisted of 100 RSEs. Each RSE was approximately 100 µm in diameter and they were evenly distributed around each surface	The number of RSEs on each surface maintained the periosteum to endosteum perimeter length ratio of 8:5. The size of the RSEs were large enough to contain multiple bone cells (an osteoclast size is ~50 µm and an osteoblast is ~10 µm). The even distribution of RSEs allowed for bone adaptation to be predicted across the entirety of both bone surfaces	Sensitivity analyses on the number of RSEs, their size, and their distribution could be done. The RSEs could be nonuniformly distributed so that areas which are known to undergo significant adaptation (information gleaned from the experimental data) have a higher number of RSEs compared to other locations on the bone's surface. This may reduce computational cost
The periosteal surface only undergoes formation, whilst the endosteal surface undergoes both formation and resorption	The periosteal RSEs contained bone lining cells and active modelling osteoblasts, whereas the endosteal RSEs contained active remodelling osteoblasts and osteoclasts	Low levels of periosteal resorption previously observed in the mice (Cheong et al., 2021b)	-

Assumption	Experimental/ modelling decision	Justification	Future development
The concentrations of cells and molecules in mice are linearly equivalent to that of rats	Initial parameters for the rat model were used and then scaled by volume for the mouse	Lack of experimental mouse data	Collection of experimental data would be required to better inform the model
Adaptation algorithm			
Bone adaptation occurs perpendicularly to the bone surface	Bone adaptation occurs perpendicularly to the bone surface and the adapted surface is smoothed	Perpendicular adaptation maintains the bone surface geometry whilst not utilising excessive computational resources	Volumetric adaptation could be implemented, to predict bone adaptation in 3D, although a smoothing is likely to still be required
Comparison against experimental data			
Bone growth occurs homogenously throughout the length of the tibia	Corresponding slices from the predicted bone geometry and experimental week 20 data are compared based on their relative position along the tibial length	Comparisons between slices based on their position in the tibia allows for a direct comparison between equivalent anatomical locations	3D comparisons may allow for a more direct comparison between regions, although this would require a smoothing is between the 2D slices, or a modification to the adaptation algorithm

Assumption	Experimental/ modelling decision	Justification	Future development
Changes in bone adaptation are not due to age-related growth	The model does not account for growth within the regulatory pathways	Change to the bone due to growth mainly affect the tibial length. As a midshaft section of the tibia is modelled, growth is not considered. Although small changes in length between weeks can be seen experimentally, the mice are considered to be skeletally mature (Roberts et al., 2020)	Models that decouple growth and remodelling could be coupled with this combined model to identify specific regions of biological growth and remodelling. For instance, by employing the level-set method (Zhang et al., 2019)

The rest of this discussion outlines suggestions for future development of the model. Firstly, the cellular and molecular concentrations over time show that there is endosteal formation instability. The concentration of osteoblast precursors and active remodelling osteoblasts exponentially increase, contributing to this unstable endosteal formation, which overshadows the endosteal resorption. Therefore, the sigmoidal H functions parameters associated with osteoblast precursor proliferation and the differentiation of bone lining cells, both with respect to the SED should be adjusted and optimised. Additionally, the concentration of OPG also exponentially increases, contributing to larger amounts of the endosteal formation than resorption. As OPG is primarily released by the osteoblasts (Simonet et al., 1997; Yasuda et al., 1998), the increase in osteoblast cells results in an increase of OPG, which in turn prevents active osteoclasts from forming, by competitively binding with RANKL (represented by the OL parameter in the model). This positive feedback loop is partially mitigated by the OPG saturation parameter (OPG_{sat}). However, an adjustment to this parameter or the addition of an OPG degradation term may aid in limiting the amount of available OPG.

Another important development is the implementation of the external mechanical loading protocol within the model. The model could be adapted to mimic experimental protocol by applying solely physiological loading on days 1-7, 9, 11, 13 and 14, followed by external mechanical loading on days 8, 10, 12. This can be achieved by either running three micro-FE models with unitary loads in each Cartesian direction and linearly combining the results, or by directly implementing the load within the micro-FE model. The optimal approach should be determined by considering the computational cost. Additionally, a sensitivity analysis should be conducted to establish the optimal frequency for re-meshing and re-running the micro-FE model. This analysis should be based on updating the micro-FE model only when there are substantial geometrical changes or when the loading conditions change. To enable micro-FE model re-runs, a smoothing function must be applied between slices to prevent potentially sharp geometric transitions. Furthermore, appropriate boundary conditions for the section model need to be defined, as it is not a whole bone model. Alternatively, a sub-section micro-FE model could be considered. Both the smoothing and re-running processes should be automated.

Mechanosensation parameters also require optimisation through a systematic process to minimise errors compared to experimental week 20 data. Given that the micro-FE model takes 2 hours 30 minutes to run and the BCPM takes approximately 10 minutes, optimising the three sigmoidal functions with four parameters per function is expected to be computationally intensive. To enhance model efficiency, sensitivity analyses on the number, size, and distribution of RSEs should be performed. For instance, concentrating RSEs in regions identified as undergoing significant adaptation based on experimental data can potentially reduce computational costs without compromising model

accuracy. Improving the efficiency of the model will also allow for a larger section of the tibia to be investigated.

To further improve the interaction between the biomechanical and biochemical model components, additional regulatory pathways should be considered. In the current model, mechanical loading affects the cellular concentrations through the sigmoidal H functions. Biologically, mechanical loading affects the cellular concentrations indirectly, with the mechanical stimulus sensed by the osteocytes. Loading causes the osteocytes to release nitric oxide (NO), which downregulates RANKL production, decreasing the number of active osteoclasts. Osteocytes also release sclerostin (Scl), upregulating the Wnt/β-catenin pathway, and leading to an increase in active osteoblasts. NO and Scl are implicitly included in this model through the mechanical sigmoidal H functions. However, a previous mechanobiological, by Martin et al. (2019, 2020), has explicitly modelled both of these molecules.

For the biomechano-chemo model to be utilised for investigations of osteoporosis treatments the PTH injection term in the model requires further development. Currently, an external dose of PTH within the model causes an exponential increase in formation on both the periosteal and endosteal surfaces. Additional information on the drug acceptance and clearance from the mouse body (PTH pharmacokinetics (PK)) are required. However, there is a lack of literature available on PTH PK data relating to the mouse. A single source of PTH PK data (Cheloha et al., 2014), derived from a limited sample of three young adult male C57BL/6 mice was found. Therefore, the applicability of this data to the current model is questionable due to the restricted sample size and differences in age and gender. Regardless, this data may provide a preliminary foundation for developing the PK model. Once the PTH injection term has been updated, investigations into the optimal dose, frequency and timing of PTH administrations can be conducted.

The current biomechano-chemo model includes terms which describe the combined relationship between PTH and mechanical loading (Eqs. 5.17 and 5.18). These are included so that future iterations of the model can explore combined mechanical loading and PTH treatments. Combined treatments have been shown to have increased benefits over individual treatments in C57BL/6 mice, particularly in the mid-diaphysis. Therefore, the model should be leveraged to determine the optimal combined treatment regime.

In conclusions, this feasibility study demonstrates the potential of combined micro-FE and BCPM models to predict bone adaptation over time. However, substantial refinements are necessary to improve the predictive accuracy of the model with respect to experimental data. While this study utilised longitudinal *in vivo* data from a single mouse subjected to external mechanical loading, the available dataset includes five additional mechanically loaded mice, six PTH-treated mice, and twelve

mice exposed to two variations of combined mechanical loading and PTH treatment. It is recommended that this data be employed to validate the model's predictive capabilities. The current model can already be used to perform sensitivity analyses on several of the model parameters, in order to understand if the complexity of the model can be reduced and to learn more about the effect of these parameters on bone adaptation over space and time.

5.5 References

Alexander, J. M., Bab, I., Fish, S., Müller, R., Uchiyama, T., Gronowicz, G., et al. (2001). Human parathyroid hormone 1-34 reverses bone loss in ovariectomized mice. J. Bone Miner. Res. 16, 1665–1673. doi: 10.1359/jbmr.2001.16.9.1665

Ashrafi, M., Gubaua, J. E., Pereira, J. T., Gahlichi, F., and Doblaré, M. (2020). A mechano-chemo-biological model for bone remodeling with a new mechano-chemo-transduction approach. Biomech. Model. Mechanobiol. 19, 2499–2523. doi: 10.1007/s10237-020-01353-0

Birkhold, A. I., Razi, H., Duda, G. N., Weinkamer, R., Checa, S., and Willie, B. M. (2014). The influence of age on adaptive bone formation and bone resorption. Biomaterials 35, 9290–9301. doi: 10.1016/j.biomaterials.2014.07.051

Borggrefe, J., Graeff, C., Nickelsen, T. N., Marin, F., and Glüer, C. C. (2010). Quantitative computed tomographic assessment of the effects of 24 months of teriparatide treatment on 3D femoral neck bone distribution, geometry, and bone strength: results from the EUROFORS study. J. Bone Miner. Res. 25, 472–481. doi: 10.1359/jbmr.090820

Buenzli, P. R., Pivonka, P., Gardiner, B. S., and Smith, D. W. (2012). Modelling the anabolic response of bone using a cell population model. J. Theor. Biol. 307, 42–52. doi: 10.1016/j.jtbi.2012.04.019

Cheloha, R. W., Maeda, A., Dean, T., Gardella, T. J., and Gellman, S. H. (2014). Backbone modification of a polypeptide drug alters duration of action in vivo. Nat. Biotechnol. 32, 653. doi: 10.1038/nbt.2920

Cheong, V. S., Campos Marin, A., Lacroix, D., and Dall'Ara, E. (2020a). A novel algorithm to predict bone changes in the mouse tibia properties under physiological conditions. Biomech. Model. Mechanobiol. 19, 985–1001. doi: 10.1007/s10237-019-01266-7

Cheong, V. S., Kadirkamanathan, V., and Dall'Ara, E. (2021a). The role of the loading condition in predictions of bone adaptation in a mouse tibial loading model. Front. Bioeng. Biotechnol. 9, 676867. doi: 10.3389/fbioe.2021.676867

Cheong, V. S., Roberts, B. C., Kadirkamanathan, V., and Dall'Ara, E. (2020b). Bone remodelling in the mouse tibia is spatio-temporally modulated by oestrogen deficiency and external mechanical loading: a combined in vivo/in silico study. Acta Biomater. 116, 302–317. doi: 10.1016/j.actbio.2020.09.011

Cheong, V. S., Roberts, B. C., Kadirkamanathan, V., and Dall'Ara, E. (2021b). Positive interactions of mechanical loading and PTH treatments on spatio-temporal bone remodelling. Acta Biomater. 136, 291–305. doi: 10.1016/j.actbio.2021.09.035

Christiansen, B. A. (2016). Effect of micro-computed tomography voxel size and segmentation method on trabecular bone microstructure measures in mice. Bone Reports 5, 136–140. doi: 10.1016/j.bonr.2016.05.006

Danhof, M., De Jongh, J., De Lange, E. C. M., Della Pasqua, O., Ploeger, B. A., and Voskuyl, R. A. (2007). Mechanism-based pharmacokinetic-pharmacodynamic modeling: Biophase distribution, receptor theory, and dynamical systems analysis. Annu. Rev. Pharmacol. Toxicol. 47, 357–400. doi: 10.1146/annurev.pharmtox.47.120505.105154

De Souza, R. L., Matsuura, M., Eckstein, F., Rawlinson, S. C. F., Lanyon, L. E., and Pitsillides, A. A. (2005). Non-invasive axial loading of mouse tibiae increases cortical bone formation and modifies trabecular organization: A new model to study cortical and cancellous compartments in a single loaded element. Bone 37, 810–818. doi: 10.1016/j.bone.2005.07.022

Fritton, J. C., Myers, E. R., Wright, T. M., and Van Der Meulen, M. C. H. (2005). Loading induces site-specific increases in mineral content assessed by microcomputed tomography of the mouse tibia. Bone 36, 1030–1038. doi: 10.1016/j.bone.2005.02.013

Galea, G. L., Delisser, P. J., Meakin, L., Price, J. S., and Windahl, S. H. (2020). Bone gain following loading is site-specifically enhanced by prior and concurrent disuse in aged male mice. Bone 133. doi: 10.1016/j.bone.2020.115255

Graeff, C., Chevalier, Y., Charlebois, M., Varga, P., Pahr, D., Nickelsen, T. N., et al. (2009). Improvements in vertebral body strength under teriparatide treatment assessed in vivo by finite element analysis: results from the EUROFORS study. J. Bone Miner. Res. 24, 1672–1680. doi: 10.1359/jbmr.090416

Iida-Klein, A., Lu, S. S., Cosman, F., Lindsay, R., and Dempster, D. W. (2007). Effects of cyclic vs. daily treatment with human parathyroid hormone (1-34) on murine bone structure and cellular activity. Bone 40, 391–398. doi: 10.1016/j.bone.2006.09.010

Jilka, R. L. (2013). The relevance of mouse models for investigating age-related bone loss in humans. Journals Gerontol. Ser. A 68, 1209–1217. doi: 10.1093/gerona/glt046

Lavaill, M., Trichilo, S., Scheiner, S., Forwood, M. R., Cooper, D. M. L., and Pivonka, P. (2020). Study of the combined effects of PTH treatment and mechanical loading in postmenopausal osteoporosis using a new mechanistic PK-PD model. Biomech. Model. Mechanobiol. 19, 1765–1780. doi: 10.1007/s10237-020-01307-6

Lemaire, V., Tobin, F. L., Greller, L. D., Cho, C. R., and Suva, L. J. (2004). Modeling the interactions between osteoblast and osteoclast activities in bone remodeling. J. Theor. Biol. 229, 293–309. doi:

10.1016/j.jtbi.2004.03.023

Lerebours, C., Buenzli, P. R., Scheiner, S., and Pivonka, P. (2016). A multiscale mechanobiological model of bone remodelling predicts site-specific bone loss in the femur during osteoporosis and mechanical disuse. Biomech. Model. Mechanobiol. 15, 43–67. doi: 10.1007/s10237-015-0705-x

Lu, Y., Boudiffa, M., Dall'Ara, E., Bellantuono, I., and Viceconti, M. (2016). Development of a protocol to quantify local bone adaptation over space and time: quantification of reproducibility. J. Biomech. 49, 2095–2099. doi: 10.1016/j.jbiomech.2016.05.022

Lu, Y., Boudiffa, M., Dall'Ara, E., Liu, Y., Bellantuono, I., and Viceconti, M. (2017). Longitudinal effects of Parathyroid Hormone treatment on morphological, densitometric and mechanical properties of mouse tibia. J. Mech. Behav. Biomed. Mater. 75, 244–251. doi: 10.1016/j.jmbbm.2017.07.034

Main, R. P., Shefelbine, S. J., Meakin, L. B., Silva, M. J., van der Meulen, M. C. H., and Willie, B. M. (2020). Murine axial compression tibial loading model to study bone mechanobiology: implementing the model and reporting results. J. Orthop. Res. 38, 233–252. doi: 10.1002/jor.24466

Marques, F. C., Boaretti, D., Walle, M., Scheuren, A. C., Schulte, F. A., and Müller, R. (2023). Mechanostat parameters estimated from time-lapsed in vivo micro-computed tomography data of mechanically driven bone adaptation are logarithmically dependent on loading frequency. Front. Bioeng. Biotechnol. 11, 1140673. doi: 10.3389/fbioe.2023.1140673

Martin, M., Sansalone, V., Cooper, D. M. L., Forwood, M. R., and Pivonka, P. (2019). Mechanobiological osteocyte feedback drives mechanostat regulation of bone in a multiscale computational model. Biomech. Model. Mechanobiol. 18, 1475–1496. doi: 10.1007/s10237-019-01158-w

Martin, M., Sansalone, V., Cooper, D. M. L., Forwood, M. R., and Pivonka, P. (2020). Assessment of romosozumab efficacy in the treatment of postmenopausal osteoporosis: Results from a mechanistic PK-PD mechanostat model of bone remodeling. Bone 133, 115223. doi: 10.1016/j.bone.2020.115223

Martínez-Reina, J., and Pivonka, P. (2019). Effects of long-term treatment of denosumab on bone mineral density: insights from an in-silico model of bone mineralization. Bone 125. doi: 10.1016/j.bone.2019.04.022

Matic, I., Matthews, B. G., Wang, X., Dyment, N. A., Worthley, D. L., Rowe, D. W., et al. (2016). Quiescent bone lining cells are a major source of osteoblasts during adulthood. Stem Cells 34, 2930–2942. doi: 10.1002/stem.2474

Meakin, L. B., Todd, H., Delisser, P. J., Galea, G. L., Moustafa, A., Lanyon, L. E., et al. (2017). Parathyroid hormone's enhancement of bones' osteogenic response to loading is affected by ageing in a dose- and

time-dependent manner. Bone 98, 59–67. doi: 10.1016/j.bone.2017.02.009

Miller, C. (2023). Mechanostat regulation of cortical bone adaptation due to PTH and mechanical loading: Insights from image analysis and in silico modelling of the mouse tibia. Queensland University of Technology. doi: 10.5204/thesis.eprints.244742

Miller, C. J., Pickering, E., Martelli, S., Dall'Ara, E., Delisser, P., and Pivonka, P. (2024). Cortical bone adaptation response is region specific, but not peak load dependent: insights from μCT image analysis and mechanostat simulations of the mouse tibia loading model. Biomech. Model. Mechanobiol. 23, 287–304. doi: 10.1007/s10237-023-01775-6

Moraiti, S., Cheong, V. S., Dall'Ara, Enrico Kadirkamanathan, V., and Bhattacharya, P. (2024). A novel framework for elucidating the effect of mechanical loading on ovariectomized mouse tibia geometry using Principal Component Analysis. Front Bioeng Biotechnol. 12:1469272. doi: 10.3389/fbioe.2024.1469272

Oliviero, S., Cheong, V. S., Roberts, B. C., Orozco Diaz, C. A., Griffiths, W., Bellantuono, I., et al. (2022). reproducibility of densitometric and biomechanical assessment of the mouse tibia from in vivo micro-CT images. Front. Endocrinol. (Lausanne). 13, 915938. doi: 10.3389/fendo.2022.915938

Oliviero, S., Giorgi, M., and Dall'Ara, E. (2018). Validation of finite element models of the mouse tibia using digital volume correlation. J. Mech. Behav. Biomed. Mater. 86, 172–184. doi: 10.1016/j.jmbbm.2018.06.022

Oliviero, S., Giorgi, M., Laud, P. J., and Dall'Ara, E. (2019). Effect of repeated in vivo microCT imaging on the properties of the mouse tibia. PLoS One 14, e0225127. doi: 10.1371/journal.pone.0225127

Oliviero, S., Lu, Y., Viceconti, M., and Dall'Ara, E. (2017). Effect of integration time on the morphometric, densitometric and mechanical properties of the mouse tibia. J. Biomech. 65, 203–211. doi: 10.1016/j.jbiomech.2017.10.026

Oliviero, S., Owen, R., Reilly, G. C., Bellantuono, I., and Dall'Ara, E. (2021a). Optimization of the failure criterion in micro-Finite Element models of the mouse tibia for the non-invasive prediction of its failure load in preclinical applications. J. Mech. Behav. Biomed. Mater. 113, 104190. doi: 10.1016/j.jmbbm.2020.104190

Oliviero, S., Roberts, M., Owen, R., Reilly, G. C., Bellantuono, I., and Dall'Ara, E. (2021b). Non-invasive prediction of the mouse tibia mechanical properties from microCT images: comparison between different finite element models. Biomech. Model. Mechanobiol. 20, 941–955. doi: 10.1007/s10237-021-01422-y

Patel, T. K., Brodt, M. D., and Silva, M. J. (2014). Experimental and finite element analysis of strains induced by axial tibial compression in young-adult and old female C57Bl/6 mice. J. Biomech. 47, 451–457. doi: 10.1016/j.jbiomech.2013.10.052

Peterson, M. C., and Riggs, M. M. (2010). A physiologically based mathematical model of integrated calcium homeostasis and bone remodeling. Bone 46, 49–63. doi: 10.1016/j.bone.2009.08.053

Pivonka, P., Buenzli, P. R., and Dunst, C. R. (2012). A systems approach to understanding bone cell interactions in health and disease. Cell Interact. doi: 10.5772/51149

Pivonka, P., Zimak, J., Smith, D. W., Gardiner, B. S., Dunstan, C. R., Sims, N. A., et al. (2008). Model structure and control of bone remodeling: a theoretical study. Bone 43, 249–263. doi: 10.1016/j.bone.2008.03.025

Pivonka, P., Zimak, J., Smith, D. W., Gardiner, B. S., Dunstan, C. R., Sims, N. A., et al. (2010). Theoretical investigation of the role of the RANK–RANKL–OPG system in bone remodeling. J. Theor. Biol. 262, 306–316. doi: 10.1016/j.jtbi.2009.09.021

Rachner, T. D., Khosla, S., and Hofbauer, L. C. (2011). Osteoporosis: now and the future. Lancet 377, 1276–1287. doi: 10.1016/s0140-6736(10)62349-5

Razi, H., Birkhold, A. I., Weinkamer, R., Duda, G. N., Willie, B. M., and Checa, S. (2015a). Aging leads to a dysregulation in mechanically driven bone formation and resorption. J. Bone Miner. Res. 30, 1864–1873. doi: 10.1002/jbmr.2528

Razi, H., Birkhold, A. I., Zaslansky, P., Weinkamer, R., Duda, G. N., Willie, B. M., et al. (2015b). Skeletal maturity leads to a reduction in the strain magnitudes induced within the bone: A murine tibia study. Acta Biomater. 13, 301–310. doi: 10.1016/j.actbio.2014.11.021

Roberts, B. C., Arredondo Carrera, H. M., Zanjani-pour, S., Boudiffa, M., Wang, N., Gartland, A., et al. (2020). PTH(1–34) treatment and/or mechanical loading have different osteogenic effects on the trabecular and cortical bone in the ovariectomized C57BL/6 mouse. Sci. Reports 2020 101 10, 1–16. doi: 10.1038/s41598-020-65921-1

Roberts, B. C., Cheong, V. S., Oliviero, S., Carrera, H. M. A., Wang, N., Gartland, A., et al. (2023). Combining PTH(1-34) and mechanical loading has increased benefit to tibia bone mechanics in ovariectomised mice. J. Orthop. Res. doi: 10.1002/jor.25777

Roberts, B. C., Giorgi, M., Oliviero, S., Wang, N., Boudiffa, M., and Dall'Ara, E. (2019). The longitudinal effects of ovariectomy on the morphometric, densitometric and mechanical properties in the murine tibia: A comparison between two mouse strains. Bone 127, 260–270. doi: 10.1016/j.bone.2019.06.024

Scheuren, A. C., Vallaster, P., Kuhn, G. A., Paul, G. R., Malhotra, A., Kameo, Y., et al. (2020). Mechano-regulation of bone adaptation is controlled by the local in vivo environment and logarithmically dependent on loading frequency. doi: 10.1101/2020.05.15.097998

Schulte, F. A., Ruffoni, D., Lambers, F. M., Christen, D., Webster, D. J., Kuhn, G., et al. (2013a). Local mechanical stimuli regulate bone formation and resorption in mice at the tissue level. PLoS One 8, e62172. doi: 10.1371/journal.pone.0062172

Schulte, F. A., Zwahlen, A., Lambers, F. M., Kuhn, G., Ruffoni, D., Betts, D., et al. (2013b). Strain-adaptive in silico modeling of bone adaptation--a computer simulation validated by in vivo micro-computed tomography data. Bone 52, 485–492. doi: 10.1016/j.bone.2012.09.008

Simonet, W. S., Lacey, D. L., Dunstan, C. R., Kelley, M., Chang, M. S., Lüthy, R., et al. (1997). Osteoprotegerin: a novel secreted protein involved in the regulation of bone density. Cell 89, 309–319. doi: 10.1016/s0092-8674(00)80209-3

Stadelmann, V. A., Hocke, J., Verhelle, J., Forster, V., Merlini, F., Terrier, A., et al. (2009). 3D strain map of axially loaded mouse tibia: a numerical analysis validated by experimental measurements. Comput. Methods Biomech. Biomed. Engin. 12, 95–96. doi: 10.1080/10255840903077287

Stratford, R., Vu, C., Sakon, J., Katikaneni, R., Gensure, R., and Ponnapakkam, T. (2014). Pharmacokinetics in rats of a long-acting human parathyroid hormone–collagen binding domain peptide construct. J. Pharm. Sci. 103, 768–775. doi: 10.1002/jps.23843

Sugiyama, T., Saxon, L. K., Zaman, G., Moustafa, A., Sunters, A., Price, J. S., et al. (2008). Mechanical loading enhances the anabolic effects of intermittent parathyroid hormone (1–34) on trabecular and cortical bone in mice. Bone 43, 238–248. doi: 10.1016/j.bone.2008.04.012

Trichilo, S., Scheiner, S., Forwood, M., Cooper, D. M. L., and Pivonka, P. (2019). Computational model of the dual action of PTH — application to a rat model of osteoporosis. J. Theor. Biol. 473, 67–79. doi: 10.1016/j.jtbi.2019.04.020

Watson, S. L., Weeks, B. K., Weis, L. J., Harding, A. T., Horan, S. A., and Beck, B. R. (2018). High-intensity resistance and impact training improves bone mineral density and physical function in postmenopausal women with osteopenia and osteoporosis: the LIFTMOR randomized controlled trial. J. Bone Miner. Res. 33, 211–220. doi: 10.1002/jbmr.3284

Wein, M. N. (2017). Bone lining cells: normal physiology and role in response to anabolic osteoporosis treatments. Curr. Mol. Biol. Reports 2, 79–84. doi: 10.1007/s40610-017-0062-x

Wu, M., Chen, G., and Li, Y. P. (2016). TGF-β and BMP signaling in osteoblast, skeletal development,

and bone formation, homeostasis and disease. Bone Res. 4, 16009. doi: 10.1038/boneres.2016.9

Yang, H., Butz, K. D., Duffy, D., Niebur, G. L., Nauman, E. A., and Main, R. P. (2014). Characterization of cancellous and cortical bone strain in the in vivo mouse tibial loading model using microCT-based finite element analysis. Bone 66, 131–139. doi: 10.1016/j.bone.2014.05.019

Yasuda, H., Shima, N., Nakagawa, N., Mochizuki, S. I., Yano, K., Fujise, N., et al. (1998). Identity of osteoclastogenesis inhibitory factor (OCIF) and osteoprotegerin (OPG): a mechanism by which OPG/OCIF inhibits osteoclastogenesis in vitro. Endocrinology 139, 1329–1337. doi: 10.1210/endo.139.3.5837

Yeam, C. T., Chia, S., Tan, H. C. C., Kwan, Y. H., Fong, W., and Seng, J. J. B. (2018). A systematic review of factors affecting medication adherence among patients with osteoporosis. Osteoporos. Int. doi: 10.1007/s00198-018-4759-3

Zhang, Y., Dall'Ara, E., Viceconti, M., and Kadirkamanathan, V. (2019). A new method to monitor bone geometry changes at different spatial scales in the longitudinal in vivo µCT studies of mice bones. PLoS One 14, e0219404. doi: 10.1371/journal.pone.0219404

Zhao, R., Zhao, M., and Xu, Z. (2015). The effects of differing resistance training modes on the preservation of bone mineral density in postmenopausal women: a meta-analysis. Osteoporos. Int. 26, 1605–1618. doi: 10.1007/s00198-015-3034-0

Chapter 6: Myeloma bone disease affects the local mechanical properties of the mouse femur

This chapter is based on the following manuscript in preparation:

Myeloma bone disease affects the local mechanical properties of the mouse femur

Farage-O'Reilly S.M., Evans H., Andrews R., Trend J., Lovric G., Cheong V.S., Lawson M., Dall'Ara E.

To be submitted to Biomechanics and Modeling in Mechanobiology.

The contents of this chapter investigate the effect of myeloma bone disease (MBD) on the local mechanical properties of the mouse femur. For this study, the pipeline developed during Chapters 3 and 4 has been adapted to study the bone properties of mice affected by multiple myeloma (MM). The pipeline was modified to use synchrotron radiation computed tomography images as inputs, which have a much higher resolution than the *in vivo* micro-CT images used in previous chapters (0.65 µm compared to 10.4 µm), and focus at a lower dimensional scale (in a small portion of the cortical bone tissue). The images were provided by the Sheffield Multiple Myeloma group led by Dr Michelle Lawson. Some pre-processing of the images (cropping and segmentation) and analyses (porosity, osteocyte number, osteocyte volume) have been performed by my collaborator Ms Holly Evans (Department of Clinical Medicine, University of Sheffield).

Abstract

Introduction: Myeloma bone disease (MBD), a life-altering complication of multiple myeloma (MM), affects 80-90% of MM patients at some point during their cancer journey. The loss of trabecular bone, the decrease in bone mineral density, and the formation of lytic lesions all increase the risk of fracture. MM patients who experience a fracture have an increased mortality rate of 20% compared to those without a fracture. Understanding how MM affects the local bone mechanical properties is fundamental to develop MM treatments and establish risk of fracture in patients with MBD. The aim of this study was to develop an understanding of how MM affects the local bone mechanical properties in a murine myeloma bone disease model.

Methods: Nine 9–10-week-old female NOD scid gamma (NOD.Cg-Prkdcscidll2rgtm1Wjl/SzJ, NSG) mice were injected with 106 U266-GFP-luc cells (Disease group, n=4) or PBS (NSG, Naïve group, n=5). At 10 weeks post-inoculation, all mice were sacrificed. The right femora were removed and scanned close to the growth plate using synchrotron radiation computed tomography (SR-micro-CT; 0.65 µm voxel size). Four cube-shaped regions of interest were isolated, located 100µm proximally from the edge of the distal femoral growth plate, in the anterior, posterior, medial and lateral regions (avoiding bone lesions and blood vessels). The porosity of each cube was measured after segmentation by applying a single level threshold. SR-micro-CT based isotropic, homogeneous (E=14.8GPa, v=0.3) micro-finite element (micro-FE) models were generated from the segmented images. The model was loaded by a prescribed uniaxial displacement resulting in 1% apparent compressive strain along each of the three Cartesian directions, independently. The normalised apparent stiffness was calculated as the ratio between the sum of the reaction forces and the applied displacement, normalised for the size of the cube. The degree of anisotropy (DA) was calculated as the ratio between the maximum and minimum stiffness values among the three Cartesian directions.

Results: The preliminary results show that there was higher normalised stiffness values found in the Naïve group for the anterior ($p < 0.001$, +7.34%), posterior ($p = 0.012$, +3.85%), and lateral ($p = 0.014$, +3.21%) locations in the bone, compared to the Disease group (Mann-Whitney U test). Higher local degree of anisotropy (+1.75% to +8.44%) was found in the Disease group compared to the Naïve group for the anterior ($p = 0.032$, +8.44%) and lateral ($p = 0.032$, +5.10%) locations.

Conclusion: This preliminary study has shown that MM affects the local mechanical properties of the cortical bone tissue, by increasing the DA in the anterior and lateral areas of the bone. Considering that the models were designed to evaluate the mechanical properties of the tissues without lesions or blood vessels, the results suggest that MBD affects the properties and distributions of the osteocyte

lacunae, which affect the mechanical properties of the tissue regionally. However, it must be notes that this study is limited in the number and location of the regions of interest extracted from the bone.

6.1 Introduction

Bone is a dynamic tissue which changes over time due to both biomechanical and biochemical stimuli. In healthy bone, there is a balance between the remodelling undertaken by the osteoblasts, i.e., the bone forming cells, and the osteoclasts, i.e., the bone resorbing cells. This process is said to be orchestrated by the osteocytes, which reside within the bone matrix, embedded in lacunae and interconnected via the lacuna-canalicular network (LCN) (Bonewald, 2011; Robling and Bonewald, 2020). In diseased bone, the balance between the osteoblasts and osteoclasts can be disrupted. For example, in patients with multiple myeloma (MM), a type of bone marrow cancer, this delicate equilibrium is compromised, resulting in myeloma bone disease (MBD). MBD affects between 80-90% of patients during their cancer journey (Coleman, 1997; Kyle et al., 2003). It results in a loss of trabecular bone, a decrease in bone mineral density, and lytic lesions in both trabecular and cortical bone (Ring et al., 2018). These changes vary based on disease progression, but spine lumbar BMD has been reported to decrease by up to 11% within 18 months (Abildgaard et al., 1996, 2004). Patients often exhibit multiple lesions in various bone sites, with small lesions typically defined as less than 10 mm and large lesions exceeding this (Abildgaard et al., 2004; Muchtar et al., 2017). All these factors increase the patient's risk of fracture (Melton et al., 2005). Patients who experience fracture have an increased mortality rate of 20% compared to those without fracture (Saad et al., 2007).

The main body of MM research to date has been focused on osteoblasts and osteoclasts (Andrews et al., 2021; Ramezani et al., 2024), with limited research focusing on osteocyte bone cells and their environment, demonstrating the lack of knowledge on how MM affects the osteocyte lacunae. It is known that, in both humans and mice with MBD, the osteocyte lacunae change in number, size and shape (Giuliani et al., 2012; Ziouti et al., 2020; Evans et al., 2024). But, to the authors' knowledge, no research has investigated the effect of MBD on the mechanical properties of the cortical bone, taking into account the geometry and distribution of the osteocyte lacunae. Quantifying the mechanical properties at this dimensional scale experimentally is challenging, and no data is currently available.

Some studies within neighbouring bone research have modelled a single osteocyte lacuna and its surrounding matrix, often employing idealised geometries (Rath Bonivtch et al., 2007; Vaughan et al., 2013; Wang et al., 2015). However, to understand the complex role of the osteocyte lacuna within the bone matrix, geometrically accurate models are required. This has been done through the use of confocal imaging (Kamioka et al., 2001; Sugawara et al., 2005; Ciani et al., 2009; Sharma et al., 2012; Verbruggen et al., 2012, 2016; Kerschnitzki et al., 2013), scanning electron microscopy (Schneider et al., 2011), transmission electron microscopy (Kamioka et al., 2009, 2012), and ptychography (Dierolf et al., 2010). However, these techniques are limited by their acquisition time, spatial resolution or field

of view, often only capturing a few osteocyte lacunae. As an alternative, synchrotron radiation micro-computed tomography (SR-micro-CT) can be used (Schneider et al., 2010; Langer et al., 2012; Pacureanu et al., 2012; Varga et al., 2015). This allows for a larger volume of interest to be imaged.

SR-micro-CT has been shown to capture well the osteocyte lacunae, showing their location and distribution (Carter et al., 2013; Dong et al., 2014; Hesse et al., 2014; Evans et al., 2024). Furthermore, micro-FE models have been developed from SR-micro-CT images and used to predict strains within the bone matrix and the osteocyte lacunae (Hemmatian et al., 2021). This study was done in ageing mouse bone, using an image resolution of 0.7 µm. The high resolution allowed for multiple osteocyte lacunae within a cortical bone section to be modelled (Hemmatian et al., 2021). However, no studies to date have investigated the effect of MBD on the cortical bone mechanical properties, at a dimensional scale that includes the osteocyte lacunae.

Furthermore, the best current approach for MBD is to effectively treat the myeloma. There are also two alternative antiresorptive pharmacological treatments available for patients (bisphosphonates and denosumab), which suppress the osteoclasts and bone resorption but do not promote bone formation (Terpos et al., 2021). Due to this, even patients who reach remission from their cancer can be left in chronic pain, have poor mobility and a reduced quality of life as a result of the bone loss. This highlights the urgent need for novel therapeutic strategies. However, a comprehensive understanding of how MM impacts bone tissue is essential to develop effective treatments that address the underlying pathophysiology. The aim of this study was to investigate if MBD affects the local cortical bone stiffness, degree of anisotropy and strain distributions in a murine model.

6.2 Materials and methods

6.2.1 Experimental data, imaging and image processing

This sub-section of work was completed by Evans et al. (2024). In that study, bone from two murine models of MBD were assessed and compared to bones from healthy control mice. Using high-resolution imaging (SR-micro-CT) and histomorphometry, the structural changes of the osteocyte lacune (number, sphericity, volume) and the LCN (canalicular length and area) and investigated gene expression of key molecules in osteocytes were investigated. In this study, the local bone mechanical properties are investigated, using small regions of interest from within the SR-micro-CT images.

The images used in this study were acquired previously (Evans et al., 2024). Briefly, nine 9–10-week-old NOD scid gamma (NOD.Cg-PrkdcscidIl2rgtm1Wjl/SzJ, NSG) mice were injected with either PBS (N=5;

Naïve group) or U266-GFP-luc cells (xenograft model; N=4; Disease group). At 10 weeks post-inoculation, all the mice were sacrificed. All animal experiments were approved by the University of Sheffield Animal Ethics Committee and the UK Home Office (PPL PP3267943) in compliance with the Animal (Scientific Procedures) Act 1986.

The right femora were fixed in 10% formalin for 48 hours and then stored in 70% ethanol at study completion (Evans et al., 2024). The femora were scanned 100µm proximally from the distal growth plate (Figure 6.1), as this is an easily identifiable location within the femora across mice. The bones were scanned using synchrotron radiation micro-computed tomography (SR-micro-CT), in absorption and inline phase-contrast imaging mode (0.65µm voxel size; 3000 projections, 21keV beam energy (selected with a double-multilayer monochromator), 120ms exposure time, with a 360° rotation and a sample-to-detector propagation distance of 40mm, 250 micron thick Al filter, Paganin phase-retrieval filter) at the Swiss Light Source (TOMCAT beamline, Paul Scherrer Institut, Switzerland, Proposal ID 20220399).

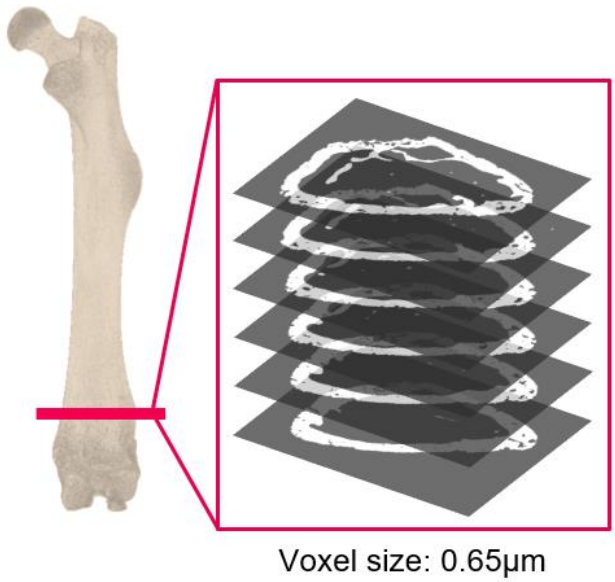

Figure 6.1: *The location of the region of the femora scanned. The region was located 100µm proximally from the distal growth plat and scanned using* synchrotron radiation micro-computed tomography (voxel size: 0.65µm).

The main steps of the image processing, creation of the micro-FE models, and post-processing to calculate the apparent mechanical properties of the considered regions of interest (ROIs) are reported in Figure 6.2.

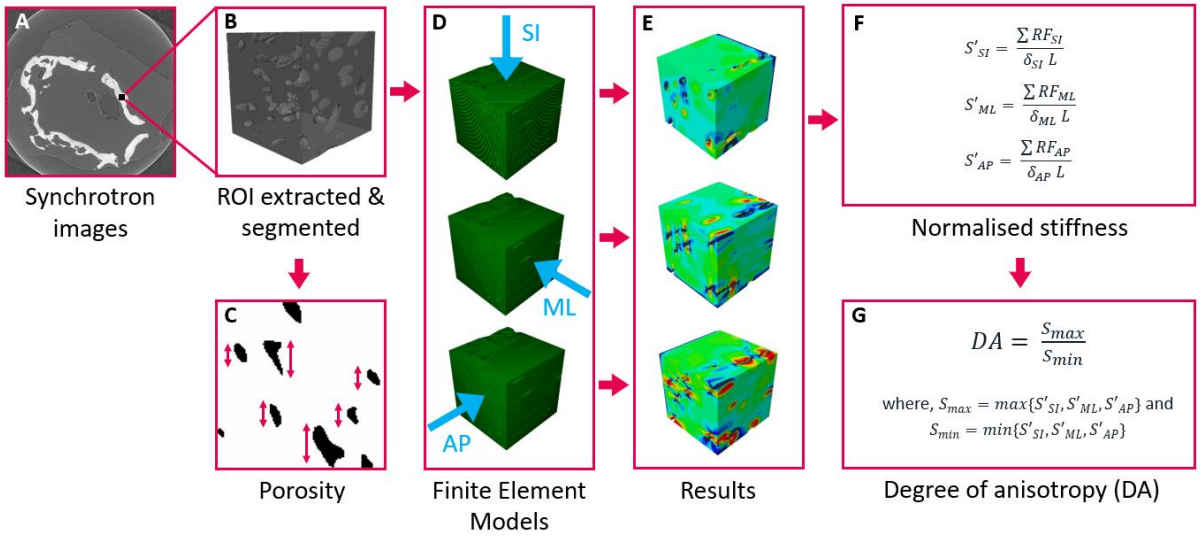

Figure 6.2: *Flowchart illustrating the main steps of the pipeline to create the micro-FE models from the SR-micro-CT images and to evaluate the apparent local mechanical properties: (A) SR-micro-CT acquisition, (B) region of interest (ROI) extraction and segmentation (binarisation), (C) calculation of the porosity from the extracted ROI, (D) micro-FE models, displaced independently in the superior-inferior (SI), medio-lateral (ML) and anterior-posterior (AP) directions, (E) results generation, post-processing of the reaction forces (RF), displacements (δL), and lengths of the ROI (L) to calculate the local mechanical properties ((F) the normalised stiffness and the (G) degree of anisotropy (DA)). Steps A, B and C were undertaken Evans et al. (2024).*

Four cube-shaped regions of interest (ROIs; 0.08 mm edge) were isolated 100µm proximally from the edge of the distal femoral growth plate (Figure 6.1) (Dragonfly v2022 for Windows, Object Research Systems (ORS) Inc, Montreal, Canada) (Evans et al., 2024). One ROI was extracted from each of the anterior, posterior, medial, and lateral portions of each bone. Each ROI was identified by avoiding both bone lesions and blood vessels, as the aim of the study was to evaluate the effect of MBD on the cortical bone tissue and not to evaluate the effect of the lesions.

The images were segmented by using a single-level threshold which was manually defined (Evans et al., 2024). To identify the osteocyte lacunae, a binary mask was created by filling in the internal pores within the binary image. The original porous bone image was subtracted from the filled binary mask. From the remaining volumes, the osteocyte lacunae were defined as smaller than 2000µm^3, vascular canals greater than 2000µm^3, and noise, defined as volumes of less than 25µm^3, were removed (Hemmatian et al., 2017; Evans et al., 2024). Porosity (%) was calculated as the volumetric ratio of

filtered osteocyte lacunae to the filled-in bone mask. The number of osteocyte lacunae and their volume (μm^3) were calculated automatically (Dragonfly v2022 for Windows, Object Research Systems (ORS) Inc, Montreal, Canada). To account for differences in bone volume between Diseased and Naïve group samples, the osteocyte lacunae volume was normalised by the respective bone volume and averaged for each ROI.

6.2.2 Micro-FE models

All segmented images were converted into micro-FE models by converting each bone voxel into a linear 8-node hexahedral element. Larger elements were not used as they would not enable a proper description of the differences in the osteocyte lacunae geometry between groups. Each model contained approximately 1.9 million nodes and 1.8 million elements. Isotropic, homogeneous, linear elastic material properties were used (E = 14.8 GPa, ν = 0.3). Due to a lack of experimental data being available for any MM murine models, the material properties have been taken from experimental measurements of the C57BL/6 mouse tibia (Webster et al., 2008; Oliviero et al., 2018). Therefore, it is important to note that the results should be interpreted relatively and not their absolute values. The inferior surface of the models was loaded by a prescribed uniaxial displacement resulting in a 1% apparent compressive strain along the each of the three directions, independently. This was done through the use of a control node, which connected the nodes on the distal surface via kinematic coupling to the control node which was located at the centroid of the distal surface with a small offset in the inferior direction. All nodes on the superior surface were constrained against the direction of applied displacement except for two nodes which were fixed in the transversal plane too, in order to prevent rigid body transformations. The three independent load cases (Figure 6.2 D) were identified by applying the displacements along the superior-inferior, medio-lateral or anterior-posterior directions, for each ROI. The minimum and maximum principal strains, and the reaction forces were calculated at the nodes. All input files for the models were generated in MATLAB. The models were solved in Abaqus 2018 (Dassault Systèmes Simulia, RI, USA) using the University of Sheffield High Performance Computing Clusters (Stanage).

6.2.3 Post processing

For each cube, at each direction, the apparent stiffness (N/mm) was calculated as the ratio between the sum of the reaction forces in that direction and the change in cube length (Eqs. 6.1 – 6.3).

$$S_{SI} = \frac{\sum RF_{SI}}{\delta_{SI}} \tag{6.1}$$

$$S_{ML} = \frac{\sum RF_{ML}}{\delta_{ML}}$$

(6.2)

$$S_{AP} = \frac{\sum RF_{AP}}{\delta_{AP}}$$

(6.3)

where, S_{SI}, S_{ML}, and S_{AP} are the stiffnesses in the superior-inferior, medio-lateral, or anterior-posterior directions, respectively; RF_{SI}, RF_{ML}, and RF_{AP} are the reaction forces in the corresponding directions (the reaction forces are a component of the total force and summed across the fixed nodes); and δ_{SI}, δ_{ML}, and δ_{AP} are the imposed displacements along each loading direction.

Subsequently, these values were normalised by the length of the cube (N/mm^2) (Eqs. 6.4 – 6.6).

$$S'_{SI} = \frac{S_{SI}}{L}$$

(6.4)

$$S'_{ML} = \frac{S_{ML}}{L}$$

(6.5)

$$S'_{AP} = \frac{S_{AP}}{L}$$

(6.6)

where, $S'_{axial,ML,AP}$ is the normalised stiffness in each the superior-inferior, medio-lateral, or anterior-posterior direction and L is the ROI length.

To evaluate the degree of mechanical anisotropy within each cube, the maximum and minimum stiffness values among its three directions were determined, and their ratio was computed (Eq. 6.7). This provided an insight into the directional dependence of the stiffness for each cube.

$$DA = \frac{S_{max}}{S_{min}}$$

(6.7)

where, DA is the degree of anisotropy for an ROI, $S_{max} = max\{S_{SI}, S_{ML}, S_{AP}\}$ and $S_{min} = min\{S_{SI}, S_{ML}, S_{AP}\}$.

6.2.4 Statistical analysis

The median and interquartile range (IQR) of the normalised stiffness, the DA, the porosity, and the osteocyte number and volume were calculated for both group (Naïve and Disease), and at each location of the ROI in the bone (anterior, posterior, medial, and lateral). The normalised stiffness median and IQR were also calculated for each direction (superior-inferior, medio-lateral, and anterior-posterior). Non-parametric tests were chosen due to the results not being normally distributed (Shapiro-Wilks test) and the small sample size. The difference between groups was assessed using the Mann-Whitney U test and the difference within groups was assessed using the non-parametric two-tailed Wilcoxon test. The statistical significance level was set at $\alpha = 0.05$ for all tests.

Linear regression analysis was used to test potential linear correlations between the normalised stiffness and the porosity, and the normalised stiffness and the osteocyte lacunae volume. These were done for the Disease (N=48) and Naïve (N=60) groups separately and for the pooled data (combined Naïve and Disease groups; N=108). The Disease group included normalised stiffnesses from 4 mice, with 4 ROIs extracted from each mouse. For each ROI, three normalised stiffness values were obtained, corresponding to the superior-inferior, medial-lateral and anterior-posterior directions (i.e., N: 4x4x3=48). While the Naïve group included normalised stiffnesses from 5 mice (i.e., N: 5x4x3=60). If the correlation was significant, the coefficient of determination (R^2), and the slope and intercept of the linear regression line was calculated. A similar analysis was performed between the DA and the porosity, and the DA and osteocyte lacunae volume, for the pooled data (N=36) and data split between Disease (N=16) and Naïve (N=20) groups (MATLAB, 2023A, The MathWorks Inc., Natick MA, USA).

6.3 Results

The results are reported as the median (IQR). The normalised stiffness in the Disease group (14300 (13600-14600) N/mm^2) was significantly lower than that of the Naïve group (14800 (14500-15000) N/mm^2) (-3.99%, $p < 0.001$; Figure 6.3). Conversely, the porosity in the Disease group (1.64 (1.39-2.16) %) was significantly higher than that of the Naïve group (0.86 (0.60-1.52) %, +59.52%, $p = 0.002$; Figure 6.3).

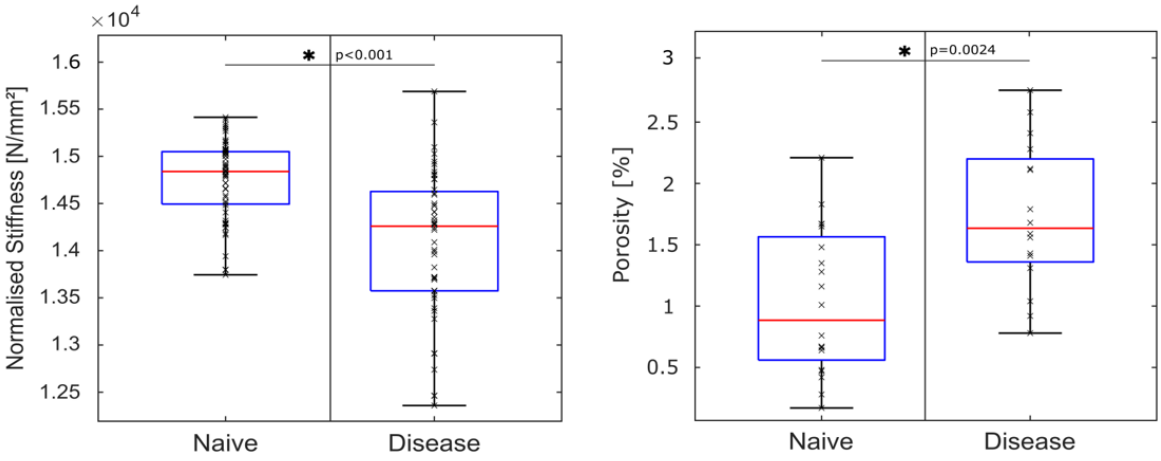

Figure 6.3: *The boxplots for the Naïve and Disease groups for the normalised stiffness (N/mm^2) (left) and the porosity (%) (right). The * indicates significance, when tested with the non-parametric two-tailed Mann-Whitney U test, with a significance level of 0.05.*

The normalised stiffness was significantly lower in the anterior (-7.34%, $p < 0.001$), posterior (-3.85%, $p = 0.012$) and lateral (-3.21%, $p = 0.014$) portions of the bone in the Disease group, when compared to the Naïve group (Figure 6.4). The comparisons between all locations for the normalised stiffness can be found in Appendix B (Figure B1), alongside the boxplots of the normalised stiffness for the Naïve and Disease groups for each ROI, for each loaded direction (Figure B2). The porosity was significantly higher only in the anterior portion of the bone in the Disease group compared to the Naïve group (+117.65%, $p = 0.016$, Figure 6.4). The comparisons between all locations for the porosity are reported in Appendix B (Figure B1).

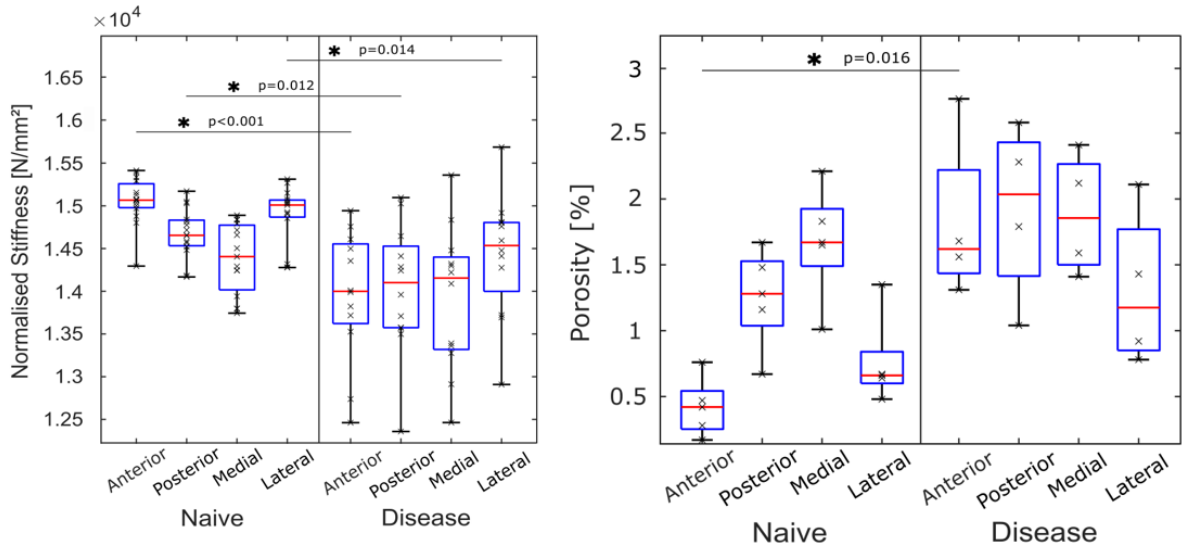

Figure 6.4: *The boxplots for the Naïve and Disease groups for each ROI location within the bone (anterior, posterior, medial, lateral) for the normalised stiffness (N/mm^2) (left) and the porosity (%) (right). The * indicates significance, when tested with the non-parametric two-tailed Mann-Whitney U test, with a significance level of 0.05.*

The degree of anisotropy (DA) increased in the anterior (+8.44%, p = 0.032) and lateral (+5.10%, p = 0.032) locations in the bone in the Disease group, compared to the Naïve group (Figure 6.5; Table 6.1; NB: a DA=1 suggests the material is isotropic). The comparisons between all locations for the DA are reported in Appendix B (Figure B1).

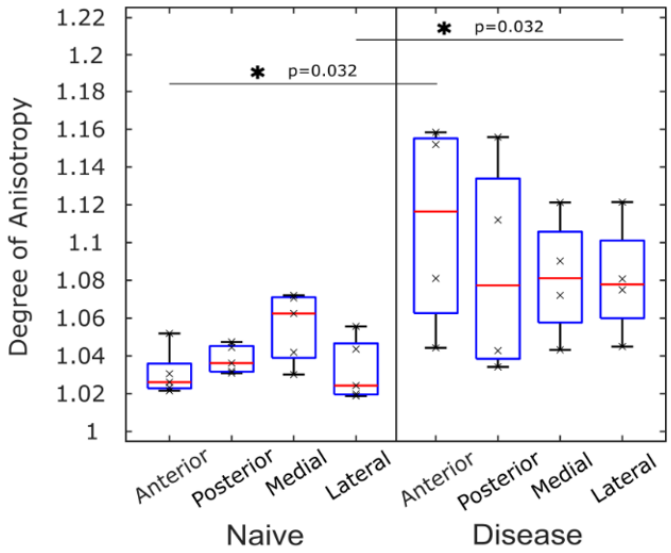

Figure 6.5: *The boxplots for the Naïve and Disease groups for each ROI location within the bone (anterior, posterior, medial, lateral) for the degree of anisotropy. The * indicates significance, when tested with the non-parametric two-tailed Mann-Whitney U test, with a significance level of 0.05.*

Table 6.1: *The degree of anisotropy (DA (%)) for each group and location of the ROI within the bone. Results are reported as median (IQR). The third column shows the percentage difference between the Naïve and Disease groups and the fourth column shows the respective p-values when tested with the non-parametric two-tailed Mann-Whitney U test, with a significance level of 0.05.*

DA (%)	Naïve	Disease	Percentage difference	P-value
Anterior	1.03 (1.02-1.03)	1.12 (1.07-1.15)	8.44 %	0.032
Posterior	1.04 (1.03-1.04)	1.08 (1.04-1.12)	3.90 %	0.286
Medial	1.06 (1.04-1.07)	1.08 (1.06-1.10)	1.76 %	0.111
Lateral	1.03 (1.02-1.04)	1.08 (1.07-1.09)	5.10 %	0.032

From the minimum principal strain distributions, it can generally be seen that the Disease group has higher strain values than the Naïve group. The strains are also more heterogeneously distributed in the Disease group than the Naïve group (two example ROIs can be seen in Figure 6.6).

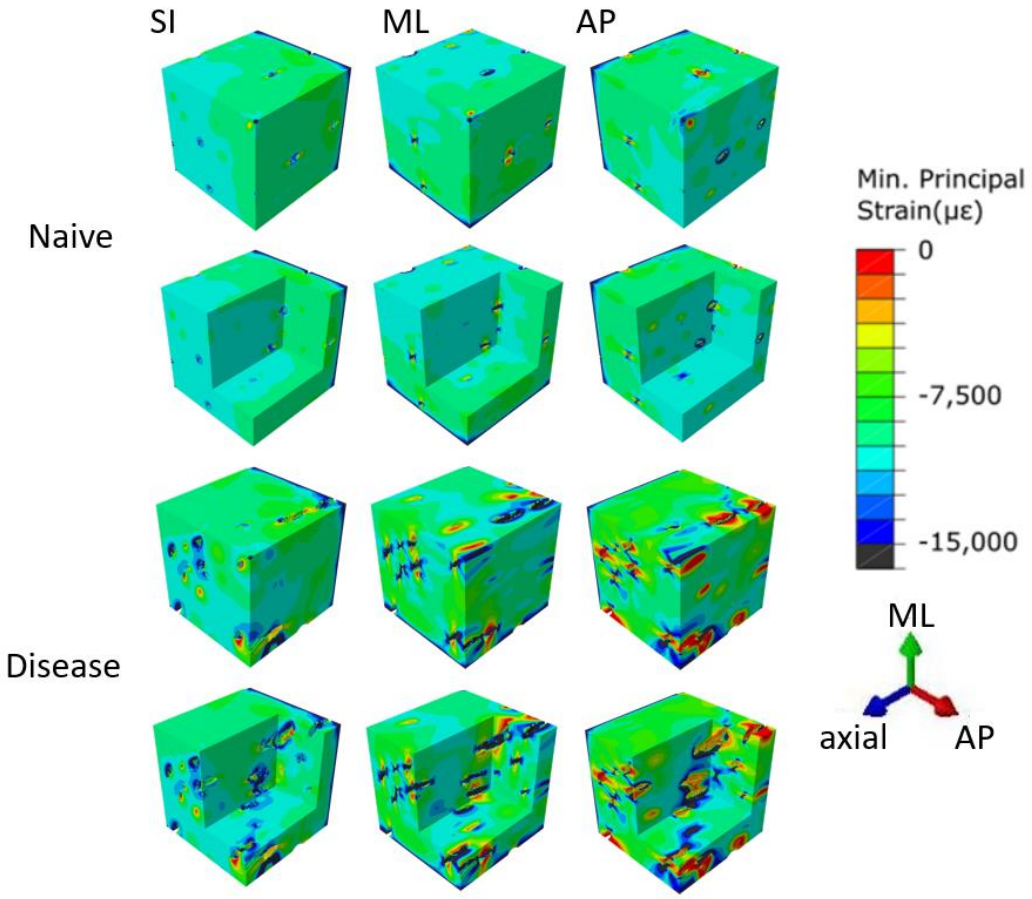

Figure 6.6: *An example ROI from each of the Naïve (top two sets of ROI) and Disease (bottom two sets of ROI) groups showing the minimum principal strain distributions when the ROI is loaded in the superior-inferior (SI), medio-lateral (ML), and the anterior-posterior (AP) cases.*

The osteocyte lacunae number in the Naïve group (35 (29-38.75)) was statistically higher than in the Disease group (26 (23.75-30.5); $p = 0.005$). In fact, the number of osteocyte lacunae was 30% less in the Disease group compared to the Naïve group (Figure 6.7). The osteocyte lacunae volume in the Disease group (334 (243-471) μm^3) was statistically higher than in the Naïve group (128 (93-190) μm^3; $p < 0.001$). In fact, the size of the osteocyte lacunae increased by 90% in the Disease group when compared to the Naïve group (Figure 6.7).

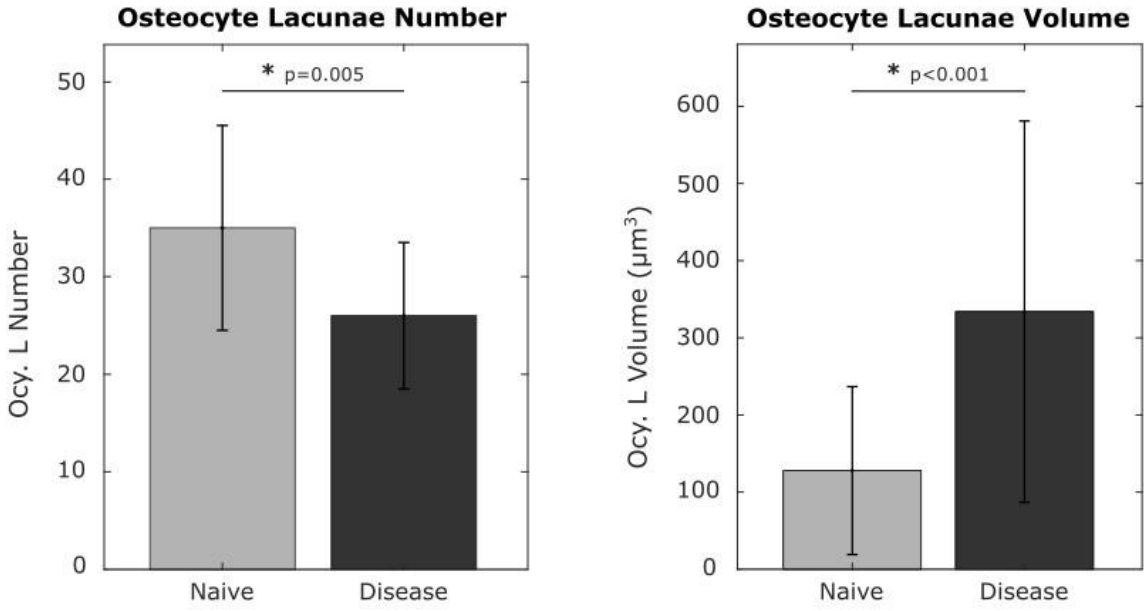

Figure 6.7: *The bar plots for the median number of osteocyte lacunae (left) and the median volume of the osteocyte lacunae (μm^3) (right) within the cube ROIs (0.08mm edge) for both the Naïve and Disease groups. The error bar represents the IQR. The * indicates significance, when tested with the non-parametric two-tailed Mann-Whitney U test, with a significance level of 0.05.*

In the pooled data (normalised stiffness for all loading directions) the porosity was correlated with the normalised stiffness but did not describe all the variability in mechanical properties (R^2: 52%, $p < 0.001$; Figure 6.8 A). The porosity described the normalised stiffness variability better for the Naïve group (R^2: 53%, $p < 0.001$; Figure 6.8 B blue) than for the Disease group (R^2: 37%, $p < 0.001$; Figure 6.8 B red). Similar trends existed for correlation between the DA and the porosity: they were correlated for the pooled DA (R^2: 47%, $p < 0.001$; Figure 6.8 C), and were better correlated with the Naïve group (R^2: 49%, $p < 0.001$; Figure 6.8 D blue) than the Disease group (R^2: 28%, $p = 0.035$; Figure 6.8 D red). The normalised stiffness pooled data (R^2: 53%, $p = 0.016$; Figure 6.8 E) and the DA pooled data (R^2: 32%, $p < 0.001$; Figure 6.8 G) were both correlated with the osteocyte lacunae volume, but neither the Naïve nor Disease groups for each were correlated with the osteocyte lacunae volume. Furthermore, the frequency plot demonstrating the variability of the number of osteocyte lacunae among the cubes is not normally distributed (Figure 6.9).

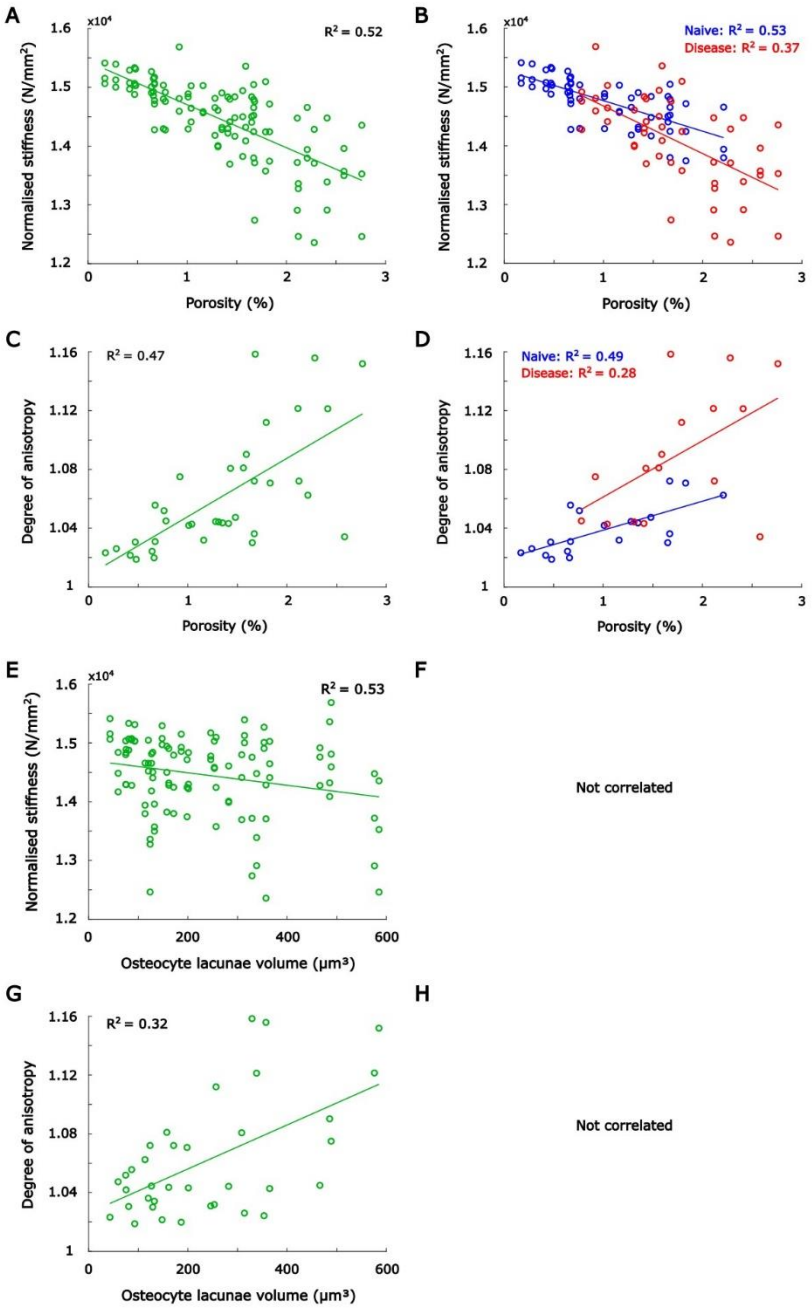

Figure 6.8: *The linear regressions for the (A) normalised stiffness and the porosity for the pooled Naïve and Disease data (green), (B) normalised stiffness and the porosity for the Naïve (blue) and Disease (red) groups, (C) the degree of anisotropy and the porosity for the pooled Naïve and Disease data (green), (D) the degree of anisotropy and the porosity for the Naïve (blue) and Disease (red) groups, (E) the normalised stiffness and the osteocyte lacunae volume for the pooled Naïve and Disease data (green), (F) the normalised stiffness and the osteocyte lacunae volume are not correlated for either the Naïve or the Disease groups, (G) the degree of anisotropy and the osteocyte lacunae volume for the pooled Naïve and Disease data (green), and (H) the degree of anisotropy and the osteocyte lacunae volume are not correlated for either the Naïve or the Disease groups.*

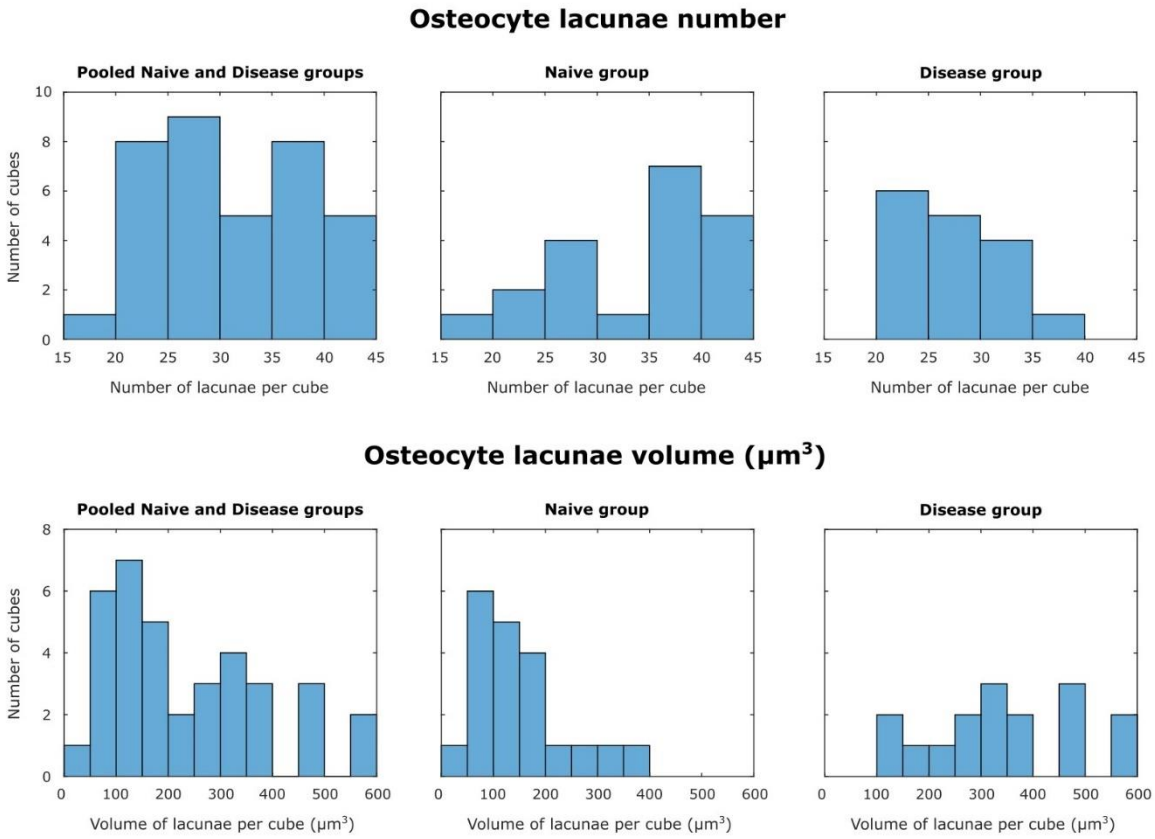

Figure 6.9: *The frequency plot showing the variability of the number of osteocyte lacunae among the ROIs and the variability of the osteocyte lacunae volume among the ROIs, for the pooled Naïve and Disease groups (left), the Naïve group (middle) and the Disease group (right).*

6.4 Discussion

The goal of this study was to investigate if MM affects the local bone mechanical properties in a murine model of MBD. Using micro-FE models based on SR-micro-CT images, the apparent local mechanical properties of multiple ROI taken from the distal region of the mouse femur were calculated. As expected, the porosity increased in the Disease group, compared to the Naïve group. Although the number of osteocyte lacunae decreased by 30% in the ROI in the Disease group, compared to the Naïve group, the osteocyte lacunae volume almost doubled. This is in line with a recent study, which showed a similar trend across the whole section of the same mouse femurs (Evans et al., 2024). This suggests that MBD may cause the osteocytes residing within the bone to undergo peri-lacunae remodelling (PLR), changing the size and distribution of the osteocyte lacunae, and hence the porosity (Evans et al., 2024).

The normalised stiffness was lower in the Disease group, compared to the Naïve group, confirming an inverse relationship between the normalised stiffness and the porosity (Figure 6.8). This inverse relationship was extended to the normalised stiffness and the porosity at each bone location (anterior, posterior, medial, lateral portions of the bone). Furthermore, the normalised stiffness was reduced in all considered regions of the bone except the medial region, indicating that as a result of the MBD, the ROI were less able to resist deformation in these areas.

The DA was higher in the anterior (8.44%) and lateral (5.10%) locations in the ROI from the Disease group compared to the ROI from the Naïve group, suggesting that MBD affects the local isotropy of the bone. These changes in the DA could be attributed to alterations in osteocyte lacunae due to MBD, as their number decreases and volume increases, affecting their distribution and orientation within the bone. These results show that the tissue surrounding the lacunae is anisotropic and varies between different regions. Therefore, micro-FE models, which consider the bone microstructure and exclude the lacunae and vessels, should consider this tissue anisotropy to accurately represent bone mechanical behaviour.

Higher strains can be seen in the Disease group compared to the Naïve group (Figure 6.5) as the osteocyte lacunae have a higher volume in the former. This is in line with a previous study which reported that higher strains occurred in the bone surrounding larger lacunae compared to smaller lacunae (Hemmatian et al., 2021). Additionally, it is known that MBD causes a decrease in canalicular length, network area coverage and altered organisation, comprising the LCN (Evans et al., 2024), which may also have an effect on the strain distribution. However, the spatial resolution of the images used in this study (0.65 µm) was insufficient to visualise the LCN. Acquiring higher resolution images would enable the creation of micro-FE models for both healthy and diseased bone, including the LCN and osteocyte lacunae from the matrix. This approach would facilitate investigations into the impact of altered LCN and osteocyte lacunae geometries on bone matrix properties.

While porosity is often correlated with bone mechanical properties, the linear regression analysis revealed a weak correlation between the porosity and both the normalised stiffness and the DA, suggesting that other factors contribute significantly to these properties. The distribution, orientation, and shape of osteocyte lacunae are potential contributors to this variability and warrant further investigation through multifactorial analysis. Micro-FE models offer a valuable tool to elucidate these complexities by providing detailed information on local strain distributions around lacunae, which cannot be captured through porosity analysis alone.

Multiple limitations need to be highlighted when discussing these models. Firstly, and most significantly, the material properties assigned to the model have been taken from a different strain of

mice (C57BL/6 mice in place of NSG mice) and a different bone (tibia in place of femur). No experimental data could be found in the literature on the mouse femur for MM models. This is required to be able to better inform the models. However, assuming both diseased and healthy MM bone have the same material properties, the relative differences in the results found in this study can be examined to study the effect of the change in geometry. However, due to the linearity of the models, any differences found in the material properties between the two groups could be accounted for by scaling the results found in this study. Additionally, homogenous, isotropic material properties were assumed for the model. Future investigations should consider heterogenous material properties, by using a monochromatic beam in place of a pink beam so that the local bone material properties can be calculated from the image grey levels. Additionally, the bone was considered within the range before yield, where bone generally exhibits a linear mechanical response. However, these material properties may not capture well the areas within the bone that are undergoing PLR. Areas undergoing PLR, which surround the osteocyte lacunae may not be mineralised and hence the material may not be as able to resist deformation. In this case, the models assumed that all bone had the same material properties, irrespective of the proximity to the osteocyte lacunae. Therefore, any differences between the two groups may be larger with modified material properties assigned to consider the lack of mineralisation in discrete areas in the bone due to PLR.

Another limitation is the number and location of the ROI extracted from the bone. The ROI had to avoid both bone lesions and blood vessels, as the aim of the study was to evaluate the effect of MM on the bone tissue and not to evaluate the effect of the lesions. Therefore, when the ROI were extracted, they were not taken from exactly the same location across the bones. Furthermore, it is known that the distribution of the osteocyte lacunae is heterogeneous, and their volume varies across location (Evans et al., 2024). Therefore, comparison of ROI between mice may be affected by the ROI location within the bone. More analyses of ROI taken from additional locations within the bone are needed to generalise the findings of this study. This is further highlighted through the results of the frequency plots which show the variability of the number of osteocyte lacunae among the cubes.

The results of this study, while not directly clinically applicable, could contribute to an organ-level model composed of elements the size of the modelled ROIs, with material properties assigned based on the data obtained. For example, models of the Disease group could incorporate the increased degree of anisotropy by defining anisotropic elastic tensors for the affected regions. Further studies could involve testing additional ROIs, particularly from mice subjected to treatments, to evaluate their effects on osteocyte lacunae.

In conclusion, this preliminary study has shown that MM affects the local mechanical properties of the bone, by reducing the normalised stiffness in the anterior, posterior, and lateral areas of the bone, and increasing the DA in the anterior and lateral areas of the bone. This suggests that MBD does not homogeneously affect the local mechanical properties of bone but instead affects them regionally. This should be taken into account when considering the mechanical properties in future models of MBD.

6.5 References

Abildgaard, N., Brixen, K., Eriksen, E. F., Kristensen, J. E., Nielsen, J. L., and Heickendorff, L. (2004). Sequential analysis of biochemical markers of bone resorption and bone densitometry in multiple myeloma. Haematologica. Available at: https://www.academia.edu/27887468/sequential_analysis_of_biochemical_markers_of_bone_resorption_and_bone_densitometry_in_multiple_myeloma (Accessed August 27, 2024).

Abildgaard, N., Brixen, K., Kristensen, J. E., Vejlgaard, T., Charles, P., and Nielsen, J. L. (1996). Assessment of bone involvement in patients with multiple myeloma using bone densitometry. Eur. J. Haematol. 57, 370–376. doi: 10.1111/j.1600-0609.1996.tb01395.x

Andrews, R. E., Brown, J. E., Lawson, M. A., and Chantry, A. D. (2021). Myeloma bone disease: the osteoblast in the spotlight. J. Clin. Med. 2021, Vol. 10, Page 3973 10, 3973. doi: 10.3390/jcm10173973

Bonewald, L. F. (2011). The amazing osteocyte. J. Bone Miner. Res. 26, 229–238. doi: 10.1002/jbmr.320

Carter, Y., Thomas, C. D. L., Clement, J. G., Peele, A. G., Hannah, K., and Cooper, D. M. L. (2013). Variation in osteocyte lacunar morphology and density in the human femur — a synchrotron radiation micro-CT study. Bone 52, 126–132. doi: 10.1016/j.bone.2012.09.010

Ciani, C., Doty, S. B., and Fritton, S. P. (2009). An effective histological staining process to visualize bone interstitial fluid space using confocal microscopy. Bone 44, 1015–1017. doi: 10.1016/j.bone.2009.01.376

Coleman, R. E. (1997). Skeletal complications of malignancy. Cancer 80, 1588–1594. doi: 10.1002/(sici)1097-0142(19971015)80:8

Dierolf, M., Menzel, A., Thibault, P., Schneider, P., Kewish, C. M., Wepf, R., et al. (2010). Ptychographic X-ray computed tomography at the nanoscale. Nat. 2010 4677314 467, 436–439. doi: 10.1038/nature09419

Dong, P., Haupert, S., Hesse, B., Langer, M., Gouttenoire, P. J., Bousson, V., et al. (2014). 3D osteocyte lacunar morphometric properties and distributions in human femoral cortical bone using synchrotron radiation micro-CT images. Bone 60, 172–185. doi: 10.1016/j.bone.2013.12.008

Evans, H., Andrews, R., Abedi, F. A., Sprules, A., Trend, J., Lovric, G., et al. (2024). Evidence for peri-lacunar remodeling and altered osteocyte lacuno-canalicular network in mouse models of myeloma-induced bone disease. JBMR Plus. doi: 10.1093/jbmrpl/ziae093

Giuliani, N., Ferretti, M., Bolzoni, M., Storti, P., Lazzaretti, M., Dalla Palma, B., et al. (2012). Increased

osteocyte death in multiple myeloma patients: role in myeloma-induced osteoclast formation. Leuk. 2012 266 26, 1391–1401. doi: 10.1038/leu.2011.381

Hemmatian, H., Bakker, A. D., Klein-Nulend, J., and van Lenthe, G. H. (2021). Alterations in osteocyte lacunar morphology affect local bone tissue strains. J. Mech. Behav. Biomed. Mater. 123. doi: 10.1016/j.jmbbm.2021.104730

Hemmatian, H., Laurent, M. R., Ghazanfari, S., Vanderschueren, D., Bakker, A. D., Klein-Nulend, J., et al. (2017). Accuracy and reproducibility of mouse cortical bone microporosity as quantified by desktop microcomputed tomography. PLoS One 12. doi: 10.1371/journal.pone.0182996

Hesse, B., Männicke, N., Pacureanu, A., Varga, P., Langer, M., Maurer, P., et al. (2014). Accessing osteocyte lacunar geometrical properties in human jaw bone on the submicron length scale using synchrotron radiation μCT. J. Microsc. 255, 158–168. doi: 10.1111/jmi.12147

Kamioka, H., Honjo, T., and Takano-Yamamoto, T. (2001). A three-dimensional distribution of osteocyte processes revealed by the combination of confocal laser scanning microscopy and differential interference contrast microscopy. Bone 28, 145–149. doi: 10.1016/s8756-3282(00)00421-x

Kamioka, H., Kameo, Y., Imai, Y., Bakker, A. D., Bacabac, R. G., Yamada, N., et al. (2012). Microscale fluid flow analysis in a human osteocyte canaliculus using a realistic high-resolution image-based three-dimensional model. Integr. Biol. 4, 1198–1206. doi: 10.1039/c2ib20092a

Kamioka, H., Murshid, S. A., Ishihara, Y., Kajimura, N., Hasegawa, T., Ando, R., et al. (2009). A method for observing silver-stained osteocytes in situ in 3-μm sections using ultra-high voltage electron microscopy tomography. Microsc. Microanal. 15, 377–383. doi: 10.1017/s1431927609990420

Kerschnitzki, M., Kollmannsberger, P., Burghammer, M., Duda, G. N., Weinkamer, R., Wagermaier, W., et al. (2013). Architecture of the osteocyte network correlates with bone material quality. J. Bone Miner. Res. 28, 1837–1845. doi: 10.1002/jbmr.1927

Kyle, R. A., Gertz, M. A., Witzig, T. E., Lust, J. A., Lacy, M. Q., Dispenzieri, A., et al. (2003). Review of 1027 patients with newly diagnosed multiple myeloma. Mayo Clin. Proc. 78, 21–33. doi: 10.4065/78.1.21

Langer, M., Pacureanu, A., Suhonen, H., Grimal, Q., Cloetens, P., and Peyrin, F. (2012). X-Ray phase nanotomography resolves the 3d human bone ultrastructure. PLoS One 7, e35691. doi: 10.1371/journal.pone.0035691

Melton, L. J., Kyle, R. A., Achenbach, S. J., Oberg, A. L., and Rajkumar, S. V. (2005). Fracture risk with multiple myeloma: a population-based study. J. Bone Miner. Res. 20, 487–493. doi:

10.1359/jbmr.041131

Muchtar, E., Dagan, A., Robenshtok, E., Shochat, T., Oniashvili, N., Amitai, I., et al. (2017). Bone mineral density utilization in patients with newly diagnosed multiple myeloma. Hematol. Oncol. 35, 703–710. doi: 10.1002/hon.2303

Pacureanu, A., Langer, M., Boller, E., Tafforeau, P., and Peyrin, F. (2012). Nanoscale imaging of the bone cell network with synchrotron X-ray tomography: optimization of acquisition setup. Med. Phys. 39, 2229–2238. doi: 10.1118/1.3697525

Ramezani, A., Tafazoli, A., Salimi, F., Ghavami, M., Arjmandi, H., Khalesi, B., et al. (2024). Current knowledge on therapeutic, diagnostic, and prognostics applications of exosomes in multiple myeloma: Opportunities and challenges. Arch. Biochem. Biophys. 756, 109994. doi: 10.1016/j.abb.2024.109994

Rath Bonivtch, A., Bonewald, L. F., and Nicolella, D. P. (2007). Tissue strain amplification at the osteocyte lacuna: a microstructural finite element analysis. J. Biomech. 40, 2199–2206. doi: 10.1016/j.jbiomech.2006.10.040

Ring, E. S., Lawson, M. A., Snowden, J. A., Jolley, I., and Chantry, A. D. (2018). New agents in the Treatment of Myeloma Bone Disease. Calcif. Tissue Int. 102, 196. doi: 10.1007/s00223-017-0351-7

Robling, A. G., and Bonewald, L. F. (2020). The osteocyte: new insights. Annu. Rev. Physiol. 82, 485–506. doi: 10.1146/annurev-physiol-021119-034332

Saad, F., Lipton, A., Cook, R., Chen, Y. M., Smith, M., and Coleman, R. (2007). Pathologic fractures correlate with reduced survival in patients with malignant bone disease. Cancer 110, 1860–1867. doi: 10.1002/cncr.22991

Schneider, P., Meier, M., Wepf, R., and Müller, R. (2010). Towards quantitative 3D imaging of the osteocyte lacuno-canalicular network. Bone 47, 848–858. doi: 10.1016/j.bone.2010.07.026

Schneider, P., Meier, M., Wepf, R., and Müller, R. (2011). Serial FIB/SEM imaging for quantitative 3D assessment of the osteocyte lacuno-canalicular network. Bone 49, 304–311. doi: 10.1016/j.bone.2011.04.005

Sharma, D., Ciani, C., Marin, P. A. R., Levy, J. D., Doty, S. B., and Fritton, S. P. (2012). Alterations in the osteocyte lacunar–canalicular microenvironment due to estrogen deficiency. Bone 51, 488–497. doi: 10.1016/j.bone.2012.05.014

Sugawara, Y., Kamioka, H., Honjo, T., Tezuka, K. I., and Takano-Yamamoto, T. (2005). Three-dimensional reconstruction of chick calvarial osteocytes and their cell processes using confocal microscopy. Bone

36, 877–883. doi: 10.1016/j.bone.2004.10.008

Terpos, E., Zamagni, E., Lentzsch, S., Drake, M. T., García-Sanz, R., Abildgaard, N., et al. (2021). Treatment of multiple myeloma-related bone disease: recommendations from the bone working group of the international myeloma working group. Lancet Oncol. 22, e119–e130. doi: 10.1016/s1470-2045(20)30559-3

Varga, P., Hesse, B., Langer, M., Schrof, S., Männicke, N., Suhonen, H., et al. (2015). Synchrotron X-ray phase nano-tomography-based analysis of the lacunar–canalicular network morphology and its relation to the strains experienced by osteocytes in situ as predicted by case-specific finite element analysis. Biomech. Model. Mechanobiol. 14, 267–282. doi: 10.1007/s10237-014-0601-9

Vaughan, T. J., Verbruggen, S. W., and Mcnamara, L. M. (2013). Are all osteocytes equal? Multiscale modelling of cortical bone to characterise the mechanical stimulation of osteocytes. Int. J. Numer. Method. Biomed. Eng. 29, 1361–1372. doi: 10.1002/cnm.2578

Verbruggen, S. W., Vaughan, T. J., and McNamara, L. M. (2012). Strain amplification in bone mechanobiology: a computational investigation of the in vivo mechanics of osteocytes. J. R. Soc. Interface 9, 2735–2744. doi: 10.1098/rsif.2012.0286

Verbruggen, S. W., Vaughan, T. J., and McNamara, L. M. (2016). Mechanisms of osteocyte stimulation in osteoporosis. J. Mech. Behav. Biomed. Mater. 62, 158–168. doi: 10.1016/j.jmbbm.2016.05.004

Wang, L., Dong, J., and Xian, C. J. (2015). Strain amplification analysis of an osteocyte under static and cyclic loading: a finite element study. Biomed Res. Int. 2015. doi: 10.1155/2015/376474

Ziouti, F., Soares, A. P., Moreno-Jiménez, I., Rack, A., Bogen, B., Cipitria, A., et al. (2020). An early myeloma bone disease model in skeletally mature mice as a platform for biomaterial characterization of the extracellular matrix. J. Oncol. 2020. doi: 10.1155/2020/3985315

Chapter 7: Conclusions and future work

This thesis presented different computational models to investigate how the skeletal diseases osteoporosis and myeloma bone disease individually affect the apparent bone mechanical properties. The following sections will summarise the research conducted and how this work satisfies the research objectives, outline original contributions to the literature, highlight the studies limitations, present possible future avenues for development, and conclude with a final reflection on the overall research journey.

7.1 Research objective summary and contributions

The results presented in this thesis, while not directly clinically applicable, could contribute significantly to the treatment discovery pipeline. Faster progress through this pipeline ultimately benefits patients by expediting the delivery of effective treatments. The overarching aim of this research is to develop biomechanical *in silico* models to enhance the understanding of how the skeletal diseases, osteoporosis and MBD, affect the bone properties. This understanding is critical for improving the ability to predict bone remodelling during treatments for these conditions. Biomechanical strains and biochemical effects are key drivers of bone remodelling. This thesis investigates several critical factors influencing these processes: the extent to which loading direction affects failure load (Chapter 3) and mechanical strain (Chapter 4); the influence of nano-scale geometric features, such as osteocyte lacunae, on mechanical strain (Chapter 6); and the role which the biomechanical and biochemical stimuli affect bone remodelling.

Overall, the findings of this thesis bridge the gap between basic research and preclinical applications by enhancing the reliability of experimental models used to study skeletal disease treatments. Additionally, they provide a foundation for developing *in silico* models with the potential to accelerate the treatment discovery pipeline, ultimately improving patient outcomes.

7.1.1 Objective 1 – Bone mechanical properties at the organ level

The first study, covered in Chapter 3, created a biomechanical micro-FE model of the mouse tibia, including both cortical and trabecular bone. The mice had all undergone ovariectomy and half had also undergone mechanical loading, using the *in vivo* tibial loading model. This previously validated model

was then used to investigate the effect of the loading direction on the bone's mechanical properties and to investigate the relationship between the mouse tibia midshaft cortical thickness and the bone strength, across the investigated range of loading directions.

The main findings of this study were:

- The bone is optimised for a different loading direction to the assumed axial case, ignoring any contribution of the fibula.
- Mechanical loading increased the failure load of the bone, irrespective of the loading direction, when compared against an untreated group.
- The failure load of the bone was highly sensitive to the loading direction and ranged from 50% to 200% of that of the assumed axial case.
- If the direction of the load is within a 10° cone from the longitudinal axis of the tibia, the cortical thickness in the midshaft could be used as an accurate predictor for the failure load.

This study provides additional insight into the effect of mechanical loading on the failure load of the bone. This information is important for optimising the protocols for the *in vivo* tibial loading experiments on mice.

7.1.2 Objective 2 – Bone mechanical properties at the tissue level

The second study, covered in Chapter 4, showed the critical role of the loading direction on the strain distributions within the mouse tibia. The same mice were used as in the previous chapter, as was the biomechanical model. Though, a larger load magnitude was applied (12 N) to simulate that used in the *in vivo* tibial loading model.

The main findings of this work were:

- The strain energy density distributions changed dramatically depending on the loading direction. The bone was sensitive to both a change in the loading direction in the inferior-superior direction and a change in the load direction in the anterior-posterior and medial-lateral directions.
- The highest strain energy density values were found for loading directions which correspond to that of the highest failure load and the lowest strain energy values were found for loading directions which correspond to that of the lowest failure load.

This study provides important insights for understanding the influence of the loading direction on the local deformation of the tissue, which is the usual input for mechanoregulation models that predict bone adaptation over time. Hence highlighting that the loading direction is a potential source of error that could affect the accuracy of such models.

7.1.3 Objective 3 – Bone adaptation considering the cellular to organ level

The third study, covered in Chapter 5, used a section of the micro-FE model of one of the mice which had undergone mechanical loading in the previous studies, and combined this with a bone cell population model, so that predictions of bone changes over time could be made. The combined model was used to investigate the heterogeneity of biomechanical, biochemical and bone adaptation parameters within a midshaft cortical section of the mouse tibia.

The main findings of this work were:

- Combined micro-FE and bone cell population models can be used to model localised, daily changes in bone adaptation.
- The micro-FE model should be re-meshed and re-run after two days of simulation so that the biomechanical stimulus can be updated to account for geometrical changes that may affect the local strain energy density and therefore the predictions of bone adaptation.

This biomechano-chemo model provides a foundation for future studies exploring the complex interplay between mechanical loading and cellular responses in bone adaptation.

7.1.4 Objective 4 – Application of the micro-CT to micro-FE pipeline to synchrotron images

The last study, covered in Chapter 6, adapted the micro-CT to micro-FE pipeline used in the first two studies to input high resolution synchrotron images of the mouse femur. This allowed for the visualisation of the osteocyte lacunae within the bone matrix and was used to investigate the effect of myeloma bone disease on the local bone mechanical properties.

The main finding of this work was:

- Myeloma bone disease regionally affects the local mechanical properties of the bone, reducing the normalised stiffness in the anterior, posterior and lateral locations and increasing the degree of anisotropy in the anterior and lateral locations of the bone.

This study provides a pipeline for future studies which utilise high-resolution images. It also suggests that modelling the effect of myeloma induced bone disease at a higher dimensional scale should consider heterogeneity and anisotropy of the tissue.

7.2 Limitations

While significant progress has been made in *in silico* models of bone adaptation, there are several limitations to note in regard to the studies. These limitations have been divided into the following categories: data set limitations, micro-FE limitations, and biomechano-chemo model limitations.

7.2.1 Data set limitations

The main limitation within both data sets is the number of mice. For the osteoporosis data set, the OVX group contained only five mice, and the OVX+ML group contained six mice. For the multiple myeloma data set, the Naïve group contained five mice, but the Disease group only contained four mice. However, all pipelines to create models from the data sets within this thesis have been automated, allowing for the processing of alternative data sets.

7.2.1.1 Osteoporosis data set

Firstly, the OVX and OVX+ML datasets were not acquired at the same time, and in fact use different generations of mice. Due to this, the grey levels acquired during imaging at week 18 (where both groups have been ovariectomised and are untreated) were different. Although this impact is negated in this thesis, due to the single-level thresholding used in the segmentation of the images, it must be noted that the TMD values (obtained from the grey levels of the images) between the two groups may differ. Additionally, the mice used in this thesis were aged 18-20 weeks old, meaning that they had not reached skeletal maturity (Somerville et al., 2004). However, the motivation behind these studies it to aid in the investigations of osteoporosis in humans, which is most common among adults over the age of 50 (Sözen et al., 2017). The mouse bone adapts differently in aged bone compared to young bone (Galea et al., 2015; Razi et al., 2015a; Cunningham et al., 2023) and therefore the bone failure load and strain distributions may be overpredicted when compared to older mouse bone.

7.2.1.2 Multiple myeloma data set

A limited number of regions of interest were extracted from each mouse. It is known that the osteocyte lacunae are heterogeneously distributed (Evans et al., 2024) and therefore the findings cannot be

generalised for different regions within the femur or other bones. However, an automatic pipeline was developed, which converts synchrotron images into micro-FE models, and therefore if more ROI are extracted, they can be processed. Lastly, the regions of interest investigated were relatively small. This was to exclude the blood vessels and lesions as the study aimed to investigate the effect of the osteocyte lacunae on the local mechanical properties. For research questions relating to the bone strength, a property known to be affected by the lesions (Borggrefe et al., 2015), the whole bone should be considered.

7.2.2 Micro-FE model limitations

7.2.2.1 Micro-CT based micro-FE models

The micro-CT based micro-FE models do not include the fibula. It has been shown that the fibula affects the cortical strain distribution and the overall bone stiffness (Yang et al., 2014). However, including the fibula in the model would have required additional assumptions in relation to modelling the tibiofibular joint material properties. For the same reason, the growth plate was not modelled. Additionally, the models were validated for compressive loads (Oliviero et al., 2018). Some of the loading directions investigated in this thesis increased bending in the tibia. However, the micro-FE models should still lead to accurate results for these cases, as both the geometry and microstructure were considered. Furthermore, bone is known to be heterogenous, anisotropic, and viscoelastic (Rho et al., 1998). However, the micro-FE models use homogeneous isotropic material properties. Heterogenous material properties based on the TMD obtained from the images have been previously investigated. However, homogeneous models were better correlated with experimental data (Oliviero et al., 2021b). The assumption of linearity was made as the models investigate loads applied which would deform the bone within its elastic limit.

7.2.2.2 SR-micro-CT based micro-FE models

The SR-micro-CT based micro-FE models used hexahedral elements with homogenous material properties. Although the osteocyte lacunae are rounded in nature, the small element size allows for their geometry to be captured. Homogeneous material properties were chosen due to the lack of existing experimental data. Either nano-indentation testing (Oyen et al., 2019) or imaging scanning of the bone using a monochromatic beam is required to be able to apply suitable material properties (Obata et al., 2020). In any case, if alternative homogenous material properties are suggested the results could be scaled accordingly, due to the linear nature of the models. Furthermore, there is no validation against experimental data. This is due to current limitations with conducting experiments at this dimensional scale.

7.2.3 Biomechano-chemo model limitations

This feasibility study was conducted on one mouse, at one time point. However, the creation of the automatic pipeline, allows the number of specimens to be expanded, for example, the same mouse data used in the first two studies of this thesis could be used. Furthermore, the pipeline currently removes trabeculae and would need to be modified to be applied to sections of the bone which include trabecular bone. Another limitation of the model is the OPG concentration. This currently exponentially increases, which leads to continual, unstable growth beyond 14 days of the simulation. This is due to the knock-on effect this variable has on the increased concentration of osteoblasts. These parameters should be optimised, adjusting the maximum OPG saturation and degradation terms in the model to control the OPG production. Other parameters which need to be optimised include the mechanisation sigmoidal function parameters. This will increase the accuracy of the predictions made by the model. However, this optimisation will take a significant amount of computational resources, due to the nature of the model. Lastly, there is a lack of validation against experimental data. The variables in the pipeline first need to be optimised before any validation can take place.

7.3 Future developments

7.3.1 Micro-FE models

A potential development for the micro-FE models would be to include the fibula. This would allow for an investigation into the load distribution between the tibia and fibula. However, additional knowledge of the material properties of the tibio-fibula joint, including the growth plate and the tibio-fibula complex, are required to implement this. Additionally, it would be interesting to spatially plot the changes in the strain distributions due to the loading direction across the tibia. This would allow for the location of potential remodelling to be identified. Alternatively, the micro-FE model could be paired with a mechanoregulation algorithm, similarly to that done by Cheong et al. (2021a), to see if the changes in strain due to altering the loading direction are significant enough to induce mechanoregulated remodelling. However, the parameters of the mechanoregulation algorithm would first have to be optimised. Furthermore, multiple mechanoregulation thresholds could be used, varying across the tibia. For example, it is known that more remodelling occurs in the proximal end of the bone compared to the distal end (Roberts et al., 2020), so the parameters of the algorithm used in the proximal end could be different to those used for the distal end. However, this would not capture changes which occur biochemically due to the influence of the loading on the molecular signalling pathways.

7.3.2 Mechano-chemo-bio model

Considerable future research is needed for the biomechano-chemo model to run efficiently. Firstly, the biomechanical input should be updated automatically. This would require a loop after two days, once geometrical changes can be seen, so that the micro-FE model is automatically re-meshed and re-run. However, it should be noted that smoothing may be required across the slices in the section. These changes would allow for predictions to be made over a longer time period, so that they can be compared against experimental data. The current data set would allow for comparisons to be made every 14 days. Once the updated micro-FE and bone cell population model runs for the full 14 days, an optimisation of the parameters used within the sigmoidal H functions should be conducted. This should be done by modifying the parameters gradually to produce the least error when compared to the experimental data. The model should then be run for multiple mice within the group. Another development to the model would input a larger section of interest, or one which contained trabecular bone. However, the model would have to be modified as currently it can only differentiate two surfaces, the periosteum and endosteum, so would not identify the trabecular bone correctly. If the model were to be adapted to input the whole tibia, the initial cell concentrations could be revised. This modification would alter local adaptation, depending on the available number of bone cells. One method of obtaining this data would be to do 3D histomorphology.

Additional developments to the bone cell population model would be to explicitly include the effect of nitric oxide (NO) and sclerostin (Scl). The mechanical loading sigmoidal H functions indirectly accounts for these. However, additional equations would be needed to model their interactions. This would further increase the interplay between mechanical and biochemical stimuli. Mechanical loading causes osteocytes to release NO which down-regulates RANKL production, decreasing the number of active osteoclasts (Fan et al., 2004, 2006). Osteocytes also release Scl, which has a knock-on effect on the number of active osteoblasts (Galea et al., 2017; Buck et al., 2024). Both NO and Scl have been included in previous bone cell population models (Martin et al., 2019, 2020). Furthermore, a PTH injection term has already been included in this model. However, careful parameter selection is essential to prevent excessive bone formation within the model, a current limitation. There is a lack of data in the literature regarding the pharmacokinetics (PK) of PTH acceptance and clearance from the mouse body. A literature search identified a single source of PTH PK data (Cheloha et al., 2014), derived from a limited sample of three young adult male C57BL/6 mice. Therefore, the applicability of this data to the current model is questionable due to the restricted sample size and differences in age and gender. Regardless, this data may provide a preliminary foundation for developing the PK model. This would allow for investigations into PTH treatment methods and combined mechanical loading and PTH

treatments. Lastly, validation of the model is required against experimental data. The current dataset offers longitudinal micro-CT images of the mouse tibia, which could be used for validation.

7.3.3 SR-micro-CT based micro-FE models

Significant additional research is necessary for the SR-micro-CT based micro-FE models. Firstly, no data was found in the literature which describes the material properties of the NSG mouse femur used in this study. Therefore, the material properties were taken from another bone in a different strain of mice (the tibia of C57BL/6 mice (Oliviero et al., 2018)). Nano-indentation testing should be done to determine the mechanical properties (Oyen et al., 2019). This would reduce the number of assumptions which are made in the model. Alternatively, imaging could be conducted using a monochromatic beam instead of a pink beam, which although increases the scanning time, would provide useful information about the tissue mineral density across the bone (Obata et al., 2020). Additionally, the model could be optimised so that larger volumes of interest could be investigated. This would open the door for a new avenue of research questions, such as the effect of the bone lesions on the strength of the bone. The model could also be adapted to investigate the mechanosensitivity of the osteocytes. By dividing the sum of the strains experienced in the bone by the number of osteocyte lacunae, new information could be gleaned as to whether the decrease in the number of osteocytes in bones with myeloma causes a reduction in signalling, which could affect bone remodelling (Verbruggen et al., 2012). Additionally, creating specific strain maps for individual osteocyte lacunae could provide more localised information about the relationship between strain and osteocyte mechanosensitivity.

7.4 Closing thoughts

Bone remodelling is an intricate process governed by multiple factors. As research advances, *in silico* models of bone adaptation become increasingly complex, mirroring the biological system's inherent complexity. This thesis aimed to further the knowledge of bone mechanics, by examining key assumptions, building upon existing models, and developing novel modelling approaches to analyse previously inaccessible data. The resulting modelling pipelines provide a foundation for future research in bone remodelling, hopefully ultimately contributing to the development of improved treatments for osteoporosis and myeloma bone disease. This work lays a foundation for exciting new avenues of research in bone remodelling.

7.5 References

Borggrefe, J., Giravent, S., Campbell, G., Thomsen, F., Chang, D., Franke, M., et al. (2015). Association of osteolytic lesions, bone mineral loss and trabecular sclerosis with prevalent vertebral fractures in patients with multiple myeloma. Eur. J. Radiol. 84, 2269–2274. doi: 10.1016/j.ejrad.2015.07.024

Buck, H. V., Torre, O. M., Leser, J. M., Gould, N. R., Ward, C. W., and Stains, J. P. (2024). Nitric oxide contributes to rapid sclerostin protein loss following mechanical load. Biochem. Biophys. Res. Commun. 727, 150315. doi: 10.1016/j.bbrc.2024.150315

Cheloha, R. W., Maeda, A., Dean, T., Gardella, T. J., and Gellman, S. H. (2014). Backbone modification of a polypeptide drug alters duration of action in vivo. Nat. Biotechnol. 32, 653. doi: 10.1038/nbt.2920

Cheong, V. S., Kadirkamanathan, V., and Dall'Ara, E. (2021). The role of the loading condition in predictions of bone adaptation in a mouse tibial loading model. Front. Bioeng. Biotechnol. 9, 676867. doi: 10.3389/fbioe.2021.676867

Cunningham, H. C., Orr, S., Murugesh, D. K., Hsia, A. W., Osipov, B., Go, L., et al. (2023). Differential bone adaptation to mechanical unloading and reloading in young, old, and osteocyte deficient mice. Bone 167. doi: 10.1016/j.bone.2022.116646

Evans, H., Andrews, R., Abedi, F. A., Sprules, A., Trend, J., Lovric, G., et al. (2024). Evidence for peri-lacunar remodeling and altered osteocyte lacuno-canalicular network in mouse models of myeloma-induced bone disease. JBMR Plus. doi: 10.1093/jbmrpl/ziae093

Fan, X., Rahnert, J. A., Murphy, T. C., Nanes, M. S., Greenfield, E. M., and Rubin, J. (2006). Response to mechanical strain in an immortalized pre-osteoblast cell is dependent on ERK1/2. J. Cell. Physiol. 207, 454–460. doi: 10.1002/jcp.20581

Fan, X., Roy, E., Zhu, L., Murphy, T. C., Ackert-Bicknell, C., Hart, C. M., et al. (2004). Nitric oxide regulates receptor activator of nuclear factor-κB ligand and osteoprotegerin expression in bone marrow stromal cells. Endocrinology 145, 751–759. doi: 10.1210/en.2003-0726

Galea, G. L., Hannuna, S., Meakin, L. B., Delisser, P. J., Lanyon, L. E., and Price, J. S. (2015). Quantification of alterations in cortical bone geometry using site specificity software in mouse models of aging and the responses to ovariectomy and altered loading. Front. Endocrinol. doi: 10.3389/fendo.2015.00052

Galea, G. L., Lanyon, L. E., and Price, J. S. (2017). Sclerostin's role in bone's adaptive response to mechanical loading. Bone 96, 38. doi: 10.1016/j.bone.2016.10.008

Martin, M., Sansalone, V., Cooper, D. M. L., Forwood, M. R., and Pivonka, P. (2019). Mechanobiological osteocyte feedback drives mechanostat regulation of bone in a multiscale computational model. Biomech. Model. Mechanobiol. 18, 1475–1496. doi: 10.1007/s10237-019-01158-w

Martin, M., Sansalone, V., Cooper, D. M. L., Forwood, M. R., and Pivonka, P. (2020). Assessment of romosozumab efficacy in the treatment of postmenopausal osteoporosis: Results from a mechanistic PK-PD mechanostat model of bone remodeling. Bone 133, 115223. doi: 10.1016/j.bone.2020.115223

Obata, Y., Bale, H. A., Barnard, H. S., Parkinson, D. Y., Alliston, T., and Acevedo, C. (2020). Quantitative and qualitative bone imaging: a review of synchrotron radiation microtomography analysis in bone research. J. Mech. Behav. Biomed. Mater. 110, 103887. doi: 10.1016/j.jmbbm.2020.103887

Oliviero, S., Giorgi, M., and Dall'Ara, E. (2018). Validation of finite element models of the mouse tibia using digital volume correlation. J. Mech. Behav. Biomed. Mater. 86, 172–184. doi: 10.1016/j.jmbbm.2018.06.022

Oliviero, S., Roberts, M., Owen, R., Reilly, G. C., Bellantuono, I., and Dall'Ara, E. (2021). Non-invasive prediction of the mouse tibia mechanical properties from microCT images: comparison between different finite element models. Biomech. Model. Mechanobiol. 20, 941–955. doi: 10.1007/s10237-021-01422-y

Oyen, M., Shean, T. A. V., Ashby, M. F., Cook, R. F., Van Vliet, K. J., Chen, X., et al. (2019). Handbook of nanoindentation: with biological applications. CRC Press. Available at: https://books.google.co.uk/books?hl=en&lr=&id=fj-rdwaaqbaj&oi=fnd&pg=pp1&ots=nxvhrdcwsg&sig=wx9egscdeg5bnmxh2sejfnmleyu&redir_esc=y#v=onepage&q&f=false (Accessed August 11, 2024).

Razi, H., Birkhold, A. I., Weinkamer, R., Duda, G. N., Willie, B. M., and Checa, S. (2015). Aging leads to a dysregulation in mechanically driven bone formation and resorption. J. Bone Miner. Res. 30, 1864–1873. doi: 10.1002/jbmr.2528

Rho, J. Y., Kuhn-Spearing, L., and Zioupos, P. (1998). Mechanical properties and the hierarchical structure of bone. Med. Eng. Phys. 20, 92–102. doi: 10.1016/s1350-4533(98)00007-1

Roberts, B. C., Arredondo Carrera, H. M., Zanjani-pour, S., Boudiffa, M., Wang, N., Gartland, A., et al. (2020). PTH(1–34) treatment and/or mechanical loading have different osteogenic effects on the trabecular and cortical bone in the ovariectomized C57BL/6 mouse. Sci. Reports 101 10, 1–16. doi: 10.1038/s41598-020-65921-1

Somerville, J. M., Aspden, R. M., Armour, K. E., Armour, K. J., and Reid, D. M. (2004). Growth of C57Bl/6 mice and the material and mechanical properties of cortical bone from the tibia. Calcif. Tissue Int. 74, 469–475. doi: 10.1007/s00223-003-0101-x

Sözen, T., Özışık, L., and Başaran, N. Ç. (2017). An overview and management of osteoporosis. Eur. J. Rheumatol. 4, 46. doi: 10.5152/eurjrheum.2016.048

Verbruggen, S. W., Vaughan, T. J., and McNamara, L. M. (2012). Strain amplification in bone mechanobiology: a computational investigation of the in vivo mechanics of osteocytes. J. R. Soc. Interface 9, 2735–2744. doi: 10.1098/rsif.2012.0286

Yang, H., Butz, K. D., Duffy, D., Niebur, G. L., Nauman, E. A., and Main, R. P. (2014). Characterization of cancellous and cortical bone strain in the in vivo mouse tibial loading model using microCT-based finite element analysis. Bone 66, 131–139. doi: 10.1016/j.bone.2014.05.019

Appendix A

This appendix verifies the use of the scaling and superposition of the effects methods used within Chapters 3 and 4, to combine the results during post-processing of the linear models run with unitary loads.

A1 Materials and methods

A1.1 Experimental *in vivo* data

Please refer to section 3.2.1 for the detailed explanation of the experimental *in vivo* data (in this study, one of the mice from the mechanical loading (OVX+ML) group at week 18 was used). In summary, a female C57BL/6 mouse was ovariectomised at age 14 weeks. At weeks 19 and 21, the mouse underwent mechanical loading treatment, using the *in vivo* tibial loading model. *In vivo* micro-CT images were acquired of the right tibiae of the mouse at weeks 18 and 20 of age.

A1.2 Image processing and micro-FE models

The main steps of the image processing, creation of the section micro-FE models, and post-processing of the strains and stresses to test the scaling and superposition principals are reported in Figure A1.

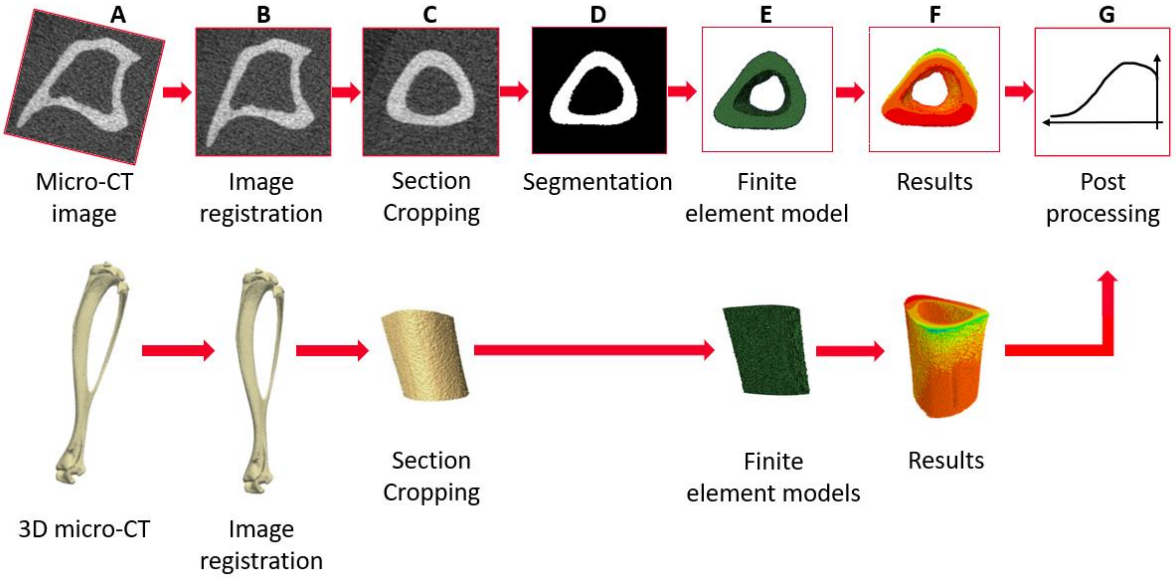

Figure A1: *Flowchart illustrating the main steps of the pipeline to create the section 5 micro-FE models from the micro-CT images: (from A to G) micro-CT acquisition, image registration, section cropping, image segmentation (binarisation), creation of the section micro-FE models, results generation, post-processing of the strains and stresses.*

Please refer to section 3.2.2 for a detailed explanation of the image processing and generation of the micro-FE models methods, although these have been adapted here for section models instead of a model of the whole tibia. Briefly, the images were registered to the reference tibia, taken at week 14 (Amira 6.3.0, Thermo Fisher Scientific, France), as detailed in Lu et al. (2016, 2017). After alignment, the fibula was virtually removed from all the images and the images were cropped from the slice below the proximal growth plate towards the distal end of the tibia, resulting in 80% of the total tibia length (Cheong et al., 2020b, 2021). The 80% tibial length was divided into 10 sections. Section 1 refers to the most distal section of the tibia, whilst section 10 refers to the most proximal section of the tibia. Two regions of interest were individually selected and cropped: sections 5 and 10 (Figure A2). Section 5 was selected due to it being a midshaft section which contains cortical bone and a visible amount of bone remodelling (Cheong et al., 2020b). Section 10 was selected due to being the only section of the 80% tibial length that includes both cortical and trabecular bone.

The images of the two sections were then independently segmented and converted into micro-FE models by converting each bone voxel into a finite element (linear 8-node hexahedral elements). Isotropic, homogeneous, linear elastic material properties were used (E = 14.8 GPa, v = 0.3), which is in line with previous validation studies which showed good agreement with experimental measurements (Oliviero et al., 2018, 2021a, 2021b). The boundary conditions were set to simulate the

in vivo tibial loading model: the nodes in the proximal end of the section were fully constrained, and the nodes in the distal end of the section were connected via kinematic coupling to a control node which was located at the centroid of the distal surface with a small offset in the superior direction. This was done to avoid over-constraining the tibia (Cheong et al., 2020a). Six independent unitary loads and unitary moments were applied along or about the inferior-superior, medio-lateral or anterior-posterior axes for both section models. For analyses between the micro-FE models and the post-processed outputs, an additional three cases were carried out using the same protocol as above: (1) a load of 12 N in each the inferior-superior, medio-lateral and anterior-posterior directions applied simultaneously, and (2) a unitary moment applied about the inferior-superior, medio-lateral and anterior-posterior axes simultaneously. From here onwards, these additional cases will be referred to as the Combined_FE cases. The nodal strains and stresses were recorded for all models. All input files for the models were generated in MATLAB. The models were solved in Abaqus 2018 (Dassault Systèmes Simulia, RI, USA) using the University of Sheffield High Performance Computing Clusters (ShARC).

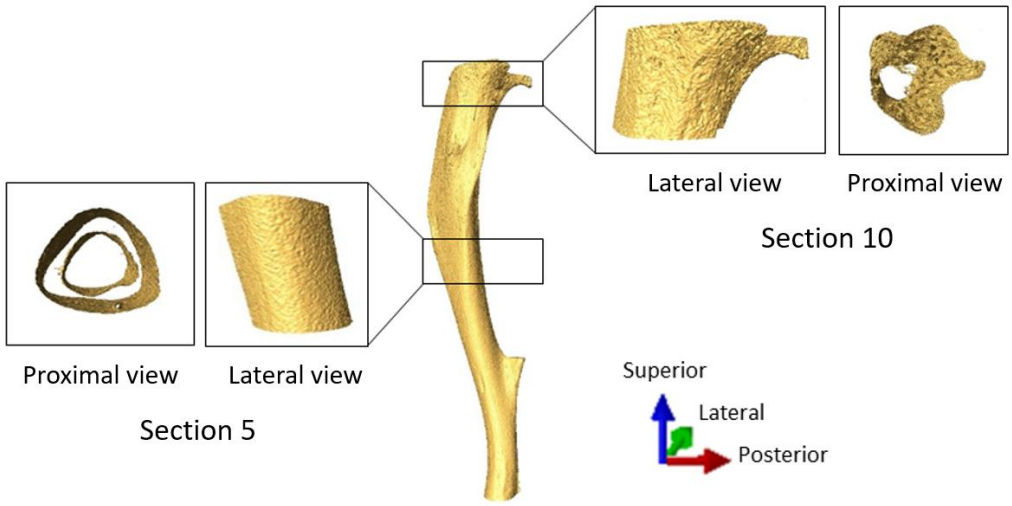

Figure A2: *The cropped micro-CT images of the tibia belonging to the mouse investigated, showing 80% length of the tibia (beginning the crop from below the proximal growth plate), the removal of the fibula, and the location of Sections 5 and 10.*

A1.3 Post processing

Scaling and superposition of the effects were used to combine the results from the unitary models during post-processing, to calculate the nodal strain and stress components (Eqs. A1 – A4) for each of

the three cases corresponding to Combined_FE cases. From here onwards, these postprocessed cases will be referred to as the Combined_PP cases. Calculations were performed as a function of the angle from the inferior-superior axis (θ, 0-30° range, 5° steps) and the angle from the anterior-posterior axis (ϕ, 0°: anterior axis, positive anticlockwise (inferior-superior view), 0-355° range, 5° steps) (section 3.2.3, Figure 3.3).

$$\sigma^{\theta,\phi}, \varepsilon^{\theta,\phi} = F^{IS}[\sigma^{IS}, \varepsilon^{IS}] + F^{ML}[\sigma^{ML}, \varepsilon^{ML}] + F^{AP}[\sigma^{AP}, \varepsilon^{AP}] + M^{IS}[\sigma^{IS}, \varepsilon^{IS}] + M^{ML}[\sigma^{ML}, \varepsilon^{ML}] + M^{AP}[\sigma^{AP}, \varepsilon^{AP}] \quad (A1)$$

where, $\sigma^{\theta,\phi}, \varepsilon^{\theta,\phi}$ is the stress or strain value, respectively, calculated in each node for the loading direction defined by the angles θ and ϕ, $\sigma^{IS}, \varepsilon^{IS}; \sigma^{ML}, \varepsilon^{ML}; and\ \sigma^{AP}, \varepsilon^{AP}$ are the stress and strain values, respectively, calculated in each node for each of the six unitary cases, and F^{IS} , F^{ML} , F^{AP}, M^{IS} , M^{ML} , and M^{AP} are scaling coefficients, such that:

$$F^{IS} = F\cos\theta \quad (A2)$$

$$F^{ML} = F\sin\theta\ \sin\phi \quad (A3)$$

$$F^{AP} = F\sin\theta\ \cos\phi \quad (A4)$$

where, F is the applied force in the model. Eqs. A2 – A4 also hold true for M^{IS} , M^{ML} , and M^{AP}.

The strain energy density (SED), principal strains ($\varepsilon_{max,mid,min}$) and stresses ($\sigma_{max,mid,min}$), and effective strain (ε_{eff}) were calculated from the strain and stress components (Eqs. A5 – A9):

$$SED = \frac{1}{2}(\varepsilon_{11}\sigma_{11} + \varepsilon_{22}\sigma_{22} + \varepsilon_{33}\sigma_{33} + 2\varepsilon_{12}\sigma_{12} + 2\varepsilon_{13}\sigma_{13} + 2\varepsilon_{23}\sigma_{23}) \quad (A5)$$

where, ε_{ij} are the strain tensor components and σ_{ij} are the stress tensor components, where $i, j \in \{1,2,3\}$.

The principal stresses were calculated by finding the eigenvalues of the stress tensors. A generalised Hooke's law was utilised to calculate the principal strains from the principal stresses, Young's modulus, and Poisson's ratio (Eqs. A6 – A8).

$$\varepsilon_{max} = \frac{1}{E}(\sigma_{max} - v(\sigma_{mid} + \sigma_{min}))$$

(A6)

$$\varepsilon_{mid} = \frac{1}{E}(\sigma_{mid} - v(\sigma_{max} + \sigma_{min}))$$

(A7)

$$\varepsilon_{min} = \frac{1}{E}(\sigma_{min} - v(\sigma_{max} + \sigma_{mid}))$$

(A8)

where, ε_{max} is the maximum principal strain; ε_{mid} is the intermediate principal strain; ε_{min} is the minimum principal strain; σ_{max} is the maximum principal stress; σ_{mid} is the intermediate principal stress; σ_{min} is the minimum principal stress; E is the Young's Modulus; and v is the Poisson's ratio.

Furthermore, the effective strain was calculated from the principal strains (Eq. A9):

$$\varepsilon_{eff} = \frac{\sqrt{2}}{3}((\varepsilon_{max} - \varepsilon_{mid})^2 + (\varepsilon_{mid} - \varepsilon_{max})^2 + (\varepsilon_{max} - \varepsilon_{min})^2)^{\frac{1}{2}}$$

(A9)

where ε_{eff} is the effective strain.

A1.4 Case comparisons and statistical analysis

A linear regression analysis of between the Combined_FE and the Combined_PP cases were conducted, and the R^2 value was recorded (MATLAB R2018a, The MathWorks Inc., Natick MA, United States). Furthermore, a frequency plot for the maximum and minimum principal strains, the effective strain, and the SED for each case were plotted to allow for comparison between the Combined_FE and Combined_PP.

A2 Results and discussion

The linear regression graphs for the maximum and minimum principal strains, the effective strain, and the SED for Section 5, case 1 (summation of the inferior-superior unitary force, the posterior-anterior unitary force, and the medial-lateral unitary force, all scaled by 12) are reported in Figure A3. The graphs show a one-to-one relationship between Combined_FE (Abaqus-generated results including the FE all generalised components of the force) and Combined_PP (post-processed results using the six unitary load simulations). This implies that both methods produce the same outcomes (with negligible errors), confirming as expected the validity of scaling and the principle of superposition for linear models. The advantage of Combined_PP is that it is much less computationally expensive to run than Combined_FE, as the Abaqus simulations do not need to be run each time a new loading combination is required. The same can be seen for Section 5, case 2 (summation of the inferior-superior unitary moment, with the posterior-anterior unitary moment, and the medial lateral unitary moment) (Figure A4); Section 10, case 1 (Figure A5); and Section 10, case 2 (Figure A6).

Section 5, Case 1: Summation of the inferior-superior unitary force, the posterior-anterior unitary force, and the medial-lateral unitary force, all scaled by 12.

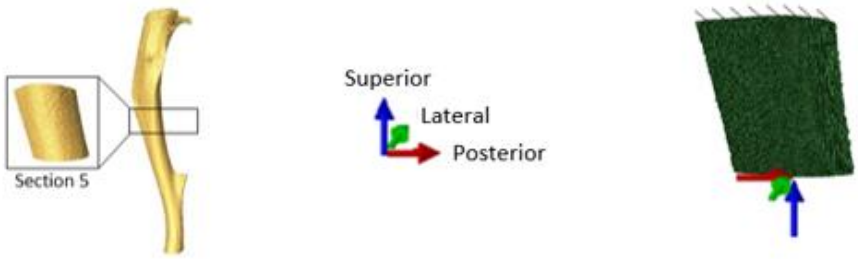

Components	Force	Moment
Inferior-Superior	1 N x12	0
Anterior-Posterior	1 N x12	0
Medial-Lateral	1 N x12	0

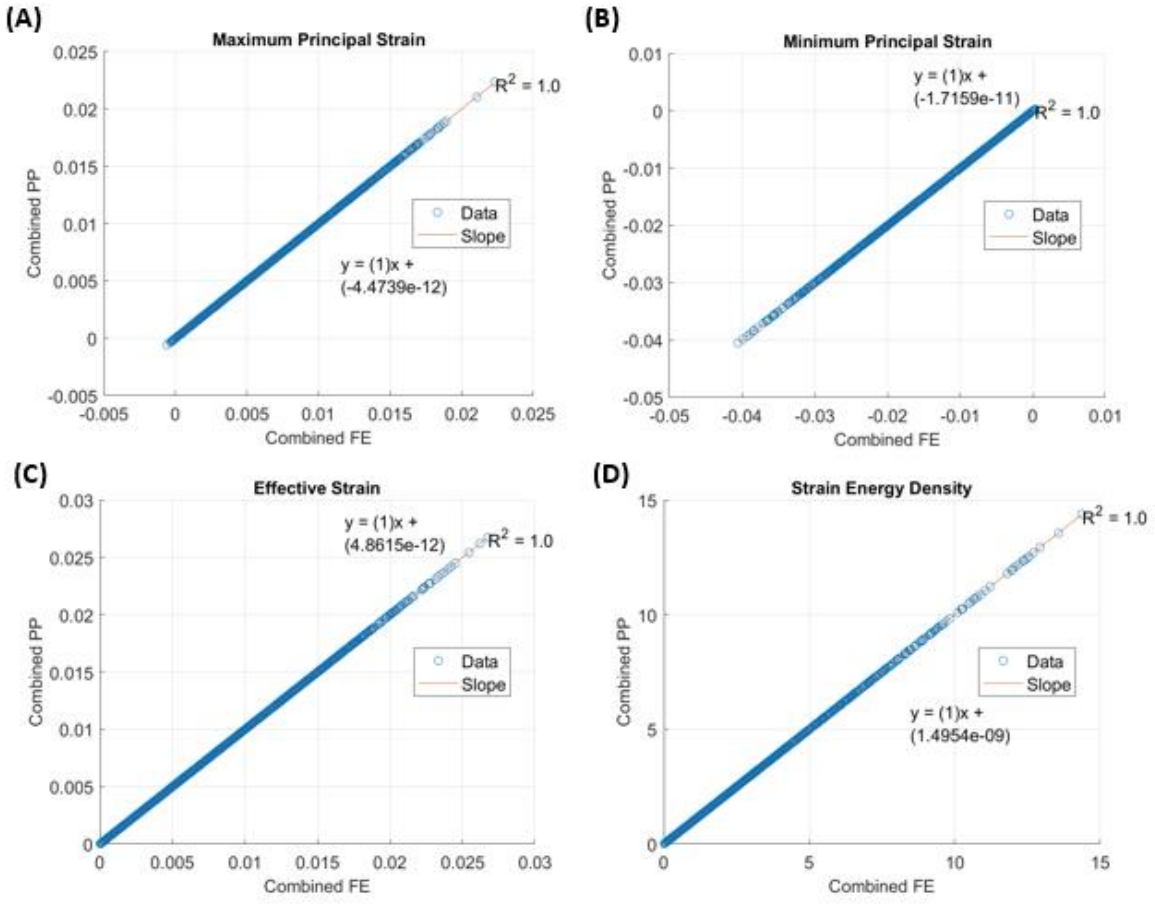

Figure A3: *Top: The location of the section of interest is depicted alongside the reference system and a schematic of the boundary conditions. Middle: The table shows the magnitude of the force and moment components in each axial direction for case 1. Bottom: The linear regression graphs for case 1, showing the: (A) maximum principal strain; (B) minimum principal strain; (C) effective strain; and the (D) strain energy density.*

Section 5, Case 2: Summation of the inferior-superior unitary moment, with the posterior-anterior unitary moment, and the medial lateral unitary moment.

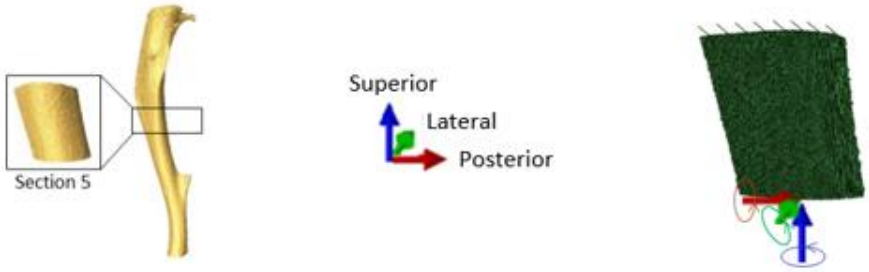

Components	Force	Moment
Inferior-Superior	0	1 Nm
Anterior-Posterior	0	1 Nm
Medial-Lateral	0	1 Nm

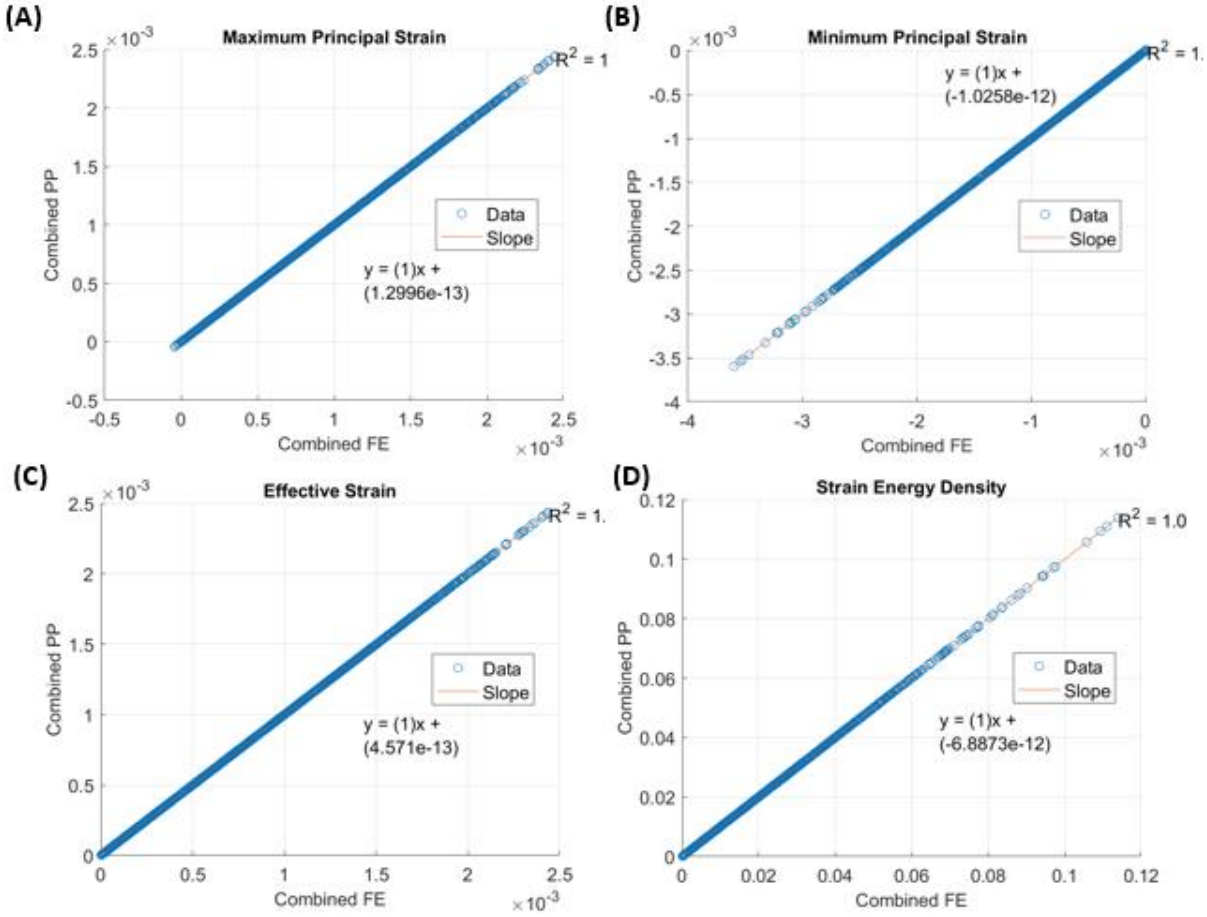

Figure A4: *Top: The location of the section of interest is depicted alongside the reference system and a schematic of the boundary conditions. Middle: The table shows the magnitude of the force and moment components in each axial direction for case 2. Bottom: The linear regression graphs for case 2, showing the: (A) maximum principal strain; (B) minimum principal strain; (C) effective strain; and the (D) strain energy density.*

Section 10, Case 1: Summation of the inferior-superior unitary force, the posterior-anterior unitary force, and the medial-lateral unitary force, all scaled by 12.

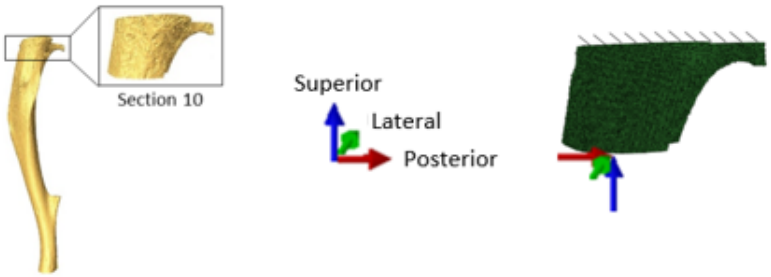

Components	Force	Moment
Inferior-Superior	1 N x12	0
Anterior-Posterior	1 N x12	0
Medial-Lateral	1 N x12	0

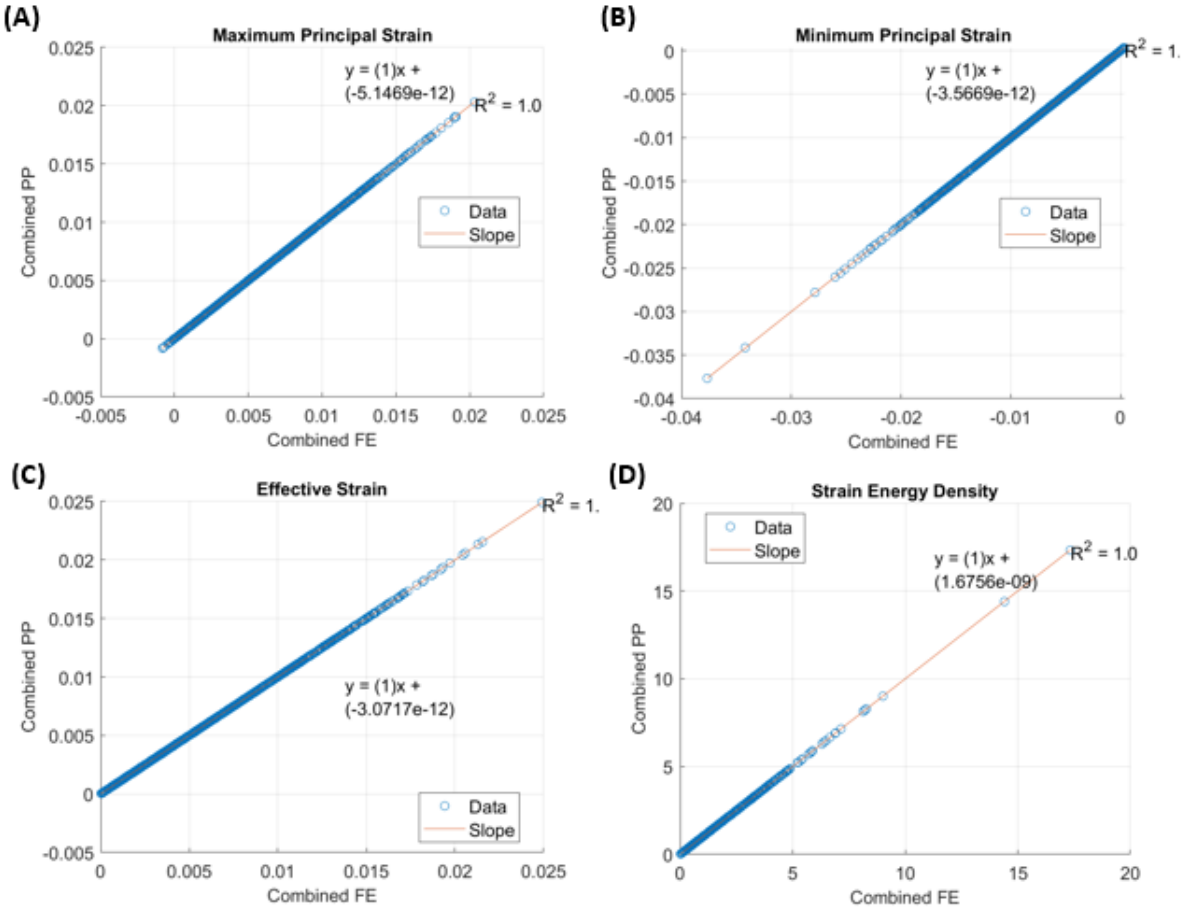

Figure A5: *Top: The location of the section of interest is depicted alongside the reference system and a schematic of the boundary conditions. Middle: The table shows the magnitude of the force and moment components in each axial direction for case 1. Bottom: The linear regression graphs for case 1, showing the: (A) maximum principal strain; (B) minimum principal strain; (C) effective strain; and the (D) strain energy density in Section 10 of the tibia.*

Section 10, Case 2: Summation of the inferior-superior unitary moment, with the posterior-anterior unitary moment, and the medial lateral unitary moment

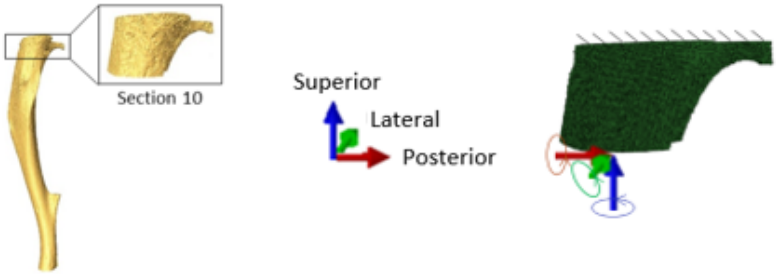

Components	Force	Moment
Inferior-Superior	0	1 Nm
Anterior-Posterior	0	1 Nm
Medial-Lateral	0	1 Nm

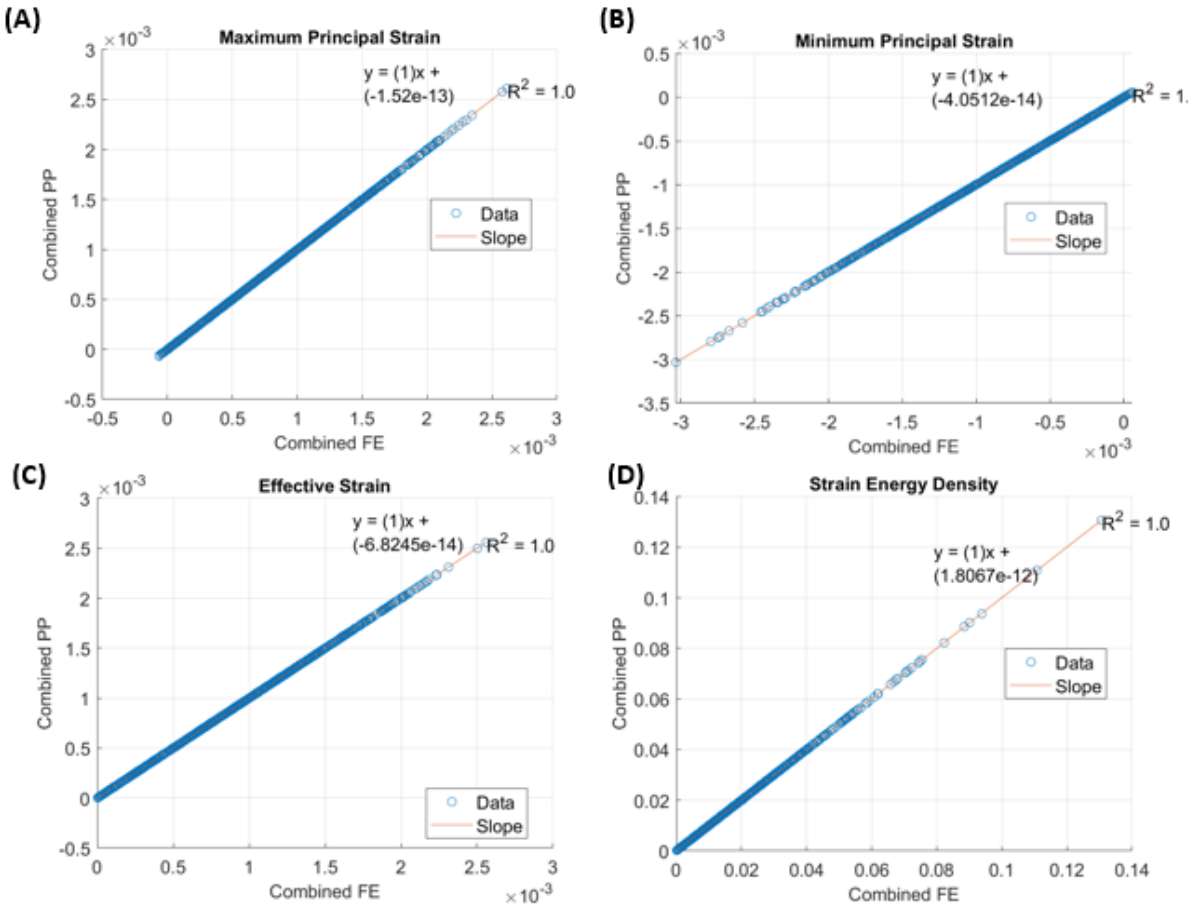

Figure A6: *Top: The location of the section of interest is depicted alongside the reference system and a schematic of the boundary conditions. Middle: The table shows the magnitude of the force and moment components in each axial direction for case 2. Bottom: The linear regression graphs for case 2, showing the: (A) maximum principal strain; (B) minimum principal strain; (C) effective strain; and the (D) strain energy density in Section 10 of the tibia.*

The frequency plots for Section 5 for the unitary forces (Figures A7 and A8) and moments (Figures A9 and A10) are shown below for the maximum and minimum principal strains, the effective strain, and the SED. As are the frequency plots for the Combined_FE case 1 (Figures A11) and case 2 (Figure A12). The section 10 frequency plots have been omitted. The frequency plots show the number of nodes which have a particular strain measurement. From these strain values the bones mechanical properties can be estimated. It can be seen that if the unitary load cases in Figure A7 and A8 are scaled and combined, the output is similar to that of Figure A11. Similarly, the unitary moment cases in Figure A9 and A10 combine to output a frequency plot similar to that of Figure A12, thus verifying the scaling and superposition of effects for both the unitary forces and moments.

In conclusion, the results showed that scaling and superposition of effects was valid for all force and moment cases. This implies that the Combined_PP (post-processing) can be used to obtain outputs from the unitary simulations, instead of re-running the Abaqus simulation for each new loading scenario. This is much less computationally expensive and allows for a range of loading scenarios to be investigated.

Section 5, Unitary Force Load Cases: Maximum and minimum principal strains

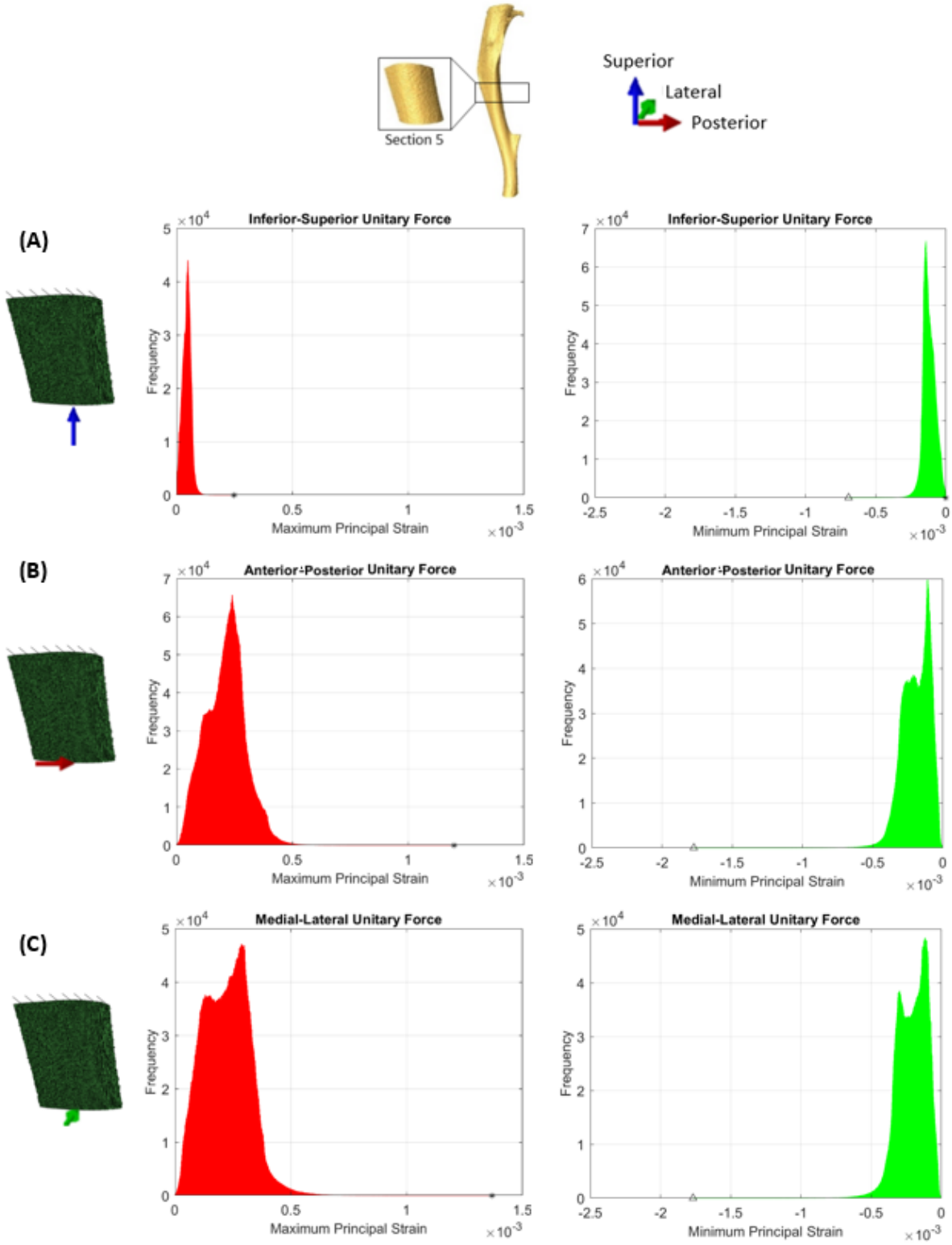

Figure A7: *Top: The location of the section of interest is depicted alongside the reference system. Bottom: A schematic of the boundary conditions for the three unitary force cases (A, B & C) alongside the frequency plots which show the maximum and minimum principal strains in Section 5 of the tibia. The black star (*) shows the maximum value of strain and the black triangle (▲) shows the minimum value of strain.*

Section 5, Unitary Force Load Cases: Effective strain and strain energy density

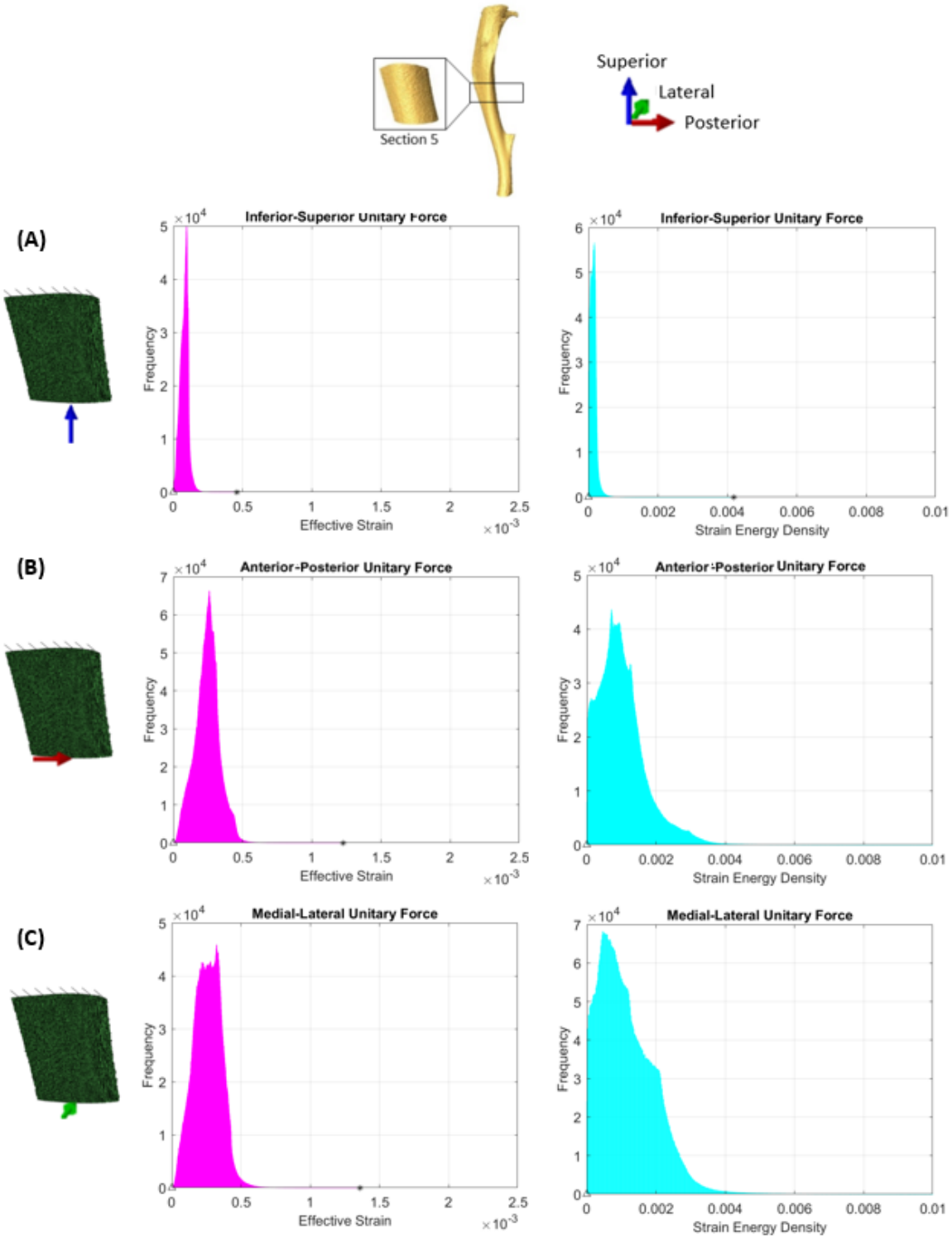

Figure A8: Top: The location of the section of interest is depicted alongside the reference system. Bottom: A schematic of the boundary conditions for the three unitary force cases (A, B & C) alongside the frequency plots which show the effective strain and the strain energy density in Section 5 of the tibia. NB: the SED graph has been scaled in the x-axis to allow for a clearer view of the frequency plot. The black star (*) shows the maximum value of strain and the black triangle (▲) shows the minimum value of strain.

Section 5, Unitary Moment Cases: Maximum and minimum principal strains

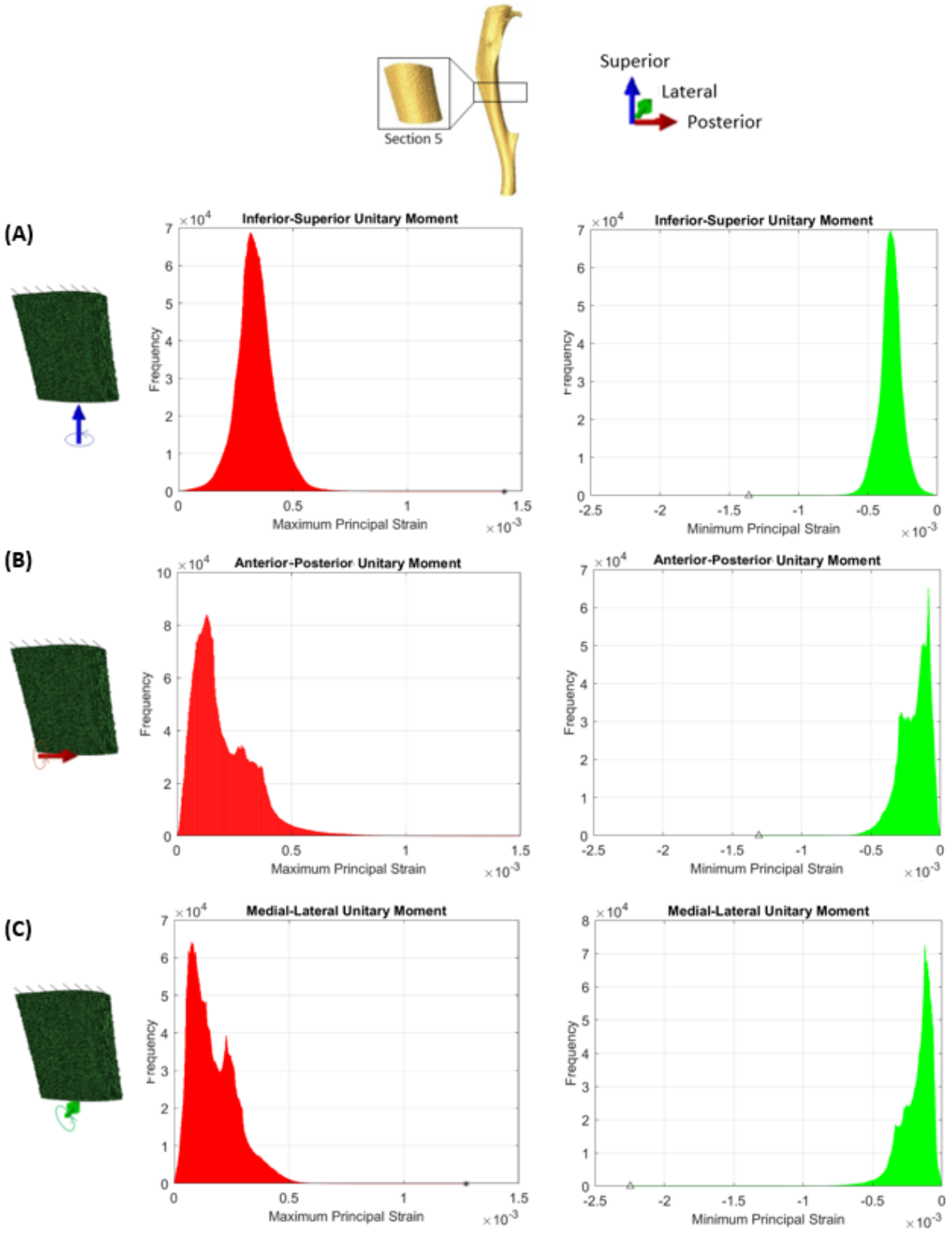

Figure A9: Top: The location of the section of interest is depicted alongside the reference system. Bottom: A schematic of the boundary conditions for the three unitary moment cases (A, B & C) alongside the frequency plots which show the maximum and minimum principal strains in Section 5 of the tibia. The black star (*) shows the maximum value of strain and the black triangle (▲) shows the minimum value of strain.

Section 5, Unitary Moment Cases: Effective Strain and Strain Energy Density

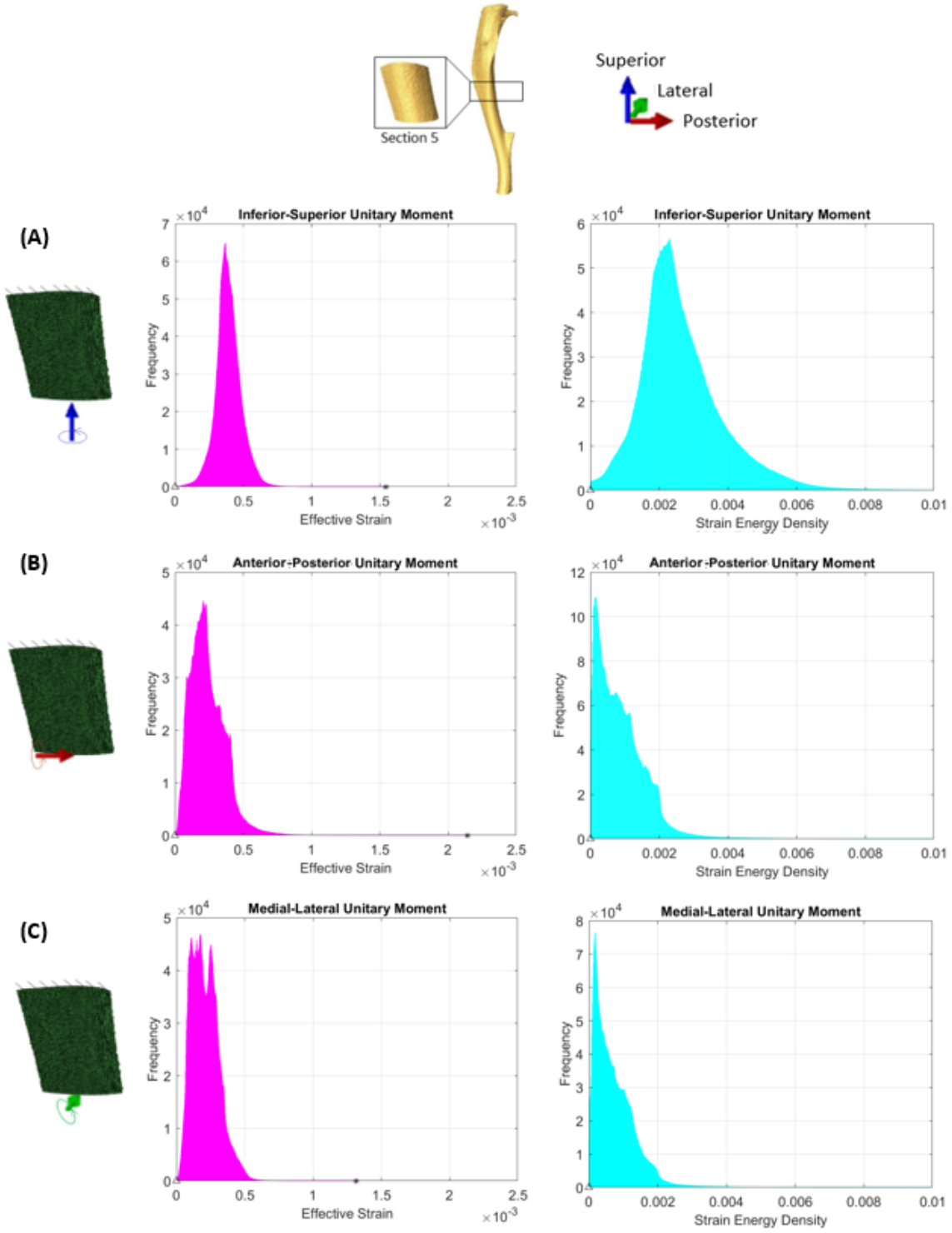

Figure A10: *Top: The location of the section of interest is depicted alongside the reference system. Bottom: A schematic of the boundary conditions for the three unitary moment cases (A, B & C) alongside the frequency plots which show the effective strain and the strain energy density in Section 5 of the tibia. NB: the SED graph has been scaled in the x-axis to allow for a clearer view of the frequency plot. The black star (*) shows the maximum value of strain and the black triangle (▲) shows the minimum value of strain.*

Section 5, Case 1: Summation of the inferior-superior unitary force, the posterior-anterior unitary force, and the medial-lateral unitary force, all scaled by 12

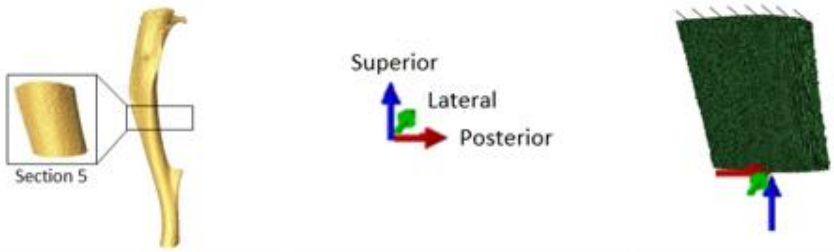

Components	Force	Moment
Inferior-Superior	1 N x12	0
Anterior-Posterior	1 N x12	0
Medial-Lateral	1 N x12	0

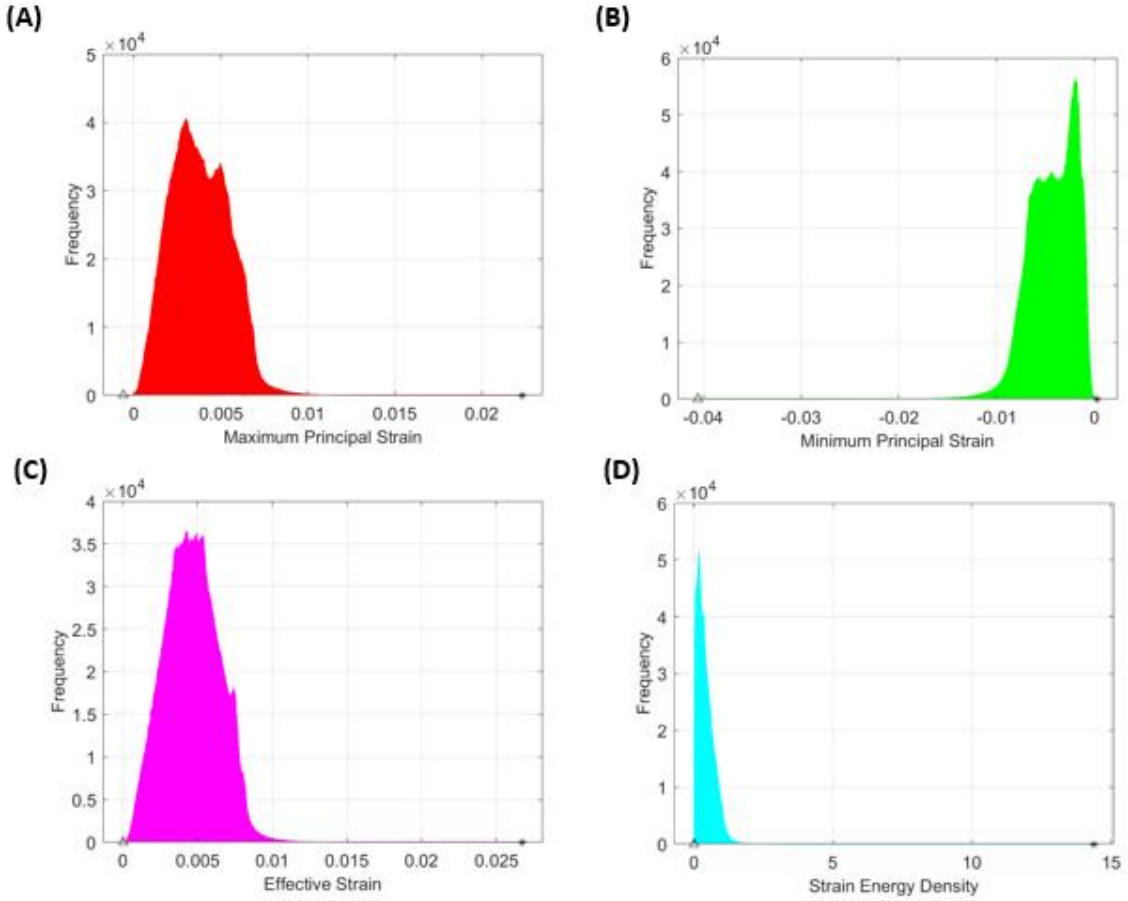

Figure A11: *Top: The location of the section of interest is depicted alongside the reference system and a schematic of the boundary conditions. Middle: The table shows the magnitude of the force and moment components in each axial direction for case 1. Bottom: The frequency plots which show the (A) maximum and (B) minimum principal strains, (C) the effective strain and the (D) strain energy density in Section 5 of the tibia. The black star (*) shows the maximum value of strain and the black triangle (▲) shows the minimum value of strain.*

Section 5, Case 2: Summation of the inferior-superior unitary moment, with the posterior-anterior unitary moment, and the medial lateral unitary moment

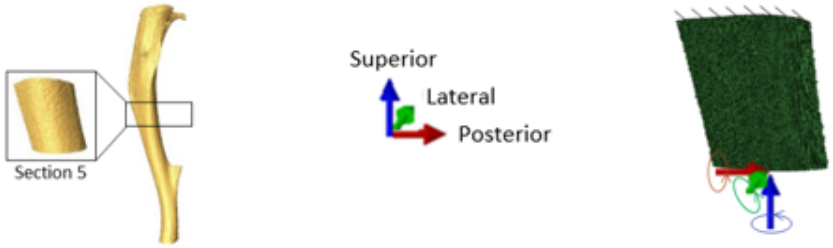

Components	Force	Moment
Inferior-Superior	0	1 Nm
Anterior-Posterior	0	1 Nm
Medial-Lateral	0	1 Nm

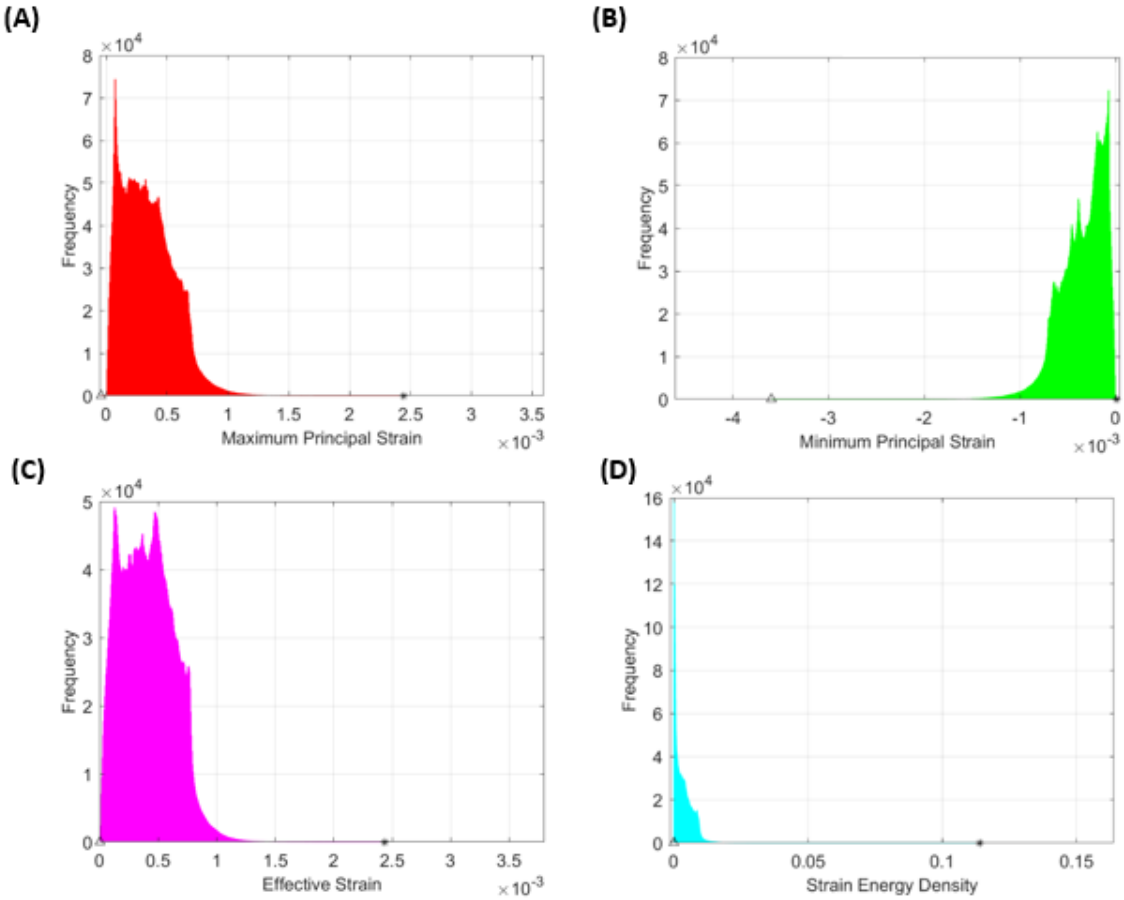

Figure A12: *Top: The location of the section of interest is depicted alongside the reference system and a schematic of the boundary conditions. Middle: The table shows the magnitude of the force and moment components in each axial direction for case 2. Bottom: The frequency plots which show the (A) maximum and (B) minimum principal strains, (C) the effective strain and the (D) strain energy density in Section 5 of the tibia. The black star (*) shows the maximum value of strain and the black triangle (▲) shows the minimum value of strain.*

A3 References

Cheong, V. S., Campos Marin, A., Lacroix, D., and Dall'Ara, E. (2020a). A novel algorithm to predict bone changes in the mouse tibia properties under physiological conditions. Biomech. Model. Mechanobiol. 19, 985–1001. doi: 10.1007/s10237-019-01266-7

Cheong, V. S., Roberts, B. C., Kadirkamanathan, V., and Dall'Ara, E. (2020b). Bone remodelling in the mouse tibia is spatio-temporally modulated by oestrogen deficiency and external mechanical loading: A combined in vivo/in silico study. Acta Biomater. 116, 302–317. doi: 10.1016/j.actbio.2020.09.011

Cheong, V. S., Roberts, B. C., Kadirkamanathan, V., and Dall'Ara, E. (2021). Positive interactions of mechanical loading and PTH treatments on spatio-temporal bone remodelling. Acta Biomater. 136, 291–305. doi: 10.1016/j.actbio.2021.09.035

Lu, Y., Boudiffa, M., Dall'Ara, E., Bellantuono, I., and Viceconti, M. (2016). Development of a protocol to quantify local bone adaptation over space and time: quantification of reproducibility. J. Biomech. 49, 2095–2099. doi: 10.1016/j.jbiomech.2016.05.022

Lu, Y., Boudiffa, M., Dall'Ara, E., Liu, Y., Bellantuono, I., and Viceconti, M. (2017). Longitudinal effects of Parathyroid Hormone treatment on morphological, densitometric and mechanical properties of mouse tibia. J. Mech. Behav. Biomed. Mater. 75, 244–251. doi: 10.1016/j.jmbbm.2017.07.034

Oliviero, S., Giorgi, M., and Dall'Ara, E. (2018). Validation of finite element models of the mouse tibia using digital volume correlation. J. Mech. Behav. Biomed. Mater. 86, 172–184. doi: 10.1016/j.jmbbm.2018.06.022

Oliviero, S., Owen, R., Reilly, G. C., Bellantuono, I., and Dall'Ara, E. (2021a). Optimization of the failure criterion in micro-Finite Element models of the mouse tibia for the non-invasive prediction of its failure load in preclinical applications. J. Mech. Behav. Biomed. Mater. 113, 104190. doi: 10.1016/j.jmbbm.2020.104190

Oliviero, S., Roberts, M., Owen, R., Reilly, G. C., Bellantuono, I., and Dall'Ara, E. (2021b). Non-invasive prediction of the mouse tibia mechanical properties from microCT images: comparison between different finite element models. Biomech. Model. Mechanobiol. 20, 941–955. doi: 10.1007/s10237-021-01422-y

Appendix B

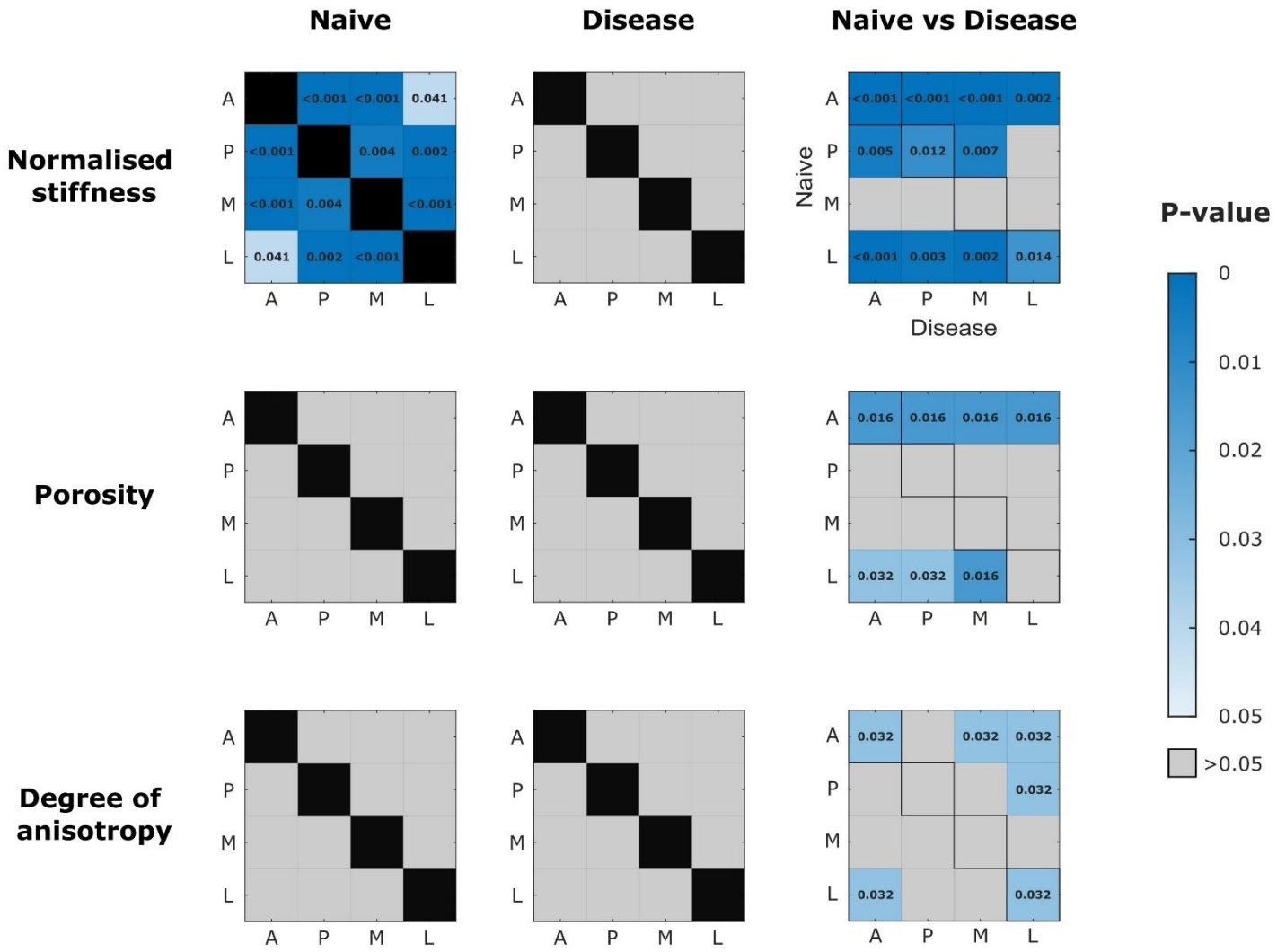
Naive
Disease
Naive vs Disease
Normalised stiffness
Porosity
Degree of anisotropy
A
P
M
L
Naive
Disease
<0.001
0.041
0.004
0.002
0.005
0.012
0.007
0.003
0.014
0.016
0.032
P-value
0
0.01
0.02
0.03
0.04
0.05
>0.05

Figure B1: *The heatmaps for every comparison between each location (anterior (A), posterior (P), medial (M), lateral (L)) within the bone within the Naïve group (first column), Disease group (second column), and for the Naïve compared to the Disease group (third column) for the normalised stiffness (first row), porosity (second row), and degree of anisotropy (third row). The cells are coloured based on their p-value when tested with the non-parametric two-tailed Mann-Whitney U test (first and second columns) or with the non-parametric two-tailed Wilcoxon test (third column). The black represents that no test was done, as intra-location comparisons are irrelevant. All statistical tests were conducted using a significance level of 0.05.*

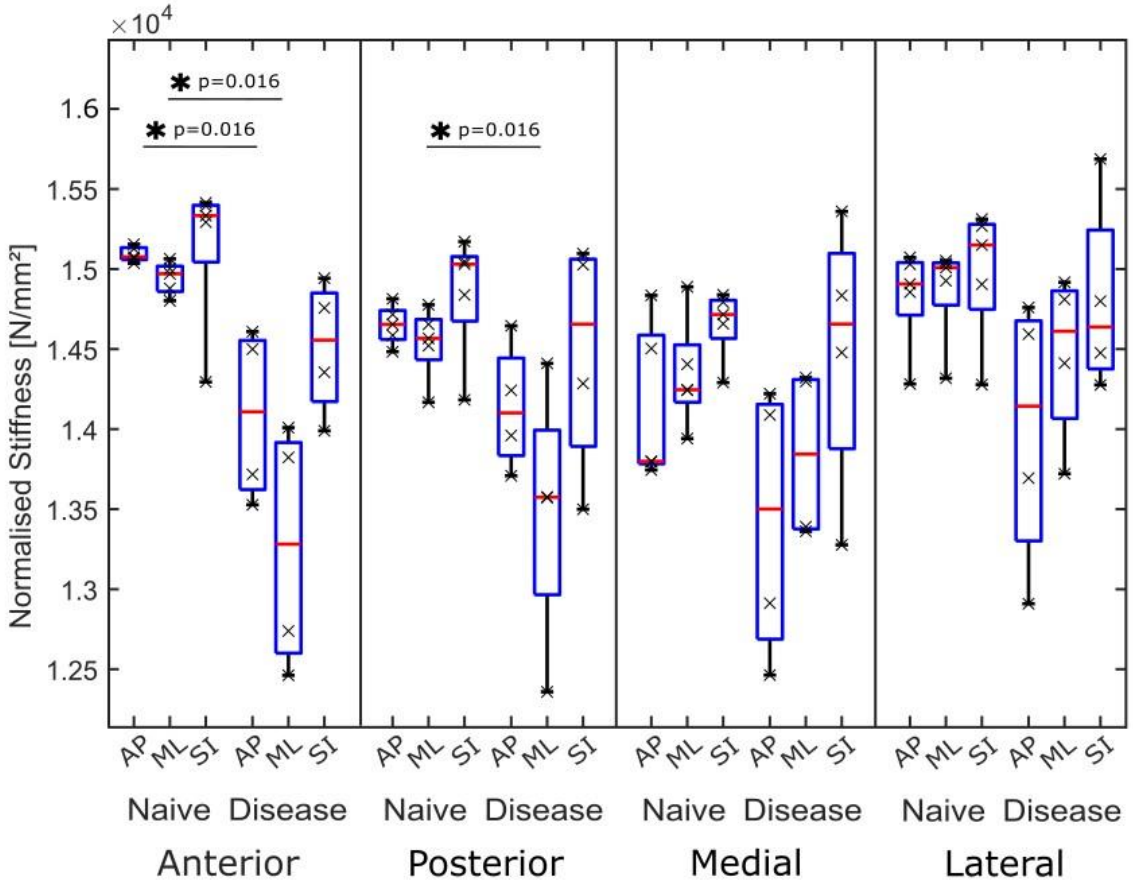

Figure B2: *The boxplots for the Naïve and Disease groups for each ROI loaded in each direction (superior-inferior (SI), medio-lateral (ML), anterior-posterior (AP)) and at each location (anterior, posterior, medial, lateral) within the bone for the normalised stiffness (N/mm^2). The * indicates significance, when tested with the non-parametric two-tailed Mann-Whitney U test, with a significance level of 0.05.*